Magnetic resonance with quantum microwaves

Audrey Bienfait

NNT : 2016SACLS297

THESE DE DOCTORAT
DE
L'UNIVERSITE PARIS-SACLAY
PREPAREE A
L'UNIVERSITE PARIS-SUD

ECOLE DOCTORALE N° 564
Physique de l'Ile de France

Spécialité de doctorat : Physique

Par
Audrey Bienfait

MAGNETIC RESONANCE WITH QUANTUM MICROWAVES

réalisée
dans le groupe QUANTRONIQUE
SPEC - CEA SACLAY
France

Thèse présentée et soutenue à Gif-sur-Yvette, le 14 octobre 2016.

Composition du Jury :

Prof. Jean-François Roch	Laboratoire Aimé-Cotton	Président du Jury
Prof. Gunnar Jeschke	ETH Zürich	Rapporteur
Prof. Wolfgang Wernsdorfer	Institut Néel	Rapporteur
Prof. Michel Pioro-Ladrière	Université de Sherbrooke	Examinateur
Prof. Andreas Wallraff	ETH Zürich	Examinateur
Dr. Patrice Bertet	SPEC, CEA-Saclay	Directeur de thèse

A papa,
c'est une grande joie que d'avoir marché (un petit peu) dans tes pas.

Remerciements

Beaucoup de personnes ont contribué à rendre ces trois années et demie passées dans le groupe Quantronique formidables et inoubliables, et je voudrais par ces quelques mots les remercier toutes très chaleureusement.

Il y a en premier ceux que j'ai cotoyés tous les jours et qui m'ont appris énormément. Merci tout d'abord à Patrice, pour ta disponibilité, ton incroyable clarté, ton optimisme et ta très grande gentillesse qui ont fait de ces mois passés au labo et à rédiger ce mémoire des moments chouettes, certes très riches en physique, parfois frustrants, mais aussi remplis d'enthousiasme et captivants! Si Patrice m'a appris la physique, c'est bien Yui que je dois remercier pour m'avoir appris bien des techniques expérimentales et de nano-fabrication (ainsi que de la mécanique!). Je n'aurais pas pu avoir un prof plus sympa, patient et rigoureux tout à la fois !
Merci aux permanents de Quantronique (au sens large): Carles, Cristian, Daniel, Denis, Fabien, Hélène, Hugues, Marcelo, Pascal, Philippe, et Pief, d'être aussi passionnés et passionnants, et d'avoir été aussi disponibles pour discuter, filer des coups de main et des encouragements.
Merci à la jeune génération qui a garanti la bonne ambiance à table, au labo et en-dehors: mes prédécesseurs Cécile, Olivier, et Vivien, les post-docs Xin, Michael, Sebastian, Philippe, Simon, Caglar, Marc et Leandro, mes co-thésards et « compagnons de rédaction » Kristinn (could not have picked a better office and car mate!), Camille, Pierre et Chloé, et enfin les tous derniers arrivants Bartolo et Fernanda.
Merci à ceux qui ont rendu possible cette thèse. Merci à l'atelier mécanique, Dominique, Jean-Claude et Vincent d'avoir réalisé toutes nos pièces même si elles étaient coriaces... Merci à l'atelier de cryogénie, Patrick, Philippe et Matthieu, les héros qui ont sauvé le cryostat (deux fois!) d'une situation plus que précaire; merci au secrétariat et à la direction du SPEC.

Il y a ensuite tous ceux qui ont contribué directement aux expériences qui sont présentées ici et avec qui j'ai interagi avec beaucoup de plaisir. Merci à toute l'équipe de Londres, Jarryd, Gary, Eva et John Morton, qui nous ont fait découvrir ce sacré champion de bismuth, « the new black stuff », et qui nous ont apporté tant d'idées fructueuses. Merci aussi à Klaus Mølmer, Brian Julsgaard et Alexander Holm-Kiilerich, nos collaborateurs théoriciens d'Aarhus, avec qui ce fut un plaisir de travailler par quelque moyen que ce soit (après avoir essayé Skype, Hangouts, RendezVous et autres, nous concluons d'ailleurs que le téléphone reste sacrément pratique!).

Finalement, je voudrais remercier ma famille, absents comme présents, et mes amis, pour leur encouragements et pouvoir avoir été là. Merci surtout à Félix, de m'avoir soutenue et supportée dans les moments difficiles, et d'avoir accepté mes horaires parfois incongrus, qui nous ont menés à commander bien trop de pizzas !

Contents

Remerciements iii

Résumé détaillé 1

1 Introduction 11
- 1.1 Circuit quantum electrodynamics for magnetic resonance . . . 11
- 1.2 Quantum microwaves and spin dynamics . . . 12
- 1.3 Electron spin resonance at the quantum-limit of sensitivity . . . 14
- 1.4 The Purcell effect applied to spins . . . 17
- 1.5 Squeezing-enhanced magnetic resonance . . . 18

I Background 20

2 Quantum circuits and quantum noise 21
- 2.1 Quantum microwaves and quantum circuits . . . 21
  - 2.1.1 Quantum description of an electromagnetic mode : quantum noise and quantum states . . . 21
  - 2.1.2 Lumped element LC resonator . . . 25
  - 2.1.3 Lossless transmission line . . . 26
  - 2.1.4 Probing and characterizing a resonator . . . 29
- 2.2 Amplification at the quantum-limit . . . 33
  - 2.2.1 Input-output relations for linear amplifiers . . . 33
  - 2.2.2 Quantum limits on the noise added by the amplifier . . . 35
  - 2.2.3 The flux-pumped Josephson Parametric Amplifier . . . 36

3 Spins in a cavity 40
- 3.1 Spin dynamics in a classical microwave field . . . 40
  - 3.1.1 Coherent spin evolution . . . 40
  - 3.1.2 Relaxation and decoherence . . . 42
  - 3.1.3 Inductive detection of magnetic resonance . . . 43
- 3.2 Spin dynamics in a quantum microwave field . . . 44
  - 3.2.1 One spin coupled to a harmonic oscillator . . . 45
  - 3.2.2 Collective effects . . . 50

4 Bismuth donors in silicon 54
- 4.1 A substitutional donor in silicon . . . 55
  - 4.1.1 Electronic states . . . 55
- 4.2 Spin levels and ESR-allowed transitions. . . . 58
- 4.3 Donors in strained silicon . . . 63
- 4.4 Relaxation times . . . 64
  - 4.4.1 T_1 relaxation . . . 64
  - 4.4.2 Coherence times . . . 67
- 4.5 Optical transitions via donor-bound exciton states . . . 69
- 4.6 Fabrication . . . 69

II Magnetic resonance at the quantum limit 71

5 Design and realization of a spectrometer operating at the quantum limit of sensitivity 72
5.1 Nanoscale ESR . . . 72
5.1.1 State-of-the-art . . . 72
5.1.2 Pulsed inductive detection at the nanoscale . . . 73
5.2 Experimental setup . . . 77
5.2.1 Low-temperature operation . . . 77
5.2.2 Room-temperature setup . . . 79
5.2.3 JPA characterization . . . 79
5.3 Design of a superconducting ESR resonator with high quality factor and small mode volume . . . 82
5.3.1 Design choices . . . 82
5.3.2 Electromagnetic simulations . . . 85
5.3.3 Coupling to bismuth donor spins . . . 85
5.3.4 Experimental implementation . . . 88

6 ESR spectroscopy of Bismuth donors in silicon 92
6.1 Hahn-echo detected ESR . . . 92
6.1.1 Experimental techniques . . . 92
6.1.2 Hahn-echo sequence . . . 93
6.1.3 Rabi oscillations . . . 94
6.2 Strain-broadened transitions . . . 97
6.2.1 Doublet-shaped transitions . . . 98
6.2.2 Rabi frequency dependence on B_0 . . . 99
6.2.3 Induced strain, a likely suspect . . . 101
6.3 Relaxation times . . . 103
6.3.1 Energy relaxation . . . 103
6.3.2 Coherence times . . . 104

7 Spectrometer sensitivity 105
7.1 Determining the number of spins . . . 105
7.1.1 Direct counting of the donors . . . 105
7.1.2 Estimate based on numerical simulations . . . 107
7.2 Characterization of the sensitivity . . . 112
7.2.1 Single-echo signal-to-noise ratio . . . 112
7.2.2 Sensitivity enhancement by CPMG echoes . . . 114
7.3 Conclusion . . . 115

III The Purcell effect applied to spins 116

8 Controlling spin relaxation with a cavity 117
8.1 Cavity-enhanced spontaneous emission . . . 118
8.1.1 Spontaneous emission into free space . . . 118
8.1.2 The Purcell effect . . . 120
8.1.3 Experimental realizations . . . 120
8.1.4 Spontaneous emission with spins . . . 121
8.2 Experimental implementation for electronic spins . . . 122
8.2.1 Cavity-spin system . . . 122
8.2.2 Experimental estimate of g . . . 123
8.2.3 T_1 at resonance . . . 124
8.3 Controlling spin relaxation . . . 125
8.3.1 Tuning T_1 via the spin-cavity coupling g_0 . . . 125

8.3.2 Tuning T_1 via the spin-resonator detuning . . . 127
8.4 Conclusion . . . 133

IV Squeezing-enhanced magnetic resonance **135**

9 Squeezing-enhanced magnetic resonance **136**
9.1 Squeezing-enhanced measurements . . . 136
9.1.1 State-of-the-art . . . 136
9.1.2 Squeezed states for magnetic resonance . . . 138
9.2 Detecting and characterizing microwave squeezed states . . . 141
9.2.1 Microwave squeezed-states . . . 141
9.2.2 Characterization of the flux-pumped JPA as a squeezing generator . . . 142
9.2.3 Noise reduction below the quantum limit with an ESR resonator . . . 145
9.2.4 Detection of displaced squeezed states . . . 146
9.3 An ESR signal emitted in squeezed vacuum . . . 147
9.3.1 Squeezing-enhanced ESR: proof-of-principle . . . 147
9.3.2 Absolute sensitivity . . . 148
9.3.3 Theoretical limit of a squeezing-enhanced ESR spectrometer . . . 150
9.4 Conclusion . . . 154

10 Conclusion and future directions **155**
10.1 Magnetic resonance with quantum microwaves . . . 155
10.2 Future research directions . . . 155

A Thermal occupancy calibration **159**

Bibliography **164**

Résumé détaillé

1 Électrodynamique quantique des circuits appliquée à la résonance magnétique

"Photon" et "spin" sont deux notions fondamentales apparues dés le début de la mécanique quantique et essentielles dans de nombreux domaines de recherche. La découverte par Rabi [1], Bloch [2] et Purcell [3] que les spins peuvent absorber ou émettre un rayonnement micro-onde quand ils sont couplés à un résonateur accordé à leur fréquence de précession de Larmor a donné par example naissance à la résonance magnétique, un domaine de recherche qui englobe à la fois la résonance magnétique nucléaire (RMN [4]) et la résonance paramagnétique électronique (RPE [5]). La résonance magnétique permet ainsi l'identification de spins présents dans un échantillon et l'étude de leurs interactions, donnant lieu à une compréhension plus profonde de la matière et de son organisation au niveau atomique. Cette puissante technique de spectroscopie a aujourd'hui un large éventail d'applications en biologie, chimie et science des matériaux, allant de la bio-imagerie non destructive à la découverte de médicaments [6]. Entre autres, elle a rendu possible le développement de l'information quantique, où les spins sont utilisés comme qubits, les porteurs quantiques de l'information [7].

Dans les expériences de résonance magnétique réalisées jusqu'à présent, les spins sont toujours traités comme des objets quantiques pour expliquer les interactions entre spins, leur cohérence et leurs mécanismes de relaxation, tandis que les champs micro-ondes utilisés pour les manipuler et les détecter sont seulement considérés comme des objets classiques. Ce traitement semi-classique de l'interaction spin-champ est justifié par deux éléments. Tout d'abord, le couplage des spins au rayonnement est généralement si faible que la nature quantique du champ micro-onde a des effets négligeables sur la dynamique des spins comparé à leur couplage aux vibrations du réseau cristallin ou à d'autres spins voisins. Deuxièmement, à la température où la plupart des expériences de résonance magnétique sont réalisées, les fluctuations micro-ondes du champ du vide sont négligeables par rapport aux fluctuations thermiques du champ – et l'absence d'un détecteur micro-onde suffisamment sensible empêche de toute façon leur détection. Ces deux derniers arguments sont étroitement liés à la faible sensibilité des spectromètres RPE: le faible couplage des spins au champ micro-onde nécessite l'utilisation d'un nombre conséquent de spins pour que le signal collecté devienne comparable le bruit expérimental, lui-même généralement largement supérieur au bruit quantique.

En revanche, dans le domaine de l'électrodynamique quantique en cavité (CQED [8]), les systèmes individuels à deux niveaux (TLS) interagissent de manière cohérente avec le champ électromagnétique. Le TLS peut être implémenté par des circuits supraconducteurs non-linéaires, les qubits "Josephson", interagissant avec des résonateurs micro-ondes à haut facteur de qualité dans une architecture appelée circuit-QED (cQED [9, 10]), prometteuse pour le calcul quantique. Au sein de cQED, de nouvelles techniques ont été développées pour la manipulation et la détection de l'état quantique du champ micro-onde. En particulier, des amplificateurs micro-ondes à très faible bruit ont été conçus pour la lecture des qubits Josephson. Ces amplificateurs paramétriques Josephson (JPA) ajoutent le bruit minimum requis par la mécanique quantique, allant jusqu'à pouvoir amplifier sans bruit une quadrature du champ [11, 12, 13]. Cette thèse rapporte **l'application des concepts et techniques de cQED à la détection RPE dans le but d'effectuer des expériences de résonance**

magnétique dans un nouveau régime, où les fluctuations quantiques du champ micro-onde ont un impact majeur sur la sensibilité du spectromètre et sur la dynamique des spins.

La première partie du mémoire vise à fournir les outils conceptuels nécessaires à la compréhension des expériences. Nous donnons une brève description des champs micro-ondes quantiques, des résonateurs, et de leur interaction avec un TLS – l'essence même de cQED. Ceci nous permet de présenter un traitement quantique de la détection d'un signal RPE. Nous présentons également les spins utilisés dans nos expériences : des donneurs de bismuth implantés dans le silicium (Si:Bi).

Dans la deuxième partie de cette thèse, nous présentons la conception et l'implémentation d'un spectromètre RPE à la sensibilité largement améliorée par les outils de CQED. Les éléments-clés de notre dispositif sont l'utilisation de températures cryogéniques, de l'ordre de quelques millikelvins, un résonateur supraconducteur de haut facteur de qualité et de petit volume de mode, fortement couplé à des spins Si:Bi, et un JPA qui amplifie le signal émis par les spins. Le bruit de sortie du spectromètre est entièrement dominé par les fluctuations quantiques du champ micro-onde, lui permettant d'atteindre une sensibilité de détection limitée quantiquement. Nous démontrons une sensibilité sans précédent de 2000 spins par séquence expérimentale [14], ce qui représente une amélioration de quatre ordres de grandeur par rapport à l'état de l'art [15].

Les très basses températures utilisées dans nos expériences ont pour avantage supplémentaire de polariser entièrement l'ensemble de spins lors de leur détection RPE. Néanmoins, elles peuvent également augmenter de façon spectaculaire le temps de relaxation spin-phonon [16], conduisant à des taux de répétition beaucoup trop faibles pour mettre en pratique nos expériences. Dans la troisième partie de cette thèse, nous démontrons que le couplage des spins à un résonateur RPE de haut facteur de qualité et de petit volume de mode conduit à exacerber la relaxation des spins par émission spontanée de photons micro-ondes jusqu'à en faire le mécanisme de relaxation dominant, avec un taux nettement supérieur au taux de relaxation par phonons. Ce phénomène, bien connu en CQED et prédit par Edwin Purcell en 1946, est ainsi observé pour des spins électroniques pour la première fois [17].

Comme déjà mentionné, les fluctuations du vide du champ micro-onde sont la seule source de bruit de notre spectromètre. Bien que cela semble représenter une limite fondamentale à sa sensibilité, ce seuil peut être surmonté en utilisant des états quantiques dits comprimés, bien connus en optique quantique [18, 19, 20]. Pour de tels états quantiques du champ, le bruit sur une quadrature est réduit au-dessous du niveau de vide alors que le bruit sur l'autre quadrature est augmenté afin de respecter l'inégalité de Heisenberg. Nous rapportons dans la quatrième partie de cette thèse l'utilisation d'états micro-ondes comprimés pour améliorer la sensibilité de notre spectromètre RPE au-delà de la limite quantique.

2 Micro-ondes quantiques et dynamique de spins

Il existe plusieurs raisons justifiant un traitement quantique du champ micro-onde lors d'une expérience de résonance magnétique. Un signal micro-onde classique de fréquence ω est décrit par son amplitude A et sa phase ϕ, ou de manière équivalente par ses quadratures $X = A\cos(\phi)$ et $Y = A\sin(\phi)$. Dans une description quantique, détaillée dans le ch. 2, les variances des quadratures[1] du champ respectent l'inégalité de Heisenberg $\sqrt{\langle \Delta X^2 \rangle \langle \Delta Y^2 \rangle} \geqslant 1/4$. Par conséquent, même à des températures suffisamment basses pour que le champ micro-onde soit dans son état fondamental, des fluctuations persistent. En exprimant les fluctuations du champ pour une température T par la quantité adimensionnelle $n_{\mathrm{eq}}(T) = \langle \Delta X^2 \rangle$, les fluctuations du vide se caractérisent par l'atteinte d'un minimum $n_{\mathrm{eq}} = 1/4$ (voir Fig.1a). Ces fluctuations du vide représentent donc une limite fondamentale pour la sensibilité de nombreuses mesures, en particulier pour la spectroscopie RPE.

[1] réécrites dans des unités sans dimension, telles que $\hbar\omega(\langle X^2 \rangle + \langle Y^2 \rangle)$ est égal à l'énergie du mode du champ

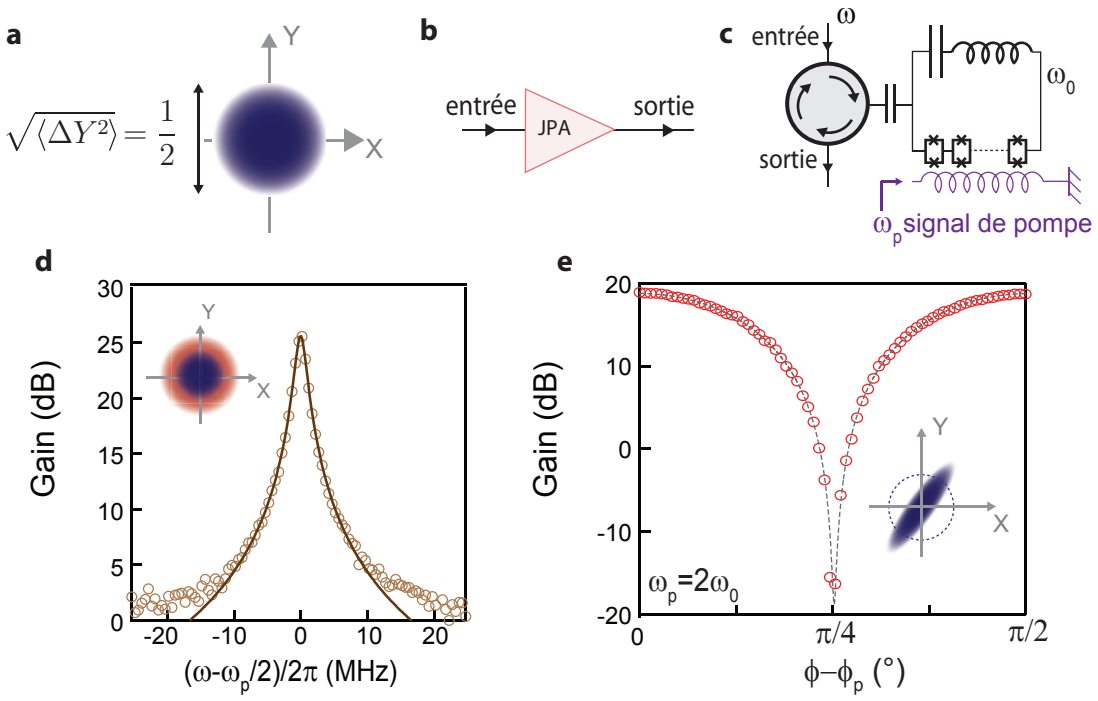

FIGURE 1: **Fluctuations quantiques et limite quantique à l'amplification a** A des températures $k_B T \ll \hbar\omega$, le champ micro-onde est refroidit dans son état fondamental : ses quadratures ont pour variance $\sqrt{\langle \Delta X^2 \rangle} = \sqrt{\langle \Delta Y^2 \rangle} = 1/2$, correspondant au minimum de fluctuations autorisées pour le champ (disque bleu). **b-c** Un amplificateur paramétrique Josephson, implémenté ici par un résonateur comprenant un réseau de SQUIDs et pompé en flux, peut être utilisé pour détecter des champs micro-ondes quantiques. **d** Utilisé en mode non-dégénéré ($\omega_p \neq 2\omega$), le JPA ajoute un demi-photon de bruit (disque rouge) au demi-photon de bruit (disque bleu) correspondant aux fluctuations du vide à l'entrée du JPA. **e** En mode dégénéré ($\omega_p = 2\omega$), le JPA amplifie une quadrature aux dépends de l'autre; dans ce cas l'amplification est sans bruit. Agissant sur le vide, le JPA crée un état comprimé, ayant des fluctuations réduites en-dessous du niveau du vide sur une quadrature mais amplifiées sur l'autre (ellipse bleue).

Les développements réalisés par cQED fournissent les outils nécessaires pour détecter les fluctuations micro-ondes quantiques. Comme plusieurs ordres de grandeur séparent la faible puissance des signaux micro-ondes quantiques et le niveau de bruit typique des appareils de mesure à température ambiante, il est nécessaire d'amplifier les signaux. Lors de l'amplification, la mécanique quantique impose certaines contraintes sur le bruit n_{amp} ajouté à la quadrature X (également exprimé en unités adimensionnelles). Cette théorie quantique de l'amplification est présentée au ch. 2. Les amplificateurs paramétriques Josephson ont été conçus précisément pour ajouter le moins de bruit possible et opérer près de la limite quantique. Ils sont donc des éléments-clés dans les mesures micro-ondes de haute sensibilité. Dans ce travail, nous utilisons un JPA, représenté schématiquement Fig. 1c, et dont la conception est expliquée au ch. 2. Notre JPA est constitué d'un résonateur comprenant un réseau de SQUIDs et d'une ligne de pompe permettant de moduler le flux magnétique traversant les SQUIDs. Un signal micro-onde de pompe de fréquence $\omega_p \approx 2\omega$ envoyé sur cette ligne crée un gain paramétrique pour un signal de fréquence ω. Ce JPA pompé en flux possède deux modes de fonctionnement. Si $\omega_p \neq 2\omega$ (mode "non-dégénéré"), les deux quadratures du signal sont amplifiées et $n_{\text{amp}} = 1/4$ de sorte que le bruit total détecté $n = n_{\text{eq}} + n_{\text{amp}}$ sur une quadrature est $n = 1/2$. Si $\omega_p = 2\omega$ (mode "dégénéré"), une seule quadrature est amplifiée, ce qui permet d'échapper à la limite quantique à l'amplification avec $n_{\text{amp}} = 0$ et $n = n_{\text{eq}} = 1/4$. Les JPAs ont été utilisés pour détecter l'état de qubits supraconducteurs [21], d'oscillateurs nanomécaniques [22], l'état de charge

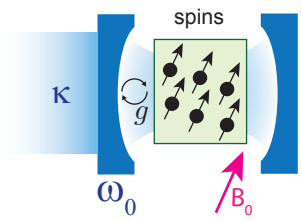

FIGURE 2: **Description quantique de l'interaction spin-photon.** Un ensemble de spins placé dans une cavité de fréquence ω_0 et de facteur de qualité $Q = \omega_0/\kappa$ interagit avec une force d'interaction g avec le champ micro-onde.

d'une boîte quantique [23], ainsi que pour améliorer la sensibilité de mesures de magnétométrie [24]. Fonctionnant à des fréquences gigaHerz, ils sont facilement utilisables pour l'amplification des faibles signaux micro-ondes émis par les spins comme cela est montré dans la deuxième partie de cette thèse. Ils peuvent également générer des états comprimés, qui ont moins de fluctuations sur une quadrature que le vide, au prix de fluctuations accrues sur l'autre quadrature de sorte à satisfaire l'inégalité de Heisenberg (voir Fig. 1d). Nous utilisons ces états pour effectuer des mesures au-delà de la limite quantique dans la quatrième partie.

Les fluctuations quantiques du champ sont également essentielles pour décrire l'interaction entre les spins et le champ micro-onde d'un résonateur de fréquence ω_0 et de facteur de qualité Q. Le paramètre-clé décrivant cette interaction est la constante de couplage spin-photon notée g, qui est le produit du moment dipolaire magnétique d'un spin et les fluctuations du vide du champ magnétique à l'emplacement du spin. Au ch. 3, nous utilisons le modèle de Jaynes-Cummings pour décrire les expériences de résonance magnétique, où un ensemble de spins est placé dans un résonateur micro-onde (voir Fig. 2). Contrairement à la plupart des expériences cQED, les expériences de résonance magnétique ont lieu dans le régime de couplage faible où $g \ll \kappa$, avec $\kappa = \omega_0/Q$. Nous montrons que dans cette limite, une description semi-classique de la dynamique des spins est suffisante, pourvu qu'elle soit complétée par un mécanisme de relaxation supplémentaire: l'émission spontanée de photons micro-ondes par le spin dans le résonateur, déclenchée par les fluctuations quantiques de le champ. Le taux de relaxation de cet effet, appelé effet Purcell, est:

$$\Gamma_p = \kappa \frac{g^2}{\Delta^2 + \kappa^2/4}$$

où Δ est le désaccord fréquentiel entre le spin et le résonateur. Bien que cette relaxation radiative de spin ait toujours été négligée par rapport à d'autres mécanismes de relaxation de spins, nous montrons dans la troisième partie qu'elle peut devenir le mécanisme dominant pour des spins placés dans un résonateur à haut facteur de qualité et petit volume de mode. L'utilisation du modèle de Jaynes-Cummings permet aussi d'exprimer le champ émis par les spins dans le guide d'onde de détection: $\langle X \rangle = 2g/\sqrt{\kappa}\langle S_- \rangle$ (voir ch. 3). La maximisation du signal de sortie est donc obtenue dans les mêmes conditions que la maximisation de l'émission spontanée par l'effect Purcell, à savoir l'utilisation d'un résonateur de petit mode volume et de haut facteur de qualité.

Dans cette thèse, nous présentons trois expériences de résonance magnétiques où l'impact des fluctuations micro-ondes quantiques est mis en évidence. Pour réaliser nos expériences, nous utilisons le spin des donneurs de bismuth du silicium. Ces donneurs sont des atomes du réseau cristallin du silicium. A basse température, ils sont à l'état neutre grâce au piégeage d'un électron de la bande de conduction du silicium (voir Fig. 3 a). Les propriétés-clés de ces systèmes sont leur long temps de cohérence (pouvant atteindre des secondes [25]), et l'existence d'une séparation de 7.4 GHz entre les niveaux de spin électronique à champ nul [26]. Il est donc possible de coupler des spins Si:Bi à des résonateurs supraconducteurs en utilisant de faibles champs magnétiques (< 10 mT), compatibles avec la plupart des matériaux supraconducteurs et en particulier l'aluminium utilisé

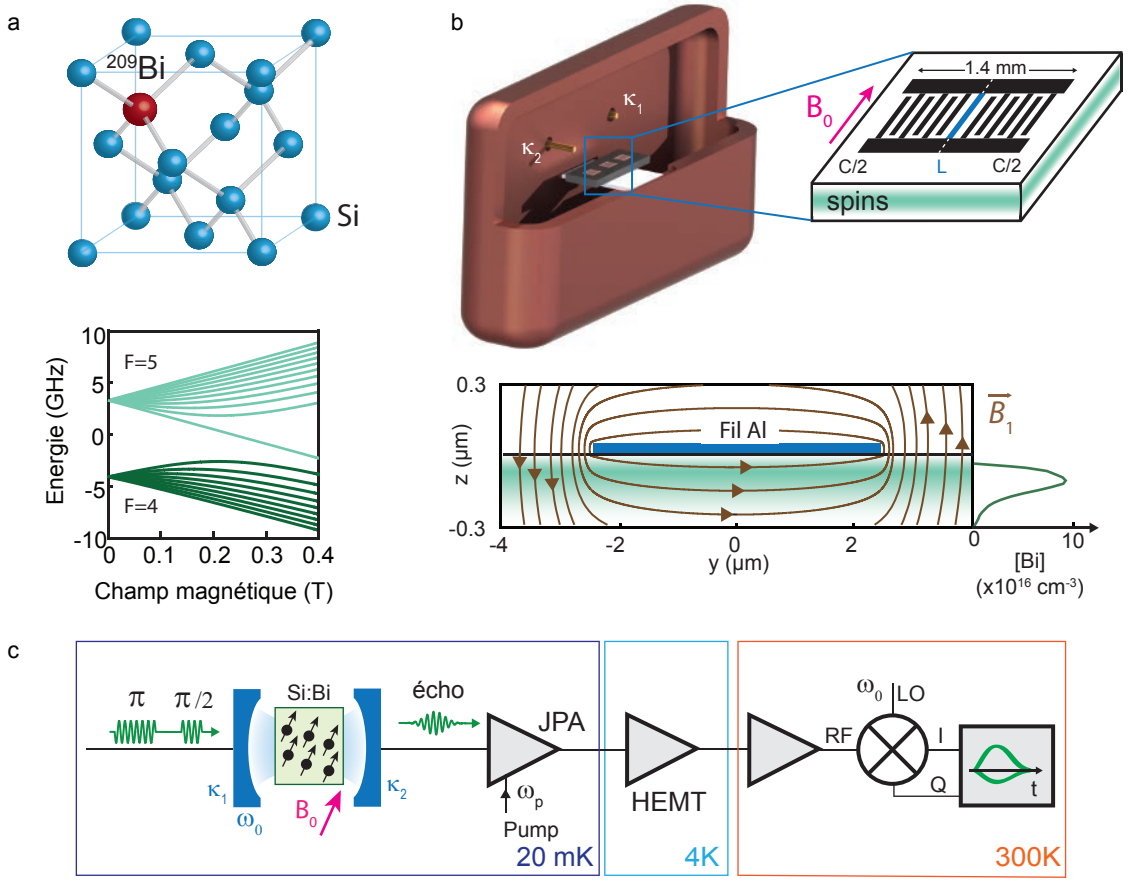

FIGURE 3: **RPE limitée quantiquement : principe et dispositif expérimental. a** Un donneur de bismuth dans le silicium est un atome de bismuth substitué dans le réseau cristallin du silicium. A l'état neutre, il piège un électron de la bande de conduction, responsable du signal RPE. Les vingt niveaux d'énergie des donneurs de bismuth à l'état neutre, représentes ici en fonction du champ statique magnétique appliqué, sont le fruit d'une interaction hyperfine conséquente entre le spin $S = 1/2$ de l'électron piégé et le spin nucléaire $I = 9/2$ de l'atome de bismuth. En particulier, il y a une levée de dégénérescence de 7.4 GHz entre deux groupes de niveaux à champ nul. **b** Le résonateur RPE est un dispositif planaire réalisé en aluminium et composé d'une capacité interdigitée placée en parallèle d'un fil inductif large de 5 microns et fabriqué directement sur le substrat de silicium implanté en atomes de bismuth. L'échantillon comprend trois résonateurs quasi-identiques; il est mesuré via un porte-échantillon en cuivre assurant un couplage capacitif aux lignes de mesures via des antennes micro-ondes. **c** Les spins, thermalisé à 20 mK, sont détectés via des impulsions micro-ondes envoyées au résonateur déclenchant l'émission d'un écho de spin dans la ligne de détection micro-onde. Le signal d'écho de spin est amplifié d'abord par un JPA puis par un HEMT à 4 K avant d'être amplifié et démodulé à température ambiante.

dans ce travail. Nous décrivons la structure et les propriétés des donneurs de bismuth dans le silicium au ch. 4.

3 Détection de signaux RPE avec une sensibilité limitée quantiquement

Dans la deuxième partie de la thèse, nous présentons la conception et la réalisation d'un spectromètre RPE dont la sensibilité est largement améliorée par l'utilisation des techniques et des concepts cQED. Comme tous les spectromètres RPE existants, notre dispositif expérimental se compose d'un résonateur de fréquence ω_0 et de facteur de qualité Q couplé à un ensemble de spins dont la fréquence de Larmor est accordée au résonateur par l'application d'un champ magnétique externe B_0. L'application d'impulsions micro-ondes à résonance génère une aimantation de spin transverse qui conduit à l'émission de signaux micro-ondes généralement appelés "échos". La séquence de RPE la plus connue, l'écho de Hahn, se compose d'une impulsion $\pi/2$ suivie après un délai τ d'une impulsion π qui conduit à un rephasage des spins après un second délai τ et à l'émission d'un écho de Hahn. La sensibilité d'un spectromètre est caractérisée par le nombre minimum de spins $N_{\min}$ détectables par écho de Hahn avec un rapport signal sur bruit (SNR) unité.

Sur la base des concepts introduits dans la première partie, nous dérivons au ch. 5 une expression quantitative de $N_{\min}$, qui met en évidence les quantités à optimiser pour améliorer la sensibilité d'un spectromètre RPE. Ainsi, la constante de couplage spin-photon g et le facteur de qualité du résonateur Q doivent être maximisés; l'utilisation de températures cryogéniques conduit à une polarisation accrue des spins et à un bruit réduit. Les spectromètres usuels utilisant des résonateurs tridimensionnels à température ambiante ont une sensibilité typique de $N_{\min} \approx 10^{13}$ spins. Ce nombre a été considérablement réduit en utilisant des résonateurs supraconducteurs de taille micronique refroidit à 4 K et des amplificateurs possédant des températures de bruit de l'ordre de 4 K, donnant lieu à des sensibilités mesurées de $N_{\min} = 10^7$ spins [15].

Aux ch. 5-7, nous présentons notre implémentation d'un spectromètre RPE utilisant les outils de cQED, et en particulier l'amplification micro-onde à la limite quantique. Le spectromètre est basé sur un résonateur à éléments discrets supraconducteur de haut facteur de qualité, fabriqué sur un substrat de silicium qui contient l'ensemble des spins Si:Bi. Le résonateur est placé dans un porte-échantillon de cuivre et couplé capacitivement aux antennes d'excitation et de détection (voir Fig. 3b). La géométrie du résonateur est conçue pour que le couplage spin-photon atteigne $g/2\pi \approx 50$ Hz et l'échantillon est thermalisé à 20 mK pour obtenir une polarisation de spin totale. Le signal d'écho de spin est amplifié par un JPA, suivi d'une amplification supplémentaire à 4 K et à température ambiante (voir Fig. 3c). Le ch. 5 décrit la conception et la mise en œuvre expérimentale du spectromètre.

Nous utilisons ce dispositif expérimental pour effectuer une spectroscopie détaillée des spins Si:Bi (voir Fig. 4a&c) ainsi que des mesures du temps de cohérence (voir Fig. 4b). Nous observons une forme de ligne inhabituelle, où chaque résonance apparait sous la forme d'un double pic asymétrique. Au ch. 6, nous soutenons que cette forme de raie est due aux contraintes mécaniques induites dans le substrat par les contractions thermiques du film d'aluminium déposé sur le silicium.

Au ch. 7, nous caractérisons la sensibilité du spectromètre. Par des mesures précises du rapport signal sur bruit (voir Fig. 4c-d), complétées par des simulations numériques, nous démontrons une sensibilité sans précédent de 2000 spins détectables par écho avec un signal sur bruit unité. Ceci représente une amélioration de quatre ordres de grandeur par rapport à l'état de l'art de la détection RPE {[15], obtenue grâce à l'utilisation combinée de températures cryogéniques permettant la polarisation totale des spins, le grand facteur de qualité et le petit volume de mode du résonateur, et le JPA.

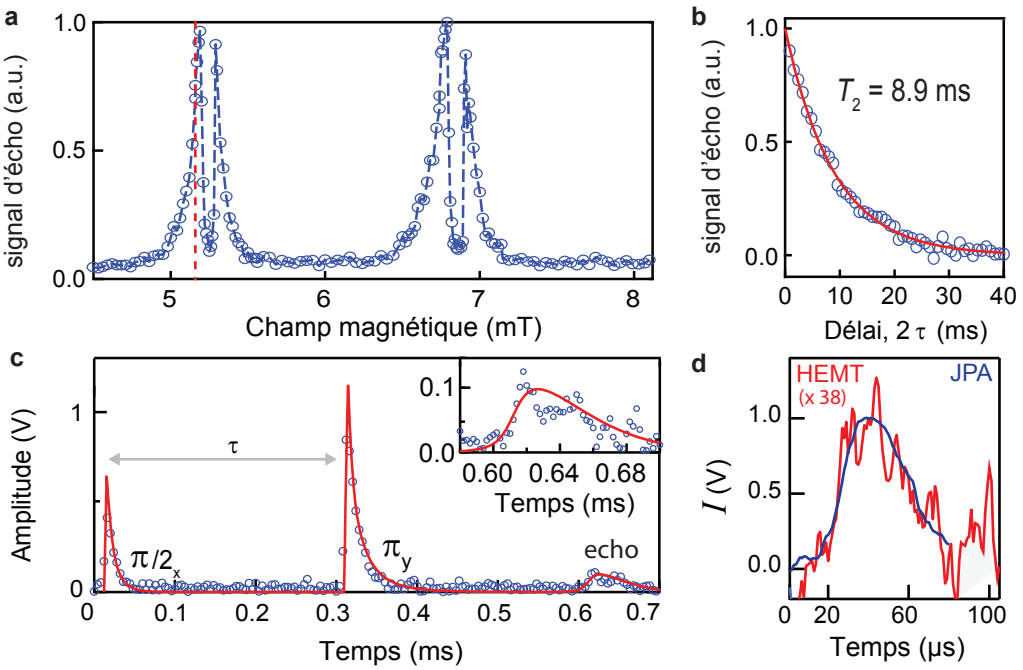

FIGURE 4: **RPE limitée quantiquement : principaux résulats. a** Spectroscopie par écho de Hahn de deux transitions consécutives des spins Si:Bi, mettant en évidence deux doublets asymétriques, au lieu des deux raies gaussiennes attendues. **b** Un temps de cohérence $T_2 = 8.9$ ms est mesuré à $B_0 = 5.13$ mT. **c** Séquence d'écho de Hahn mesurée à $B_0 = 5.13$ mT. Les points bleus sont les points expérimentaux, ajustés par un modèle numérique (ligne rouge continue) démontrant que 1.2×10^4 spins sont excités par la première impulsion $\pi/2$. **d** Le JPA apporte une amélioration d'un facteur dix du signal sur bruit.

4 Effet Purcell appliqué aux spins

Un autre élément-clé de la sensibilité est le taux de répétition de la mesure. Aux basses températures où sont réalisées nos expériences, le taux de relaxation des spins peut devenir extrêmement faible, limitant de fait la sensibilité absolue du spectromètre. Au ch. 8, nous proposons l'effet Purcell comme mécanisme de relaxation universel, pouvant s'appliquer à n'importe quel type de spins [27], apportant ainsi une solution au problème de la ré-initialisation des spins. Cet effet est induit par les fluctuations quantiques du champ micro-onde de la cavité, comme évoqué plus tôt. L'émission spontanée, renforcée par la concentration du champ permise par la cavité, offre aux spins un nouveau canal de relaxation pour atteindre l'équilibre thermique lorsqu'ils sont accordés à résonance avec la cavité. L'effet Purcell est employé couramment pour contrôler le temps de vie d'autres TLS, notamment d'atomes [28] et d'hétérostructures semiconductrices [29] insérés dans des cavités micro-ondes et/ou optiques. C'est aussi un des principes-clés pour la réalisation de sources de photons uniques brillantes [30]. Pour des spins néanmoins, leur faible couplage au champ électromagnétique de l'espace libre rend leur temps de relaxation par émission spontanée tout à fait négligeable comparé aux autres mécanimes de relaxation possibles.

Cependant, nous montrons au ch. 8 que pour notre géométrie un taux $\Gamma_p \approx 3\ \mathrm{s}^{-1}$ est attendu. Une mesure expérimentale du temps T_1 en utilisant notre dispositif donne $T_1 = 0.35$ s pour des spins à résonance, comme illustré sur la Fig. 5b. Une conséquence directe est que toutes nos mesures peuvent être répétées à un taux de 1 Hz; le spectromètre décrit au-dessus a donc une sensibilité absolue de 1700 spins/$\sqrt{\mathrm{Hz}}$.

Même si le temps T_1 mesuré expérimentalement est similaire à celui attendu par la théorie, nous réalisons deux expériences supplémentaires prouvant définitivement que l'effet Purcell est bien

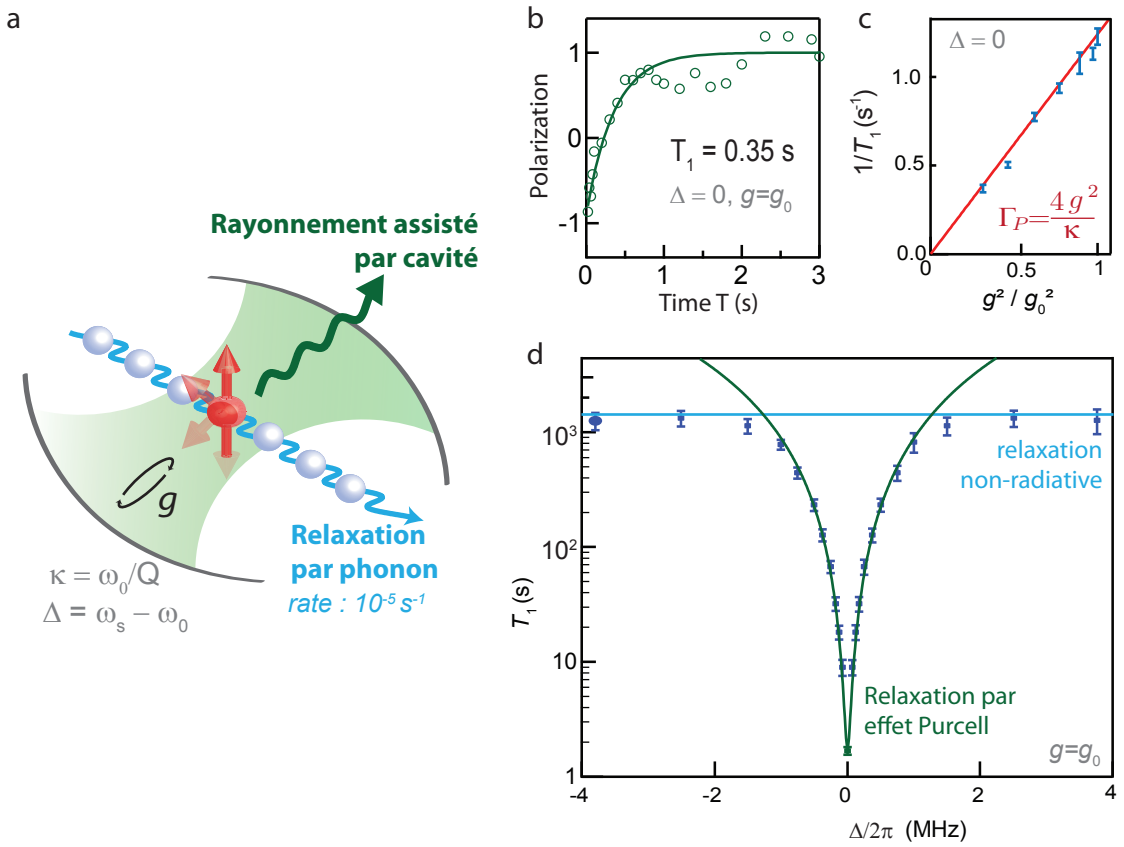

FIGURE 5: **Observation de l'effet Purcell pour des spins a** Un spin placé dans une cavité résonante peut voir sa relaxation par émission spontanée devenir le mécanisme de relaxation dominant, devant d'autres processus intrinsèques comme la relaxation par phonon. **b** Pour des spins Si:Bi accordés à résonance en utilisant le setup de la Fig. 3, l'effet Purcell induit un temps de relaxation de $T_1 = 0.35$ s. **c** Temps de relaxation T_1 en fonction de g^2; la ligne continue est un ajustement linéaire. **d** Une augmentation de T_1 sur trois ordres de grandeur est démontrée en désaccordant les spins de moins de 0.2 mT, jusqu'à ce qu'un processus non-radiatif devienne plus efficace que l'effet Purcell, et place une borne supérieure au temps T_1 de 1500 s.

le mécanisme de relaxation dominant dans notre dispositif. Premièrement, nous montrons que le temps T_1 varie linéairement en fonction de g^{-2} (cf Fig. 5c), conformément à l'expression de Γ_p à résonance. Deuxièmement, la Fig. 5d démontre une variation lorentzienne de T_1 en fonction du désaccord Δ. En contrôlant Δ, T_1 augmente de trois ordres de grandeur, jusqu'à un maximum de 1500 s. Au-delà, T_1 devient indépendant de Δ, mettant en évidence qu'un autre mécanisme de relaxation, non-radiatif, devient dominant.

Nous concluons cette troisième partie par une discussion brève des applications possibles de cette émission spontanée assistée par cavité.

5 États comprimés et résonance magnétique

Dans un spectromètre RPE à la limite quantique, le bruit provient presque entièrement des fluctuations quantiques du champ micro-onde. Il est possible de réduire ces fluctuations en utilisant des état quantiques comprimés. Cette idée de mesures au-delà de la simple limite quantique a été proposée

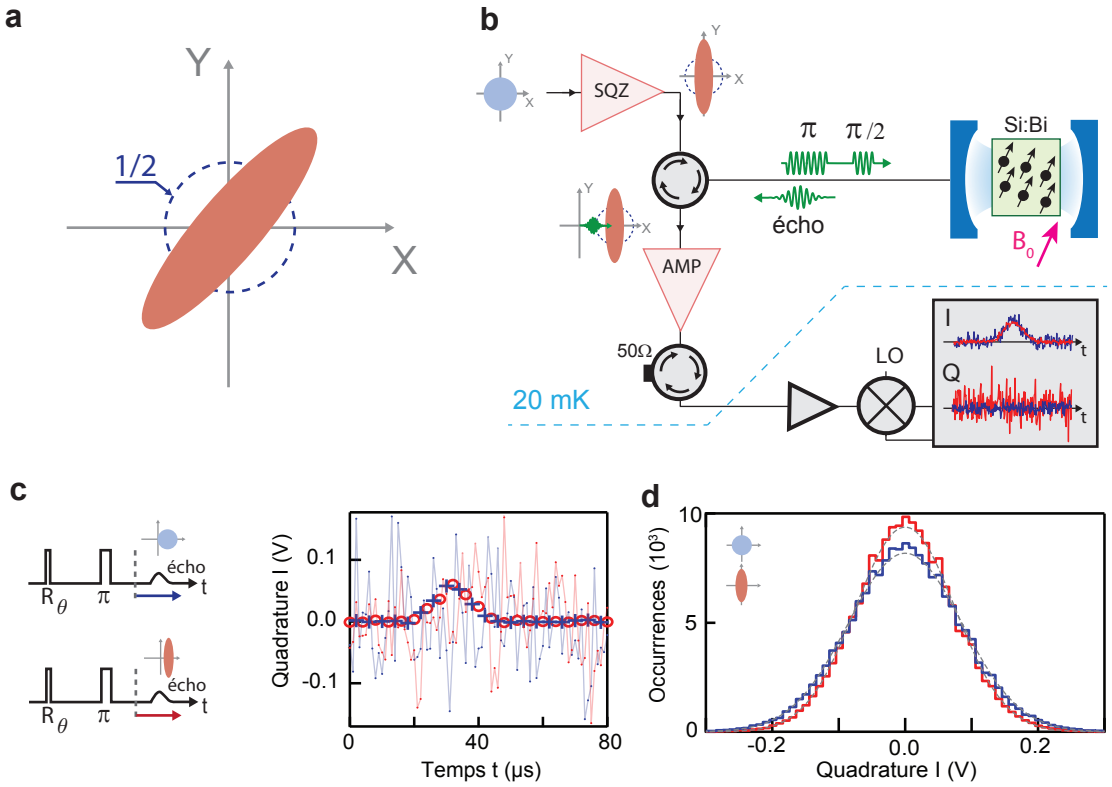

FIGURE 6: **Amélioration de la sensiblité d'une détection RPE par des états comprimés.** **a** Un état comprimé a moins de fluctuations sur une quadrature que le vide. **b** Un état comprimé incident sur un résonateur RPE peut réduire le bruit quantique pendant la détection d'un écho de spin. **c** Un signal d'écho mesuré en utilisant ou non un état comprimé est détecté avec la même amplitude mais son histograme de bruit est réduit, comme illustré en **d**.

d'abord par Caves [18] pour des mesures d'interférométrie. Un état comprimé possède moins de fluctuations que le vide sur une quadrature, l'autre quadrature ayant plus de fluctuations de sorte à satisfaire l'inégalité de Heisenberg (voir Fig. 6a). Depuis, des champs optiques comprimés ont été mesurés [19] et utilisés pour améliorer la sensibilité de la mesure dans diverses expériences, allant des détecteurs d'ondes gravitationnelles [31] à la magnétométrie par gaz atomiques [32]. Ils ont été aussi générés à des fréquences micro-ondes [33] et utilisés lors d'expériences fondamentales sur l'interaction lumière-matière [34] ainsi que pour la détection de résonateurs nano-mécaniques [35].

Dans la quatrième partie de cette thèse, nous utilisons un champ micro-onde comprimé, schématisé Fig. 6b pour améliorer la sensibilité de notre spectromètre au-delà de la limite quantique. Notre expérience consiste à générer un état du vide comprimé en incidence du résonateur RPE lors de l'émission d'un écho de Hahn par les spins. La quadrature comprimée est mise en correspondance avec la quadrature d'émission de l'écho, ce qui mène à une réduction du bruit détecté. L'état comprimé est généré par un deuxième JPA - noté SQZ - placé en amont du résonateur.

Les résultats principaux sont montrés Fig. 6. Premièrement, l'amplitude moyennée de l'écho est conservée en présence de compression du vide (cf Fig. 6c). Cependant, les histogrammes de bruit révèlent que le bruit est effectivement réduit pendant la détection (cf Fig. 6d). Le fait que le signal est inchangé mais que le bruit diminue démontre une amélioration significative du signal sur bruit d'un facteur 1.12. C'est aussi une preuve de principe qu'une détection RPE au-delà de la limite quantique est possible. L'amélioration modeste du signal sur bruit est due au faible taux de compression atteint,

principalement limité par les pertes micro-ondes présentes dans le dispositif. Nous concluons cette partie en analysant les limites de cette mise en œuvre expérimentale d'états comprimés pour la détection RPE, et il apparait qu'en principe une amélioration du signal sur bruit de 10 dB pourrait être envisageable.

Chapter 1

Introduction

1.1 Circuit quantum electrodynamics for magnetic resonance

Photons and spins are two fundamental concepts born in the early days of quantum mechanics and are key in many active research fields. The discovery that spins can absorb or emit microwave radiation when coupled to a resonator matched to their Larmor precession frequency by Rabi [1], Bloch [2] and Purcell [3] gave birth to the field of magnetic resonance, which encompasses both magnetic resonance of nuclear (NMR [4]) and electronic (ESR[5]) spins. Magnetic resonance made it possible to identify spin species contained in a sample and study their interactions, leading to a deeper understanding of matter and its organisation at the atomic level. These powerful spectroscopy techniques have nowadays a wide range of applications throughout biology, chemistry and materials science, ranging from non-destructive bio-imaging [36] to drug discovery [6]. Another application is Quantum Information Processing (QIP), where the spins are used as "qubits", the carriers of quantum information [7].

In all magnetic resonance experiments so far, independently of the application, spins are always treated quantum mechanically for what regards spin-spin interactions, spin coherence and spin relaxation phenomena, while the microwave fields used to manipulate and detect them are described classically. This semi-classical treatment of the spin-field interaction is justified by two facts. First, the spin-photon coupling is generally so weak that the quantum nature of the microwave field has negligible effects on the spins dynamics compared to their coupling to the lattice vibrations or to other neighboring spins. Second, at the temperature where most magnetic resonance experiments are realized, the vacuum fluctuations of the microwave field are negligible compared to thermal fluctuations; moreover, the lack of a microwave detector with high quantum-efficiency prevents their detection. These two arguments are closely related to the poor sensitivity of ESR spectrometers: it is because spins are weakly coupled to the microwave field that a successful detection requires a large number of spins for the collected signal to overcome the experimental noise, which itself is largely above the quantum noise limit.

In stark contrast, in the field of Cavity Quantum ElectroDynamics (CQED, [8]), individual two-level systems (TLS) interact coherently with the electromagnetic field at the single-photon level. The TLS can be implemented by superconducting non-linear circuits called Josephson qubits, interacting with high-quality factor microwave resonators in an architecture called Circuit-QED (cQED, [9, 10]) which is promising for quantum computing. Within cQED, novel techniques have been developed to engineer and detect the quantum state of the microwave field; in particular, ultra-low-noise microwave amplifiers have been developed for the readout of Josephson qubits. These Josephson Parametric Amplifiers (JPA) add as little noise to the signal as quantum mechanics allows, and they are in fact able to amplify noiselessly one quadrature of the field [11, 12, 13]. This thesis reports **the application of cQED techniques and concepts to ESR in order to perform magnetic resonance experiments in a novel regime where quantum fluctuations of the microwave field have a major influence on the spectrometer sensitivity as well as on the spin dynamics.**

The first part of the manuscript aims at providing the conceptual tools needed to understand the experiments. We give a brief account of the quantum description of microwave fields and resonators, and of their interaction with TLS, which is the essence of cQED. This allows us to present a quantum treatment of ESR spectroscopy detection. We also present the spin-system with which all the experimental work was realized: bismuth donors in silicon.

In the second part of this thesis, we present the design and physical realization of a "circuit-QED-enhanced" ESR spectrometer. It relies on a high-quality factor superconducting resonator of small mode volume, strongly coupled to bismuth donor spins, and on a JPA that amplifies the spin signal. The output noise of this spectrometer is entirely set by quantum fluctuations of the microwave field; in that sense, it reaches the quantum limit of sensitivity. We demonstrate an unprecedented sensitivity of 2000 spins per experimental sequence [14], which represents a four orders of magnitude improvement compared to the state-of-the-art [15].

Performing ESR at millikelvin temperatures has the additional benefit that the spin ensemble is fully polarized at thermal equilibrium. However, such low temperatures can also increase dramatically the spin-lattice relaxation time [16] leading to impractically low repetition rates. In the third part of this thesis, we demonstrate that the coupling of the spins to an ESR resonator of high-quality-factor and small-mode-volume leads to a strong enhancement of the rate at which they relax to their ground state by spontaneously emitting a microwave photon, to the point where it becomes a spin relaxation mechanism more efficient than phonon emission. This phenomenon, well-known in CQED and predicted by Purcell in 1946, is observed with spins for the first time [17].

As already discussed, the only remaining source of noise in our spectrometer is the vacuum fluctuations of the microwave field. Although this seems to represent a fundamental limit for sensitivity, it is known from quantum optics that this limit can be overcome using so-called quantum squeezed states [18, 19, 20]. In such quantum states of the field, the noise on one quadrature is reduced below the vacuum level whereas the noise on the other quadrature is increased to fulfill Heisenberg uncertainty principle. We report in part four the use of microwave squeezed states to enhance the sensitivity of our ESR spectrometer beyond the quantum-limit.

1.2 Quantum microwaves and spin dynamics

There are multiple reasons for a quantum treatment of microwave fields to become relevant in magnetic resonance experiments. A classical microwave signal at frequency ω is described by its amplitude A and its phase ϕ, or equivalently by its in-phase and out-of-phase quadratures $X = A\cos(\phi)$ and $Y = A\sin(\phi)$. In a quantum-mechanical description outlined in ch. 2, the quadrature[1] variances are constrained by the Heisenberg inequality $\sqrt{\langle \Delta X^2 \rangle \langle \Delta Y^2 \rangle} \geqslant 1/4$. As a consequence, even at low temperatures $k_B T \ll \hbar\omega$ where the field is in its quantum-mechanical ground state, fluctuations remain. Expressing the amount of fluctuations per quadrature for a microwave field at temperature T by the dimensionless quantity $n_{\mathrm{eq}}(T) = \langle \Delta X^2 \rangle$, the vacuum fluctuations are characterized by reaching the minimum value of $n_{\mathrm{eq}} = 1/4$ (see Fig.1.1a). These vacuum fluctuations thus represent a fundamental limit to the sensitivity of many measurements, and in particular to ESR spectroscopy.

A major progress brought by cQED is to provide the tools needed to detect quantum microwave fluctuations. As several orders of magnitudes separate the small power of the quantum microwave signals and the noise figure of typical room-temperature measurement apparatus, it is essential for the signal to be amplified. Upon amplification, quantum mechanics "takes its due a second time", by imposing some constraints on the noise n_{amp} added to the quadrature X (also expressed in dimensionless units). This quantum theory of amplification is presented in ch. 2. The Josephson Parametric Amplifiers have been developed precisely to add as little noise as required by quantum

[1] re-written in dimensionless units, such that $\hbar\omega(\langle X^2 \rangle + \langle Y^2 \rangle)$ equals the field mode energy

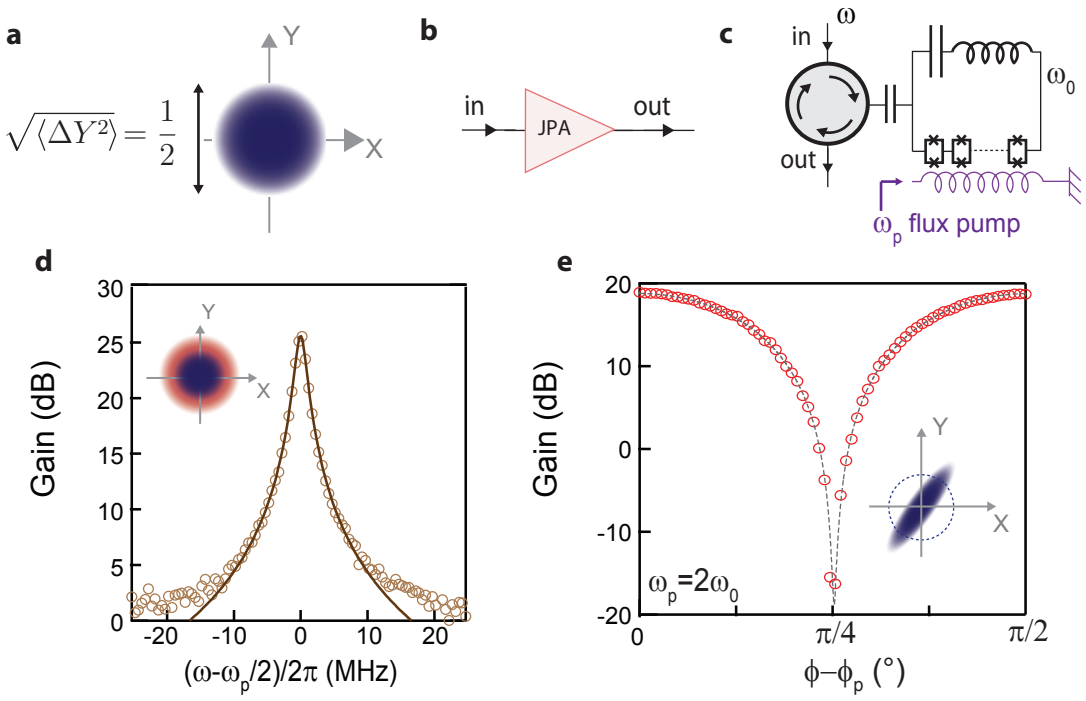

FIGURE 1.1: **Quantum fluctuations and quantum-limited amplification. a** At temperatures $k_B T \ll \hbar\omega$, the ground state of the microwave field is reached, with its quadrature variances given by $\sqrt{\langle \Delta X^2 \rangle} = \sqrt{\langle \Delta Y^2 \rangle} = 1/2$ imposing a minimum to the field fluctuations (blue shade). **b-c** A Josephson Parametric Amplifier, here implemented by a flux-pumped SQUID resonator, can be used to detect quantum microwave fields. **d** When employed in non-degenerate mode ($\omega_p \neq 2\omega$), the JPA adds half a noise photon (red shade) to the half-noise photon (blue shade) arising from the input vacuum fluctuations. **e** When operated in its degenerate mode ($\omega_p = 2\omega$), it amplifies one quadrature at the expense of the other; in this case the amplification is noiseless. Acting on a vacuum state, it produces a squeezed state, with fluctuations deamplified for one quadrature but amplified on the other one (blue shade).

mechanics and are thus key novel tools in high-sensitivity microwave measurements. In this work, we use a JPA whose design is explained in ch. 2 and is schematically shown in Fig. 1.1c. The JPA is powered by a pump microwave signal at frequency $\omega_p \approx 2\omega$ which modulates the magnetic flux threading the loops of an array of SQUIDs embedded in a resonator, resulting in parametric gain at ω. This flux-pumped JPA has two modes of operation. If $\omega_p \neq 2\omega$ ("non-degenerate mode"), both signal quadratures are amplified equally with $n_{\text{amp}} = 1/4$ so that the overall detected noise $n = n_{\text{eq}} + n_{\text{amp}}$ for one quadrature is $n = 1/2$. If $\omega_p = 2\omega$ ("degenerate mode"), only a single quadrature is amplified, allowing to evade the quantum limit for amplification so that $n_{\text{amp}} = 0$ and $n = n_{\text{eq}} = 1/4$. JPAs have been used to read-out the state of superconducting qubits [21], the motion of nanomechanical oscillators [22], and the charge state of a quantum dot [23], as well as for high-sensitivity magnetometry [24]. Working at gigaHerz frequencies, they are readily applicable to the amplification of weak microwave signals emitted by spins as will be shown in part two of this thesis. They can also generate squeezed states, which have less fluctuations on one quadrature, but increased fluctuations on the other one to fulfill Heisenberg uncertainty principle (see Fig. 1.1d). We use such states to perform measurements beyond the quantum-limit in part four.

Quantum microwave fluctuations are also key to describe the interaction between the spins and the microwave field in a resonator of frequency ω_0 and quality factor Q. The key parameter describing this interaction is the so-called spin-photon coupling constant noted g, which is the product of the spin magnetic dipole moment and the magnetic field vacuum fluctuations at the

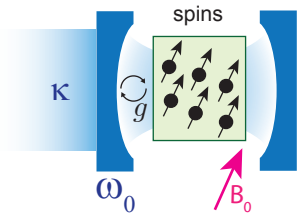

FIGURE 1.2: **Quantum description of the spin-microwave interaction.** An ensemble of spins placed inside a cavity of frequency ω_0 and quality factor $Q = \omega_0/\kappa$ interact with strength g with the microwave field.

spin location. In ch. 3, we apply the Jaynes-Cummings model to describe magnetic resonance experiments, where an ensemble of spins is placed inside a microwave resonator (see Fig. 1.2). Contrary to most cQED experiments, magnetic resonance takes place in the so-called weak-coupling regime $g \ll \kappa$, where $\kappa = \omega_0/Q$ is the resonator damping rate. In ch. 3, we show that in this limit the semi-classical description of the spin dynamics is adequate, supplemented by an additional decay channel: spontaneous emission of microwave photons into the resonator, triggered by the quantum fluctuations of the field. The relaxation rate of this so-called Purcell effect is:

$$\Gamma_p = \kappa \frac{g^2}{\Delta^2 + \kappa^2/4}$$

where Δ is the spin-resonator detuning. While this radiative spin relaxation has always been neglected compared to usual T_1 energy relaxation mechanisms, we show in part three that it can become dominant for spins embedded in a small-mode-volume high-quality-factor resonator. The application of the Jaynes-Cummings model also yields that the field radiated by the spins into the detection waveguide is given by $\langle X \rangle = 2g/\sqrt{\kappa}\langle S_- \rangle$ (see ch. 3); maximizing this output signal is achieved under the same conditions as cavity-enhanced spontaneous emission, namely a resonator of small-mode-volume and high-quality-factor.

In this thesis, we present three experiments in which the impact of microwave quantum fluctuations on magnetic resonance experiments is highlighted. To perform our experiments, we use the spin degree of freedom of bismuth donors in silicon; they consist of substitutional bismuth atoms in the silicon lattice in their neutral state, where they trap a conduction electron (see Fig.1.3a). Key properties of these systems are their long coherence times (which can reach seconds [25]), and the existence of a 7.4 GHz [26] zero-field splitting. This makes it possible to design superconducting resonators which are resonant with bismuth donor spins at low magnetic fields (< 10 mT), compatible with most superconducting materials and in particular aluminum as used in this work. We describe the structure and properties of bismuth donors in silicon in ch. 4.

1.3 Electron spin resonance at the quantum-limit of sensitivity

In the second part of the thesis we present the design and realization of an ESR spectrometer with a sensitivity enhanced by the use of cQED techniques and concepts. As all existing ESR spectrometers, our setup consists of a resonator of frequency ω_0 and quality factor Q coupled to an ensemble of spins, whose Larmor frequency is tuned to ω_0 by the application of an external magnetic field B_0. The application of microwave pulses at ω_0 results in a transverse spin magnetization which leads to the emission of microwave signals broadly known as "echoes". The most popular ESR sequence, known as the Hahn echo, consists of a $\pi/2$ pulse followed after a delay τ by a π pulse which leads to rephasing of the spins after a further delay τ and to the Hahn echo emission. The sensitivity

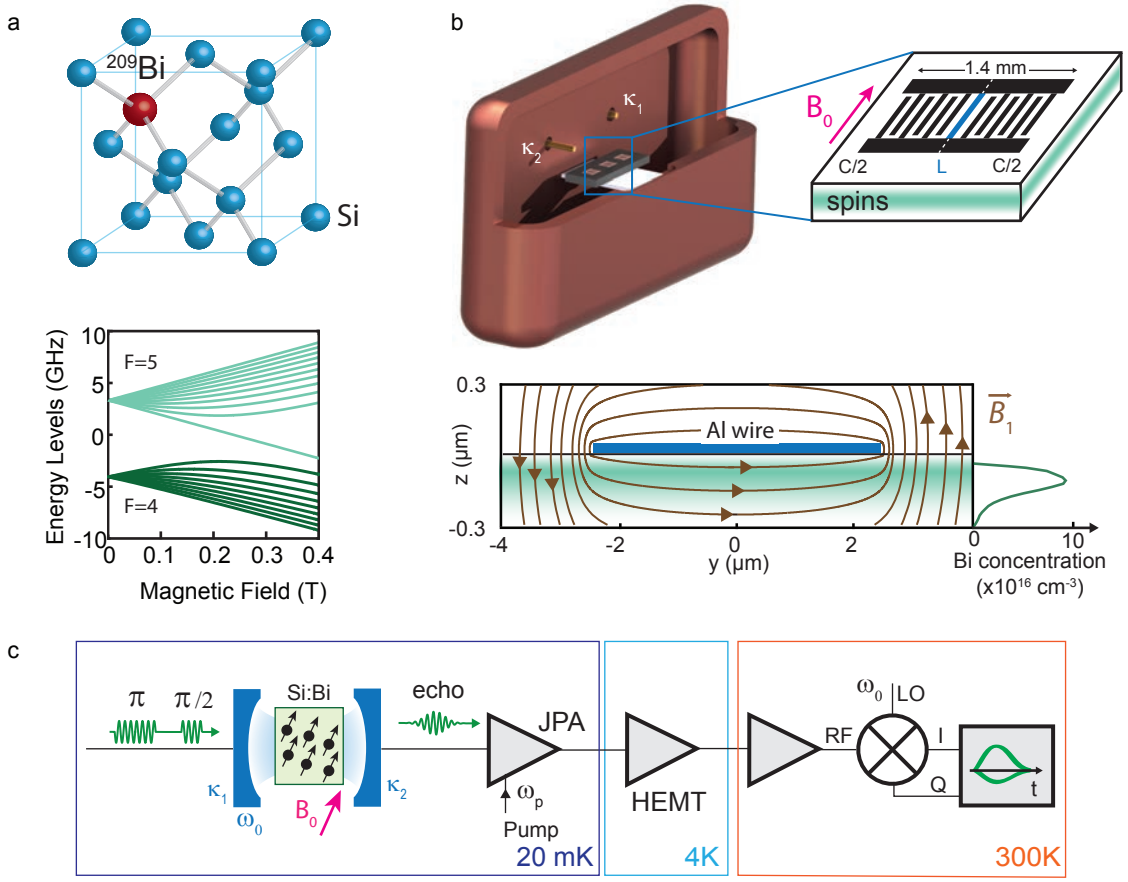

FIGURE 1.3: **Quantum-limited ESR : principle and experimental setup a** A bismuth donor in silicon consists of a substitutional bismuth atom in the silicon lattice. In its neutral charge state, it traps a conduction electron that yields the ESR signal. The 20 energy levels of neutral bismuth donors, shown here as a function of an applied static magnetic field, are the result of the large hyperfine interaction between the $S = 1/2$ electron spin to the $I = 9/2$ nuclear spin of the bismuth atom; in particular there is a 7.4 GHz separation between level multiplets at zero applied field. **b** The ESR resonator consists of an interdigitated capacitor in parallel with a 5-µm-wide inductor, patterned in a superconducting thin film of aluminum deposited on top of a silicon chip implanted with bismuth spins. The chip contains three nearly identical resonators; it is enclosed in a copper sample holder coupled via microwave antennas to the measurement waveguides. **c** The resonator with the Si:Bi spins is anchored at 20 mK (blue) and is probed by microwave signals triggering the emission of an echo in the detection waveguide. The echo signal is amplified successively by a JPA, a HEMT at 4 K before being amplified and demodulated at room-temperature.

of a spectrometer is characterized by the minimum number of spins $N_{\min}$ detectable in a single Hahn-echo with a signal-to-noise (SNR) unity.

Based on the concepts introduced in the first part, we derive in ch. 5 a quantitative expression of $N_{\min}$, which clearly shows which quantities need to be optimized to improve the sensitivity of an ESR spectrometer. The spin-photon coupling constant g and the resonator quality factor Q should be maximized; and low-temperatures lead to increased spin polarization and reduced noise. Regular spectrometers using three-dimensional resonators and operating at room-temperature have a typical sensitivity of $N_{\min} \approx 10^{13}$ spins. This number has been greatly improved by combining micron-scale superconducting resonators operating at 4 K and the use of amplifiers with noise temperatures of 4 K, yielding reported sensitivities of $N_{\min} = 10^7$ spins [37].

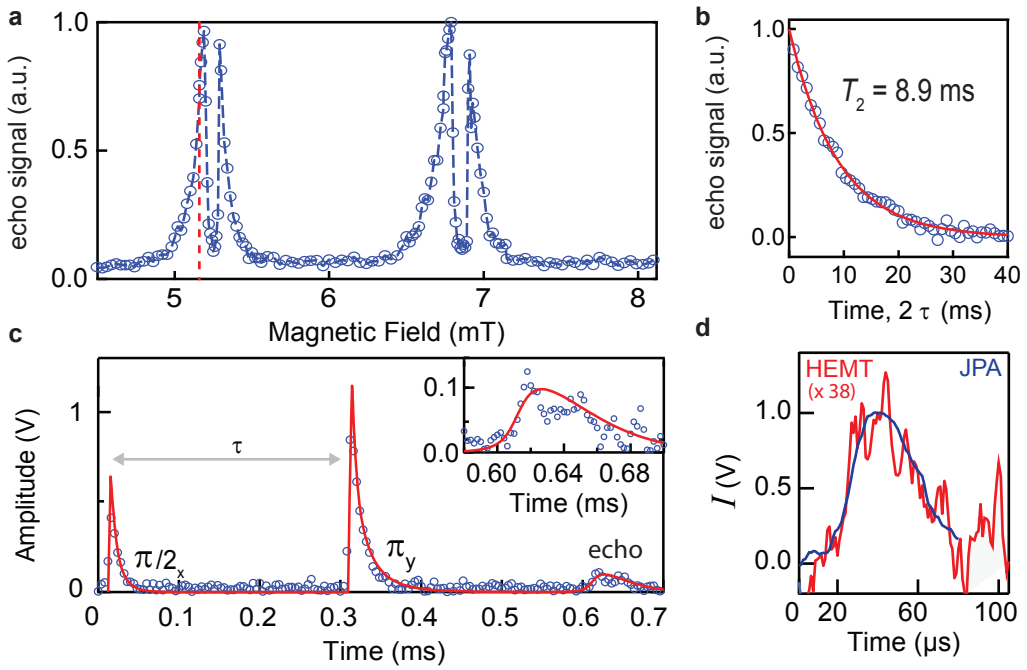

FIGURE 1.4: **Quantum-limited ESR : main results. a** Hahn-echo detected Si:Bi spectroscopy of two consecutive transitions, evidencing asymmetric split peaks instead of the expected Gaussian lineshapes. **b** A coherence time $T_2 = 8.9$ ms is measured at $B_0 = 5.13$ mT. **c** Hahn-echo sequence recording at $B_0 = 5.13$ mT. Blue points are raw data, fitted by a numerical model (red line) proving that 1.2×10^4 spins are excited by the first $\pi/2$ pulse. **d** The JPA brings a ten-fold enhancement to the signal-to-noise ratio.

In ch. 5-7, we present our implementation of an ESR spectrometer using the tools of cQED, and in particular microwave amplification at the quantum limit. The spectrometer is based on a high-quality factor superconducting lumped element resonator, deposited on top of a silicon substrate which contains the ensemble of Si:Bi donor spins, enclosed in a copper sample holder, and coupled to the detection waveguides by excitation and detection antennas (see Fig. 1.3b). The resonator geometry is designed so that the spin-photon coupling reaches $g/2\pi \approx 50$ Hz and the sample is anchored at 20 mK to have full spin polarization. The spin-echo signal is amplified by a JPA, followed by further amplification at 4 K and room-temperature (see Fig. 1.3c). Chapter 5 describes the spectrometer design and experimental implementation.

In ch. 6, using Hahn-echo detected field sweeps (see Fig. 1.4a-c), we use this setup to perform detailed spectroscopy of Si:Bi donors spins as well as coherence time measurements (see Fig. 1.4b). We observe a peculiar line shape, with each Si:Bi resonance appearing as an asymmetric split peak. In ch. 6 we argue that this line shape is caused by mechanical strain due to thermal contractions of the deposited aluminum film onto the silicon substrate.

In ch. 7, we characterize the spectrometer sensitivity. By careful signal-to-noise ratio measurements (see Fig. 1.4c-d) complemented with numerical simulations, we demonstrate an unprecedented sensitivity of 2000 detectable spins per echo with SNR=1. This represents a four-order-of-magnitude improvement compared to the state-of-the-art of inductive detection, obtained thanks to the combined use of cryogenic temperatures allowing for the full polarization of the spins, the high quality factor of the resonator, and the JPA.

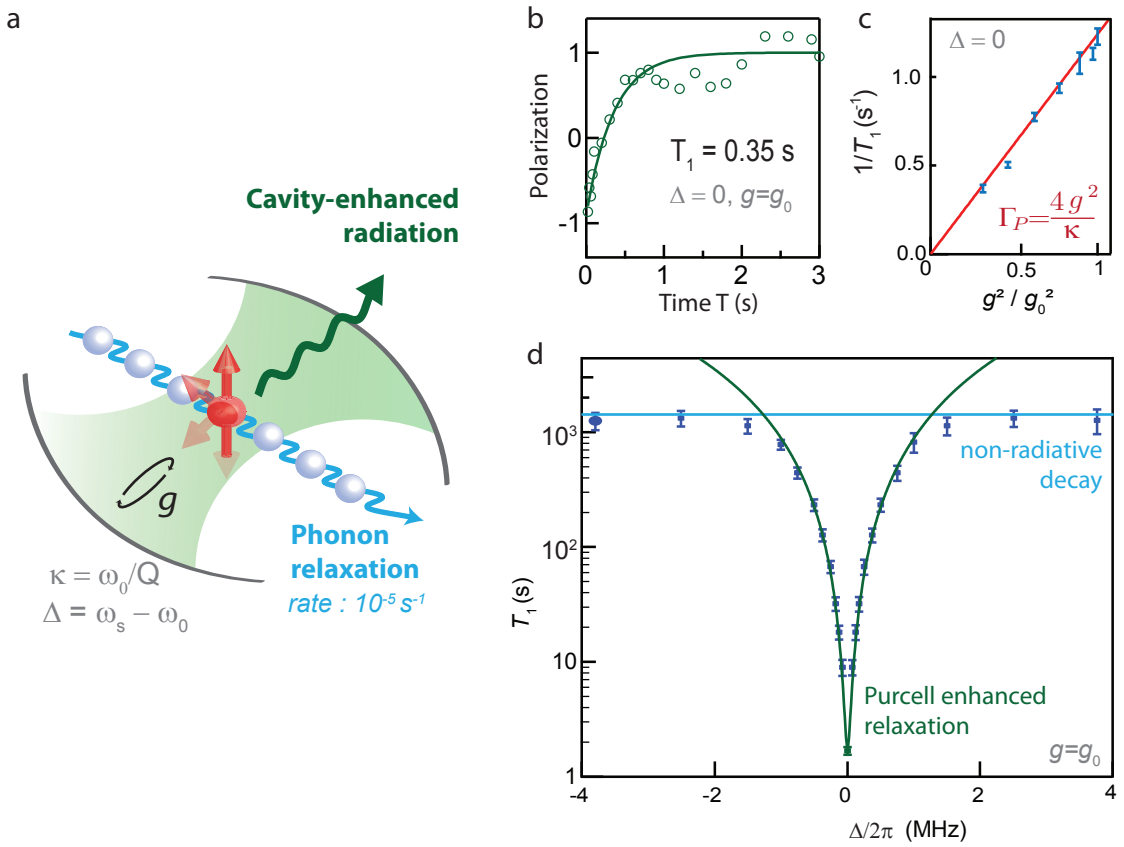

FIGURE 1.5: **The Purcell effect for spins. a** By placing a spin in a resonant cavity, radiative spin relaxation can be made to dominate over intrinsic processes such as phonon-induced relaxation. **b** For Si:Bi spins tuned at resonance, the Purcell effect gives a relaxation time of $T_1 = 0.35$ s using the setup of Fig. 1.3. **c** Measured relaxation time T_1 as a function of g^2; the solid line is a linear fit. **d** A change in T_1 by 3 orders of magnitude is demonstrated by detuning the spins by less than 0.2 mT, up until a non-radiative relaxation process dominates the Purcell effect and effectively limits T_1 to 1500 s.

1.4 The Purcell effect applied to spins

Another key aspect of the sensitivity is the repetition rate. At the low temperatures of our experiments, the spin relaxation rate may become exceedingly low, limiting effectively the absolute sensitivity of the spectrometer. In ch. 8, we use the Purcell effect to demonstrate a re-initialization mechanism applicable to any spin system [27]. This effect arises from the quantum fluctuations of the cavity field, as mentioned earlier. Cavity-enhanced spontaneous emission provides a new way to reach thermal equilibrium for the spin ensemble. It strengthens the spontaneous emission of microwave photons by the spin when it is tuned at resonance with the cavity and thus ensures its eventual return to thermal equilibrium. The Purcell effect has been used extensively to control the lifetime of other TLS such as atoms [28] and semi-conducting heterostructures [29] placed in microwave and optical cavities. It is also a key concept in the realization of bright single-photon sources [30]. For spins however, due to their very weak coupling to the free space electromagnetic field, the estimated rate is usually so low that it is commonly dismissed as a possible source of relaxation.

We show in ch. 8 that for our resonator characteristics, we expect $\Gamma_p \approx 3\ \mathrm{s}^{-1}$. An experimental measurement of T_1 using our setup yields $T_1 = 0.35$ s for spins at resonance, as shown in Fig. 1.5b.

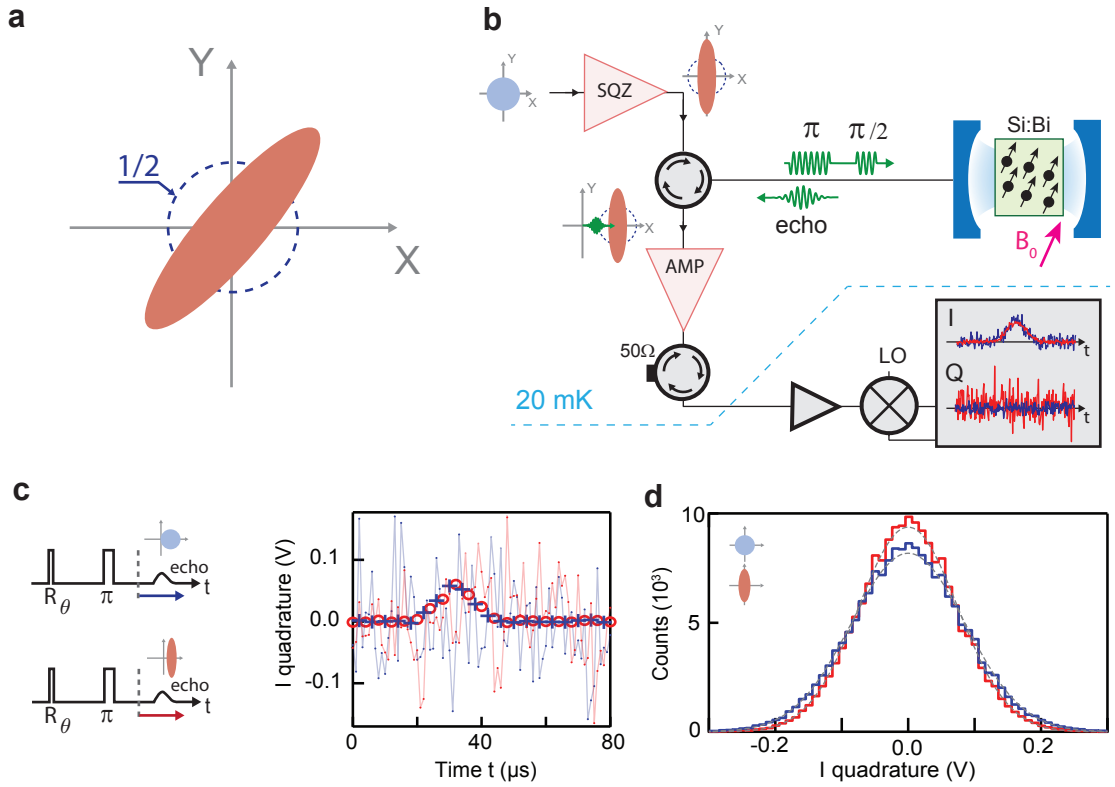

FIGURE 1.6: **Enhancing the sensitivity of ESR spectroscopy with squeezed vacuum states.** **a** A squeezed-state has reduced fluctuations on one quadrature compared to the vacuum level. **b** Sending a squeezed vacuum state onto an ESR resonator can reduce the quantum noise in the detection during the echo emission. **c** An echo signal measured with or without squeezing shows the same average signal amplitude but has a reduced noise histogram as shown in **d**.

This has the direct consequence that all our measurements can be repeated at a 1-Hz-rate and thus the spectrometer described above has an absolute sensitivity of 1700 spins/$\sqrt{\text{Hz}}$.

While the experimental T_1 is in good agreement with the expected Purcell rate, we realize two additional experiments providing direct evidence that the Purcell effect is the dominant relaxation mechanism. First, we show that T_1 depends linearly on g^{-2} (see Fig. 1.5c) as expected from the expression of Γ_p at resonance. Second, Fig. 1.5d demonstrates the expected Lorentzian dependence of T_1 on Δ. By controlling Δ, T_1 is tunable over three orders of magnitude, up to 1500 s, at which point it stops increasing with $|\Delta|$, which shows that another relaxation mechanism, non-radiative, then becomes dominant.

We conclude the third part of this thesis with a brief discussion of the potential applications of this cavity-enhanced spin relaxation.

1.5 Squeezing-enhanced magnetic resonance

In a quantum-limited ESR spectrometer, the noise arises almost entirely from the microwave field quantum fluctuations. It is possible to reduce these fluctuations using quantum-mechanical squeezed states. The idea of performing measurement beyond the standard quantum limit with such engineered states was first proposed by Caves [18] in the context of interferometric measurements.

For squeezed states, the noise in one field quadrature is reduced below the vacuum level whereas the other quadrature has more noise, to fulfill Heisenberg uncertainty principle (see Fig. 1.6a). Since then, optical squeezed vacuum fields have been observed [19] and used to enhance the sensitivity in a number of experiments, ranging from gravitational waves detectors [31] to atom-based magnetometry [32]. They have also been produced at microwave frequencies [33] and used for fundamental light-matter interaction studies [34] and enhanced sensing of a mechanical resonator [35].

In the fourth part of this thesis, we use a squeezed microwave field as depicted in Fig. 1.6b to improve the sensitivity of the spectrometer beyond the quantum limit. Our experiment consists in sending a squeezed vacuum state onto the input of the ESR resonator, while driving the spins with a Hahn echo sequence. The squeezed quadrature is aligned with the quadrature on which the echo is emitted, leading to reduced noise. The squeezed vacuum state is produced by a second JPA - called the squeezer SQZ - placed at the cavity input.

The main results are shown in Fig. 1.6. First, the average echo amplitude is unchanged when the squeezing is on (see Fig. 1.6c). However the noise histograms reveal that the noise has indeed been reduced in the detection (see Fig. 1.6d). The fact that the signal is unaffected while the noise is decreased demonstrates a net enhancement of the signal-to-noise ratio of the experiment by a factor 1.12. It gives a proof-of-concept that magnetic resonance beyond the standard quantum limit is possible. The modest improvement in SNR is due to the limited degree of squeezing achieved, which is in particular due to losses in the microwave setup. We conclude this part by a thorough analysis of the experiment limitations, and we find that in principle, SNR enhancements as large as 10 dB could be achieved in the future.

Part I

Background

Chapter 2

Quantum circuits and quantum noise

For our purpose to perform magnetic resonance with quantum microwave fields, a quantum description of the resonator and of the microwave field is needed. Such description has been used extensively in the field of superconducting circuits and we give here only the results pertaining to the experimental work detailed later on. First, we describe the principal properties of quantum microwave fields as well as the principal quantum states used later on. We then recall the quantization of the mode of a LC resonator as well as of a microwave field propagating along a transmission line. We finally give elements of input-output theory, which describes how the intra-cavity field of a linear or non-linear resonator is related to the propagating modes of the transmission lines to which it is coupled for measurement. In the second part of this chapter, we present the quantum theory of linear amplifiers; in particular we derive the so-called quantum limit of amplification, which gives the minimum amount of noise necessarily added by any amplifier to satisfy the basic principles of quantum mechanics. We also describe the design and working principle of a Josephson Parametric Amplifier, a device which reaches this quantum limit.

2.1 Quantum microwaves and quantum circuits

In our experiment, the resonator circuit is coupled to external measurement fields via transmission lines. At temperatures lower than $\hbar\omega/k_B$, the microwave fields residing in the resonator and propagating fields in the transmission lines are cooled down to their ground state and thus require a quantum mechanical description.

2.1.1 Quantum description of an electromagnetic mode : quantum noise and quantum states

A good review of the quantization of electromagnetic modes and quantum states can be found in [38]. We consider a given mode of the electromagnetic field, at frequency ω. Classically, this mode is characterized by its complex amplitude $A = |A|e^{i\phi}$. It can be equivalently described by its in-phase and out-of-phase quadratures usually defined as $X = \mathrm{Re}(A)$ and $Y = \mathrm{Im}(A)$. In the frame rotating at frequency ω, the field can thus be represented in phase space as a point of polar coordinates $(|A|, \phi)$ or cartesian coordinates (X, Y) (see Fig. 2.1a). The choice of the quadratures is relative to the phase reference. Choosing a phase reference different by an angle θ so that the microwave signal has a phase $\phi - \theta$ leads to the definition of new quadratures (X_θ, Y_θ) related to (X, Y) by:

$$X_\theta = X\cos(\theta) + Y\sin(\theta) \tag{2.1}$$

$$Y_\theta = -X\sin(\theta) + Y\cos(\theta) \tag{2.2}$$

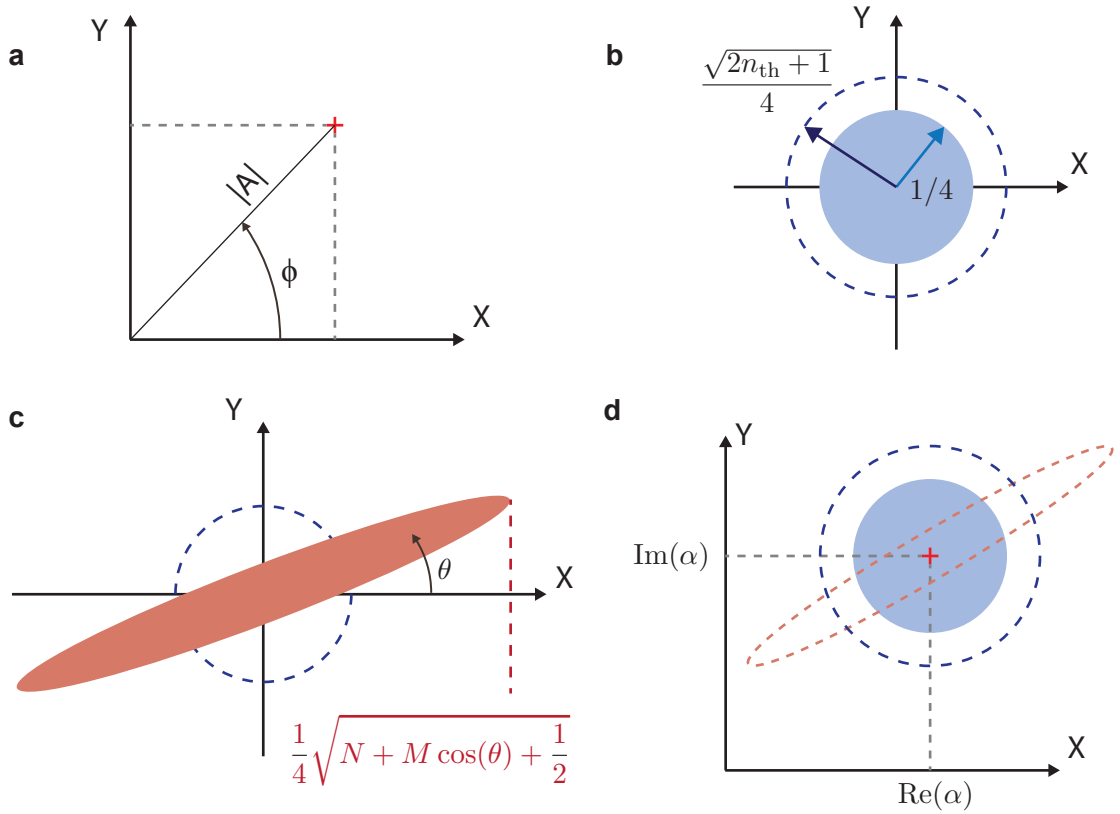

FIGURE 2.1: **Microwave field states phase-space representation** using the convention given in the text. **a** Classical picture. **b** Thermal (dashed) and vacuum (solid fill) states. **c** Squeezed state. **d** Coherent state (blue fill), coherent thermal state (dashed blue line), displaced squeezed state (red dashed line).

In quantum physics, the field quantization is obtained by promoting the quadratures of the field as quantum operators obeying the commutation relation $\left[\hat{X},\hat{Y}\right]=i/2$. $\hat{X}$ and $\hat{Y}$ are canonically conjugate variables, and the commutation relation imposes the following Heisenberg uncertainty relation for any pure state $|\Psi\rangle$ or statistical mixture of states described by a density matrix ρ: $\langle\Delta\hat{X}^2\rangle\langle\Delta\hat{Y}^2\rangle \geq |\langle[\hat{X},\hat{Y}]\rangle|^2/4$, i.e. :

$$\langle\Delta\hat{X}^2\rangle\langle\Delta\hat{Y}^2\rangle \geqslant \frac{1}{16} \tag{2.3}$$

where the notations $\langle\hat{o}\rangle$ and $\langle\Delta\hat{o}^2\rangle$ stand respectively for the operator expectation value $\mathrm{Tr}(\rho\hat{o})$ and for its variance $\langle\hat{o}^2\rangle-\langle\hat{o}\rangle^2$. Therefore no field can have a perfectly well-defined value for either of its quadratures and these quantum fluctuations need to be taken into account in experiments that aim at reaching ultimate measurement sensitivity.

The uncertainty on $\hat{X}$ and $\hat{Y}$ makes it impossible to have a point-like representation. Instead, one needs to use a quasi-probability distribution such as the Wigner function distribution [39]. In the following, we also represent states schematically by shading regions (X,Y) such that $|X-X_{\rm max}|\leqslant\sqrt{\langle\Delta\hat{X}^2\rangle/2}$, and equivalently for Y, with $(X_{\rm max},Y_{\rm max})$ being the position of the Wigner function maximum. The field can be equivalently described by the annihilation and creation operators $\hat{a}^\dagger$ and $\hat{a}$ defined as:

$$\hat{a} = \hat{X}+i\hat{Y} \tag{2.4}$$
$$\hat{a}^\dagger = \hat{X}-i\hat{Y} \tag{2.5}$$

that obey the commutation relation $[\hat{a}, \hat{a}^\dagger] = 1$.

We now briefly describe the field states used in this thesis, their representation and their noise properties. Note that we will restrict ourselves to the so-called Gaussian states, for which the statistical distribution of the quadratures is a Gaussian. As a result they are fully characterized by their mean value and variance, and we will now concentrate on these quantities.

Vacuum state

We first define the Fock states $|n\rangle$ as eigenstates of the number operator $\hat{n} = \hat{a}^\dagger\hat{a}$. The lowest-energy-state $n = 0$ is called the vacuum state. It satisfies:

$$\langle\hat{X}\rangle = \langle\hat{Y}\rangle = 0 \tag{2.6}$$
$$\langle\Delta\hat{X}^2\rangle = \langle\Delta\hat{Y}^2\rangle = 1/4. \tag{2.7}$$

and thus reaches the minimal variance authorized by the Heisenberg uncertainty principle for a state verifying $\langle\Delta\hat{X}^2\rangle = \langle\Delta\hat{Y}^2\rangle$. In phase-space, using the Wigner function, the vacuum state is represented by a disk centered on $(0, 0)$ of radius $1/4$ (see Fig. 2.1b). Its incompressible quantum fluctuations set a limit on the signal-to-noise ratio of many experiments and are known as the standard quantum limit. As will be explained in ch. 3, they also set the coupling strength between a TLS and the microwave field.

Thermal state

We also need to describe electromagnetic modes that are in thermal equilibrium with a bath at temperature T; they are said to be "in a thermal state". Such a thermal state is a statistical mixture of Fock states $|n\rangle$ with a Boltzmann distribution, and its mean-value and variance can be shown to be:

$$\langle\hat{X}\rangle = \langle\hat{Y}\rangle = 0 \tag{2.8}$$
$$\langle\Delta\hat{X}^2\rangle = \langle\Delta\hat{Y}^2\rangle = \frac{2n_{\mathrm{th}} + 1}{4}, \tag{2.9}$$

where n_{th} is the mean thermal photon number occupying the field, which obeys:

$$n_{\mathrm{th}} = \left[\exp\left(\frac{\hbar\omega}{k_B T}\right) - 1\right]^{-1} \tag{2.10}$$

In phase-space, a thermal vacuum is represented by a disk centered on $(0, 0)$ of radius $\sqrt{2n_{\mathrm{th}} + 1}/4$, as shown in Fig. 2.1b. In the high temperature limit $k_B T \gg \hbar\omega$, the thermal state fluctuations are simply given by $k_B T/2\hbar\omega$ and thus depend linearly on T (see Fig. 2.2). In the low temperature limit $k_B T \ll \hbar\omega$, the field occupies mostly the $|0\rangle$ vacuum state and thus reaches the quantum limit with $\langle\Delta\hat{X}^2\rangle = 1/4$.

Squeezed states

In this thesis we also encounter squeezed states of the field. Compared to the thermal and vacuum states, they are non-isotropic with one quadrature X_θ having less fluctuations than the vacuum state, while its other quadrature Y_θ has increased fluctuations to fulfill Heisenberg uncertainty principle.

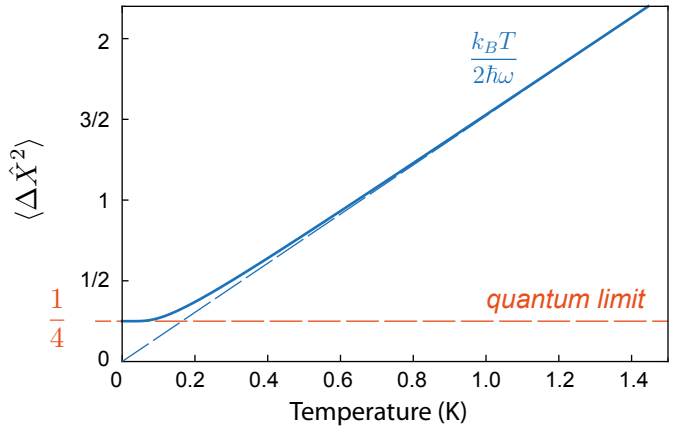

FIGURE 2.2: **Thermal state fluctuations** as a function of temperature for a mode at frequency $\omega/2\pi =$ 7 GHz.

The usual definition of these states makes use of a squeezing parameter ζ such that:

$$\langle \hat{X}_\theta \rangle = \langle \hat{Y}_\theta \rangle = 0 \tag{2.11}$$

$$\langle \Delta \hat{X}_\theta^2 \rangle = \frac{e^{-\zeta}}{4} \tag{2.12}$$

$$\langle \Delta \hat{Y}_\theta^2 \rangle = \frac{e^{\zeta}}{4} \tag{2.13}$$

Their phase-space representation is an ellipsoid centered on $(0, 0)$ (see Fig. 2.1c) with a phase-dependent radius $r(\phi)$ since:

$$\langle \Delta \hat{X}_\phi^2 \rangle = \frac{1}{2}\left(N + M\cos(\phi - \theta) + \frac{1}{2}\right) \tag{2.14}$$

where N and M are defined as $N = \cosh(\zeta)/2 - 1/2$ and $M = \sinh(\zeta)/2$. A squeezed state has minimal uncertainty in the sense of Heisenberg inequality (see Eq. 2.3). Even though it is abusively called "squeezed vacuum", it is important to note that this state contains a finite number of photons since it can be shown that $\langle \hat{a}^\dagger \hat{a} \rangle \geqslant N$. Moreover, the stronger the squeezing, the larger N, and thus the larger the energy of the state. A state with an infinitely squeezed quadrature $\hat{X}$ would have infinite energy. Since one of its quadratures has less fluctuations than the standard quantum limit, squeezed states are very interesting for ultra-precise measurement and are a key resource in quantum metrology [40]. In ch. 9, we make use of them to perform magnetic resonance spectroscopy beyond the standard quantum limit.

Squeezed thermal states also exist. Similarly than for a squeezed vacuum state, one of their quadrature has less fluctuations than a thermal state of thermal occupancy n_{th} while the other one has increased fluctuations. Eqs. 2.12-2.13 are modified as follows:

$$\langle \Delta \hat{X}_\theta^2 \rangle = (2n_{\text{th}} + 1)\frac{e^{-\zeta}}{4} \tag{2.15}$$

$$\langle \Delta \hat{Y}_\theta^2 \rangle = (2n_{\text{th}} + 1)\frac{e^{\zeta}}{4} \tag{2.16}$$

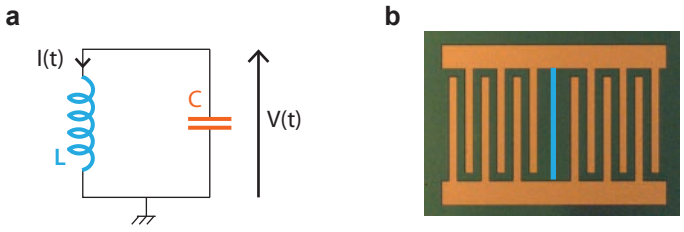

FIGURE 2.3: ***LC* oscillator.** **a** Schematic. **b** Example of implementation: a superconducting planar resonator comprising a interdigitated capacitance (orange) in parallel with a wire (inductance, blue).

while N and M are now defined as:

$$N = \frac{1}{2}\left[(2n_{\mathrm{th}}+1)\cosh(\zeta)-1\right] \tag{2.17}$$

$$M = \frac{1}{2}(2n_{\mathrm{th}}+1)\sinh(\zeta) \tag{2.18}$$

Coherent states

Throughout this manuscript, the microwave signals that drive the spins are classical and can be described by coherent states. Coherent states $|\alpha\rangle$ are eigenstates of the operator $\hat{a}$ such that the number of photons contained in this state is $\langle\alpha \mid \hat{a}^\dagger\hat{a} \mid \alpha\rangle = |\alpha|^2$. For $\alpha = 0$, the coherent state is the vacuum state $|0\rangle$. Coherent states are characterized by their mean value $\langle\hat{X}\rangle = \mathrm{Re}(\alpha)$, $\langle\hat{Y}\rangle = \mathrm{Im}(\alpha)$, and their variances $\langle\Delta\hat{X}^2\rangle = 1/4$ and $\langle\Delta\hat{Y}^2\rangle = 1/4$ which are identical to those of the vacuum state. One can also have coherent thermal states whose fluctuations are then given by Eq. 2.9.

After having introduced various quantum states, we now discuss physical implementations of the electromagnetic modes relevant for our work.

2.1.2 Lumped element LC resonator

The simplest implementation of an electromagnetic field mode is the lumped-element LC oscillator, which is also highly relevant for the rest of this work as will be clear in the following. A good review of the quantization of a simple LC resonator is given in [41, 42]. Consider an oscillator comprising an inductor L in parallel with a capacitor C as schematized in Fig. 2.3a. We introduce the operator $\hat{\Phi}$, describing the magnetic flux in the inductor, and $\hat{q}$, describing the charge on the capacitor. $\hat{\Phi}$ and $\hat{q}$ obey the conjugation relation $[\hat{\phi},\hat{q}] = i\hbar$. The Hamiltonian of this harmonic oscillator is:

$$\hat{H}(\hat{\phi},\hat{q}) = \frac{\hat{\phi}^2}{2L} + \frac{\hat{q}^2}{2C} \tag{2.19}$$

which may also be written as:

$$\hat{H} = \hbar\omega_0\left(\hat{a}^\dagger\hat{a} + \tfrac{1}{2}\right) \tag{2.20}$$

where $\hat{a}$ and $\hat{a}^\dagger$ are linked to $\hat{\phi}$ and $\hat{q}$ by:

$$\hat{a} = \frac{1}{\sqrt{2\hbar Z_0}}(\hat{\phi} + iZ_0\hat{q}) \tag{2.21}$$

$$\hat{a}^\dagger = \frac{1}{\sqrt{2\hbar Z_0}}(\hat{\phi} - iZ_0\hat{q}) \tag{2.22}$$

with $\omega_0 = 1/\sqrt{LC}$ being the resonator frequency and $Z_0 = \sqrt{L/C}$ the resonator impedance. The voltage $\hat{V}$ across the capacitor and the current $\hat{I}$ flowing through the inductor are thus expressed in terms of the bosonic operators as:

$$\hat{V} = \frac{\hat{q}}{C} = i\omega_0\sqrt{\frac{\hbar Z_0}{2}}(\hat{a}^\dagger - \hat{a}) \tag{2.23}$$

$$\hat{I} = \frac{\hat{\phi}}{L} = \omega_0\sqrt{\frac{\hbar}{2Z_0}}(\hat{a} + \hat{a}^\dagger) \tag{2.24}$$

The eigenstates of $\hat{H}$ are the Fock states $|n\rangle$ and satisfy $\hat{H}|n\rangle = \hbar\omega_0\left(n + \frac{1}{2}\right)|n\rangle$. The rms vacuum fluctuations of the voltage and the current when the resonator field is in its quantum ground state are then:

$$\delta I^2 = \langle 0|\hat{I}^2|0\rangle = \frac{\hbar\omega_0^2}{2Z_0} \tag{2.25}$$

$$\delta V^2 = \langle 0|\hat{V}^2|0\rangle = \frac{\hbar Z_0\omega_0^2}{2} \tag{2.26}$$

The rms voltage and rms current generate, respectively, a spatially dependent electric field $\hat{\mathbf{E}}(\mathbf{r}) = i\boldsymbol{\delta E}(\mathbf{r})(\hat{a} - \hat{a}^\dagger)$ in the space between the capacitor plates, and magnetic field $\hat{\mathbf{B}}(\mathbf{r}) = \boldsymbol{\delta B}(\mathbf{r})(\hat{a} + \hat{a}^\dagger)$ around the inductor, with $\boldsymbol{\delta E}(\mathbf{r})$ and $\boldsymbol{\delta B}(\mathbf{r})$ their vacuum rms fluctuations at position $\boldsymbol{r}$. Throughout this thesis, the rms magnetic field vacuum fluctuations play an important role as they are proportional to the coupling constant between the spins and the resonator. An example of a LC resonator used in later chapters is depicted in Fig. 2.3b.

2.1.3 Lossless transmission line

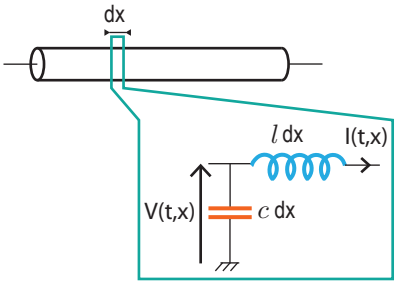

FIGURE 2.4: **Transmission Line**. Each infinitesimal part of a transmission line can be modeled as a LC.

A transmission line, for instance any coaxial cable, supports the propagation of electromagnetic modes. A good overview of the quantization procedure for a transmission line is given in [43]. The transmission line can be modeled as an assembly of elementary circuits, as shown in Fig. 2.4, where l and c are the inductance and capacitance per unit-length. To analyze this circuit, a local flux variable dependent on the position is defined as $\phi(x,t) = \int_{-\infty}^{t} V(x,\tau)d\tau$ where $V(x,t)$ is the local voltage

on the transmission line at position x and time t. In each segment, the charge in the capacitor is given by $q(x,t) = cV(x,t)$, the voltage drop across the inductance $l\ dx$ is $-dx\ \partial_x\partial_t\phi(x,t)$, yielding the flux through this inductance $-dx\ \partial_x\phi(x,t)$ and the corresponding current $I(x,t) = -\partial_x\phi(x,t)/l$.

The Lagrangian for an infinite line is given by $\mathcal{L} = \int dx\mathcal{L}_x$, with the Lagrangian density $\mathcal{L}_x$ being:

$$\mathcal{L}_x = \frac{q^2}{2\ c\ dx} - \frac{l\ dx\ I^2}{2} = \frac{c}{2}(\partial_t\phi)^2 - \frac{1}{2l}(\partial_x\phi)^2 \tag{2.27}$$

The corresponding equation of motion for ϕ is then given by the wave equation $lc\ \partial_t^2\phi - \partial_x^2\phi = 0$, with a propagation speed $v_t = 1/\sqrt{lc}$. By differentiating with respect to the time, one finds a similar expression for $V(x,t)$. Without any boundary conditions, the solutions of this equation may be expressed as a composition of right and left propagating waves:

$$V(x,t) = V^{\rightharpoonup}\left(t - \tfrac{x}{v_t}\right) + V^{\leftharpoondown}\left(t + \tfrac{x}{v_t}\right) \tag{2.28}$$

The solution for the current is related to V by $l\partial_t I = -\partial_x V$, thus:

$$I(x,t) = Z_c^{-1}\left[V^{\rightharpoonup}\left(t - \tfrac{x}{v_t}\right) - V^{\leftharpoondown}\left(t + \tfrac{x}{v_t}\right)\right] \tag{2.29}$$

where $Z_c = \sqrt{l/c}$ is the characteristic impedance of the line. The left and right propagating waves are independent for an infinite transmission line. If the line is terminated by a load Z_l at $x = 0$, they are linked by the following equation of continuity for classical fields:

$$V^{\rightharpoonup}(t) + V^{\leftharpoondown}(t) = \frac{Z_l}{Z_c}(V^{\rightharpoonup}(t) - V^{\leftharpoondown}(t)). \tag{2.30}$$

The microwave power transmitted to the right is then given by:

$$P = V \times I = \frac{1}{Z_c}[(V^{\rightharpoonup})^2 - (V^{\leftharpoondown})^2]. \tag{2.31}$$

We now turn to the quantum description of propagating fields. From the Lagrangian density, one can extract the density Hamiltonian by noticing that the charge is the conjugate quantity of the flux:

$$\frac{\partial\mathcal{L}_x}{\partial(\partial_t\phi)} = c\partial_t\phi = cV = q \tag{2.32}$$

and thus $H = \int H_x dx$, with:

$$H_x = \partial_t\phi\frac{\partial\mathcal{L}}{\partial(\partial_t\phi)} - \mathcal{L}_x = \frac{q^2}{2c} + \frac{(\partial_x\phi)^2}{2l} \tag{2.33}$$

The field quantization is obtained by treating ϕ and q as quantum operators obeying:

$$[\partial_x\hat{\phi}(x,t), \hat{q}(x',t)] = \partial_x[\hat{\phi}(x,t), \hat{q}(x',t)] = i\hbar\partial_x\delta(x - x') \tag{2.34}$$

Using expressions 2.28 and 2.29, one can express $\hat{\phi}$ and $\hat{q}$ as a function of the voltage amplitude operators $\hat{V}^{\rightharpoonup}(\tau^-)$ and $\hat{V}^{\leftharpoondown}(\tau^+)$ where we set $\tau^{\pm} = t \pm \frac{x}{v_t}$. Using the fact that left and right fields for an infinite transmission line are independent, one can derive from Eq. 2.34 the following

commutation relation for $\hat{V}^{\rightleftharpoons}(\tau)$:

$$[\hat{V}^{\rightleftharpoons}(\tau), \hat{V}^{\rightleftharpoons}(\tau')] = -\frac{i\hbar}{2} Z_c \partial_\tau \delta(\tau - \tau') \tag{2.35}$$

To find the expression of the voltage as a function of annihilation and creation operators $\hat{a}^{\rightleftharpoons}(\omega)$, Eq. 2.35 is expressed in the frequency domain, by defining:

$$\hat{V}^{\rightleftharpoons}(\omega) = \int_{-\infty}^{\infty} \hat{V}^{\rightleftharpoons}(\tau) e^{i\omega\tau} d\tau. \tag{2.36}$$

and thus:

$$[\hat{V}^{\rightleftharpoons}(\omega), \hat{V}^{\rightleftharpoons}(\omega')] = 2\pi \frac{\hbar}{2} Z_c \omega \delta(\omega - \omega') \tag{2.37}$$

One can notice that while $\hat{V}^{\rightleftharpoons}(\tau)$ is hermitian, $\hat{V}^{\rightleftharpoons}(\omega)$ is non-hermitian with $\hat{V}^{\rightleftharpoons}(\omega)^\dagger = \hat{V}^{\rightleftharpoons}(-\omega)$. To have $[\hat{a}^{\rightleftharpoons}(\omega), \hat{a}^{\rightleftharpoons\dagger}(\omega')] = 2\pi\delta(\omega - \omega')$, we now define $\hat{a}^{\rightleftharpoons}(\omega)$ as:

$$\hat{a}^{\rightleftharpoons}(\omega) = \sqrt{\frac{2}{\hbar|\omega|Z_c}} \hat{V}^{\rightleftharpoons}(\omega) \tag{2.38}$$

and thus one has by reverting to the time domain:

$$V^{\rightharpoonup}(x,t) = \int_0^{\infty} \frac{d\omega}{2\pi} \sqrt{\frac{\hbar\omega Z_c}{2}} (\hat{a}^{\rightharpoonup}(\omega) e^{-i\omega(t - x/v_t)} + h.c.) \tag{2.39}$$

$$V^{\rightharpoondown}(x,t) = \int_0^{\infty} \frac{d\omega}{2\pi} \sqrt{\frac{\hbar\omega Z_c}{2}} (\hat{a}^{\rightharpoondown}(\omega) e^{-i\omega(t + x/v_t)} + h.c.) \tag{2.40}$$

where $h.c.$ stands for hermitian conjugate.

We are typically interested in a relatively narrow band of frequencies centered on ω_a. In this case, it is useful to work in the time-domain in a frame rotating at ω_a. Using Eq 2.40 and assuming that the only relevant frequencies are near ω_a (performing the so-called rotating wave approximation), one finds for $x = 0$:

$$V^{\rightharpoonup}(t) = \sqrt{\frac{\hbar\omega_a Z_c}{2}} (\hat{a}^{\rightharpoonup}(t) + \hat{a}^{\rightharpoonup\dagger}(t)) \tag{2.41}$$

where we have defined the annihilation and creation operators in the time domain to be:

$$\hat{a}^{\rightleftharpoons}(t) = \int_0^{\infty} \frac{d\omega}{2\pi} \hat{a}^{\rightleftharpoons}(\omega) e^{i\omega\tau} \tag{2.42}$$

Instead of keeping the basis of "infinite-bandwidth" operators $\hat{a}(t)$, the notations can be further simplified by introducing a new operator which defines propagating spatio-temporal modes of finite temporal and spectral extension. We write

$$\hat{a} = \int \hat{a}(t) u(t) dt \tag{2.43}$$

$u(t)$ being the propagating signal mode temporal envelope, of bandwidth $\Delta\omega$, normalized so that $\int [u(t)]^2 dt = 1$. With this definition, we define left and right modes $\hat{a}^{\rightleftharpoons}$ which obey $[\hat{a}^{\rightleftharpoons}, \hat{a}^{\rightleftharpoons\dagger}] = 1$ and that are equivalent to the annihilation and creation operators used in 2.1.1. As a result, quantum microwave fields propagating along a transmission line can be described using the results of 2.1.1.

2.1.4 Probing and characterizing a resonator

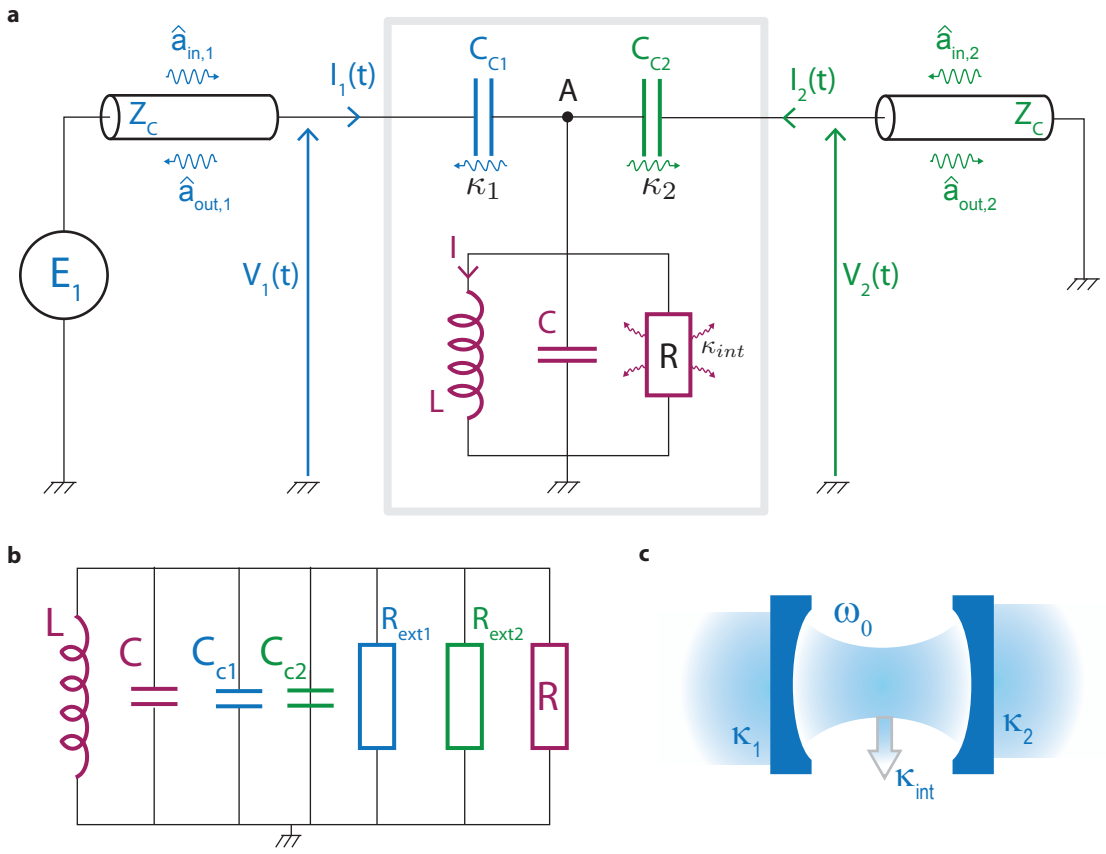

FIGURE 2.5: **Probing a LC resonator from the outside. a** When a RLC circuit is coupled capacitively to measurement lines of characteristic impedance Z_c, the energy stored in the inductive and capacitive elements can leak out with rate κ_{int} into the internal resistance, and with rate κ_1 and κ_2 into the measurement lines. A master equation established for the intra-resonator field $\hat{a}$(t) allows to link the input and output field operators via these dissipation rates in an input-output framework. **b** Norton equivalent circuit. **c** Quantum Optics equivalent representation.

The LC resonator used in our experiments is coupled to two transmission lines of characteristic impedances Z_c via two coupling capacitances C_{c1} and C_{c2}, as shown in Fig. 2.5. We also introduce a resistance R in the LC to model the internal losses of the resonator. In this paragraph, we would like to provide a quantum description of the evolution of the intra-resonator field $\hat{a}$ in response to external drives and internal losses. We first present a few results obtained by a classical description of the system to define a number of useful quantities.

Coupling to a measurement transmission line

As the RLC circuit is coupled to input and output transmission lines, its frequency ω_0 and its characteristic impedance Z_0 are slightly modified. Indeed, the admittance viewed from A (see

Fig 2.5a) has two additional terms $Z_{\text{ext},i=1,2} = Z_c + 1/iC_{Ci}\omega$:

$$Z_A^{-1} = \frac{1}{R} + i\left(C\omega - \frac{1}{L\omega}\right) + \frac{1}{Z_{\text{ext1}}} + \frac{1}{Z_{\text{ext2}}} \tag{2.44}$$

$$Z_A^{-1} = \left(\frac{1}{R} + \sum_{i=1,2} \frac{Z_c C_{Ci}^2 \omega_0^2}{1 + (Z_c C_{Ci}\omega_0)^2}\right) + i\left[\left(C + \sum_{i=1,2} \frac{C_{Ci}}{1 + (Z_c C_{Ci}\omega_0)^2}\right)\omega - \frac{1}{L\omega}\right] \tag{2.45}$$

In the limit $Z_c C_{Ci}\omega_0 \ll 1$ and in the vicinity of ω_0, this corresponds to a $R'L'C'$ circuit impedance (see Figure 2.5b), with $L' = L$ and:

$$C' = C + \sum_{i=1,2} \frac{C_{Ci}}{1 + (Z_c C_{Ci}\omega_0)^2} \approx C + C_{C1} + C_{C2}. \tag{2.46}$$

thus renormalizing slightly the resonator frequency in $\omega_0' = 1/\sqrt{\mathrm{LC}'}$ and its characteristic impedance in $Z_0' = \sqrt{L/C'}$. In the following, we take into account this renormalization but keep the notations ω_0 and Z_0. In addition, three dissipation terms corresponding to internal losses or losses via coupling to the transmission lines can be identified:

$$\frac{1}{R'} = \frac{1}{R} + \frac{1}{R_{\text{ext},1}} + \frac{1}{R_{\text{ext},2}} \quad \text{with} \quad \frac{\mathrm{R_{ext,i}}}{\mathrm{Z_c}} = 1 + \frac{1}{(\mathrm{Z_c C_{Ci}}\omega_0)^2} \approx 1/\mathrm{Z_c^2 C_{Ci}^2}\omega_0^2 \tag{2.47}$$

The dissipation terms set the damping of the resonator motion via its quality factor $Q^{-1} = R\sqrt{L/C}$ (for a parallel RLC circuit), allowing us to identify three distinct contributions $Q^{-1} = Q_{\text{ext},1}^{-1} + Q_{\text{ext},2}^{-1} + Q_{\text{int}}^{-1}$ given respectively by the internal losses $Q_{\text{int}}^{-1} = R\sqrt{L/C'}$ and the coupling to the transmission lines $Q_{\text{ext},i}^{-1} = R_{\text{ext},i}\sqrt{L/C}$. The energy damping rate into each "port", either internal or external, is then defined as $\kappa = \omega_0/Q$.

This mapping is valid in the high-quality factor limit where $Z_c C_{Ci}\omega_0 \ll 1$. One interpretation is that the coupling capacitances are acting as semi-reflecting mirrors: the strong impedance mismatch between the transmission line and the LC oscillator ensures that the electromagnetic field is confined inside the resonator.

Input-output theory

When probing the resonator with classical microwave fields, the input and output resonator fields can be related using a scattering matrix approach [44]. Consider the two-port device comprising the coupling capacitances and the RLC circuit, denoted by the grey box shown in Fig. 2.5, with each port directly connected to the left and right transmission lines. An ideal voltage source E_1 with a matched output impedance connected to the left transmission line generates a voltage $V_1(t)$ and a current $I_1(t)$ on port 1 as well as a voltage $V_2(t)$ and a current $I_2(t)$ on port 2. As seen above, $V_1(t)$ can be separated in two contributions: a right propagating term incident on the device given by $V_1^{\rightarrow}(t) = V_1(t) + Z_c I_1(t)$ and a left propagating term outcoming of the device given by $V_1^{\leftarrow}(t) = V_1(t) - Z_c I_1(t)$, and similarly for $V_2(t)$. One can consider equivalently that the incident term $V_1^{\rightarrow}$ gives rise to a transmitted wave $V_2^{\rightarrow}$ in the right transmission line and a reflected term $V_1^{\leftarrow}$ in the left transmission line. The relation between the input and output power waves defined as $a_{\text{in},j} = V_j^{\rightarrow}/\sqrt{Z_c}$ and $a_{\text{out},i} = V_i^{\rightarrow}/\sqrt{Z_c}$ can be expressed by the scattering matrix coefficient S_{ij}:

$$S_{ij} = \frac{a_{\text{out},i}}{a_{\text{in},j}} \quad \text{evaluated with } \forall \mathrm{k} \neq \mathrm{j}, \mathrm{a_{in,k}} = 0 \tag{2.48}$$

The device behavior is entirely characterized by knowledge of the S-matrix. This scattering matrix approach has been extended to a quantum-mechanical description of the device by Gardiner and

Collett [45]. This theory describes the very general case of a system of Hamiltonian $\hat{H}$ coupled to different continuums of modes with coupling strengths κ_i.

In our particular case, the system is the LC resonator described by the intra-resonator field operator $\hat{a}(t)$ introduced in Eq. 2.22 described in the Heisenberg picture. The two transmission lines provide two baths, described by the propagating operators $\hat{a}_{\text{in},i=1,2}$ introduced in Eq. 2.38. The coupling rates κ_i can be identified to the energy damping rates introduced above if one performs a Markovian approximation valid in the limit of coupling to a continuum of modes (see Figure 2.5c). In the treatment introduced by Gardiner and Collett, the evolution of $\hat{a}(t)$ is given by the following master equation (in the Heisenberg picture):

$$\partial_t \hat{a}(t) = \frac{[\hat{a}, \hat{H}]}{i\hbar} - \frac{1}{2}\left(\sum_i \kappa_i + \kappa_{\text{int}}\right)\hat{a}(t) + \sum_i \sqrt{\kappa_i}\hat{a}_{\text{in},i}(t) + \sqrt{\kappa_{\text{int}}}\hat{a}_{\text{int}}(t) \tag{2.49}$$

where $[\hat{a}, \hat{H}]/i\hbar = -i\omega_0\,\hat{a}$ for a LC oscillator. The terms $\sqrt{\kappa_i}\,\hat{a}_i^{\rightarrow}(t)$ are the source terms and the terms $\frac{1}{2}\left(\sum_i \kappa_i + \kappa_{\text{int}}\right)\hat{a}(t)$ are the damping terms. The internal losses are associated to an additional port at thermal equilibrium. The classical continuity equation Eq. 2.30 translates into the important following relation between input and intra-resonator field:

$$\hat{a}_i^{\rightarrow}(t) + \hat{a}_i^{\leftarrow}(t) = \sqrt{\kappa_i}\hat{a}(t) \tag{2.50}$$

External drive by coherent states

In our experiments, the resonators are driven by classical fields which can be described as coherent states $|\alpha_{\text{in},i}\rangle$. The incident power on the resonator is thus given by $P = \hbar\omega|\alpha_{\text{in},i}|^2$. Under a classical drive $\alpha_{\text{in},i}$ on port i, the mean-value of the intra-resonator $\langle\hat{a}\rangle(t) = \alpha(t)$ is then given by Eq. 2.49:

$$\partial_t \alpha(t) = -i\omega_0\alpha(t) - \frac{\kappa_1 + \kappa_2 + \kappa_{\text{int}}}{2}\alpha(t) + \sqrt{\kappa_i}\alpha_{\text{in},i}(t) \tag{2.51}$$

and thus by Fourier transform, one finds the steady state solution of α:

$$\alpha(\omega) = \frac{2\sqrt{\kappa_i}}{\kappa_1 + \kappa_2 + \kappa_{\text{int}} - 2i(\omega - \omega_0)}\alpha_{\text{in},i}(\omega) \tag{2.52}$$

At resonance, under a drive of power P_i the intra-cavity photon number $\bar{n} = |\alpha|^2$ is:

$$\bar{n} = \frac{4\kappa_i P_i}{\hbar\omega_0(\kappa_1 + \kappa_2 + \kappa_{\text{int}})^2} \tag{2.53}$$

In the following chapters, we are also interested in the current flowing through the inductor and the associated generated magnetic field. Upon an incident resonant signal of power P, they are given by:

$$\langle\hat{I}\rangle(t) = 2\delta I\sqrt{\bar{n}}\cos(\omega_0 t) \tag{2.54}$$

$$\langle\hat{\mathbf{B}}\,(\mathbf{r})\rangle(t) = 2\boldsymbol{\delta B}\,(\mathbf{r})\,\sqrt{\bar{n}}\cos(\omega_0 t) \tag{2.55}$$

Measurements

In ch. 5, the frequency and coupling rates of the resonator are determined experimentally by using a Vector Network Analyser (VNA). This apparatus measures the S-matrix components in transmission ($S_{21}(\omega)$ and $S_{12}(\omega)$) and in reflexion ($S_{11}(\omega)$ and $S_{22}(\omega)$). The power waves $a_{\text{in},i}$ and

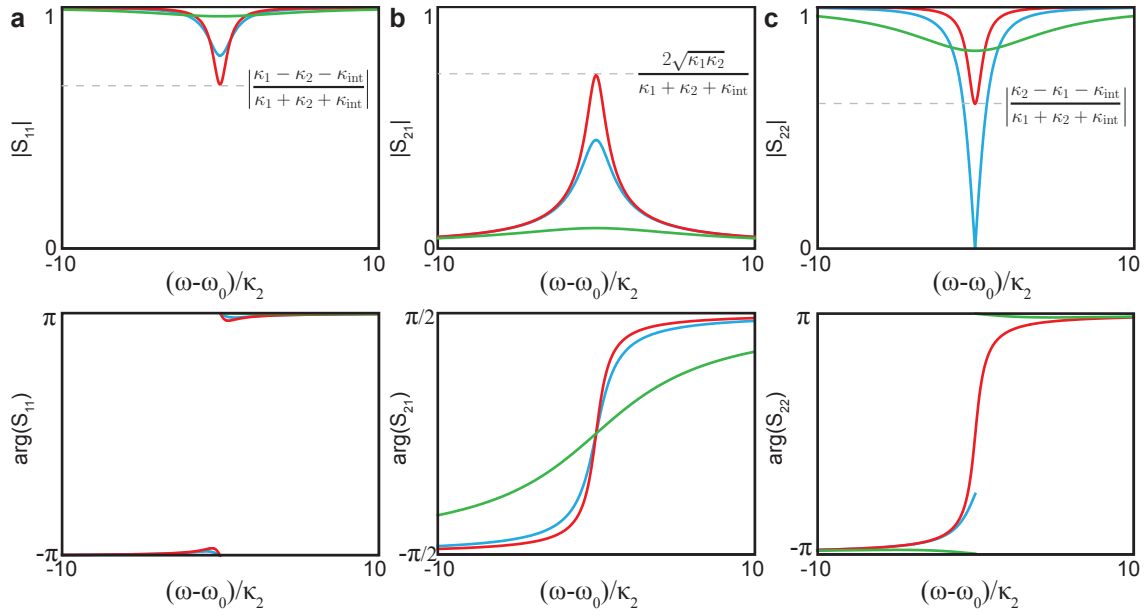

FIGURE 2.6: **Transmission and reflexion measurements** evaluated for $\kappa_1 = 0.2\,\kappa_2$ and three values of $\kappa_{\rm int}$: $\kappa_{\rm int} + \kappa_1 = \kappa_2$ (blue), $\kappa_{\rm int} + \kappa_1 = 0.25\,\kappa_2$ (green), $\kappa_{\rm int} + \kappa_1 = 10\,\kappa_2$ (red). **a, b and c** are respectively the modulus (top) and argument (bottom) of $S_{11}(\omega)$, $S_{21}(\omega)$ and $S_{22}(\omega)$

$a_{{\rm out},i}$ introduced earlier to define the S-parameters can be replaced by the coherent signals $\alpha_{{\rm in},i}$ and $\alpha_{{\rm out},i}$. Eq. 2.50 yields the relation $\alpha_{{\rm in},i}(\omega) + \alpha_{{\rm out},i}(\omega) = \sqrt{\kappa_i}\alpha(\omega)$, and thus one can compute the dependencies of $S_{ij}(\omega)$ expected for a LC resonator coupled to two transmission lines:

in transmission:

$$S_{21}(\omega) = S_{12}(\omega) = \left.\frac{\sqrt{\kappa_2}\alpha(\omega) - \alpha_{{\rm in},2}}{\alpha_{{\rm in},1}}\right|_{\alpha_{{\rm in},2}=0} = \frac{2\sqrt{\kappa_1\kappa_2}}{\kappa_1 + \kappa_2 + \kappa_{\rm int} - 2i(\omega - \omega_0)} \tag{2.56}$$

in reflexion:

$$S_{ii}(\omega) = \left.\frac{\sqrt{\kappa_i}\alpha(\omega) - \alpha_{{\rm in},i}}{\alpha_{{\rm in},i}}\right|_{\alpha_{{\rm in},j}=0} = \frac{\kappa_i - \kappa_j - \kappa_{\rm int} + 2i(\omega - \omega_0)}{\kappa_i + \kappa_j + \kappa_{\rm int} - 2i(\omega - \omega_0)} \tag{2.57}$$

Depending on the relative strength of the internal damping rate $\kappa_{\rm int}$ compared to the external coupling rate $\kappa_c = \kappa_1 + \kappa_2$, it is interesting to distinguish three regimes, as illustrated on Fig. 2.6. In our experiment, the coupling to port 1 and 2 are asymmetric with $\kappa_1 \ll \kappa_2$. Seen from port 2, we thus have:

- **The under-coupled regime, where $\kappa_{\rm int} \gg \kappa_2, \kappa_1$:** (green curves) In reflexion on both ports, only a small dip in amplitude is observed with a small phase shift in phase. The transmission peak width is essentially set by $\kappa_{\rm int}$.
- **The critical coupling regime, where $\kappa_{\rm int} + \kappa_1 = \kappa_2$:** (blue curves). The reflexion on port 2 goes to 0 with a π-shift discontinuity. The transmission reaches $\sqrt{\kappa_1/\kappa_2}$. The reflexion on port 1 is in the under-coupled regime.
- **The over-coupled regime, where $\kappa_{\rm int} + \kappa_1 \ll \kappa_2$:** (red curves) For both reflexion measurements only a slight dip in amplitude occurs, however the phase when reflecting on port 2 shifts by 2π while the shift on port 1 is less than π. The transmission at resonance is close to $2\sqrt{\kappa_1/\kappa_2}$.

In order to determine ω_0, κ_1, κ_2 and κ_{int} experimentally on a two-port device with asymmetric couplings, the measurement of at least two elements of the scattering matrix among $S_{11}(\omega)$, $S_{22}(\omega)$ and $S_{21}(\omega)$ is required. However, measuring the transmission $S_{21}(\omega)$ generally only brings knowledge of the total damping rate κ since exploiting the peak height to obtain the quantity $\sqrt{\kappa_1\kappa_2}$ requires prior precise calibration of the measurement lines. The best determination of the resonator parameters is thus obtained by measuring and fitting $S_{11}(\omega)$ and $S_{22}(\omega)$ because they are in a sense "self-calibrated" by the fact that $|S_{11}| = |S_{22}| = 1$ far from resonance. In the following, we also measure single-port resonators, which are treated with the same formulas as already presented, with $\kappa_1 = 0$. It should also be noted that the S-parameters measured by the VNA are defined as the conjugates quantities $S_{ij}(\omega)^*$ of what is derived here.

2.2 Amplification at the quantum-limit

Several orders of magnitude separate the small power of the quantum microwave signals that we wish to detect and the noise level of typical room-temperature measurement apparatus. It is thus essential to amplify the signals with as little noise as possible. Quantum mechanics imposes some constraints on the minimum amount of noise that an amplifier has to add to the signal, as shown by Haus and Mullen [46], and Caves [11]. While usual microwave amplifiers add in general much more noise, novel amplifiers developed for cQED research and called Josephson Parametric Amplifiers (JPA) do reach this quantum limit. In this section, we will give an overview of the theoretical aspects of quantum-limited amplification, and we will also expose the working principle of the flux-pumped JPA used in this work.

2.2.1 Input-output relations for linear amplifiers

A signal of frequency ω and of bandwidth $\Delta\omega$ is emitted in a transmission line connected to a linear amplifier with power gain G. The amplified signal then propagates via a second transmission line to either a homodyne detection yielding the I and Q quadratures of the microwave signal, or a frequency spectrum analyser. The signal being narrow-band, we can use the right-propagating spatio-temporal modes defined in 2.1.1 to describe the input and output signals $\hat{a}_{\text{in}}$, $\hat{a}_{\text{in}}^\dagger$, $\hat{a}_{\text{out}}$, $\hat{a}_{\text{out}}^\dagger$, and their associated quadrature operators.

The outcome of the measurement in the case of homodyne detection is directly linked to the quadrature operators. Indeed, the signal is mixed with a strong microwave tone at frequency ω and phase θ. By filtering the two output voltages using a low-pass filter (typically smaller than $2\pi/\Delta\omega$), one gets outcomes proportional to $\hat{X}_{\text{out},\theta}$ and $\hat{Y}_{\text{out},\theta}$. For one quadrature, the averaged signal is proportional to $\langle\hat{X}_{\text{out},\theta}\rangle$ and the variance to $\langle\Delta\hat{X}^2_{\text{out},\theta}\rangle$. When measuring the signal with a spectrum analyser, set with a resolution bandwidth suited to the signal, the noise power detected in the absence of signal is simply $\langle\hat{X}^2_{\text{out},\theta}\rangle+\langle\hat{Y}^2_{\text{out},\theta}\rangle$. In the remainder of the chapter, we consider only the quadratures $\hat{X}$ and $\hat{Y}$ related to $\hat{X}_\theta$ and $\hat{Y}_\theta$ by Eq. 2.2. We now derive the input-output relations for linear amplifiers as well as their noise properties using these operators.

It is tempting to relate the output and input quadratures of a linear amplifier by defining $\hat{X}_{\text{out}} = \sqrt{G_X}\hat{X}_{\text{in}}$ and $\hat{Y}_{\text{out}} = \sqrt{G_Y}\hat{Y}_{\text{in}}$. This definition is however incompatible with the commutation relations for $\hat{a}_{\text{out}}$ and $\hat{a}_{\text{in}}$, except if $\sqrt{G_X G_Y} = 1$. Following Caves [11], two types of amplifiers are usually distinguished.

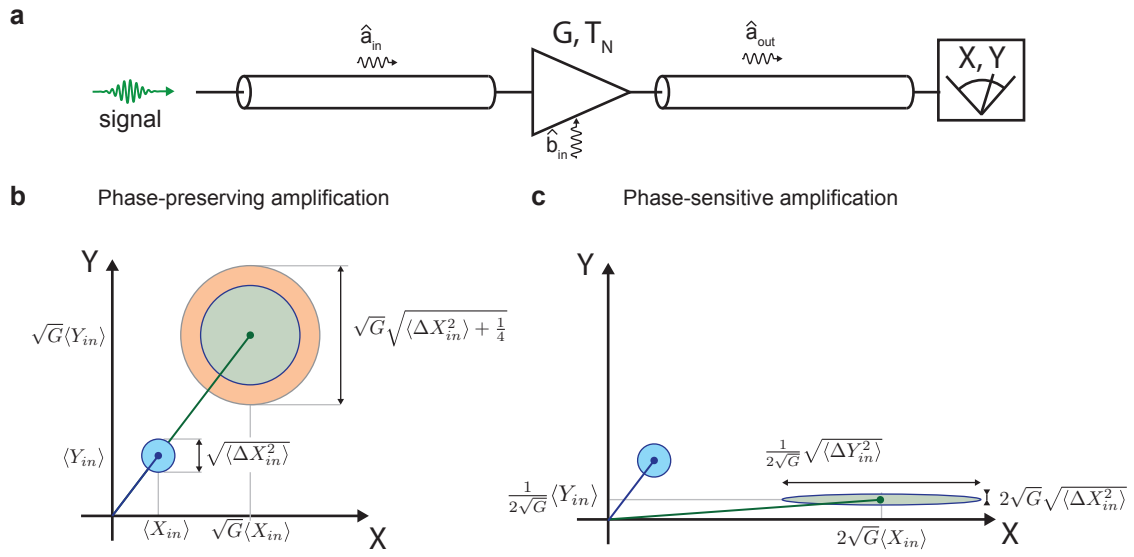

FIGURE 2.7: **Linear amplifiers. a** A linear amplifier of gain G and noise temperature T_N is used to detect a narrow-band signal. **b-c** Phase-preserving and phase-sensitive amplification in phase-plane representation in the limit of high gain. The disks indicate the contour of the Wigner function. A phase preserving amplifier degrades the SNR, with the added noise represented in red. In phase-sensitive amplification, one quadrature is amplified at the expense of the other, but one can evade the noise added by the Heisenberg uncertainty principle.

Phase-preserving amplification

Phase-preserving amplifiers have identical gain on both quadratures $G_X = G_Y = G$. According to the above discussion, one needs to introduce a mode $\hat{b}_{\rm in}$ internal to the amplifier that commutes with $\hat{a}_{\rm in}$ to describe the amplification:

$$\hat{a}_{\rm out} = \sqrt{G}\hat{a}_{\rm in} + \sqrt{G-1}\hat{b}^\dagger_{\rm in} \tag{2.58}$$

with $\hat{b}_{\rm in}$ defined such that $[\hat{b}_{\rm in}, \hat{b}^\dagger_{\rm in}] = 1$ and $[\hat{b}_{\rm in}, \hat{a}^\dagger_{\rm in}] = 0$. By imposing $\langle \hat{b}_{\rm in} \rangle = 0$, one finds

$$\langle \hat{X}_{\rm out} \rangle = \sqrt{G}\langle \hat{X}_{\rm in} \rangle \tag{2.59}$$
$$\langle \hat{Y}_{\rm out} \rangle = \sqrt{G}\langle \hat{Y}_{\rm in} \rangle \tag{2.60}$$

which are the expected relations for the amplified signal.

Phase-sensitive amplification

A phase-sensitive device amplifies one quadrature at the expense of the other. We consider here only amplifiers for which $G_s = G_X = 1/G_Y$, so that the condition $\sqrt{G_X G_Y} = 1$ is satisfied. In that case, the input and output quadratures are linked by:

$$\hat{X}_{\rm out} = \sqrt{G_s}\hat{X}_{\rm in} \tag{2.61}$$
$$\hat{Y}_{\rm out} = \frac{1}{\sqrt{G_s}}\hat{Y}_{\rm in} \tag{2.62}$$

Interestingly, the phase-sensitive amplifier is just a particular case of the phase-preserving amplifier. Writing $\hat{a}_{\text{out}} = \sqrt{G_s}\hat{X}_{\text{in}} + i\frac{1}{\sqrt{G_s}}\hat{Y}_{\text{in}}$ yields Eq. 2.58 by choosing $\hat{b}_{\text{in}} = \hat{a}_{\text{in}}$ and $\sqrt{G_s} = \sqrt{G} + \sqrt{G-1}$. At large gains, one can identify $\sqrt{G_s} = 2\sqrt{G}$.

2.2.2 Quantum limits on the noise added by the amplifier

Phase-preserving amplifier

For a phase-preserving amplifier, one can derive from the input-output equations (Eq. 2.58) that the outcoming noise referred to the input in the absence of a signal is:

$$\frac{\langle \Delta\hat{X}^2_{\text{out}}\rangle + \langle \Delta\hat{Y}^2_{\text{out}}\rangle}{G} = \langle \Delta\hat{X}^2_{\text{in}}\rangle + \langle \Delta\hat{Y}^2_{\text{in}}\rangle + \left(1 - \frac{1}{G}\right)\left(\langle \Delta\hat{X}^2_b\rangle + \langle \Delta\hat{Y}^2_b\rangle\right) \tag{2.63}$$

where $\langle \hat{X}^2_b\rangle$ are the internal mode fluctuations. We thus arrive to the important conclusion that the output noise is the sum of two contributions : the input noise and the noise added by the amplifier given by the internal mode fluctuations. We note $n = \langle \hat{X}^2_{\text{out}}\rangle/G$ the noise detected on a single quadrature and $n_{\text{eq}} = \langle \Delta\hat{X}^2_{\text{in}}\rangle$ and $n_{\text{amp}} = \langle \Delta\hat{X}^2_{\text{b}}\rangle$ its two contributions so that $n = n_{\text{eq}} + n_{\text{amp}}$.

For an incoming field in a thermal equilibrium state, the input noise n_{eq} is given by Eq. 2.10. The vacuum state with fluctuations equaling the Heisenberg uncertainty relation $n_{\text{eq}} = \frac{1}{4}$ is reached for temperatures $k_B T \ll \hbar\omega$. While operating in this limit, the detected noise is purely of quantum origin due to the incompressible fluctuations of the field, in opposition to being set by thermal fluctuations.

The amplifier added noise is also bound by the Heisenberg uncertainty principle since $\langle \hat{X}^2_b\rangle\langle \hat{Y}^2_b\rangle \geqslant \frac{1}{16}$. Imposing that the added noise is phase-insensitive for a phase-preserving amplifier $\langle \hat{X}^2_b\rangle = \langle \hat{X}^2_b\rangle \geqslant 1/4$ [11], the quantum limit on amplifier-added noise is:

$$\frac{\langle \hat{X}^2_{\text{out}}\rangle + \langle \hat{Y}^2_{\text{out}}\rangle}{G} \underset{G\gg 1}{\geqslant} \langle \hat{X}^2_{\text{in}}\rangle + \langle \hat{Y}^2_{\text{in}}\rangle + \frac{1}{2} \tag{2.64}$$

showing that a phase-preserving amplifier adds at best the equivalent of half a photon ($n_{\text{amp}} \geqslant 1/4$) of noise at the input in the case of large gains, as stated by Haus-Caves theorem. In terms of amplifier noise temperature, this limit can be re-written as:

$$T_N \geqslant \frac{\hbar\omega}{2k_B(1 - 1/G)} \tag{2.65}$$

Phase-sensitive amplifier

A phase-sensitive amplifier can escape the quantum-limit on amplification since according to Eq. 2.62:

$$\frac{\langle \Delta\hat{X}^2_{\text{out}}\rangle}{G_s} = \langle \Delta\hat{X}^2_{\text{in}}\rangle \tag{2.66}$$

The price to pay for this noiseless amplification is that we access only one quadrature of the field. This does not necessarily constitute an issue if the output signal phase is constant and known, which

is precisely the case for spin-echoes[1]. When one performs a noiseless amplification without thermal population in the incoming waveguide, the measurement reaches the standard quantum limit with $\langle \Delta \hat{X}^2_{\text{out}} \rangle / G_s = 1/4$.

Note that in the absence of a signal, the de-amplified quadrature has less fluctuations than the input state:

$$\langle \Delta \hat{Y}^2_{\text{out}} \rangle \underset{G_S \gg 1}{=} \frac{\langle \Delta \hat{Y}^2_{\text{in}} \rangle}{4G_S} \ll \frac{1}{4} \tag{2.67}$$

creating a squeezed-state of squeezing parameter $e^{\zeta} = G_s$. In ch. 9, we use a JPA to generate a squeezed state and detect a signal below the standard quantum limit.

2.2.3 The flux-pumped Josephson Parametric Amplifier

In the last decade, various designs for an amplifier operating at the quantum limit have been developed [47, 48, 49, 50, 51, 52, 53, 54]. These designs are based on Josephson junctions embedded in superconducting resonators following pioneering work by Yurke et al. [12]. These elements enable parametric amplification of a signal at frequency $\omega_s \approx \omega_0$ by transfer of energy from a pump at frequency ω_p to the signal and to a complementary idler of frequency ω_I. In the device used in this thesis, the tunability of a variant of the Josephson junction, the SQUID (Superconducting Quantum Interference Device), is used to modulate the resonator frequency at $\omega_p \approx 2\omega_0$ and create a three-wave mixing process with $\omega_p = \omega_s + \omega_I$ [51, 52, 53, 54]. Due to the use of dissipationless elements these amplifiers can add the minimum amount of noise allowed quantum mechanically when operated in phase-preserving mode ($\omega_s \neq \omega_I$) and no noise in the amplified quadrature for phase-sensitive amplification ($\omega_s = \omega_I$). In this paragraph, we only intend to give an overview of the device operating principle. We refer the reader to [54, 55, 56] for more details and rigorous demonstrations.

The SQUID, a flux-tunable inductance

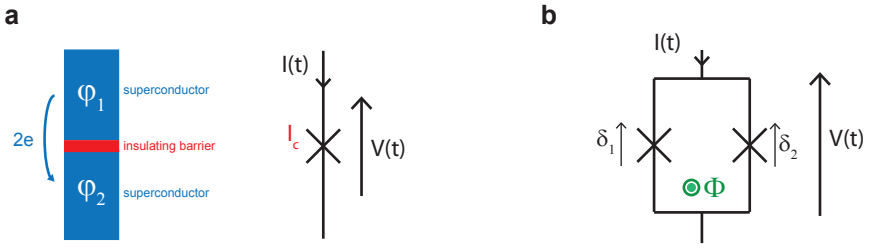

FIGURE 2.8: **Josephson junction and its tunable equivalent: a SQUID. a** A Josephson junction is composed of an insulating barrier between two superconducting electrodes. The Josephson relations describing the current and voltage for this element give rise to a non-linearity. **b** When two Josephson junctions are inserted in a loop, they form a Josephson junction of characteristics tunable by the amount of flux threaded through the loop.

A Josephson junction is made out of two superconducting electrodes separated by a thin insulating barrier (see Figure 2.8). On each superconducting electrode, the electrons form a Cooper pairs condensate described by a macroscopic quantum mechanical wavefunction of phase φ. Due to the small thickness of the barrier, the wavefunctions of each condensate overlap allowing for the

[1] Indeed, for TLS, the phase of the spin-echo is set by the phases chosen for the drive pulses. For multi-level systems however, the spin-echo phase may vary and this variation can be of interest. Retaining the phase information in such cases prevents the use of phase-sensitive amplifiers.

tunneling of Cooper pairs. The Josephson relations describing the current I_J of Cooper pairs across the junction are [57]:

$$I_J = I_c \sin(\delta) \tag{2.68}$$

$$V = \varphi_0 \frac{\partial \delta}{\partial t} \tag{2.69}$$

where $\delta = \varphi_2 - \varphi_1$ is the phase difference across the junction, I_c is the junction critical current, $\varphi_0 = \hbar/2e$ is called the reduced superconducting flux quantum, and V is the voltage across the junction. From Eqs. 2.68 & 2.69, one gets:

$$\frac{dI_J}{dt} = \frac{I_c\sqrt{1-(I_J/I_c)^2}}{\varphi_0} V. \tag{2.70}$$

A Josephson junction thus behaves as a non-linear inductance $L_J(I_J)$ with

$$L_J = \frac{\varphi_0}{I_c\sqrt{1-(I_J/I_c)^2}} \approx \frac{\varphi_0}{I_c}\left(1 + \frac{(I_J/I_c)^2}{2} + O\left[(I_J/I_c)^4\right]\right) \tag{2.71}$$

When two Josephson junctions are connected in a superconducting loop, as shown in Fig. 2.8b, they form a SQUID[58]. The total current I through the SQUID is the sum of each branch current. In the case of two junctions with identical critical current I_c, the current is expressed as:

$$I = I_c[\sin(\delta_1) + \sin(\delta_2)] = 2I_c \cos\left(\tfrac{\delta_2-\delta_1}{2}\right) \sin\left(\tfrac{\delta_2+\delta_1}{2}\right) \tag{2.72}$$

where $\delta_{1,2}$ are the phase differences across each junction. Due to the flux quantization in the superconducting SQUID loop, the phases $\delta_{1,2}$ are linked to the total magnetic flux Φ_{tot} threading the SQUID by:

$$\delta_2 - \delta_1 = 2\pi \frac{\Phi_{\text{tot}}}{\Phi_0} \tag{2.73}$$

in which $\Phi_0 = 2\pi\varphi_0$. Φ_{tot} is the sum of the applied flux Φ and the flux generated by the circulating current in the SQUID loop. The latter can be neglected for small SQUID loops, which we assume to be the case in the following. The total current can then be expressed as:

$$I = 2I_c \cos\left(\pi \frac{\Phi}{\Phi_0}\right) \times \sin(\delta) \tag{2.74}$$

with $\delta = (\delta_2 + \delta_1)/2$. Thus a symmetric SQUID can be seen as a Josephson junction whose supercurrent is flux-tunable, with $I_c^S(\Phi) = 2I_c \cos\left(\pi \frac{\Phi}{\Phi_0}\right)$. The SQUID is thus a tunable inductance:

$$L_J(\Phi) = \frac{\varphi_0}{I_c^S(\Phi)} \tag{2.75}$$

When the current I approaches the SQUID critical current $I_c^S(\Phi)$ however the non-linearity of the SQUID Josephson junctions plays a role, as we will see in the following.

A tunable resonator for parametric amplification

The tunability of the SQUID inductance is exploited to provide parametric amplification. Consider a resonator with the geometry shown in Fig. 2.9a: a capacitance C_g in parallel with an inductance L_g and an array of N symmetric SQUID loops, probed via a transmission line of characteristic impedance Z_c coupled by a capacitance C_c to the resonator. As illustrated in Fig. 2.9a, the resonator

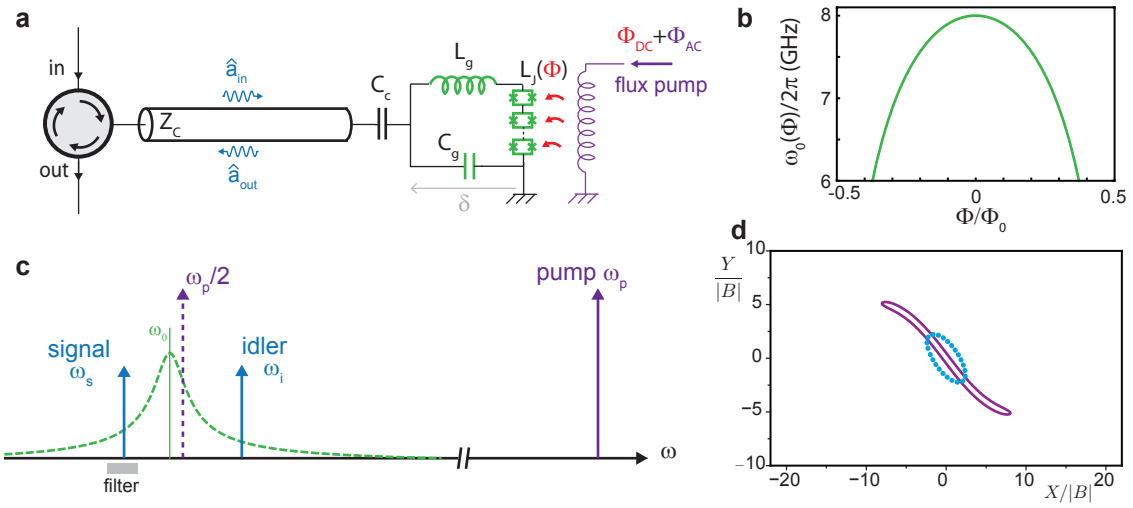

FIGURE 2.9: **Flux-pumped Josephson Parametric Amplifier. a** The JPA comprises a geometrical inductance and capacitance in parallel with an array of SQUIDs, it is probed in reflexion via a transmission line capacitively coupled. **b** Modulation of the frequency of the resonator as a function of the SQUIDs DC flux bias. **c** Phase-preserving amplification operation of the JPA: a pump applied at $\omega_p \approx 2\omega_0$ amplifies the signal and generates an idler signal. The idler signal can be removed by filtering. **d** Evidence of the phase kick on the intra-cavity field induced by the non-linearity of the SQUID, extracted from [55].

is probed in reflexion: a circulator is needed to route the input signal to the resonator, and the output signal towards the output line.

Using the results we derived in section 2.1.4, the resonator frequency is:

$$\omega_0(\Phi)^{-2} = (C + C_c)(L_g + NL_J(\Phi)) \tag{2.76}$$

Denoting $p = NL_J/(L_g + NL_J)$ the participation ratio of the Josephson inductance to the total inductance, the Taylor expansion to the second-order in $\pi\frac{\Phi}{\Phi_0}$ of the resonator frequency yields:

$$\frac{\omega_0(\Phi)}{\omega_0(0)} \approx 1 - \frac{1}{4}p\left(\pi\frac{\Phi}{\Phi_0}\right)^2 \tag{2.77}$$

The tunability of ω_0 with respect to Φ is obtained by placing a flux line nearby the SQUIDs array (see Figure 2.9a). For a resonator of bare frequency $\omega_0(0)/2\pi = 8$ GHz and characteristic impedance $Z_0 = 100\ \Omega$, the frequency tunability ranges over several hundreds of megaHertz as shown in Fig. 2.9b.

According to Landau [59], modulating at a frequency close to $2\omega_0$ the resonator frequency gives rise to the phenomenon of parametric amplification. The amplifier thus consists in a tunable resonator $\omega_0(\Phi_{DC})$, a pump signal sent through the flux-line at frequency $\omega_p \approx 2\omega_0$, and an input port through which a signal at a frequency $\omega \approx \omega_0$ is sent, with the reflected signal being amplified.

The JPA being composed of entirely dissipation-less elements and based on the simple parametric amplification process, it reaches the quantum limit of amplifier-added noise discussed earlier. More precisely, it can be used in either of the two modes of operation:

- **Non degenerate operation ($\omega_p \neq 2\omega_s$):**

  In this case, gain at the idler $\omega_I = \omega_p - \omega_s$ and the signal frequencies appear (see Figure 2.9c). The power gain G achieved on the signal by this process increases as a function of the pump

amplitude until it exceeds the damping occurring via the transmission line and enters an auto-oscillation regime. Below this threshold, this system behaves as a phase-preserving amplifier. As explained earlier, it amplifies each quadrature with half a photon of noise added. In practice, in order to amplify a signal at ω_s, a narrow-band filter is used to get rid of the idler contribution (see Fig. 2.9).

- **Degenerate operation ($\omega_p = 2\omega_s$):**

  In this case interferences between the idler mode and the input signal leads to a phase sensitive amplification depending on the relative phase between the signal and the pump $\Delta\phi$:

$$G(\Delta\phi) = \left(G_s - \frac{1}{G_s}\right)\cos^2\Delta\phi + \frac{1}{G_s} \tag{2.78}$$

  As discussed earlier, this degenerate amplifier does not add noise to the incoming signal and amplifies noiselessly one of its quadratures. As a consequence, this device can also be used to generate a squeezed vacuum state, as shown in ch. 9. A strong advantage of this device compared to other designs is that the pump line is physically isolated from the input and output line preventing any leakage of the strong pump tone and thus it can avoid spoiling the produced squeezed vacuum state as well as saturating the next amplification stage.

Limitations

The limitations of this JPA design arise from the non-linearity of the Josephson junction [55, 54]. When the incoming signal amplitude increases, the AC currents flowing through the SQUIDs also increase and eventually approach the SQUID critical current; the resulting Kerr effect leads to a further shift of the resonator frequency which perturbs the parametric amplification process. As a result, the phase response is distorted (see Fig. 2.9d), and the amplifier saturates. In our device, this occurs even for input signal powers as low as -130 dBm. Compared to noisier amplification schemes, all parametric amplifiers also suffer from a limited bandwidth. A strong effort is currently made to circumvent these limitations by exploring different designs and pumping schemes [52, 60].

While the device presented here only provides a gain above 25 dB in a bandwidth limited to a few megaHertz with an operating frequency tunable over several hundreds of megaHertz, it is particularly suited for the amplification of weak and narrow-band signals, such as a narrow-line ESR signal. We refer the reader to ch. 5 for a complete characterization of the device used in our experiment.

Chapter 3

Spins in a cavity

In this chapter, we model the behavior and dynamics of an ensemble of spins coupled to one mode of an electromagnetic resonator, such as a LC circuit for instance. We first give a brief account of the spin dynamics in a classical drive field, as can be found for instance in magnetic resonance textbooks. We then attempt to treat the same problem quantum-mechanically: first in the case where only one spin is coupled to a cavity, then for a spin ensemble. The quantum treatment allows us in particular to derive the cavity-induced spin relaxation rate which is the subject of ch. 8.

We restrict our study in this chapter to electronic spins $1/2$. Our discussion can be trivially extended to nuclear spins $1/2$; for multilevel systems, our treatment applies to a two-level restriction of the full energy spectrum.

3.1 Spin dynamics in a classical microwave field

3.1.1 Coherent spin evolution

Consider an electronic spin $1/2$, submitted to a classical magnetic field $\boldsymbol{B}(t)$. The two systems interact via the Hamiltonian $\hat{H} = -\hat{\boldsymbol{\mu}} \cdot \boldsymbol{B}(t)$, which involves the spin magnetic dipole $\hat{\boldsymbol{\mu}} = -\gamma_e \hbar \hat{\boldsymbol{S}}$. Here $\gamma_e = 28$ GHz/T is the so-called gyromagnetic ratio, and $\hat{\boldsymbol{S}} = (\hat{S}_x, \hat{S}_y, \hat{S}_z)$ is the dimensionless vectorial spin operator whose components obey the commutation relations $[\hat{S}_i, \hat{S}_j] = i\epsilon_{ijk}\hat{S}_k$. Using the Ehrenfest theorem one readily derives the equation of motion of the expectation value of the magnetic moment $\boldsymbol{\mu} = \langle \hat{\boldsymbol{\mu}} \rangle$:

$$\frac{d\boldsymbol{\mu}}{dt} = -\gamma_e \boldsymbol{\mu} \times \boldsymbol{B}(t). \tag{3.1}$$

For an ensemble of N spins in a volume V, each magnetic moment $\boldsymbol{\mu}_i$ adds up to a macroscopic magnetic moment $\sum_i \boldsymbol{\mu}_i$. The detectable quantity is then the macroscopic magnetization per unit volume defined by the vector:

$$\boldsymbol{M} = \frac{1}{V} \sum_i \boldsymbol{\mu}_i \tag{3.2}$$

that obeys:

$$\frac{d\boldsymbol{M}}{dt} = -\gamma_e \boldsymbol{M} \times \boldsymbol{B}(t). \tag{3.3}$$

The coherent dynamics of the magnetization vector $\boldsymbol{M}$ thus exclusively consist of rotations around $B(t)$; note in particular that the vector length does not change in this process. As a result, a good representation for the magnetization vector evolution is given by the Bloch sphere: the end point of the magnetization vector stays on a sphere of radius M.

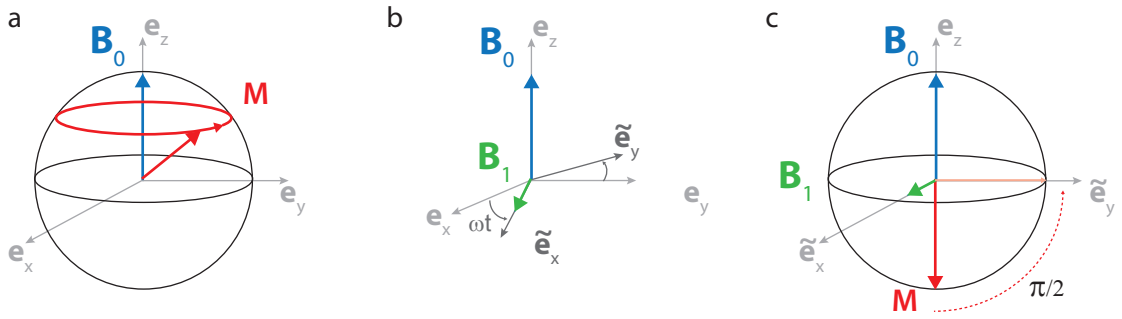

FIGURE 3.1: **Spin dynamics. a** Under a static magnetic field $\boldsymbol{B}_0$, the magnetization vector $\boldsymbol{M}$ precesses at frequency ω_0 in the laboratory frame. **b** Rotating frame of an oscillating magnetic field $\boldsymbol{B}_1$. **c** In this rotating frame, applying a short microwave pulse allows to rotate the magnetization vector.

When a static field $\boldsymbol{B}_0 = B_0\boldsymbol{e}_z$ is applied, the equation reduces to $\dot{\boldsymbol{M}} = -\omega_s \boldsymbol{M} \times \boldsymbol{e}_z$ with $\omega_s = \gamma_e B_0$. The magnetization vector precesses around $\boldsymbol{B}_0$ at frequency ω_s, the so-called Larmor frequency (see Figure 3.1a).

Consider next the application of an oscillating microwave field $\boldsymbol{B}_1(t) = 2\cos(\omega t)B_1\boldsymbol{e}_x$ orthogonal to $\boldsymbol{B}_0$. In the frame rotating at ω around $\boldsymbol{e}_z$, $\boldsymbol{B}_1(t)$ is expressed as a time-independent component $\boldsymbol{B}_1 = B_1\tilde{\boldsymbol{e}}_x$ if one neglects the fast-rotating terms in 2ω[1] (see Fig. 3.1b). In the rotating frame $(\tilde{\boldsymbol{e}}_x, \tilde{\boldsymbol{e}}_y, \boldsymbol{e}_z)$, the equation of motion is:

$$\frac{d}{dt}\tilde{M}_x = \Delta_s \tilde{M}_y \tag{3.4}$$

$$\frac{d}{dt}\tilde{M}_y = -\Delta_s \tilde{M}_x - \omega_1 M_z \tag{3.5}$$

$$\frac{d}{dt}M_z = \omega_1 \tilde{M}_y \tag{3.6}$$

where $\Delta_s = \omega - \omega_s$ and $\omega_1 = \gamma_e B_1$. A convenient representation for the magnetization vector in this frame is given by the Bloch sphere. Under this drive, the magnetization vector $\boldsymbol{M}$ rotates around the vector $\omega_1\tilde{\boldsymbol{e}}_x + \Delta_s\boldsymbol{e}_z$ at an angular speed called the Rabi frequency:

$$\Omega_R = \sqrt{\Delta_s^2 + \omega_1^2}. \tag{3.7}$$

In the particular case of a resonant microwave excitation $\Delta_s = 0$, the magnetization vector precesses at speed ω_1 around $\tilde{\boldsymbol{B}}_1$. Thus, a microwave pulse applied for a duration τ_p rotates the Bloch vector by an angle $\omega_1\tau_p$ around the axis set by $\tilde{\boldsymbol{B}}_1$ (see Figure 3.1c). In the following, we use mainly $\pi/2$ and π pulses of fixed lengths and adjust the drive power ω_1 to perform the desired rotations. The rotation axis is chosen by setting the phase of the microwave pulse: a microwave field with phase χ, $\boldsymbol{B}_1(t) = 2\cos(\omega t + \chi)\boldsymbol{B}_1$ becomes $\tilde{\boldsymbol{B}}_1 = B_1\cos(\chi)\tilde{\boldsymbol{e}}_x + B_1\sin(\chi)\tilde{\boldsymbol{e}}_{y(r)}$ in the rotating frame and thus any rotation axis within the $\tilde{x} - \tilde{y}$ plane can be chosen. Rotation around $\boldsymbol{e}_z$ can be performed by decomposing the motion in two rotations in the $\tilde{x} - \tilde{y}$ plane. Such a control allows to bring the magnetization vector to every point of the Bloch sphere.

[1]This approximation is valid when the AC magnetic field acts just as a perturbation of the static field: $B_1 \ll B_0$. This condition is always fulfilled in our experiments and we restrict our study to this regime. For an extended derivation, see [5].

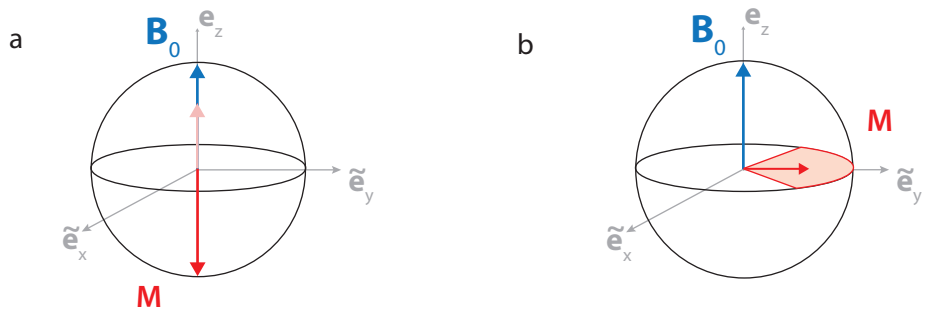

FIGURE 3.2: T_2 **and** T_1 **processes.** **a** A T_2 process describes the decoherence of the spin and leads to a fan-out of the spin transverse magnetization. **b** A T_1 process describes the longitudinal relaxation of the spin ensemble back to its thermal equilibrium.

3.1.2 Relaxation and decoherence

In addition to the coherent dynamics induced by microwave drives, the magnetization relaxes due to its interaction with the environment. We will here only provide a phenomenological description of these incoherent processes. More details will be given in ch. 4 for the specific case of Si:Bi spins. Two different relaxation processes can be distinguished:

- **Spin relaxation** describes the loss of energy by the spin ensemble and the decay of its longitudinal magnetization M_z back to its equilibrium state M_{th}, which is also the initial condition of the Bloch equations. At finite temperature, the equilibrium is a statistical mixture of excited and ground populations given by Boltzmann statistics. The overall equilibrium magnetization is $M_{\text{th}} = pM_0$, where p is the polarization and $M_0 = N\boldsymbol{\mu}$ is the maximum spin polarization. For an ensemble of spins-1/2 at temperature T, the polarization is given by the Curie law: $p = \tanh(\hbar\omega_s/k_BT)$. Energy relaxation consists in a progressive damping of the longitudinal magnetization M_z towards M_{th}, in a characteristic time T_1 which is called the spin relaxation time.
- **Spin decoherence:** the relaxation of the transverse magnetization components M_x and M_y is usually governed by completely different processes, and occurs on a time scale T_2 generally much shorter than its maximum value $2T_1$.

Longitudinal and transverse relaxation are included in Eq. 3.5 & 3.6 in the following way:

$$\frac{d}{dt}\tilde{M}_x = \Delta_s\tilde{M}_y - \frac{\tilde{M}_x}{T_2} \tag{3.8}$$

$$\frac{d}{dt}\tilde{M}_y = -\Delta_s\tilde{M}_x - \omega_1 M_z - \frac{\tilde{M}_y}{T_2} \tag{3.9}$$

$$\frac{d}{dt}M_z = \omega_1\tilde{M}_y - \frac{M_z - M_{\text{th}}}{T_1} \tag{3.10}$$

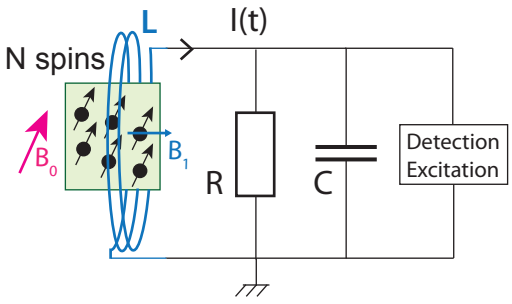

FIGURE 3.3: **ESR scheme**. A sample containing N spins is embedded inside a resonant structure. A static magnetic field $\boldsymbol{B}_0$ is applied to match the spin Larmor frequency to the RLC circuit. The inductive element L is used to apply magnetic microwave pulses $\boldsymbol{B}_1$ to excite the spins as well as to detect the transverse magnetization.

This set of equations is known as the Bloch equations. The steady-state $M^{(s)}$ reached under a coherent drive in the drive rotating frame is thus:

$$\tilde{M}_x^{(s)} = \frac{(T_2\Delta_s)(T_2\omega_1)}{1+(T_2\Delta_s)^2+T_1T_2\omega_1^2}M_{\text{th}} \tag{3.11}$$

$$\tilde{M}_y^{(s)} = \frac{T_2\omega_1}{1+(T_2\Delta_s)^2+T_1T_2\omega_1^2}M_{\text{th}} \tag{3.12}$$

$$M_z^{(s)} = \frac{1+(T_2\Delta_s)^2}{1+(T_2\Delta_s)^2+T_1T_2\omega_1^2}M_{\text{th}} \tag{3.13}$$

For increasing drive powers, the transverse magnetization components $\tilde{M}_x^{(s)}$ and $\tilde{M}_y^{(s)}$ on resonance ($\Delta_s = 0$) reach a maximum when $T_1T_2\omega_1^2 = 1$ before the overall magnetization vanishes for saturating drive powers $\omega_1 \gg 1/T_1T_2$. When saturation is reached, the two spin-levels are equally populated and essentially no longer interact with microwave fields.

Inhomogeneous and homogeneous broadening

Due to T_2 relaxation processes, the spin resonance acquires a linewidth $1/T_2$. In addition to this "homogeneous" broadening, the linewidth of a large ensemble of spins can also have an "inhomogeneous" distribution that arises from the difference in local environments of each spin, causing their Larmor frequency to have a distribution $\rho(\omega_s)$.

An inhomogeneously broadened ensemble can be seen as a collection of homogeneously-broadenend subsets, each described by the Bloch equations. Summing all inhomogeneously broadened contributions results in a decay of $M_{x,y}$ at a rate $1/T_2^*$, with $1/T_2^* = \Delta\omega$ being the width of $\rho(\omega_s)$, which can be much larger than $1/T_2$.

3.1.3 Inductive detection of magnetic resonance

Consider now the setup depicted in Fig. 3.3. The ensemble of spins is now embedded in a LC circuit of frequency ω_0 which generates the oscillating field $\boldsymbol{B}_1(\omega)$ at the spins location orthogonally to the static magnetic field $\boldsymbol{B}_0$. B_0 is chosen so that the spins Larmor frequency match the LC circuit frequency: $\omega_s \approx \omega_0$. The transverse components M_x and M_y expressed in the laboratory frame are related to $\tilde{M}_x$ and $\tilde{M}_y$ by:

$$M_x + iM_y = (\tilde{M}_x + i\tilde{M}_y)e^{i\omega_s t}$$

This precessing transverse magnetization gives rise to an induced electromotive force and hence to an AC current flowing in the resonant detection circuit:

$$I(t) \propto (\tilde{M}_x + i\tilde{M}_y)e^{i\omega_s t} \tag{3.14}$$

which allows spin detection. This "inductive detection" is the most widely used magnetic resonance measurement method [4]. While the precise link between the measured current and the transverse magnetization depends on the circuit geometry, the current is proportional to the filling factor of the circuit, defined as:

$$\eta = \frac{\int_{\text{sample}} f(\boldsymbol{r})d\boldsymbol{r}}{\int_{\text{detector}} f(\boldsymbol{r})d\boldsymbol{r}} \tag{3.15}$$

where $f(\boldsymbol{r}) = B_1(\boldsymbol{r})/\max[B_1(\boldsymbol{r})]$. As the transverse magnetization cannot be larger than M_{th}, the maximum current I_m that can be measured is $I_m \propto \eta p M_0$.

The transverse magnetization can result from either a continuous or a pulsed excitation. In the case of a continuous drive, the real and imaginary parts of the transverse magnetization induce a phase shift and/or absorption of the incoming microwave signal, which can be detected by lockin techniques. A transient transverse magnetization can also be induced by more or less complex pulse sequences. We focus on the latter technique, pulsed ESR, in the rest of the thesis.

Free induction decay

Starting from equilibrium, applying a microwave pulse of tipping angle $\theta = \pi/2$ brings the equilibrium magnetization $\boldsymbol{M}_{\text{th}}$ to the equator of the Bloch sphere, $\boldsymbol{M} = M_{\text{th}}\tilde{\boldsymbol{e}}_y$. Subsequently to the pulse, the magnetization vector precesses at frequency ω_s around $\boldsymbol{e}_z$ with its transverse and longitudinal component being damped respectively at rate T_2^* and T_1 for an inhomogeneous ensemble (Eqs. 3.9-3.10, see Fig. 3.4). This oscillating magnetization induces a decaying rf current in the inductor called the free-induction decay (FID) signal:

$$I_{\text{FID}}(t) \propto (\tilde{M}_x + i\tilde{M}_y)e^{i\omega_s t}e^{-t/T_2^*} \tag{3.16}$$

Spin-echo

Inhomogeneous broadening can be counteracted by a pulse sequence known as the Hahn echo [61] which will be used extensively throughout this thesis. The principle of a Hahn echo is shown in Fig. 3.4. A first $\pi/2$ pulse is applied to the spins along the x axis; the transverse magnetization along y generated by this pulse decays in a characteristic time T_2^*, due to inhomogeneous broadening. After a delay $\tau \gg T_2^*$, a π pulse is applied along the y axis. Its action is equivalent to a time reversal for the spins [61]: as a result, after another waiting time τ, the transverse magnetization comes back to its initial value. This generates a signal in the detection circuit known as "spin-echo". Like the FID, the echo amplitude is proportional to $\eta p M_0$. The echo signal itself decays with time constant T_2 as a function of time 2τ, due to spin decoherence, as already explained.

The spin-echo technique, in opposition to the FID detection, has for advantage that the signal is not emitted next to a microwave pulse whose strength may prevent the detection of the echo.

3.2 Spin dynamics in a quantum microwave field

After having introduced basic ESR concepts in the previous section, we now turn to the quantum-mechanical description of the spin-resonator interaction. Consider the system depicted in Fig. 3.5

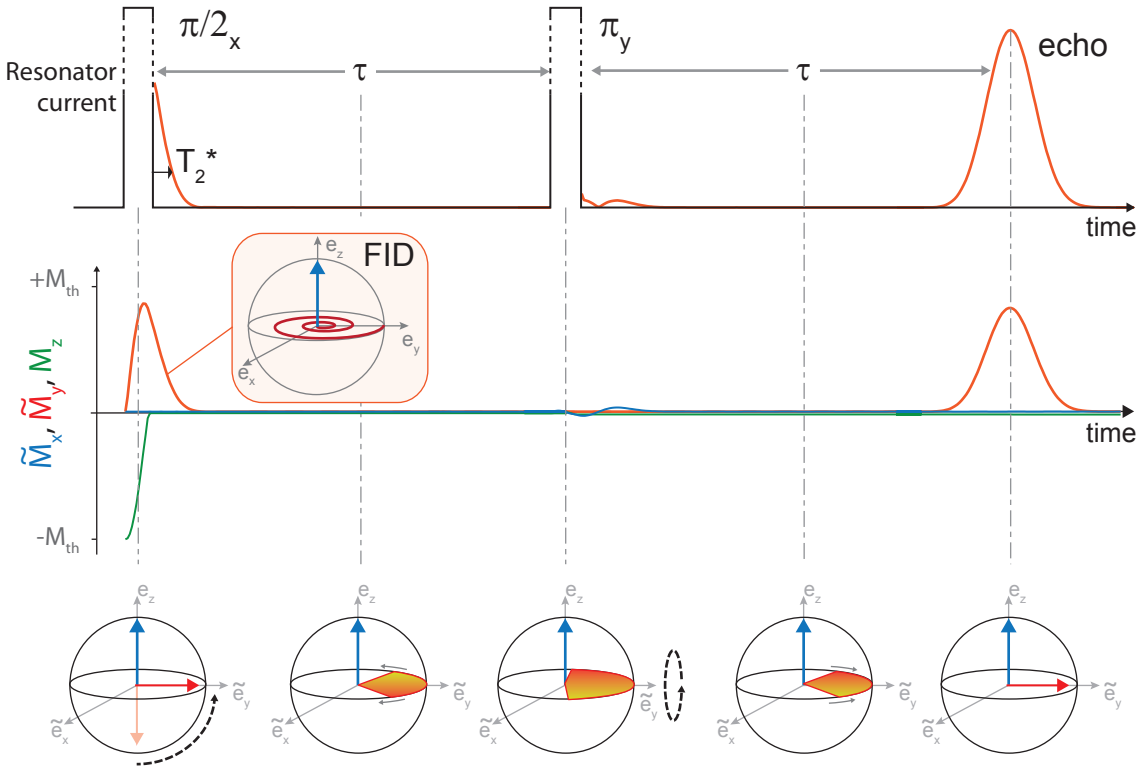

FIGURE 3.4: **Free induction decay and echo**. Starting from equilibrium, a $\pi/2$ pulse around $\tilde{\boldsymbol{e}}_x$ brings the magnetization vector to the equator of the Bloch sphere. Afterwards, in the laboratory frame the transverse magnetization precesses around $\boldsymbol{B}_0$ while in the drive rotating frame it vanishes in a time T_2^* due to inhomogeneous broadening. A π pulse around the $\tilde{y}$-axis applied after a delay τ refocusses the magnetization at time 2τ, giving rise to an echo. Top-middle graphs: The black lines sketch the control pulses while the colored lines represent the induced current in the resonator as well as the evolution of the magnetization components (extracted from numerical simulations for typical ESR parameters). The Bloch spheres illustrate the sequence at times indicated by dot-dashed grey lines

with N spins embedded into a resonator. As seen in 2.1.2, the LC resonator Hamiltonian is $\hat{H}_c = \hbar\omega_0\left(\hat{a}^\dagger\hat{a} + \frac{1}{2}\right)$. Its total damping rate $\kappa = \kappa_{\text{int}} + \kappa_c$ consists of internal losses and coupling to the measurement line, with $\kappa_c = \kappa_1 + \kappa_2$ the sum of the coupling rates to input and output ports. The circuit inductance, through which flows a current $\hat{I} = \delta I(\hat{a} + \hat{a}^\dagger)$, generates an oscillating magnetic field $\hat{\boldsymbol{B}}_1(\boldsymbol{r}) = \boldsymbol{\delta B}(\boldsymbol{r})(\hat{a} + \hat{a}^\dagger)$ at the spin location.

3.2.1 One spin coupled to a harmonic oscillator

Interaction Hamiltonian

Let us first consider the case of a single spin of Hamiltonian $H_s(\boldsymbol{B}_0)$ where $\boldsymbol{B}_0 = B_0\boldsymbol{e}_z$ is the applied static magnetic field. We isolate a two-level system $\{|\mathfrak{g}\rangle, |\mathfrak{e}\rangle\}$ among the spin energy-levels, with corresponding transition frequency $\omega_s(B_0) = (E_{|\mathfrak{e}\rangle} - E_{|\mathfrak{g}\rangle})/\hbar$.

We introduce the Pauli matrices $(\hat{\sigma}_x, \hat{\sigma}_y, \hat{\sigma}_z)$, where :

$$\hat{\sigma}_x = \begin{pmatrix} 0 & 1 \\ 1 & 0 \end{pmatrix}, \quad \hat{\sigma}_y = \begin{pmatrix} 0 & -i \\ i & 0 \end{pmatrix} \text{ and } \quad \hat{\sigma}_z = \begin{pmatrix} 1 & 0 \\ 0 & -1 \end{pmatrix} \tag{3.17}$$

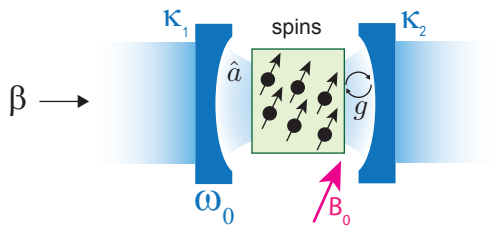

FIGURE 3.5: **The interaction between spins and resonator** is described quantum-mechanically by a spin-photon constant noted g, which is the product of the spin magnetic dipole moment and the magnetic field vacuum fluctuations at the spin location.

One can also define $\hat{\sigma}_\pm = \frac{1}{2}(\hat{\sigma}_x \pm i\hat{\sigma}_y)$, whose matrix forms are:

$$\hat{\sigma}_+ = \begin{pmatrix} 0 & 1 \\ 0 & 0 \end{pmatrix} \text{ and } \hat{\sigma}_- = \begin{pmatrix} 0 & 0 \\ 1 & 0 \end{pmatrix} \tag{3.18}$$

In the basis $\{|\mathfrak{e}\rangle, |\mathfrak{g}\rangle\}$, the spin Hamiltonian reduces to:

$$\hat{H}_s(\boldsymbol{B}_0) = \frac{\hbar\omega_s(B_0)}{2}\hat{\sigma}_z, \tag{3.19}$$

The magnetic coupling of the spin to the resonator is described by the interaction Hamiltonian:

$$\hat{H}_{\text{int}} = -\hbar\gamma_e \hat{\boldsymbol{S}} \cdot \hat{\boldsymbol{B}}_1 = -\hbar\gamma_e \boldsymbol{\delta B}(\boldsymbol{r}) \cdot \hat{\boldsymbol{S}}(\hat{a} + \hat{a}^\dagger) \tag{3.20}$$

In the spin-basis restricted to $\{|\mathfrak{e}\rangle, |\mathfrak{g}\rangle\}$, $\hat{H}_{\text{int}}^{(\mathfrak{eg})} = \sum_{i,j=\mathfrak{e},\mathfrak{g}} \langle i \left|\right| \hat{H}_{\text{int}} \mid j\rangle \quad |i\rangle\langle j| \otimes \mathbb{1}_c$, so that:

$$\hat{H}_{\text{int}}^{(\mathfrak{eg})} = \hbar(\hat{a} + \hat{a}^\dagger)[g\hat{\sigma}_+ + g^*\hat{\sigma}_- + \text{Diag}(\alpha_\mathfrak{e}, \alpha_\mathfrak{g})]$$

with:

$$g = -\gamma_e \langle \mathfrak{e} \mid \boldsymbol{\delta B}(\boldsymbol{r}) \cdot \hat{\boldsymbol{S}} \mid \mathfrak{g}\rangle \tag{3.21}$$

and $\alpha_\mathfrak{e} = -\gamma_e \langle \mathfrak{e} \mid \boldsymbol{\delta B}(\boldsymbol{r}) \cdot \hat{\boldsymbol{S}} | \mathfrak{g}\rangle$ and similarly for $\alpha_\mathfrak{g}$. The above expression can be simplified further by the following procedure (see [62]). The eigenstates $|\mathfrak{e}\rangle$ and $|\mathfrak{g}\rangle$ are first redefined so as to have $g = g^*$. Then, if the time-dependent Hamiltonian $\hat{H}_{\text{int}}^{(\mathfrak{eg})}$ is treated as a perturbation of the static Hamiltonian $\hat{H}_0 = \hat{H}_c + \hat{H}_s$, its expression in the interaction picture is $\hat{\mathcal{H}}_{\text{int}} = \hat{U}_0 \hat{H}_{\text{int}}^{(\mathfrak{eg})} \hat{U}_0^\dagger$, where $\hat{U}_0 = \exp(i\hat{H}_0 t/\hbar)$ is the interaction evolution operator. By expanding $\hat{U}_0$ in series, $\hat{\mathcal{H}}_{\text{int}}$ develops in:

$$\begin{aligned}
\hat{\mathcal{H}}_{\text{int}}(t) &= g[\hat{\sigma}_+\hat{a}e^{i(\omega_s-\omega_0)t} + \hat{\sigma}_+\hat{a}^\dagger e^{i(\omega_s+\omega_0)t} && (3.22)\\
&\quad +\hat{\sigma}_-\hat{a}e^{-i(\omega_s+\omega_0)t} + \hat{\sigma}_-\hat{a}^\dagger e^{-i(\omega_s-\omega_0)t}] && (3.23)\\
&\quad +\text{Diag}(\alpha_\mathfrak{e}, \alpha_\mathfrak{g})[\hat{a}e^{i\omega_0 t} + \hat{a}^\dagger e^{-i\omega_0 t}] && (3.24)\\
\hat{\mathcal{H}}_{\text{int}}(t) &\underset{\text{RWA}}{=} g[\hat{\sigma}_+\hat{a}e^{i(\omega_s-\omega_0)t} + \hat{\sigma}_-\hat{a}^\dagger e^{-i(\omega_s-\omega_0)t}] && (3.25)
\end{aligned}$$

where we have applied the rotating wave approximation (RWA) to neglect terms in $\pm(\omega_s + \omega_0)$ because they rotate much faster than those having frequency $\pm(\omega_s - \omega_0)$. Reverting to the Schrödinger picture yields the well-known Jaynes-Cummings Hamiltonian [63]:

$$\hat{H}_{\text{int}}^{(\mathfrak{eg})} = \hbar g(\hat{\sigma}_+\hat{a} + \hat{\sigma}_-\hat{a}^\dagger) \tag{3.26}$$

The two remaining terms in the Hamiltonian describe respectively the absorption of a photon by the

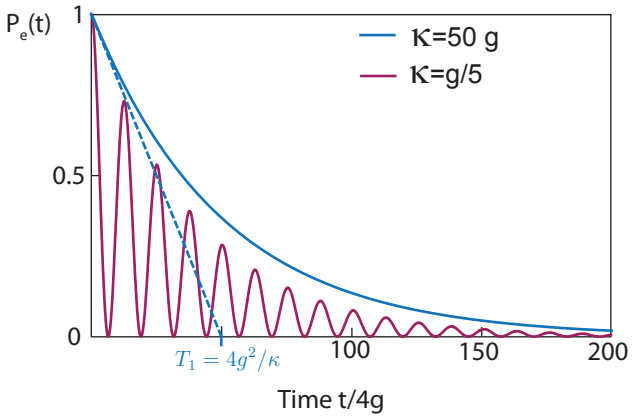

FIGURE 3.6: **Weak and strong regime for a single-spin**. The population of state $|\mathfrak{e},0\rangle$, obtained by solving Eqs. 3.30-3.33, presents oscillations when in the strong coupling regime ($g > \kappa$) and an exponential decay of characteristic rate $4g^2/\kappa$ in the weak coupling regime.

spin, and its emission; those are the basic processes on which the whole field of CQED is built. One prominent phenomenon predicted by the Jaynes-Cummings Hamiltonian is that a spin placed in the excited state can emit and re-absorb reversibly a single photon into an empty cavity at a frequency g; this phenomenon is known as vacuum Rabi oscillations [39].

If the system were perfectly isolated from any environment, these oscillations could last indefinitely. However several mechanisms limit the duration of these coherent exchanges: the resonator has a damping rate κ, giving the characteristic lifetime for an intra-resonator photon of $1/\kappa$ and the spin looses its coherence at a rate $\gamma = 1/T_2$, as described in 3.1. Thus one distinguishes two regimes:

- **Strong coupling regime** when $g \gg \kappa, \gamma$: the excitations in the system are long-lived compared to the Rabi period and one may observe Rabi oscillations [39], as shown in Fig. 3.6.
- **Weak coupling regime when** $g \ll \kappa, \gamma$: excitations decay faster than the coherent evolution between spin and the cavity, thus Rabi oscillations are suppressed.

For an electronic spin-1/2 with $\gamma_e/2\pi = 28$ GHz/T located $d = 10$ µm away from a wire-like inductance embedded in a resonator of frequency $\omega_0/2\pi = 7$ GHz and impedance $Z_0 = 50\ \Omega$, g can be estimated to:

$$g = \gamma_e |\langle \mathfrak{e} \mid \boldsymbol{\delta B}(\boldsymbol{r}) \cdot \hat{\boldsymbol{S}} | \mathfrak{g} \rangle| = \frac{\gamma_e}{2} |\boldsymbol{\delta B}_\perp(\boldsymbol{r})| \approx \frac{\gamma_e}{2} \frac{\mu_0 \delta i}{2\pi d} = \frac{\gamma_e}{2} \frac{\mu_0 \omega_0}{2\pi d} \sqrt{\frac{\hbar}{2Z_0}} \Rightarrow g/2\pi \approx 13\text{Hz} \tag{3.27}$$

This is much smaller than the damping rates of typical ESR resonant circuits, so that ESR experiments are in the weak coupling regime. In the following, we will see that even in the weak coupling regime, the quantum treatment of the spin-cavity interaction and of field relaxation via a transmission line (see 2.1.3) yields interesting new effects.

Dynamics of the spin-cavity system coupled to a bath

In an ESR experiment, the spin-cavity system is driven and probed via a transmission line coupled with rate κ_1 to the cavity mode. Assuming a coherent state drive sent on port 1, as shown in Fig. 3.5, the drive Hamiltonian is $\hat{H}_d/\hbar = i\sqrt{\kappa_1}(\beta \hat{a}^\dagger e^{-i\omega_d t} + \beta^* \hat{a} e^{i\omega_d t})$, where β is the amplitude of the drive and ω_d the drive frequency. The Hamiltonian of the system in the frame rotating at ω_d is:

$$\hat{H}/\hbar = \Delta_0 \hat{a}^\dagger \hat{a} + \frac{\Delta_s}{2} \hat{\sigma}_z + g(\hat{\sigma}_+ \hat{a} + \hat{\sigma}_- \hat{a}^\dagger) + i\sqrt{\kappa_1}(\beta \hat{a}^\dagger - \beta^* \hat{a}) \tag{3.28}$$

where $\Delta_0 = \omega_0 - \omega_d$ and $\Delta_s = \omega_s - \omega_d$. The state of the system $|\psi\rangle$ at time t is described by a matrix density $\rho(t)$. The system evolution can be described by a Lindblad equation written using ρ as:

$$\dot{\rho} = -\frac{i}{\hbar}[\hat{H}, \rho] + \sum_{\alpha} \mathcal{L}_{\alpha}[\rho] \tag{3.29}$$

where $\mathcal{L}_{\alpha}[\rho]$ are called superoperators and are defined as $\mathcal{L}_{\alpha}\rho\mathcal{L}_{\alpha}^{\dagger} - \frac{1}{2}\{\mathcal{L}_{\alpha}^{\dagger}\mathcal{L}_{\alpha}, \rho\}$. Each superoperator is used to describe an interaction with the environment. The cavity leakage due to coupling to the measurement lines or to internal losses is described by $\mathcal{L}_r = \sqrt{\kappa}\hat{a}$. Spin energy relaxation is described by $\mathcal{L}_1 = \sqrt{\Gamma_1}\hat{\sigma}_-$ and spin decoherence by $\mathcal{L}_2 = \sqrt{\gamma/2}\hat{\sigma}_z$ [64].

Eq. 3.29 fully characterizes the evolution of the system. It is valid both in the strong and weak coupling regimes. In the latter however, it can be simplified to retrieve the classical Bloch equations, supplemented by an additional effect of quantum origin : spin relaxation by the Purcell effect.

Purcell effect

To evidence cavity-enhanced spin relaxation by the Purcell effect, we now present a simple argument found in [39]. Consider the undriven spin-cavity system, with the spin prepared at time $t = 0$ in the excited state $|\mathfrak{e}\rangle$ and no photon in the cavity, and at zero temperature. The system evolution can be written using only the basis composed of $|\mathfrak{g}, 0\rangle$, $|\mathfrak{g}, 1\rangle$ and $|\mathfrak{e}, 0\rangle$ states. Using Eq. 3.29 with $\Delta = \Delta_0 - \Delta_s$ and $\Delta_s = 0$ (and neglecting non-radiative spin decoherence processes, i.e. taking $\Gamma_1 = \gamma = 0$) yields the following equations for the spin-cavity density matrix ρ:

$$\dot{\rho}_{\mathfrak{e}0,\mathfrak{e}0} = -ig(\rho_{\mathfrak{e}0,\mathfrak{g}1} - \rho_{\mathfrak{g}1,\mathfrak{e}0}) \tag{3.30}$$

$$\dot{\rho}_{\mathfrak{g}1,\mathfrak{g}1} = -\kappa\rho_{\mathfrak{g}1,\mathfrak{g}1} + ig(\rho_{\mathfrak{e}0,\mathfrak{g}1} - \rho_{\mathfrak{g}1,\mathfrak{e}0}) \tag{3.31}$$

$$\dot{\rho}_{\mathfrak{e}0,\mathfrak{g}1} = -\left(\frac{\kappa}{2} + i\Delta\right)\rho_{\mathfrak{e}0,\mathfrak{g}1} - ig(\rho_{\mathfrak{e}0,\mathfrak{e}0} - \rho_{\mathfrak{g}1,\mathfrak{g}1}) \tag{3.32}$$

$$\dot{\rho} = -\left(\frac{\kappa}{2} - i\Delta\right)\rho_{\mathfrak{g}1,\mathfrak{e}0} + ig(\rho_{\mathfrak{e}0,\mathfrak{e}0} - \rho_{\mathfrak{g}1,\mathfrak{g}1}) \tag{3.33}$$

In the weak-coupling regime $g \ll \kappa$, the probability $\rho_{\mathfrak{g}1,\mathfrak{g}1}$ of finding a photon in the cavity decays much faster than the rate at which the spin can transfer its excitation via Rabi oscillations. As a result the cavity is nearly always empty $\rho_{\mathfrak{g}1,\mathfrak{g}1} \approx 0$. In this regime, one can also assume that the coherence terms $\rho_{\mathfrak{e}0,\mathfrak{g}1}$ and $\rho_{\mathfrak{g}1,\mathfrak{e}0}$ follow adiabatically the variations of the excited state population [39] such that $\dot{\rho}_{\mathfrak{g}1,\mathfrak{e}0} \approx 0$ and $\dot{\rho}_{\mathfrak{e}0,\mathfrak{g}1} \approx 0$. According to these three assumptions, Eqs. 3.32 & 3.33 yield:

$$\rho_{\mathfrak{e}0,\mathfrak{g}1} = \frac{-ig}{\kappa/2 + i\Delta}\rho_{\mathfrak{e}0,\mathfrak{e}0} \tag{3.34}$$

$$\rho_{\mathfrak{g}1,\mathfrak{e}0} = \frac{ig}{\kappa/2 - i\Delta}\rho_{\mathfrak{e}0,\mathfrak{e}0} \tag{3.35}$$

We now replace $\rho_{\mathfrak{e}0,\mathfrak{g}1}$ and $\rho_{g1,e0}$ in Eq. 3.30, leading to:

$$\dot{\rho}_{\mathfrak{e}0,\mathfrak{e}0} = -g^2\left(\frac{1}{\kappa/2 + i\Delta} + \frac{1}{\kappa/2 - i\Delta}\right)\rho_{\mathfrak{e}0,\mathfrak{e}0} \tag{3.36}$$

We thus obtain that $\rho_{\mathfrak{e}0,\mathfrak{e}0}$ is exponentially damped, at the so-called Purcell rate given by:

$$\Gamma_p(\Delta) = \frac{\kappa g^2}{\kappa^2/4 + \Delta^2} \tag{3.37}$$

This is illustrated in Fig. 3.6 where we show a numerical integration of Eqs. 3.30-3.33 both in the strong and in the weak coupling regime. We stress that treating the resonator field quantum-mechanically is essential to derive this Purcell effect, which is a direct manifestation of the action of quantum fluctuations on the spin dynamics.

Resonator adiabatic elimination

A more rigorous treatment of the Purcell effect in a quantum optics theoretical framework, which also takes into account the presence of a drive, relies on adiabatic elimination of the resonator-field variables (see [64, 27, 65, 66] and references within). We summarize here the main results. First, one separates the field operator from its mean value by writing:

$$\hat{a} = \alpha + \hat{c}, \text{ with } \langle \hat{c} \rangle = 0 \tag{3.38}$$

In the absence of the spin, the steady-state value of α is given by the input-output relations (see Eq. 2.52): $\alpha = 2\sqrt{\kappa_1}\beta/(\kappa + 2i\Delta_0)$. In the limit $g \ll \kappa$, the adiabatic elimination of the resonator operators $\hat{c}$ and $\hat{c}^\dagger$ then yields the following master equation in the drive rotating frame [65] for the reduced spin density matrix $\tilde{\rho}$:

$$\dot{\tilde{\rho}} = -i[\hat{H}_{\text{eff}}, \tilde{\rho}] + \mathcal{L}_1[\tilde{\rho}] + \mathcal{L}_2[\tilde{\rho}] + \mathcal{L}_p[\tilde{\rho}], \tag{3.39}$$

with the effective Hamiltonian $\hat{H}_{\text{eff}}$ being [64]:

$$\hat{H}_{\text{eff}}/\hbar = \frac{\Delta_s - \xi}{2}\hat{\sigma}_z + g(\alpha\hat{\sigma}^+ + \alpha^*\hat{\sigma}^-) \tag{3.40}$$

where $\xi = \frac{\Delta g^2}{\Delta^2 + \kappa^2/4}$. The extra ξ term renormalizes slightly the spin frequency. As the correction is only of order g^2/κ, we neglect it in the following.

In addition to modifying $\hat{H}_{\text{eff}}$, the adiabatic elimination of the resonator operator is responsible for the appearance of a new spin superoperator $\mathcal{L}_p = \sqrt{\Gamma_p(\Delta)}\hat{\sigma}_-$ where Γ_p is the decay rate given in Eq. 3.37 [64]. This novel relaxation channel is precisely the cavity-enhanced spontaneous emission, i.e. the Purcell effect.

Within this approximation, the semi-classical equations of motion for the spin observables and the intra-cavity field in the drive rotating frame can be derived from Eqs. 3.38-3.39. For the sake of simplicity, we consider here that α is a real number; we write $\omega_1 = -2g\alpha$ so that:

$$\frac{d}{dt}\langle\hat{\sigma}_x\rangle = \Delta_s\langle\hat{\sigma}_y\rangle - \gamma_\perp\langle\hat{\sigma}_x\rangle \tag{3.41}$$

$$\frac{d}{dt}\langle\hat{\sigma}_y\rangle = -\Delta_s\langle\hat{\sigma}_x\rangle - \omega_1\langle\hat{\sigma}_z\rangle - \gamma_\perp\langle\hat{\sigma}_y\rangle \tag{3.42}$$

$$\frac{d}{dt}\langle\hat{\sigma}_z\rangle = \omega_1\langle\hat{\sigma}_y\rangle - [\Gamma_1 + \Gamma_p(\Delta)](\langle\hat{\sigma}_z\rangle + 1) \tag{3.43}$$

$$\langle\hat{a}\rangle = \alpha - \frac{i2g}{\kappa + 2i\Delta}\langle\hat{\sigma}_-\rangle \tag{3.44}$$

with $\gamma_\perp = \gamma + \frac{\Gamma_1}{2} + \frac{\Gamma_p}{2}$. Eqs. 3.41-3.43 are thus identical to the Bloch equations (see Eqs. 3.9-3.10) with only in addition a new T_1 relaxation channel given by the Purcell effect.

Note that in presence of a finite photon thermal population in the resonator n_{th} the Lindblad operator $\mathcal{L}_p$ is changed into the sum of $\mathcal{L}_{p+} = \sqrt{\Gamma_p n_{\text{th}}}\hat{\sigma}_+$ and $\mathcal{L}_{p-} = \sqrt{\Gamma_p(n_{\text{th}}+1)}\hat{\sigma}_-$, which describes spontaneous and stimulated emission as well as absorption. If no other relaxation process

is present ($\Gamma_1 = 0$), Eq. 3.43 is modified into [27]:

$$\frac{d}{dt}\langle\hat{\sigma}_z\rangle = \omega_1\langle\hat{\sigma}_y\rangle - (2n_{\rm th}+1)\Gamma_p(\Delta)\left[\langle\hat{\sigma}_z\rangle + \frac{1}{2n_{\rm th}+1}\right] \tag{3.45}$$

This implies that the relaxation is enhanced by a factor $(2n_{\rm th}+1)$ while the polarization is decreased by the same factor.

In addition to showing cavity-enhanced spin-relaxation, Eqs. 3.41-3.43 also provide a way to compute the signal emitted from the spin. We see that the intra-cavity field is changed by $2ig/(\kappa+2i\Delta)\langle\hat{\sigma}_-\rangle$ in the presence of the spin; the output signal leaking from the cavity is readily computed thanks to input-output theory as $\langle\hat{a}_{\rm out}\rangle = \sqrt{\kappa}\langle\hat{a}\rangle$ (see Eq.2.50). We thus come to the conclusion that the spin emits a microwave signal in the detection waveguide that is roughly given by $\langle\hat{a}_{\rm out}\rangle = 2g\langle\hat{\sigma}_-\rangle/\sqrt{\kappa}$ at resonance ($\Delta = 0$). This equation is the quantum-optics analog of the classical inductive detection described in 3.1.3. The output signal is proportional to the spin transverse magnetization, to the spin-photon coupling constant, and to $1/\sqrt{\kappa}$.

3.2.2 Collective effects

We have seen up to now that a spin weakly coupled to a resonator is well described by the classical Bloch equations, with an extra relaxation channel given by the Purcell spontaneous emission rate. In the following we discuss the validity of this description for an ensemble of spins.

N identical spins model

We consider first the ideal case of N identical spins-1/2 with frequency ω_s coupled with same coupling constant g to the resonator. The system Hamiltonian is the sum of the Jaynes-Cummings Hamiltonians associated with each spin, and is known as the Tavis-Cummings Hamiltonian [67]:

$$H_{\rm TC}/\hbar = \omega_0(a^\dagger a) + \frac{\omega_s}{2}\sum_{j=1}^{N}\hat{\sigma}_z^{(j)} + g\sum_{j=1}^{N}(\hat{\sigma}_+^{(j)}\hat{a} + \hat{\sigma}_-^{(j)}\hat{a}^\dagger) \tag{3.46}$$

where (j) refers to the operators of spin j. This Hamiltonian acts on $E_s \otimes E_c$, where E_s is the 2^N-dimensional Hilbert state spanned by the states $\{|\varepsilon_1,\ldots,\varepsilon_n\rangle, \varepsilon_i = \{\mathfrak{g}_i,\ \mathfrak{e}_i\}\}$ and E_c is the resonator Hilbert space. Introducing the collective spin operators $\hat{\mathcal{S}}_k = \sum_{j=1}^{N}\hat{\sigma}_k^{(j)}$, the Hamiltonian can be rewritten as:

$$H_{\rm TC}/\hbar = \omega_0(a^\dagger a) + \frac{\omega_s}{2}\hat{\mathcal{S}}_z + g(\hat{\mathcal{S}}_+\hat{a} + \hat{\mathcal{S}}_-\hat{a}^\dagger) \tag{3.47}$$

A remarkable property of this Hamiltonian is that the total spin angular momentum $\hat{\boldsymbol{\mathcal{S}}}^2 = \hat{\mathcal{S}}_x^2 + \hat{\mathcal{S}}_y^2 + \hat{\mathcal{S}}_z^2$ is conserved in time since $[H_{\rm TC}, \hat{\boldsymbol{\mathcal{S}}}^2] = 0$. It is therefore interesting to introduce the basis $|\mathcal{S}, m\rangle$ of joint eigenstates of $\hat{\boldsymbol{\mathcal{S}}}^2$ and $\hat{\mathcal{S}}_z$, defined as:

$$\hat{\boldsymbol{\mathcal{S}}}^2|\mathcal{S},m\rangle = \mathcal{S}(\mathcal{S}+1)|\mathcal{S},m\rangle \tag{3.48}$$

$$\hat{S}_z|\mathcal{S},m\rangle = m|\mathcal{S},m\rangle. \tag{3.49}$$

$\mathcal{S}$ can take any positive values among $\{N/2, N/2-1, ...\}$; and m can take any values among $\{-S, -S+1, ..., S-1, S\}$. Since $\mathcal{S}$ is conserved in time, the system dynamics is restricted to states having the same $\mathcal{S}$ as the initial state. Within one $\mathcal{S}$ subspace, $m+\mathcal{S}$ describes the number of excitations that can be exchanged with the resonator. For instance, emission of a photon takes the system from $|\mathcal{S},m\rangle\otimes|0\rangle$ to $|\mathcal{S},m-1\rangle\otimes|1\rangle$. Photon absorption or emission is thus impossible for all states for which $\mathcal{S} = 0$, meaning that they are strictly dark states. For other states, the

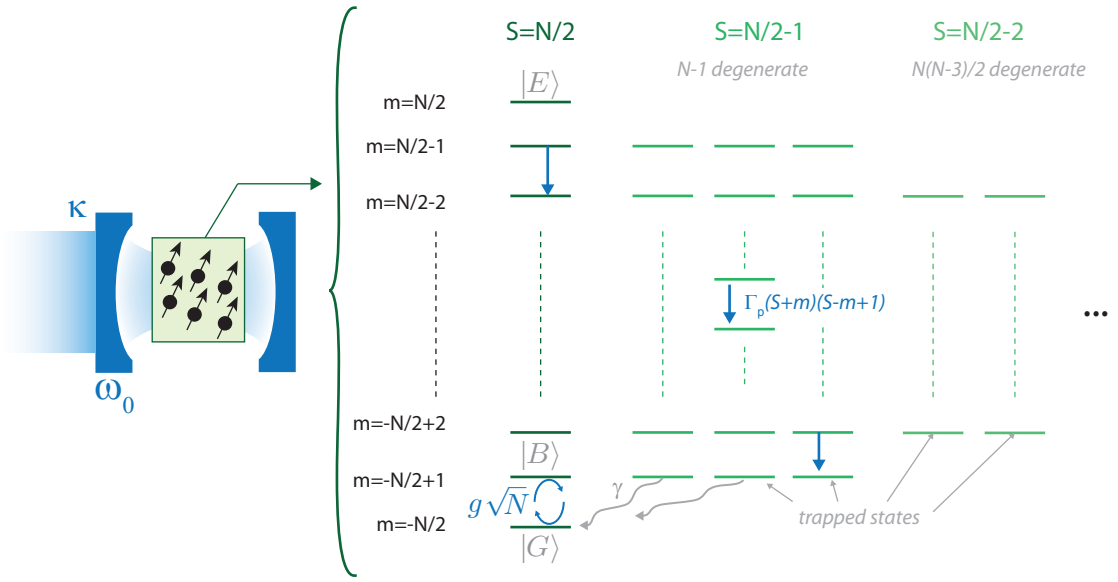

FIGURE 3.7: N **identical spins.** For a system of N identical spins, the system dynamics are confined to fixed $\mathcal{S}$ manifolds, creating state-dependent coupling to the resonator and inducing non-exponential relaxation most often towards trapped states.

coupling is dependent of $(\mathcal{S}, m)$ and is maximal for states within the $\mathcal{S} = \frac{N}{2}$ manifold. In particular this manifold comprises the ground state $|G\rangle = |\mathfrak{g}_1, \ldots, \mathfrak{g}_n\rangle$ and the one-excitation state $|B\rangle = \frac{1}{\sqrt{N}} \sum_j |\mathfrak{g}_1, \ldots, \mathfrak{e}_j, \ldots, \mathfrak{g}_n\rangle$. One can observe that:

$$\langle B, 0 \left| \hat{H}_{\mathrm{TC}} \right| G, 1\rangle = \hbar g \sqrt{N} \tag{3.50}$$

thus $|B\rangle$ and $|G\rangle$ can exchange one excitation with the resonator at an enhanced rate $g\sqrt{N}$. This collective enhancement of the vacuum Rabi oscillations has been observed first for atoms [68], and more recently with superconducting qubits [69] and spins [70]. By considering $|B\rangle$ and $|G\rangle$ as a two-level-system, it led to the implementation of quantum memories with ensemble of spins [71]. The state of another qubit, such as a superconducting qubit, can be transferred to the ensemble so as to be stored and thus benefit from the spin ensemble longer coherence time.

Another direct consequence of this model is the deep modification of the radiative properties of an ensemble of identical spins compared to the single spin spontaneous emission case ([72], see Fig. 3.7). Not only can $|\mathcal{S}, m\rangle$ only relax towards $|\mathcal{S}, m-1\rangle$ but the emission takes place at a rate $\Gamma_p(\mathcal{S}+m)(\mathcal{S}-m+1)$ which depends very strongly on $\mathcal{S}$ and m. For instance, if the spin ensemble initially starts from the fully excited state $|E\rangle = |\mathfrak{e}_1, \ldots, \mathfrak{e}_n\rangle$ which corresponds to $|\frac{N}{2}, \frac{N}{2}\rangle$, it will desexcite itself within the $\mathcal{S} = \frac{N}{2}$ manifold. As the transition probabilities are not constant (i.e. for higher m the transition probabilities start as $\propto m$ but reach a maximum $\propto \mathcal{S}^2$ when m goes through zero before decreasing again), the relaxation towards state $|G\rangle$ is not a simple exponential of rate Γ_p, but a much faster super-radiant pulse whose shape and properties have been studied in detail [72, 73], and which corresponds to the operation of a maser in pulsed mode [74].

For other initial states comprised in manifolds $\mathcal{S} \neq \frac{N}{2}$, the excitation is also non-exponential and strongly dependent on $\mathcal{S}$: the $|E\rangle$ state has a super-radiant relaxation, much faster than Γ_p, whereas states $\mathcal{S} = 0$ do not relax radiatively at all. More importantly, the ground state $|G\rangle$ cannot be reached any longer for any initial state within manifolds $\mathcal{S} \neq \frac{N}{2}$. They can only relax down to the lowest-energy states of their $\mathcal{S}$ manifold, which have the form $|\mathcal{S}, -\mathcal{S}\rangle$, and which in general still

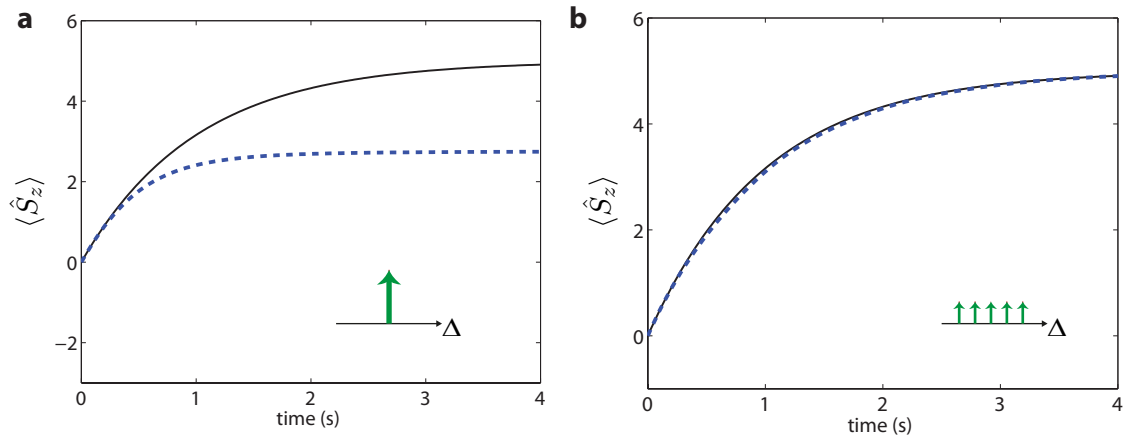

FIGURE 3.8: **Spin relaxation** simulated for 5 spins starting from a disordered state. Black: ideal exponential Purcell relaxation ($\Gamma_p = 1\ \mathrm{s}^{-1}$), blue $\langle \hat{S}_z \rangle$. **a** Without inhomogeneous broadening, the relaxation goes to a trap state **b** whereas for sufficiently large inhomogeneous broadening (spins spaced by 1 Hz), a fully exponential decay is observed. Adapted from [27].

contain many spins in their excited state. One can say that the system becomes trapped in these highly correlated states, instead of relaxing to its true ground state $|G\rangle$.

Summing up, we see that the radiative relaxation of an ensemble of identical spins seems to be completely different from the single-spin case, where an exponential relaxation of rate Γ_p is predicted. Since relaxation now depends on the initial state of the ensemble, and is in general not exponential, a description by the Bloch equations with a single relaxation time T_1 seems clearly impossible.

Collective or individual relaxation ?

The conclusions reached above on the radiative properties of an ensemble of identical spins heavily rely on symmetry properties of the system Hamiltonian. It should thus not come as a surprise that these conclusions are strongly altered when one takes into account two phenomena : spin decoherence, and inhomogeneous broadening of the spin linewidth, both of them characterized by a finite ensemble spin linewidth γ.

The rigorous treatment of the effects of inhomogeneous broadening and decoherence on the radiative properties of a spin ensemble is a difficult theoretical problem, which has been addressed in a few articles [75, 27, 76]. The outcome of all these works is that in the limit of strong decoherence or inhomogeneous broadening, collective radiative effects are suppressed, and one recovers the situation of a collection of spins radiating independently at a rate Γ_p. As a result, the spin ensemble can now truly relax to its ensemble ground state (at rate Γ_p), and trapping in correlated states does not occur any longer. To discriminate between the "independent" or "collective" radiative regime, one has to consider a dimensionless parameter called the ensemble cooperativity defined as:

$$C = \frac{2Ng^2}{\kappa\gamma} \tag{3.51}$$

Collective effects are found in the so-called strong collective coupling regime $C \gg 1$; independent radiation from each spin at rate Γ_p is obtained in the so-called weak collective coupling regime $C \ll 1$. In the remaining of this thesis, we will be in the latter regime.

A clear manifestation of these two situations is seen in Fig. 3.8, which is extracted from [27]. A collection of 5 spins $1/2$ is considered, starting at $t = 0$ from a fully unpolarized state. When all spins have the same frequency, the spins relax towards a partially polarized state for which $\langle \hat{\mathcal{S}}_z \rangle \approx 2.8$, much less than the true ground state for which $\langle \hat{\mathcal{S}}_z \rangle = 5$. When some frequency inhomogeneity is taken into account, the ensemble relaxes towards the true ground state, at a rate exactly given by the single-spin Purcell rate, Γ_p.

Dynamics of the system

In the following, we will often need to simulate the dynamics of an ensemble of N spins when coupled to the cavity. To treat numerically this problem, our collaborator Brian Julsgaard from Aarhus University has written a code [77, 78] that we will use, based on the equations that are presented in the following. Consider a spin ensemble with an inhomogeneous linewidth and non-identical coupling strengths. The spin ensemble is divided into $\mathcal{M}$ sub-ensembles regarded each as homogeneous with coupling strength g_m, spin resonance frequency $\omega_d + \Delta_m$ and containing N_m spins for $m = 1, \ldots, M$ [77]. For each sub-ensemble, collective spin observables $\hat{\mathcal{S}}_k^{(m)}$ can be introduced. The Hamiltonian of Eq. 3.46 expressed in the rotating frame in presence of a drive is transformed into:

$$H_{\mathrm{TC}}/\hbar = \Delta_0(a^\dagger a) + \sum_{m=1}^{M} \frac{\Delta_m}{2} \hat{\mathcal{S}}_k^{(j)} + \sum_{m=1}^{M} g_m(\hat{\mathcal{S}}_+^{(m)} \hat{a} + \hat{\mathcal{S}}_-^{(m)} \hat{a}^\dagger) + i\sqrt{\kappa_1}(\beta \hat{a}^\dagger - \beta^* \hat{a}) \tag{3.52}$$

Rewriting the master equation of Eq. 3.29 for these collective variables and assuming identical T_1 and T_2 processes for each sub-ensemble allows to derive the following equations for the mean-value of each operator:

$$\frac{d}{dt}\langle \hat{a} \rangle = \sqrt{\kappa_1}\beta - i\Delta_0 \langle \hat{a} \rangle - \frac{\kappa}{2}\langle \hat{a} \rangle - i \sum_{j=1}^{M} g_m \langle \hat{\mathcal{S}}_-^{(m)} \rangle \tag{3.53}$$

$$\frac{d}{dt}\langle \hat{a}^\dagger \rangle = \sqrt{\kappa_1}\beta^* + i\Delta_0 \langle \hat{a}^\dagger \rangle - \frac{\kappa}{2}\langle \hat{a}^\dagger \rangle + i \sum_{j=1}^{M} g_m \langle \hat{\mathcal{S}}_+^{(m)} \rangle \tag{3.54}$$

$$\frac{d}{dt}\langle \hat{\mathcal{S}}_x^{(m)} \rangle = -\Delta_s \langle \hat{\mathcal{S}}_y^{(m)} \rangle - \sqrt{2} g_m \langle \hat{\mathcal{S}}_z^{(m)} \rangle \langle \hat{Y} \rangle - \gamma_\perp \langle \hat{\mathcal{S}}_x^{(m)} \rangle \tag{3.55}$$

$$\frac{d}{dt}\langle \hat{\mathcal{S}}_y^{(m)} \rangle = \Delta_s \langle \hat{\mathcal{S}}_x^{(m)} \rangle - \sqrt{2} g_m \langle \hat{\mathcal{S}}_z^{(m)} \rangle \langle \hat{X} \rangle - \gamma_\perp \langle \hat{\mathcal{S}}_y^{(m)} \rangle \tag{3.56}$$

$$\frac{d}{dt}\langle \hat{\mathcal{S}}_z^{(m)} \rangle = \sqrt{2} g_m \langle \hat{Y} \rangle \langle \hat{\mathcal{S}}_x^{(m)} \rangle + \sqrt{2} g_m \langle \hat{X} \rangle \langle \hat{\mathcal{S}}_y^{(m)} \rangle - \Gamma_1 (\langle \hat{\mathcal{S}}_z^{(m)} \rangle - N_m) \tag{3.57}$$

where $\hat{X}$ and $\hat{Y}$ are the intra-resonator quadrature operators. This set of equations can be used to compute numerically the evolution of the mean values for each sub-ensemble. To solve the complete behavior of the system, spin ensemble and resonator, one needs to solve $3\mathcal{M} + 2$ differential equations, three for each sub-ensemble and two for the resonator. Provided that $\mathcal{M}$ is not too large, this can be done numerically. We use this approach in ch. 7 to simulate a complete spin-echo sequence in our experiment.

Chapter 4

Bismuth donors in silicon

In this third and last background part, we describe the spin system that we use throughout this thesis: bismuth donors in silicon (Si:Bi). Group V donors in silicon were studied as early as 1954, with pioneering works from Honig and Feher [79, 80] focusing extensively on phosphorus and arsenic. The very long values reported for T_1 (> 1000 s [81]) and $T_2 = 0.2$ ms for Si:P lead already in these early days to the idea of using the spin to store classical information [82]. Later on, Kane extended this suggestion to building a quantum computer based on Si:P [83], triggering a renewed intense interest in these systems, seen as "spins living in a semiconducting vacuum".

Indeed, in the quest for ideal qubit candidates, the thoroughly-studied silicon appears, along with carbon, as a promising host material since its main isotope ^{28}Si has zero nuclear spin so that an enriched ^{28}Si sample would provide a magnetically-silent environment for donor spins. The electronic spin $1/2$ of a donor in silicon is seen as a particularly promising qubit candidate due to its long-lived coherence and fast manipulation time. Bismuth ^{209}Bi is the heaviest group V donor in silicon (see Table 4.1); other donors include ^{31}P, ^{33}As, ^{121,123}Sb. In early studies, bismuth gathered less attention than phosphorus due to the latter simplicity and use in modern CMOS devices. However, bismuth received renewed attention recently due to the existence of optimal working points, where the Si:Bi frequency becomes insensitive to magnetic field fluctuations [84] leading to the longest measured coherence times for electronic spins in the solid state [25]. In addition, its large zero-field splitting makes it attractive for coupling to superconducting resonators which could be useful for building a quantum memory for superconducting qubit states [85].

Donor		^{31}P	^{33}As	^{121}Sb	^{121}Sb	^{209}Bi
E_D	(meV)	45.6	53.8	42.8	42.8	71.0
a_0	(nm)	16.8	15.5	17.3	17.3	11.5
ΔE	(meV)	13.0	22.5	12.3	12.3	41
I		1/2	3/2	5/2	7/2	9/2
A	(MHz)	118	198	186	101	1475.4

TABLE 4.1: **Group V donors characteristics:** ionization energy (E_D), apparent Bohr radius (a_0), nuclear spin and hyperfine coupling constant (A). Extracted from [16, 86, 87, 88].

This chapter will present the essential information to understand the experimental work presented in this thesis. When available we indicate references the reader may consult for more detailed derivations and explanations. In what follows, we briefly present the electronic structure of Si:Bi (see [89]) before describing its spin Hamiltonian, energy levels and ESR transitions (see the work of Mohammady et al. [84]). We list the known relaxation mechanisms (see [81, 90]) as well as the expected sources of decoherence (see [91]). Last we present the characteristics of the sample used in our experiments.

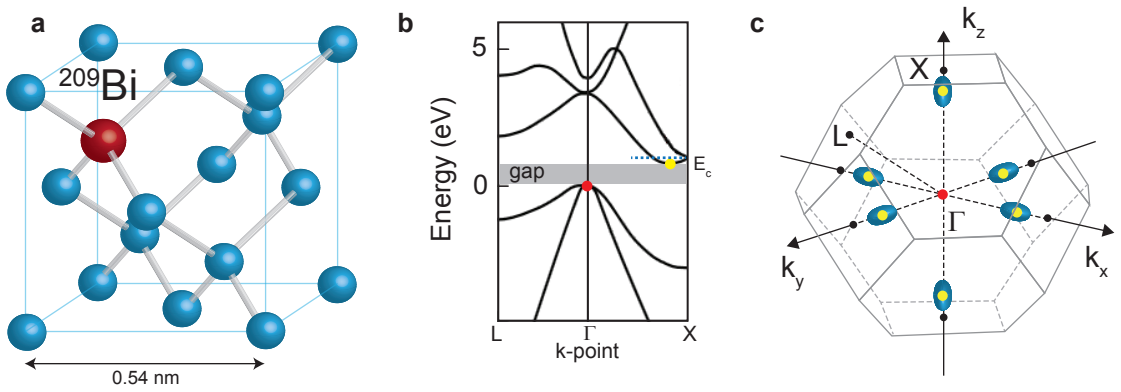

FIGURE 4.1: **An atom in silicon. a** Silicon diamond lattice with a single substitutional bismuth impurity. **b** Band diagram of silicon. **c** First Brillouin Zone, with the six-valley of the conduction band highlighted in yellow. Blue ellipsoids symbolize iso-energy surfaces. The Γ-point, center of the valence band is indicated in red.

4.1 A substitutional donor in silicon

Silicon is a group IV semi-conductor which crystallizes in a diamond structure (see Fig. 4.1a). Each Si atom forms a covalent bond with the four neighboring atoms in a tetrahedron geometry. The associated Brillouin zone is shown in Fig. 4.1c. The calculation of the band structure of silicon reveals it has an indirect band-gap $E_g = 1.1\text{eV}$ at $T = 300$ K (see Fig. 4.1b). The conduction band is six-fold degenerate with each minimum offset from the maximum of the valence band occurring at the center of the first Brillouin Zone (Γ point) by $\pm 0.85\ 2\pi/a$ along the vectors $\pm\boldsymbol{k}_x$, $\pm\boldsymbol{k}_y$, $\pm\boldsymbol{k}_z$, a being the lattice parameter (0.543 nm for silicon) as shown in Fig. 4.1c. Each minimum is referred to as a silicon valley.

Bismuth donors are substitutional impurities in silicon. A Bi atom replaces a Si atom and four of its valence electrons form covalent bonds with the electrons of the neighboring Si atoms (see Fig. 4.1a). The fifth electron can be either ionized into the conduction band (state D^+) or bound to the Bi nucleus forming a "neutral donor" (state D^0). The energy required to ionize the donor to the conduction band is $E_D = -71$ meV [88].

4.1.1 Electronic states

As $E_D \ll E_g$, Si:Bi are shallow impurities. In this case, the donor wavefunction can be expressed using combinations of the crystal Bloch wave functions using the framework of effective mass theory (EMT) (developed by Kohn and Luttinger [92], see also [93]). The attractive potential V(r) of the Bi nucleus is modeled as a Coulomb potential with $V(r) = -e^2/(\varepsilon_{\text{Si}} r)$, where ε_{Si} is the silicon dielectric constant. As it extends over many lattice sites, the donor electronic wavefunction is only weakly confined (see Fig. 4.2a). EMT predicts a six-fold degenerate 1s ground state with equivalent wavefunctions expressed as a product of the conduction-band Bloch functions $\phi_{\boldsymbol{k}_\mu}(r)$ and an hydrogen-like envelope function $F_\mu(\boldsymbol{r})$ at the μ-th conduction-band valley [94]:

$$\Psi(\boldsymbol{r}) = \sum_\mu \alpha_\mu F_\mu(\boldsymbol{r}) \phi_{\boldsymbol{k}_\mu}(\boldsymbol{r}) \tag{4.1}$$

The spatial extension of the hydrogenic envelope $F_\mu(\boldsymbol{r})$ is given by a parameter a_0 called the Bohr radius, shown in Table 4.1. The coefficients $|\alpha_\mu|^2$ give the probability of finding the donor electron

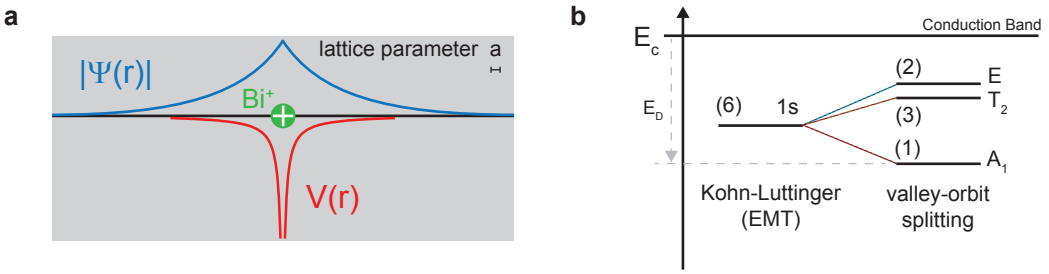

FIGURE 4.2: **Bismuth electronic states. a** Illustrative schematic of the donor wave function and of the Coulomb potential compared to the lattice parameter. **b** Six-fold degenerate ground states predicted by effective mass theory and with an additional valley-orbit interaction perturbation.

in the μ-th valley and are called valley population. In this simplistic picture, EMT produces identical results for all of the donors, with calculations indicating identical Bohr radii and $E_D = -31.3$ meV.

This is in direct contradiction with the experimental results where instead of a single degenerate state three distinct energy-levels are observed [87]. The discrepancy is explained by a break down of the EMT approach in the vicinity of the donor nucleus. To correct this effect and take into account the tetrahedral environment surrounding the donor in the central cell as well as the core and valence electrons screening the Bi nucleus attractive potential, a phenomenological interaction called "valley-orbit" is added as a perturbation of EMT [94]. With this improved model, the degeneracy of the ground state is lifted, yielding three distinct 1s states labeled by their tetrahedral symmetry group designation : a symmetrical ground-state A_1, a three-fold degenerate level T_2 and a two-fold degenerate level E. The corresponding eigenstates may be written in the same manner as in Eq 4.1 with envelope hydrogenic functions (see Fig. 4.1.1a). Written in the valley basis $\{\pm\boldsymbol{k}_x, \pm\boldsymbol{k}_y, \pm\boldsymbol{k}_z\}$, the states are:

$$A_1 = \tfrac{1}{\sqrt{6}}\{1,1,1,1,1,1\} \qquad T_{2z} = \frac{1}{\sqrt{2}}\{0,0,0,0,1,-1\} \tag{4.2}$$

$$T_{2x} = \tfrac{1}{\sqrt{2}}\{1,-1,0,0,0,0\} \qquad E_{\mathrm{xy}} = \frac{1}{2}\{1,1,-1,-1,0,0\} \tag{4.3}$$

$$T_{2y} = \tfrac{1}{\sqrt{2}}\{0,0,1,-1,0,0\} \qquad E_z = \frac{1}{\sqrt{12}}\{-1,-1,-1,-1,2,2\} \tag{4.4}$$

This treatment yields different ionization energies and Bohr radii for the five silicon donors, in agreement with measurements (see Table 4.1). Bismuth is the deepest donor, and its wavefunctions are correspondingly more confined with a smaller Bohr radius. In the remaining part of this chapter, we are mainly interested in the spin properties of the neutral Bismuth donor in its ground state A_1, but the properties of higher-energy states do play a role in the donors physics, as will be clear later.

Charge state

The charge state of the bismuth donors in silicon is found by calculating the position of the Fermi-level as a function of temperature, see Neamen [95]. At zero temperature, for a n-type semiconductor, all donors retain their electrons and thus the Fermi level energy will be situated mid-way through the donor energy level A_1 (see below) and the conduction band : $E_F = \frac{1}{2}(E_C - E_{A_1})$. At slightly higher temperature, the donors electrons start being excited to the conduction band and the fraction of ionized donors is given by:

$$\frac{N_D^+}{N_D} = \frac{1}{1 + 2e^{(E_F - E_{A_1})/k_B T}} \tag{4.5}$$

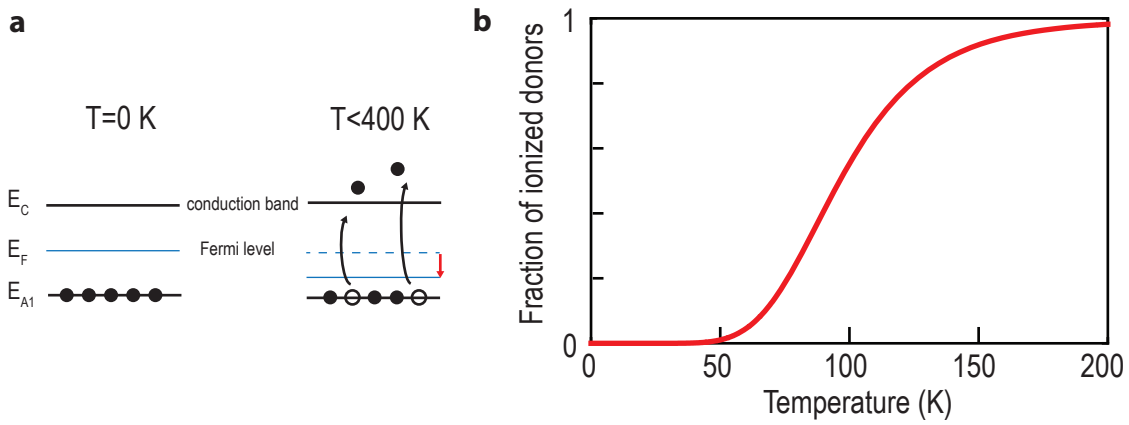

FIGURE 4.3: **Charge state of a bismuth donor. a** At non-zero temperature, electrons bound to donors are excited to the conduction band, resulting in a partial ionization of the donors and a lowering of the Fermi energy level. **b** Fraction of ionized donors N_D^+/N_D as a function of temperature in the case of bismuth, evaluated with $E_D = 71$ meV and $N_D = 10^{16}\text{cm}^{-3}$.

where N_D is the total concentration of donors and N_D^+ is the concentration of ionized donors. Since the silicon gap is much larger than the ionization energy of the shallow donors, for low enough temperatures ($T < 400$ K) the valence electrons can not be excited to the conduction band and thus the concentration of free carriers in the conduction band n is only given by the concentration of ionized donors: $n = N_D^+$. The concentration of free carriers is also linked in case of non-degenerate semi-conductors to the temperature by:

$$n = N_c e^{(E_F - E_C)/k_B T}, \tag{4.6}$$

where $N_c = 2(2\pi m^* k_B T/h^2)^{3/2}$ is the effective density of states in the conduction band with m^* being the effective mass of an electron. Thanks to these two relations, Eq 4.5 may be rewritten to determine n as a function of the temperature T, the donor ionization energy E_D and the concentration of donors:

$$n = \frac{N_D}{1 + 2n/N_\xi} \tag{4.7}$$

where $N_\xi = N_c e^{-E_D/k_B T}$.

As the electrons are moving from the donor level to the conduction band as a function of temperature, the Fermi energy tends to move downwards. Precise determination of the Fermi energy as a function of n is given by Eq 4.6. One can then access the fraction of ionized donors by evaluating Eq 4.5. With an ionization energy $E_D = 71$ meV and for a concentration $N_D = 10^{16}\text{cm}^{-3}$, bismuth donors are in their neutral state up to $T = 40$ K, see Fig. 4.3b. In our experiments which take place at millikelvins temperatures, all donors should be in their neutral state. However, note that other factors may impact the charge states of donors, such as internal electric fields [96, 97] or bending of the energy levels in presence of Schottky barriers; we will come back to this issue later in ch. 7.

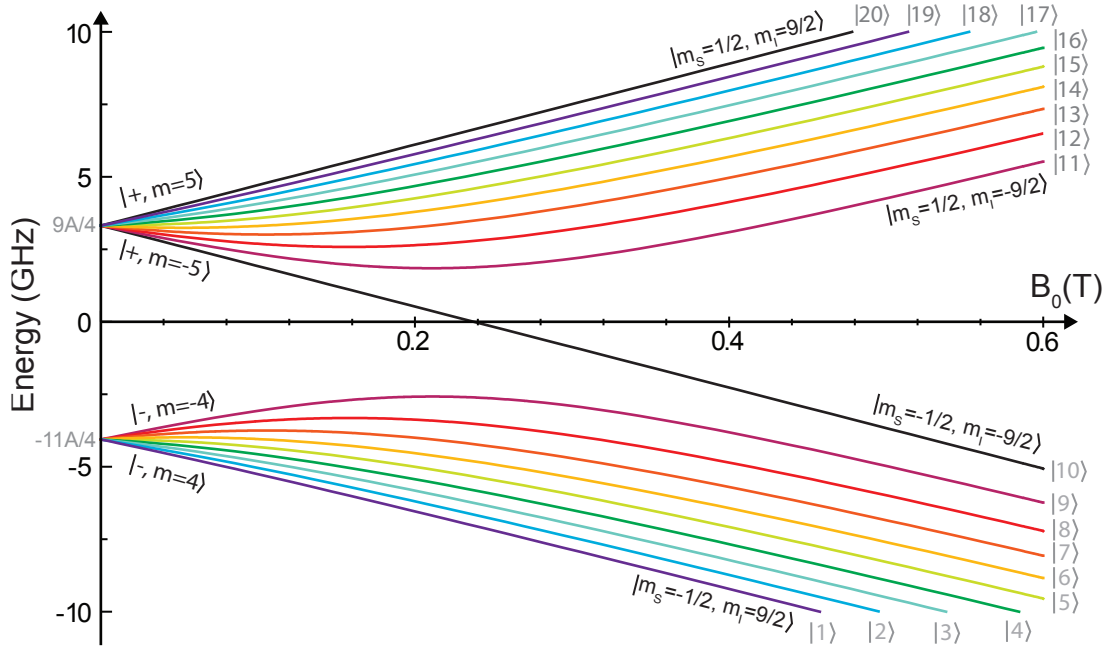

FIGURE 4.4: **Bismuth energy spectrum**. Energy-levels computed from the diagonalisation of the Si:Bi Hamiltonian as a function of B_0 (Eq 4.8). The coupled energy-levels $E_m^{\pm}$ are color-coded from purple to red, the uncoupled energy-levels are in black. Figure adapted from [99, 84].

4.2 Spin levels and ESR-allowed transitions.

A neutral bismuth donor in silicon has spin properties arising from the coupling of the $S = 1/2$ electronic spin to the ^{209}Bi $I = 9/2$ nuclear spin. When placed in an external magnetic field $\boldsymbol{B}$, its twenty energy levels are described by the following spin Hamiltonian that includes a Zeeman effect for electronic and nuclear spin and an isotropic hyperfine coupling [98]:

$$\hat{H}/\hbar = \boldsymbol{B} \cdot \left(\gamma_e \hat{\boldsymbol{S}} \otimes \mathbb{1} - \gamma_n \mathbb{1} \otimes \hat{\boldsymbol{S}}\right) + A\hat{\boldsymbol{S}} \cdot \hat{\boldsymbol{I}} \tag{4.8}$$

where $\gamma_e/2\pi = 27.997$ GHz/T and $\gamma_n/2\pi = 6.962$ MHz/T are the electronic and nuclear gyromagnetic ratio and $A/2\pi = 1.4754$ GHz is the hyperfine coupling constant [26]. To understand this system, we will follow the analysis made by Mohammady at al. in [84]. Assuming a static magnetic field directed along z, $\boldsymbol{B}_0 = B_0 \boldsymbol{e}_z$, the Hamiltonian may be re-written as:

$$\hat{H}_0/\hbar = A\hat{S}_z\hat{I}_z + \frac{A}{2}(\hat{S}_+\hat{I}_- + \hat{S}_-\hat{I}_+) + \omega_0(\hat{S}_z - \delta\hat{I}_z) \tag{4.9}$$

where $\omega_0 = B_0\gamma_e$ and $\delta = \gamma_n/\gamma_e \approx 10^{-3}$. Due to the hyperfine coupling, the Hamiltonian is not diagonal in the Zeeman basis spanned by $\{|m_s, m_i\rangle\}$ with $m_s = \pm\frac{1}{2}$ and $m_i = \frac{-9}{2} \ldots \frac{9}{2}$ and its energy states are instead hybridized electro-nuclear states. The energy spectrum as a function of magnetic field obtained from the Hamiltonian diagonalization is shown in Fig. 4.4.

Hybridized eigenstates

To understand the spectrum in Fig. 4.4 and the spin properties of the eigenstates, one can notice first that the projection $m = m_i + m_s$ of the total angular momentum operator $\hat{\boldsymbol{F}} = \hat{\boldsymbol{I}} + \hat{\boldsymbol{S}}$ onto $\boldsymbol{e}_z$ is a good quantum number since $[\hat{H}, \hat{S}_z + \hat{I}_z] = 0$. If we then consider the application of the Hamiltonian on a state of the Zeeman basis:

$$\hat{H}_0/\hbar|\pm\frac{1}{2}, m_i\rangle = \left(\pm\frac{A}{2}m_i \pm \frac{\omega_0}{2} + \omega_0\delta m_i\right)|\pm\frac{1}{2}, m_i\rangle + \frac{A}{2}\hat{I}_\pm|\mp\frac{1}{2}, m_i\rangle \tag{4.10}$$

it appears that $|\frac{1}{2}, \frac{9}{2}\rangle$ and $|-\frac{1}{2}, -\frac{9}{2}\rangle$ are unmixed eigenstates of the Hamiltonian since $\hat{I}_\pm|\mp\frac{1}{2}, \pm\frac{9}{2}\rangle = 0$. Their energies are:

$$E_{|\pm\frac{1}{2},\pm\frac{9}{2}\rangle} = \frac{9}{4}A \pm \frac{\omega_0}{2}(1 + 9\delta) \tag{4.11}$$

These states are the only ones in the spectrum (see Fig. 4.4) to have a linear energy dependence on B_0. When $|m| < 5$, $|\pm\frac{1}{2}, m_i\rangle$ hybridizes with $|\mp\frac{1}{2}, m_i \pm 1\rangle$. From these observations, the Hamiltonian expressed in the Zeeman basis can be decomposed into two one-dimensional Hamiltonians acting on bases

$$\{|\frac{1}{2}, \frac{9}{2}\rangle\} \text{and} \{|-\frac{1}{2}, -\frac{9}{2}\rangle\} \tag{4.12}$$

and nine two-dimensional Hamiltonians acting on subspaces labeled by m:

$$\{|\pm\frac{1}{2}, m_i\rangle, |\mp\frac{1}{2}, m_i \pm 1\rangle\} = \{|\pm\frac{1}{2}, m \mp \frac{1}{2}\rangle, |m| \leqslant 4\} \tag{4.13}$$

As explained in [84], the restriction of $\hat{H}_0$ to one of these two-dimensional bases is:

$$\hat{H}_m/\hbar = \frac{A}{2}R_m[\cos\theta_m\hat{\sigma}_z + \sin\theta_m\hat{\sigma}_x] - \frac{A}{2}\varepsilon\mathbb{1} \tag{4.14}$$

where:

$$R_m^2 = \left[m + \frac{\omega_0}{A}(1+\delta)\right]^2 + (25 - m^2) \tag{4.15}$$

$$\tan\theta_m = \frac{(25-m^2)^{1/2}}{m + \frac{\omega_0}{A}(1+\delta)} \tag{4.16}$$

$$\varepsilon = \frac{1}{2} + 2\omega_0\delta m \tag{4.17}$$

Since $\cos\theta_m\hat{\sigma}_z + \sin\theta_m\hat{\sigma}_x = \sigma_{0\theta_m}$, where $\sigma_{0\theta_m}$ is the Pauli spin matrix in the rotated basis, the eigen-energies are given by:

$$E_m^\pm = \frac{A}{2}(-\varepsilon \pm R_m) \tag{4.18}$$

This expression is exact for all magnetic fields and for all m and yields the energy spectrum of Fig. 4.4. The corresponding energy eigenstates are:

$$|\pm, m\rangle = a_m^\pm|\pm\frac{1}{2}, m \mp \frac{1}{2}\rangle + b_m^\pm|\mp\frac{1}{2}, m \pm \frac{1}{2}\rangle \tag{4.19}$$

where

$$a_m^\pm = \frac{1}{\sqrt{2}}(1+\cos\theta_m)^{1/2} = \cos\frac{\theta_m}{2} \text{and} \quad b_m^\pm = \pm\frac{1}{\sqrt{2}}\sin\theta_m(1+\cos\theta_m)^{-1/2} = \pm\sin\frac{\theta_m}{2} \tag{4.20}$$

From this analysis, it appears that the eigenstates can be labeled in multiple ways: by order of

increasing energy $\{|i\rangle, i = 1, \ldots .20\}$, by the coupled basis $\{|\pm, m\rangle\}$ and in the high-field limit by the Zeeman basis $\{|m_s, m_i\rangle, m_s = \pm\frac{1}{2}, m_i = \frac{-9}{2} \ldots \frac{9}{2}\}$, see Fig. 4.4. The correspondence between the Zeeman basis and the coupled basis is realized by noticing that in the high-field limit, $\tan\theta_m \to 0$ (Eq 4.17). Thus $a_m^{\pm} \to 1$ and $b_m^{\pm} \to 0$, meaning that the electro-nuclear eigenstates $|\pm, m\rangle$ converge respectively to the Zeeman eigenstates $|m_s = \pm\frac{1}{2}, m_i = m \mp \frac{1}{2}\rangle$ as expected when the hyperfine term can be neglected with respect to the Zeeman terms.

Eigen-energies at low magnetic field

The following simplified expressions are readily obtained in the "low-field limit" $\omega_0 = B_0\gamma_e \ll A$, which will be the one relevant for our experiments:

$$E_m^+ = +\frac{9}{4}A + \frac{m}{10}\omega_0(1 + \delta \mp 10\delta)B_0 \text{ with } m \in -5, ..5 \tag{4.21}$$

$$E_m^- = -\frac{11}{4}A - \frac{m}{10}\omega_0(1 + \delta \mp 10\delta)B_0 \text{ with } m \in -4, ..4 \tag{4.22}$$

The field B_0 is seen to lift linearly the nine-fold and eleven-fold degeneracy of the ground and excited multiplet (see Fig. 4.4). Transitions from the ground to the excited multiplet have frequencies centered on $5A/2\pi \approx 7.37$ GHz. In this low-field limit, the coefficients $a_m^{\pm}$ and $b_m^{\pm}$ describing the mixing of the eigenstates are strongly dependent on m.

ESR-allowed transitions

As explained in ch.3 (see Eq. 3.20 and following for instance), spin transitions can be driven if and only if $\langle i|\hat{\boldsymbol{S}}|j\rangle \neq 0$; in the following, we compute these matrix elements for Si:Bi.

S_x transitions allowed at large magnetic field.

In the high-field limit, the Bismuth donor spin eigenstates are well approximated by the Zeeman basis and the allowed transitions are thus given by the usual selection rules $|\Delta m_s| = 1$ and $\Delta m_i = 0$. The 10 transitions $|m_s = \frac{1}{2}, m_i\rangle \leftrightarrow |m_s = -\frac{1}{2}, m_i\rangle$ have a matrix element $\langle 1/2|\hat{S}_x|-1/2\rangle = 1/2$, as expected for an electronic spin $1/2$ (see Figs. 4.5 & 4.6b).

S_x transitions allowed at low magnetic field.

At lower magnetic field, states $\{|m_s = \frac{1}{2}, m_i\rangle, |m_s = -\frac{1}{2}, m_i\rangle\}$ are progressively hybridized into $\{|+, m\rangle, |-, m-1\rangle\}$ as depicted in Fig. 4.5. Correspondingly, the matrix element of these transitions becomes smaller than $1/2$ (see Fig. 4.6b). Their matrix elements are:

$$\langle +, m|\hat{S}_x|-, m-1\rangle = \frac{1}{2}a_m^+ a_{m-1}^- = \frac{1}{2}\cos\frac{\theta_m}{2}\cos\frac{\theta_{m-1}}{2}$$

and depend strongly on m at low magnetic field.

In addition to these 10 transitions, transitions between $|-, m\rangle$ and $|+, m-1\rangle$ become allowed because of this hybridization due to the hyperfine interaction. The frequency and matrix-element of these extra 9 transitions as a function of magnetic field have been plotted in Fig. 4.6c (blue arrows). Their matrix elements are:

$$\langle -, m|\hat{S}_x|+, m-1\rangle = \frac{1}{2}b_m^- b_{m-1}^+ = -\frac{1}{2}\sin\frac{\theta_m}{2}\sin\frac{\theta_{m-1}}{2}$$

and go to zero at high field, as expected.

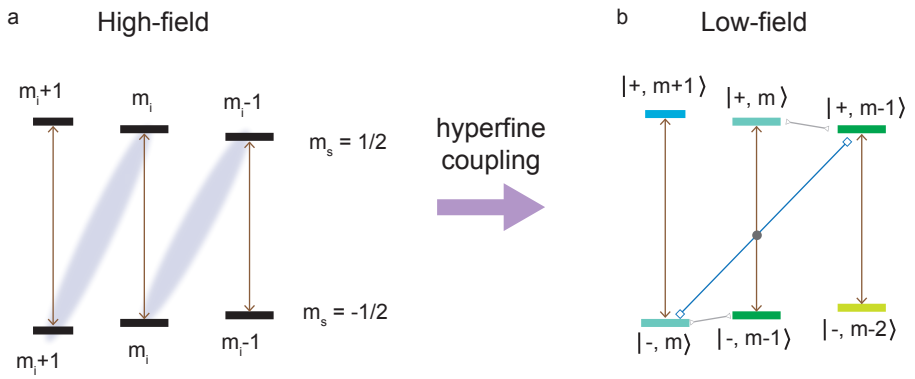

FIGURE 4.5: **Transitions schematic**. **a** At high-field, the usual ESR transitions between levels $|m_s = \frac{1}{2}, m_i\rangle \leftrightarrow |m_s = -\frac{1}{2}, m_i\rangle$ are allowed (brown arrows). At lower fields, the hyperfine coupling renders the Zeeman basis (**a**) invalid to describe the hybridized electro-nuclear states (symbolized by the blue ellipses) however an accurate description is given by the coupled basis $|\pm, m\rangle$ (**b**). **b** At low magnetic field, in the coupled basis $|\pm, m\rangle$, the high-field ESR transitions are now labeled $|+, m\rangle \leftrightarrow |-, m-1\rangle$. The mixing induced by the hyperfine term allows in addition the transitions $|-, m\rangle \leftrightarrow |+, m-1\rangle$, as well as $|+, m\rangle \leftrightarrow |+, m-1\rangle$ and $|-, m\rangle \leftrightarrow |-, m-1\rangle$.

It is interesting to note that the transitions $|+, m\rangle \leftrightarrow |-, m-1\rangle$ and $|+, m-1\rangle \leftrightarrow |-, m\rangle$ (in the $|m \leqslant 4$ manifold) are quasi-degenerate in frequency and that their matrix elements are complementary: $|a^+_m a^-_{m-1}| + |b^+_{m-1} b^-_m| \approx 1/2$. Thus, at any given magnetic field, only 10 transitions have a matrix element greater than $1/4$, see Fig. 4.6b & c (the associated pairs are denoted by a grey circle).

S_z transitions.

An unusual feature of Si:Bi (again, due to the hyperfine coupling) is the existence of 9 transitions that can be driven by a microwave field $\boldsymbol{B}_1$ parallel to the static field $\boldsymbol{B}_0$. These $\hat{S}_z$ transitions connect levels $|+, m\rangle$ and $|-, m\rangle$ in the coupled basis and their matrix element is given by:

$$\langle +, m|\hat{S}_z|-, m\rangle = \frac{\sin\theta_m}{2}.$$

Even if these transitions are forbidden in the high-field limit, they have a sizeable matrix element in the range $[0, 0.4\ \mathrm{T}]$ and can thus be observed at low-field. They are shown in pink in Fig. 4.6a, and their frequency and intensity dependence on B_0 is shown in Fig. 4.6d. It is interesting to note that each transition comes in-between two $\hat{S}_x$ transitions.

NMR transitions

In the above description, we have restricted ourselves to transitions whose frequencies lie in the gigaHertz range. In addition, transitions between $|\pm, m\rangle$ and $|\pm, m-1\rangle$ (with frequencies in the MegaHertz range) are allowed, as shown in grey in Fig. 4.6a. At high fields, these transitions can only be driven via the nuclear spin matrix element I_x; however at low field they acquire a sizeable S_x matrix element:

$$\langle +, m|\hat{S}_x|+, m-1\rangle = \frac{1}{2} a^+_m b^+_{m-1} = \frac{1}{2}\cos\frac{\theta_m}{2}\sin\frac{\theta_{m-1}}{2} \tag{4.23}$$

$$\langle -, m|\hat{S}_x|-, m-1\rangle = \frac{1}{2} a^-_{m-1} b^-_m = -\frac{1}{2}\cos\frac{\theta_{m-1}}{2}\sin\frac{\theta_m}{2} \tag{4.24}$$

These transitions can thus be driven faster than usual nuclear spin transitions, as demonstrated in [85]

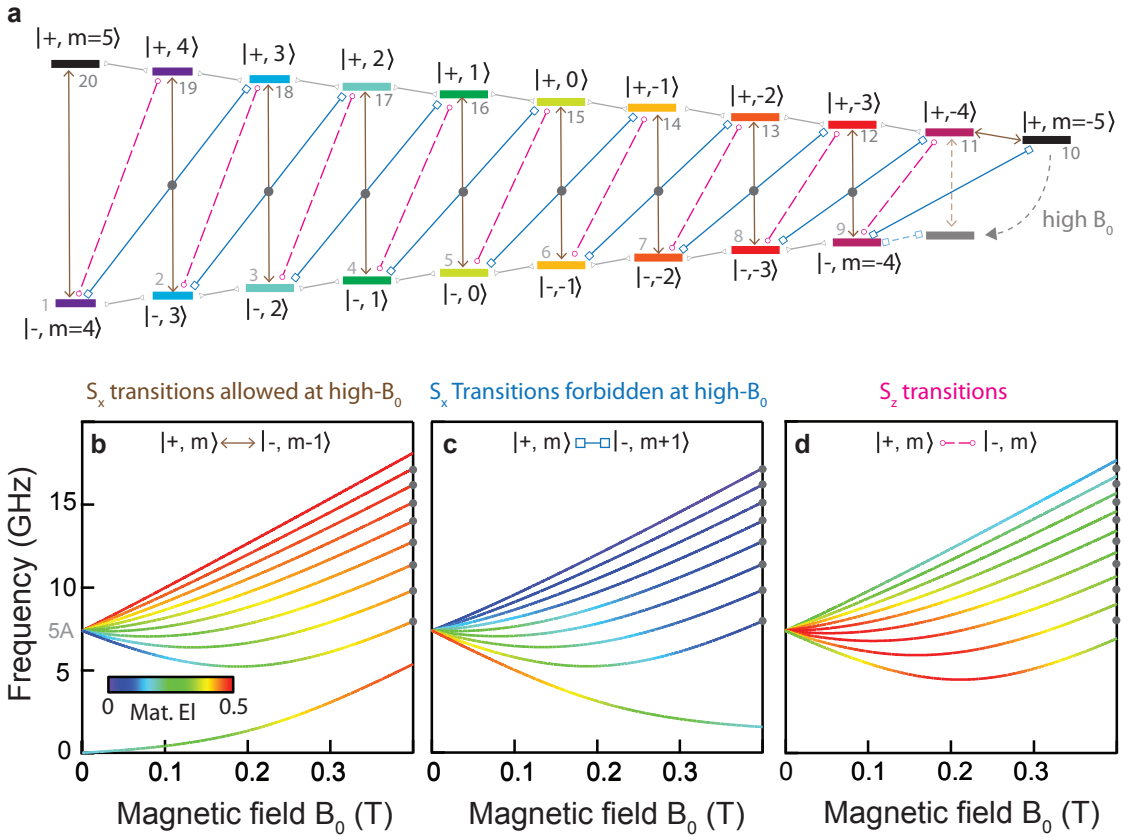

FIGURE 4.6: **Allowed ESR transitions**. **a** Energy levels diagram with ESR allowed transitions symbolized with arrows: $\hat{S}_x$-transitions allowed at large B_0 $|+,m\rangle \leftrightarrow |-,m-1\rangle$ (brown arrows, panel **b**), $\hat{S}_x$-transitions forbidden at large B_0 $|+,m\rangle \leftrightarrow |-,m+1\rangle$ (blue square arrows, panel **c**) and $\hat{S}_z$-transitions $|+,m\rangle \leftrightarrow |-,m\rangle$ (pink circle arrows, panel **d**). NMR-like transitions are shown with grey triangle arrows. The additional grey level shows the position of the $|+,-5\rangle$ level at large B_0. **b-d** Frequencies of ESR allowed transitions as a function of B_0. The curves coloring indicates the transition matrix element value. The color scale is identical for all panels and given in inset of panel **b**. The grey circles in **a** and on the right-side of panels **b-c** frames indicate degenerate transitions (see main text).

Clock-transitions

A striking feature of some group V donors in silicon is the existence of multiple $df/dB_0 = 0$ sweet-spots in their spectrum, due to the interplay between the hyperfine and Zeeman terms in their Hamiltonians. Mohamady at al. predicted theoretically the existence of $I - 1/2$ sweet-spots, called clock-transitions [84, 100]. Bismuth has eight minima in the $f - B$ space, occurring for transitions $\Delta m = \pm 1$ with $m \leqslant 0$ as can be seen in Fig. 4.6b-c. These transitions are degenerate two-by-two, giving rise to four clock-transitions (see Table 4.2). They were observed experimentally by Wolfowicz et al. [25].

These features are very interesting for quantum information applications since the decoherence arising from classical magnetic field noise is reduced at a clock-transition [101]. Phosphorus does not possess any clock-transition due to its nuclear spin $I = 1/2$. While arsenic (^{75}As, $I = 3/2$, $A = 0.198$ GHz) and antimony (^{121}Sb, $I = 5/2$, $A = 0.186$ GHz and ^{123} As, $I = 7/2$, $A = 0.101$GHz) have the necessary nuclear spin to also possess clock-transitions, their weaker hyperfine coupling constant implies that the clock-transitions occur at smaller frequencies (< 600 MHz)[25]. Thus among the group V donors, Bismuth appears the optimal candidate for quantum information

Transition label m	$m=-4$	$m=-3$	$m=-2$	$m=-1$
Magnetic field (mT)	187.8	133.3	79.8	26.6
Frequency (GHz)	5.214	6.372	7.032	7.338

TABLE 4.2: **Magnetic-field clock-transitions in Bismuth donors in silicon**. The clock transitions occur for transitions between pairs $|+,m+1\rangle \leftrightarrow |-,m\rangle$ and $|+,m\rangle \leftrightarrow |-,m+1\rangle$, with $m<0$ for magnetic fields lower than 0.2 mT and frequencies in the gigaHertz range. Adapted from [25].

storage, having four clock-transitions at gigaHertz frequencies.

4.3 Donors in strained silicon

We have so far discussed the spin Hamiltonian of bismuth donors in the case of an unperturbed silicon lattice. The effect of strain on donors in Silicon has been first observed in [94] and has triggered important theoretical work [94, 102, 103, 104, 105], with the perspective of providing a precise control over the spin properties of donors in silicon [104, 106]. Here we provide a summary of essential results needed for our experiments.

To understand the effect of stress, consider first a positive stress applied on the z-axis, which builds a compressive strain in the z-axis and a tensile strain in the x-y axis. The influence of strain on the donor eigenstates can be understood from their valley configurations: the valleys in the direction of compressive strain experience a reduction in energy, leading to a higher valley population whereas valleys in the direction of tensile strain exhibit an increased energy, leading to a lower population. As a consequence, the ground state is no longer purely given by the singlet state A_1 but should be described as a mixture of the singlet with the doublet excited states E_{xy} and E_{xyz} [94]. The T_2 states are not involved since they involve combination of opposite pairs of valleys (see 4.1.1). This change of ground state properties has two distinct effects on the spin Hamiltonian.

Hyperfine interaction

The hyperfine coupling between the electronic spin and the nuclear spin has two separate contributions: an isotropic component (also called Fermi contact) which is directly proportional to the quantum mechanical probability of finding the electron at the nucleus position $\propto |\Psi(\boldsymbol{r}_{\mathrm{Bi}})|^2$, and an anisotropic part due to dipolar interactions between both spins. The latter can be shown to be always zero due to the 1s nature of states A_1, E and T_2 [107]. Due to the symmetry of the wavefunctions described in section 4.1.1, only the symmetric A_1 state has a non-zero contact hyperfine coupling. Since strain mixes it with the other states, it leads to a reduced hyperfine interaction A. The exact reduction depends on the amount of stress applied and can be derived in the case of high-strain with density function theory [105] as well as a tight-binding model [105]. In the case of small strain, when the lattice deformation is negligible, the reduction may be approximated via a valley repopulation model based on EMT [94], giving:

$$\frac{A(x)}{A(0)} \sim 1 - \frac{x^2}{9} \tag{4.25}$$

for small values of x, the so-called "valley strain" given by $x = \Xi_u s'/\Delta E$. ΔE is the splitting between A_1 and E states, Ξ_u is the deformation potential and s' is the shear strain. The reduction of the hyperfine parameter A has the overall effect of lowering the frequencies of the considered ESR transitions.

Note also that the hyperfine coupling can be modified by Stark shift caused by applied electric fields [108, 97, 109], a promising technique for the local control of donor spins in silicon [83].

Quadrupolar interaction

In addition to modifying the hyperfine term of the spin Hamiltonian, stress also contributes to the appearance of a quadrupolar interaction term [110, 111]. Indeed, with a nuclear spin $I = 9/2$, Bismuth possesses an electric quadrupole moment Q. This quadrupole moment interacts with an electric field gradient (EFG) generated by the electron wavefunction through the operator [112]:

$$V_{\alpha\beta} = \langle\Psi|\hat{H}^{\mathrm{EFG}}_{\alpha\beta}|\Psi\rangle \tag{4.26}$$

$$\hat{H}^{\mathrm{EFG}}_{\alpha\beta} = \frac{e}{4\pi\varepsilon}\frac{3\alpha\beta - r^2}{r^5} \tag{4.27}$$

where α or $\beta = x, y, z$ are the crystal axis. In the absence of strain, the fully symmetric ground state A_1 produces no EFG and thus has a vanishing quadrupolar interaction. In the presence of stress, the mixing of A_1 with the non-symmetric E_{xyz} state produces an EFG so that a quadrupolar interaction term appears in the spin Hamiltonian. In the case of a magnetic field B_0 applied on the z direction and a resulting EFG in the z direction, the quadrupolar Hamiltonian is:

$$\hat{H}_{\mathrm{QI}} = \hat{\boldsymbol{I}} \cdot \boldsymbol{Q} \cdot \hat{\boldsymbol{I}} = \frac{eQV_{\mathrm{zz}}}{4I(2I-1)} eQV_{\mathrm{zz}}(3\hat{I}_z - I(I+1)) \tag{4.28}$$

This new term produces an energy shift of transitions between states having a different m_i, which is the case for all $\hat{S}_x$-ESR transitions in the above discussion. Note that the sign of the energy shift depends on the sign of the EFG and thus on the sign of the applied strain.

4.4 Relaxation times

4.4.1 T_1 relaxation

Spin relaxation of shallow donors in silicon has been studied extensively in the 1950s and 1960s experimentally [79, 113, 114, 80, 81, 114, 94, 115, 116, 117]. The measured relaxation times at 4 K surpassed tens of seconds, sparking strong theoretical efforts to understand and model the underlying mechanisms [118, 119, 120, 121]. A variety of relaxation mechanisms were found to be effective at different temperatures, magnetic field, impurity concentrations, and numbers of free carriers. We only wish here to briefly summarize the known mechanisms and their dependence on these parameters and give reported values in the case of bismuth donors.

Spin-lattice relaxation

The electronic spin of shallow donors can relax via exchange of energy with the lattice by emission of phonons. As schematically shown in Fig. 4.7a, two types of processes are usually distinguished: relaxation with conservation of the nuclear spin ($\Delta m_s = \pm 1$, $\Delta m_i = 0$) with a characteristic time labeled T_s, and diagonal relaxation with an additional nuclear spin flip ($\Delta m_s = \pm 1$, $\Delta m_i = \mp 1$) with a characteristic time labeled T_x (see Fig. 4.7a). The "other" diagonal relaxation $T_{x'}$ involving a double flip of the electron and of the nuclear spin ($\Delta m_s = \pm 1$, $\Delta m_i = \pm 1$) is highly forbidden [114].

Consider two levels $|\mathfrak{g}\rangle$ and $|\mathfrak{e}\rangle$ from the Si:Bi energy spectrum and consider the relaxation between $|\mathfrak{e}\rangle$ and $|\mathfrak{g}\rangle$. The levels are split by $\hbar\omega_0$ with respective populations $n_{\mathfrak{e}}$ and $n_{\mathfrak{g}}$. If the system is excited, the population difference $n = n_{\mathfrak{e}} - n_{\mathfrak{g}}$ will progressively relax towards its thermal equilibrium value $N_{\mathfrak{e}} - N_{\mathfrak{g}}$ due to interactions with the lattice, $N_{\mathfrak{e}}$ and $N_{\mathfrak{g}}$ being respectively the thermal equilibrium values of $n_{\mathfrak{e}}$ and $n_{\mathfrak{g}}$. Defining $W_{\mathfrak{e}\to\mathfrak{g}}$ and $W_{\mathfrak{g}\to\mathfrak{e}}$ as the probabilities per second for a spin to relax

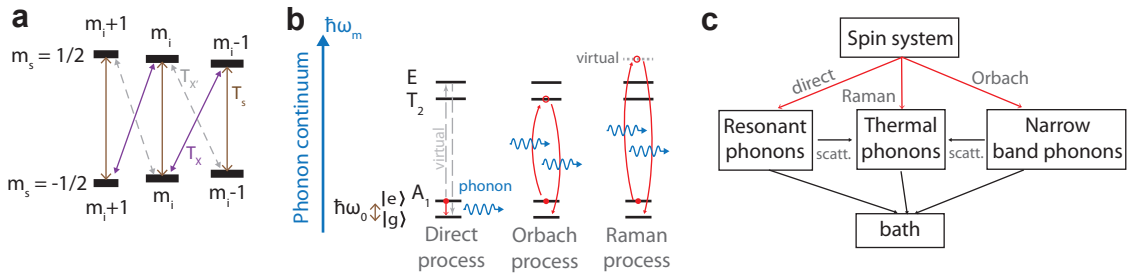

FIGURE 4.7: **Spin-lattice relaxation processes.** **a** Subset of Si:Bi level schemes with the various spin-lattice relaxation processes. **b** Direct, Orbach and Raman phonon relaxation mechanisms. **c** Relaxation paths available to the spin system.

from level $|\mathfrak{e}\rangle$ to level $|\mathfrak{g}\rangle$ and vice-versa, the change in the excited state population writes:

$$\frac{dn_{\mathfrak{e}}}{dt} = W_{\mathfrak{g}\to\mathfrak{e}} n_{\mathfrak{g}} - W_{\mathfrak{e}\to\mathfrak{g}} n_{\mathfrak{e}} \tag{4.29}$$

(and a similar expression for n_g). The rate equation for the population difference n will then be given by:

$$\frac{dn}{dt} = 2(W_{\mathfrak{g}\to\mathfrak{e}} n_{\mathfrak{g}} - W_{\mathfrak{e}\to\mathfrak{g}} n_{\mathfrak{e}}) = (W_{\mathfrak{g}\to\mathfrak{e}} - W_{\mathfrak{e}\to\mathfrak{g}})N - (W_{\mathfrak{e}\to\mathfrak{g}} + W_{\mathfrak{g}\to\mathfrak{e}})n, \tag{4.30}$$

where $N = N_{\mathfrak{e}} + N_{\mathfrak{g}} = n_{\mathfrak{e}} + n_{\mathfrak{g}}$ is the total spin population.

The phonon radiation bath of the lattice can be described as an infinite set of harmonic oscillators of characteristic energy $\hbar\omega$, whose thermal occupancy is given by the Bose-Einstein factor:

$$p(\hbar\omega) = [\exp(\hbar\omega/k_B T_{\mathrm{ph}}) - 1]^{-1} \tag{4.31}$$

where T_{ph} is the temperature of the crystal lattice. When the lattice is well coupled to the environment bath, the phonon equilibrium temperature is given by the system temperature T.

Direct-phonon process

If we consider the case of a resonant exchange of energy, where the system relaxes by emitting a phonon of energy $\hbar\omega_0$ into a lattice mode of the same frequency, see Fig. 4.7b, we can evaluate the transition probabilities as

$$\begin{aligned} W_{\mathfrak{e}\to\mathfrak{g}} &= K[p(\hbar\omega_0) + 1] \\ W_{\mathfrak{g}\to\mathfrak{e}} &= K p(\hbar\omega_0) \end{aligned} \tag{4.32}$$

where one can identify both spontaneous and stimulated emission, as well as absorption, K being a coefficient independent of temperature. Hence, from Eq 4.30:

$$\frac{dn}{dt} = KN - K[2p(\hbar\omega_0) + 1]n \tag{4.33}$$

At infinite time, the spin system is thermalized with the phonon bath, yielding the thermal population difference:

$$n_0 = N \tanh\left(\frac{\hbar\omega_0}{2k_B T}\right)$$

This allows to re-write Eq 4.30 in the well-known form $\frac{dn}{dt} = -(n - n_0)/T_1$ by identifying the relaxation time T_1 as $T_1^{-1} = K \coth\left(\frac{\hbar\omega_0}{2k_B T}\right)$. In the high-temperature limit ($\hbar\omega_0 \ll k_B T$) $T_1^{-1} \sim 2Kk_B T/\hbar\omega_0$.. This linear dependence of the relaxation rate with temperature is characteristic of direct phonon processes. At temperatures $k_B T < \hbar\omega_0$ the relaxation rate saturates to $T_1^{-1} = K$.

The value of K depends on the spin and material properties. In the case of shallow donors in silicon, both Roth [120] and Hasegawa [121] have estimated theoretically K based on two different models where the spin-lattice relaxation arises from the modulation of the spin-orbit coupling by crystal strain.

From the formula derived by Hasegawa [121, 122], one can extract the following dependency for K in the case of a T_s-type process:

$$K = c(\Delta E)^{-2}\omega_0^5, \tag{4.34}$$

where ΔE is the energy difference between the first excited valley state and the ground state and c is a coefficient factor expected to be similar for all shallow donors in silicon in the derivation of Hasegawa [121].

Two-phonon relaxation processes

At higher temperatures, other processes involving two phonons need to be taken into account. These processes are schematically shown in Fig. 4.7b. In the Orbach process, the two-phonon process is mediated by the first excited valley state. The spin relaxes by absorbing a phonon of energy ΔE and emitting a phonon of energy $\Delta E - \hbar\omega_0$. In the case of a Raman process, the excited state is replaced by a virtual state. Any phonon may absorbed or emitted, the only maching condition being that $|\hbar\omega_1 - \hbar\omega_2| = \hbar\omega_0$. At temperatures $k_B T \gg \hbar\omega_0$, the temperature and frequency dependence of T_1 is:

Orbach process [90]:	$T_1^{-1} \propto a\exp(-\Delta E/k_B T)$
Raman process [90]:	$T_1^{-1} \propto bT^9 + b'\omega_0^2 T^7$

where a, b and b' are temperature and frequency independent coefficients determined by the underlying relaxation process [117] and are expected to be different for T_s or T_x processes. The characteristic temperature dependence of the Orbach process on ΔE has been used to determine experimentally its value in the case of shallow donors in silicon [115].

Depending on the coefficients a, b, b' and c, the different processes are active in different temperature ranges. In the case of bismuth, experiments have determined for the T_s relaxation that an Orbach process is dominant down to 25 K [116, 26, 123]. At lower temperatures, a Raman process dominates, with reported T^7 [116, 26, 123, 98] and T^9 dependences [25, 124]. Wolfowicz et al. [25] reported $T_1 = 9$ s at $T = 4.2$ K. Since all reported measurements were performed at temperatures higher than 4 K, the direct-phonon process has never been observed for bismuth.

On the other hand, phosphorus donors have been measured down to lower temperatures, where the direct-phonon process is expected to dominate. Feher and Gere measured $T_1^{-1} \approx 2 \times 10^4$ s^{-1} at $T = 1.2$ K. A. Morello et al. reported more recently T_1 values with the expected ω_0^5-dependence at 40 mK: $T_1^{-1} \approx 0.015(\omega_0/\gamma_e)^5 \mathrm{s}^{-1}\mathrm{T}^{-5}$, where γ_e is the gyromagnetic ratio for phosphorus [122]. From those measurements, one can estimate the coefficient c to be $c \approx 1.5 - 3.2 \times 10^{-13}\mathrm{s}^{-1}\mathrm{GHz}^{-5}\mathrm{eV}^2$ (with $\Delta E = 13$ meV for phosphorus). This coefficient c is expected to be similar for all shallow donors in silicon, according to Hasegawa theory [121] and could give a first rough estimate for the direct phonon relaxation of bismuth donors, yielding at zero temperature and $\omega_0/2\pi = 7$ GHz, $T_1 \approx 2 \times 10^5$ s.

Phonon bottleneck

Up to now, we have assumed that the lattice is well coupled to the environment so that thermal equilibrium is always ensured (see Fig. 4.7c). When this condition is not matched, the phonons created by the spins relaxation will accumulate. This has the effect of slowing down the relaxation since the spins see an effectively hotter lattice. This phenomenon is called a phonon bottleneck and gives rise to a T^2 dependence for T_1 [90]. Considering the low concentration of our sample, we do not expect this effect to be relevant in our experiment.

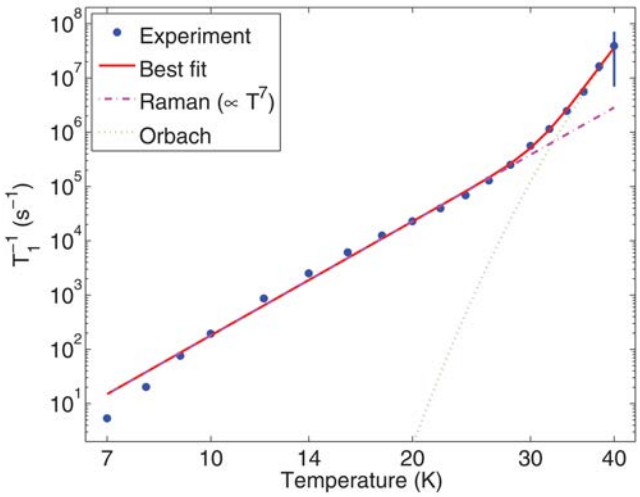

FIGURE 4.8: T_1 **dependence as a function of temperature.** Above $T = 25$ K, an Orbach process dominates whereas for lower temperature, a Raman process is observed. The experiment is realized at $B_0 = 0.57$ T, on the highest frequency transition at $f = 9.76$ GHz with a sample of concentration $[\mathrm{Bi}] = 5 \times 10^{14}\mathrm{cm}^{-3}$. Extracted from [123].

Charge hopping and spin exchange mechanisms

Feher and Gere [81], in addition to measuring the dependence of T_s and T_x on temperature and magnetic field for phosphorus donors in silicon, have studied the influence of donors and acceptors concentration and above band-gap light on spin relaxation.

Shining above band-gap light on the sample increases the number of free carriers. Pines et al. [118] proposed a spin-exchange mechanism where the conduction electrons collide with the impurity and exchange their spin during the process. The conduction electron would then relax by interaction with the lattice. This process is rapidly limited by the phonon bottleneck, except in the case of double spin exchange for which the the spin of the conduction electron remains unaffected and thus does not need to relax.

When the donor concentration is large, clusters of donor atoms form. In these clusters, the electron wavefunction is no longer well confined and an impurity conduction band appears [81]. The spin-exchange mechanism can take place through this impurity band instead of the conduction band, making the clusters of donors fast relaxing impurities. Feher and Gere have observed that for concentration of phosphorus donors higher than $10^{16}\mathrm{cm}^{-3}$, the relaxation time of the spin decreases due to those fast relaxing impurities [81]. For bismuth, this effect should take place for higher concentrations since the electron wavefunction is more confined than for phosphorus.

Last, in a highly-concentrated sample, large numbers of acceptors also speeds up spin relaxation [81]. The acceptors ionize a sizable fraction of the donors, allowing for electron hopping between donors through the impurity band. This effect was predicted by Anderson and Mott [125] and is called an impurity conduction process.

4.4.2 Coherence times

As seen in ch. 3, the coherence of a spin describes how long a superposition of states retains its phase. This phase information is lost via interaction with the environment. Even if a Hahn-echo sequence (see Fig. 4.9a) perfectly suppresses the effect of static field inhomogeneities, dynamic

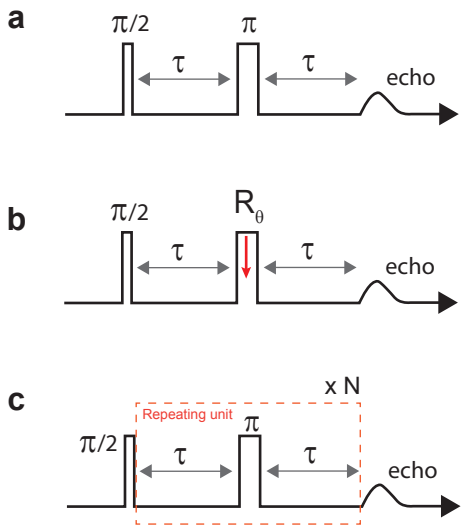

FIGURE 4.9: **Measuring the coherence times.** **a** Hahn-echo sequence. An intermediate π rotation ensures the rephasing of the spins and the emission of an echo, it also refocus the dephasing due to slow fluctuations of the environment. **b** A sequence with small refocusing pulses limit the environment fluctuations due to flip-flops of resonant spins. **c** Dynamical decoupling sequence. Successive π rotations are performed to refocus the dephasing due to dynamic fluctuations.

fluctuations of the magnetic environment during the evolving times τ of the sequence ultimately lead to the disappearance of the echo signal, with a characteristic time called the coherence time T_2. The values obtained for T_2 are governed by the dynamics of nearby magnetic impurities. For bismuth donors in silicon, the relevant species are other bismuth spins and silicon-29, which have a spin $1/2$, present in 4.7% abundance in natural silicon (whereas ^{28}Si has zero nuclear spin). At sufficiently low temperatures (< 5 K), phonon-induced spin relaxation becomes so slow that its effect on the bath dynamics can be neglected. Instead, the bath dynamics are governed by intra-bath flip-flops due to the dipolar interactions between spins. The flip-flops are either between silicon-29 spins, non-resonant Bi spins or resonant Bi spins.

This last decoherence process deserves a separate discussion. During the Hahn-echo sequence, the π pulse flips without distinction all resonant Bi spins. A given Si:Bi spin sees therefore its local environment (consisting in other Si:Bi spins) changed after the π pulse, which leads to decoherence. This effect is called "instantaneous diffusion". The decoherence rate in this process depends linearly on the donor concentration up to an intrinsic contribution $T_{2\,\mathrm{int}}^{-1}$[5, 124]. This intrinsic contribution is determined experimentally by measuring T_2 for decreasing tipping angles of the refocusing pulse which effectively flip increasingly smaller numbers of resonant spins (see Fig. 4.9b). At small donor concentrations, other flip-flop processes become dominant. More details can be found in particular in [126].

In natural silicon, $T_{2\mathrm{int}}$ is eventually limited by flip-flops in the ^{29}Si bath to 0.8 ms [124]. The T_2 sensitivity to these flip-flops is proportional to df/dB. At the clock-transitions where the sensitivity is canceled since $df/dB = 0$, the decoherence time is significantly increased. Wolfowicz et al. [25] measured an enhancement of T_2 from 0.8 ms to 90 ms by working at a clock transition in natural silicon for a donor concentration $[\mathrm{Bi}] = 1 \times 10^{15}\mathrm{cm}^{-3}$). Instantaneous diffusion is also suppressed at the clock transition.

In isotopically purified ^{28}Si samples, the ^{29}Si bath is eliminated and coherence is limited by resonant Bi spins. Flip-flops between pairs not involving the probed spins may be suppressed once again by working at the clock-transition. Wolfowicz et al. [25] measured an impressive value of $T_{2\mathrm{CT}} = 2.7$ s

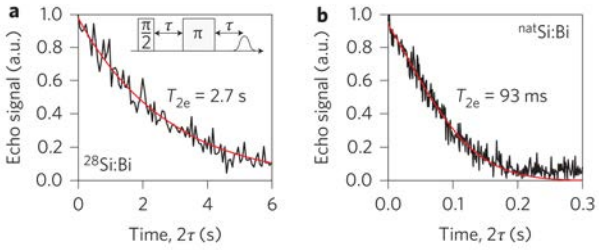

FIGURE 4.10: T_2 **at a clock transition** in **a** isotopically purified ^{28}Si and **b** natural abundance silicon measured with a Hahn-echo sequence. Extracted from [25].

(once again with a low-concentrated sample $[\mathrm{Bi}] = 4 \times 10^{14}\mathrm{cm}^{-3}$). The coherence in this case is finally limited by flip-flops involving the probed spins. This process is not completely suppressed at the clock-transition since it is a second order effect in d^2f/dB^2 and depends linearly on the donor concentration [25].

The coherence time can also be improved by using dynamical decoupling sequences such as the CPMG sequence [127, 128], see Fig. 4.9c. In natural silicon, Ma et al. [129] have measured an enhancement by two orders of magnitude of the intrinsic coherence time $T_{2\mathrm{int}}$ using a CPMG sequence with 128 pulses.

4.5 Optical transitions via donor-bound exciton states

Silicon's indirect bandgap prevents coherent optical manipulation of Si:Bi such as used for instance in NV centers in diamond [130]. However, Yang et al. showed that optical photons can be used to polarize and readout the spin state of donors in silicon, using bound exciton transitions [131]. Absorption of a photon creates an electron-hole pair which remains bound to the donor (D^0X). The D^0X state decays back to the ionized donor state (D^+) via Auger processes and comes back to the neutral state (D^0) via capture of another electron (see Fig. 4.11a). Frequency-selective optical excitation enables selective polarization of the nuclear and electronic spin states [132], especially when isotopically purified ^{28}Si samples are used so that the lines become very well-resolved [131]. With phosphorus donors, Steger et al. achieved a remarkable electronic polarization of 97% and nuclear polarization of 90% at 4.2 K [133]. The ejected Auger electron can also be detected via photo-conductivity measurements, leading to very sensitive NMR experiments with low donor concentrations [133].

Si:Bi possesses the same bound-exciton transitions as Si:P (see Fig. 4.11b). Using photoluminescence spectroscopy, Sekiguchi et al. [134] observed the expected transitions between D^0 and D^0X states (see Fig. 4.11c). They managed to resolve the zero-field hyperfine splitting, however the use of a natural abundance sample prevented them from resolving the nuclear states. Repeating the experiment with silicon-28 could provide a new way to initialize Si:Bi electronic and nuclear spins.

4.6 Fabrication

Bismuth impurities can be introduced during the silicon crystal growth to provide bulk-doped natural silicon wafers or can be implanted in existing substrates, which is done in the case of already grown isotopically enriched ^{28}Si substrates. ^{28}Si material can either be bulk samples (currently available only thanks to the Avogadro project [135]) or an epitaxial layer grown on top of a natural abundance silicon wafer. Due to the high atomic mass of bismuth (atomic weight = 209), the

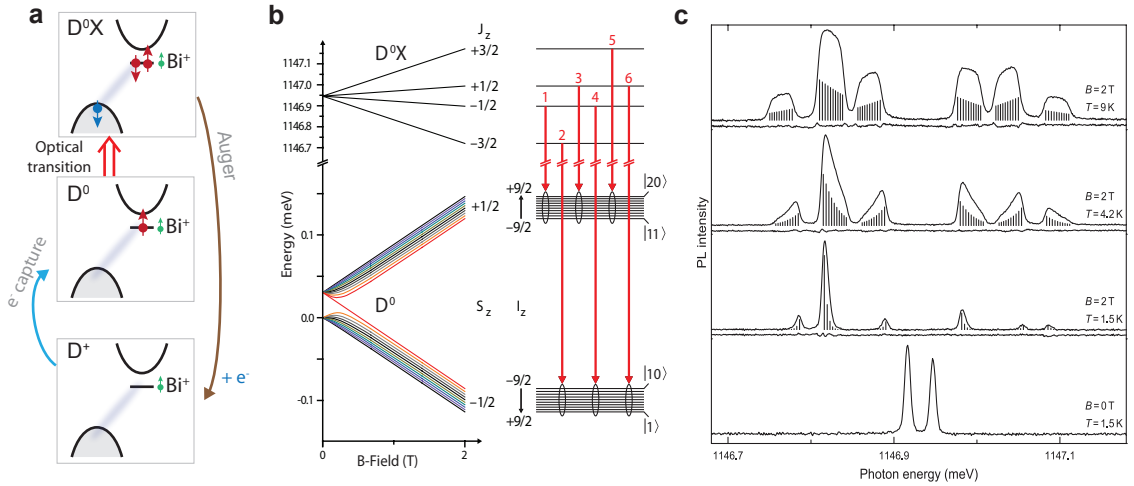

FIGURE 4.11: **Bound-exciton optical transitions. a** Sketch of the spins for states D^0X, D^0 and D^+ and the transitions in between. **b** Zeeman splitting for D^0 and D^0X along with the dipole allowed optical transitions **c** Observed stimulated photoluminescence spectrum for Si:Bi in a natural sample. **b** and **c** are extracted from [134].

implantation process creates many lattice defects. An annealing step above 600°C is required to heal the implantation damage and ensure that the implanted bismuth atoms are converted in substitutional impurities. Studer et al. [136] reported a conversion yield of $\approx 100\%$ with a two-step annealing (3 min at 650°C followed by 10 min at 900°C).

Sample used in this work

The sample used in this thesis work is a 700 nm enriched 99.95% silicon-28 epitaxially grown layer on a natural silicon (100) wafer. Bismuth implantation and sample characterization were carried out by Weis et al. [137]. Bismuth atoms were implanted at different energies so as to obtain a box-like profile at a depth comprised between 20 nm and 150 nm, see Fig. 4.12a. The peak concentration is $[\mathrm{Bi}] = 9 \times 10^{16}\mathrm{cm}^{-3}$. Electrical activation measurements revealed a 60% conversion yield obtained with an annealing step at 800°C for 20 min. Weis et al. measured an ESR linewidth of 12.2 µT at $B_0 = 0.24$ mT and a coherence time $T_2 = 0.7$ ms measured on the $|6\rangle \leftrightarrow |15\rangle$ transition (see Fig. 4.12b).

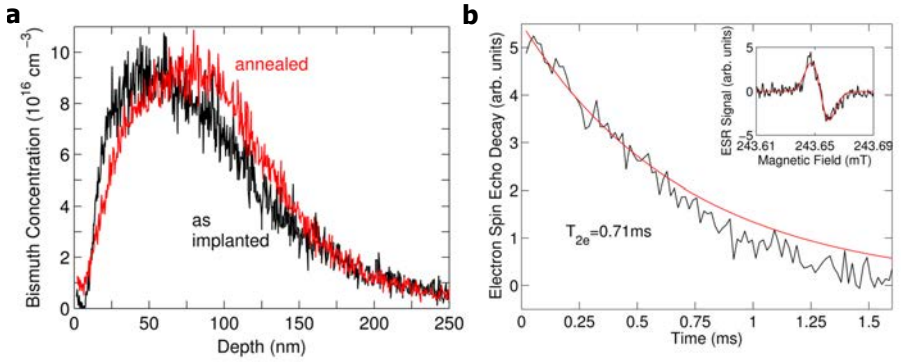

FIGURE 4.12: **Characteristics of the sample** fabricated by Weis et al. [137]. **a** Implantation profile extracted by SIMS (Secondary ion mass spectroscopy). **b** T_2 measured with a Hahn echo sequence at $B_0 = 0.243$ T.

Part II

Magnetic resonance at the quantum limit

Chapter 5

Design and realization of a spectrometer operating at the quantum limit of sensitivity

While inductively-detected ESR spectroscopy has a wide range of applications, this technique has a limited sensitivity since it relies on the detection of radiation emitted by the spins into the detection. As spins interact rather weakly with the electromagnetic field, a successful detection requires a large number of spins for the collected signal to overcome the experimental noise. This prevents the use of conventional ESR to study nanoscale samples containing only a few spins, such as a single protein molecule, or a nanoparticle. While alternative techniques such as STM tips [138], mechanical resonators [139, 140], or more recently NV centers [141] have been developed to overcome this limit, there is still a strong interest to increase the sensitivity of spectrometers based on inductive detection due to their versatility [142, 143, 37, 15].

To enhance the signal of inductively detected ESR spectroscopy, resonator geometries maximizing the coupling of the spins to the electromagnetic field are developed and when possible samples are cooled down to increase the equilibrium polarization of the spin ensemble. Working at cryogenic temperatures also allows to reduce considerably the part of the experimental noise arising from the thermal fluctuations in the detection waveguide. To benefit entirely from this reduction, cryogenic microwave amplifiers with improved noise figure can be used, such as the High Electron Mobility Transistor (HEMT) amplifiers.

In this chapter, we describe the design and experimental realization of an ESR spectrometer based on inductive detection via a high-quality factor superconducting micro-resonator, operating at millikelvin temperatures, with the spin signal amplified by a JPA. In this way, the dominant source of noise is the quantum fluctuations of the microwave field at 20 mK. The sensitivity of this spectrometer will be characterized in ch. 7.

5.1 Nanoscale ESR

5.1.1 State-of-the-art

A number of techniques are currently investigated to push the sensitivity of ESR to the nanoscale, using methods based on optically (ODMR) or electrically (EDMR) detected magnetic resonance, as well as scanning probe setups.

ODMR relies on the spin-dependent photoluminescence occurring in certain systems, such as doped pentacene single molecules [145] or individual NV centers in diamond [130]. Single spin sensitivity can be reached, mainly thanks to the use of optical pumping creating a large spin polarization and

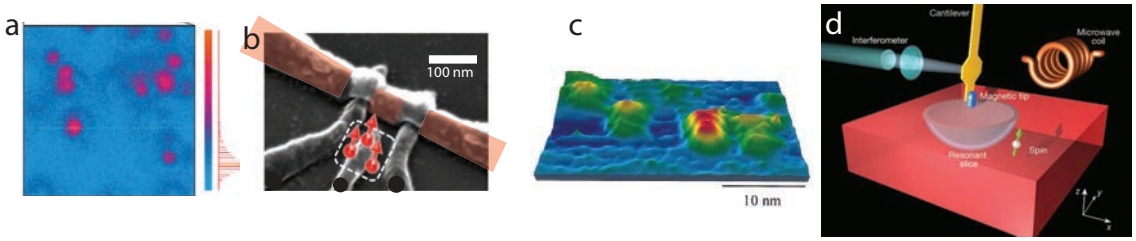

FIGURE 5.1: **Single-spin detection** has been reached using alternative techniques to conventional ESR spectroscopy. **a** Fluorescence map of a diamond comprising single NV centers, allowing for single-spin ODMR. **b** Single Si:P donor detection with a SET. **c** Imaging of four BDPA molecules using a STM. **d** Single-spin detection using a MRFM setup. Figures are extracted respectively from [130, 122, 144, 140].

to the detection of optical rather than microwave photons. In turn, these single emitters can be used as very sensitive ESR sensors; for example NV centers were used to detect nearby spins with a sub-nanometric precision [146].

In EDMR, the spin degree of freedom is converted to a charge degree of freedom. The charge can then be very efficiently detected by charge sensors such as a quantum dot [147], a field-effect transistor [148], a junction [149] or a single-electron transistor [122]. Since these sensors can detect a single charge, the sensitivity is limited by the efficiency of the spin to charge conversion, which can be of order unity for spins in semiconductors, as was demonstrated for electrostatically defined quantum dots in GaAs [147] or in silicon [150], as well as individual dopants in silicon [151]. Transport measurements of a single molecular magnet inserted in a junction [149] or a transitor [152] have also shown that the detection and manipulation of the nuclear spin of an individual metal atom embedded in the single molecule magnet is possible.

The force acting on a spin placed in a magnetic field gradient can also be used to provide single-spin detection [140]. When the magnetic field gradient is generated by the magnetic tip of an atomic force microscope (AFM) cantilever, the very sensitive measurement of the cantilever displacement can be harnessed to detect a single spin. Such a technique is called magnetic resonance force microscopy (MRFM).

Single-spin sensitivity has also been reached using scanning tunneling microscopy (STM) where the spin Larmor precession in a DC magnetic field induces a modulation in the tunneling current [138, 144]. In addition, with this technique the spin position can be determined precisely.

5.1.2 Pulsed inductive detection at the nanoscale

While the above methods have reached sufficient sensitivity to detect a very small number of spins, they lack the versatility of conventional inductive detection discussed in ch. 3, relying either on a conversion to another degree of freedom or a scanning probe setup. In the following, we provide a quantitative analysis of the sensitivity of inductively detected ESR spectroscopy, and we show that with an appropriate design and setup this sensitivity can be considerably improved compared to the state-of-the-art of inductive detection.

Sensitivity of inductively-detected ESR spectroscopy

Our analysis of the sensitivity of inductive detection ESR spectroscopy is based on the concepts presented in ch. 3. As in ch. 3 (and as shown in Fig. 5.2), we consider an ensemble of N spins coupled to a resonator of frequency ω_0 with identical coupling constant g. The resonator, of total damping rate κ, is coupled to input and output transmission lines with coupling rate κ_1 and κ_2.

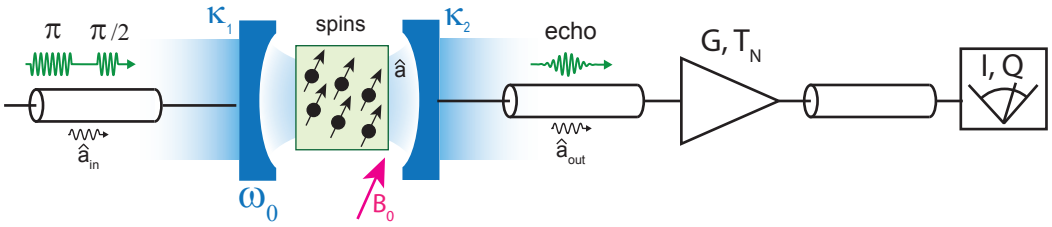

FIGURE 5.2: **ESR setup**. A train of microwave pulses sent on port 1 of the resonator triggers the emission of an echo by the spins. If $\kappa_1 \ll \kappa_2$, the echo is mainly emitted into the detection waveguide before being amplified and detected via an homodyne setup that yields the quadratures I and Q of the signal.

The spins are probed by a Hahn-echo sequence ($\pi/2 - \tau - \pi - \tau$) sent via port 1 that ultimately triggers the emission of an echo. To maximize the efficiency of the emission into the detection line connected on port 2, we assume $\kappa_2/\kappa \sim 1$ implying $\kappa_1 \ll \kappa_2$, approaching the situation frequently encountered in ESR spectrometers which are measured in reflexion, i.e. with $\kappa_1 = 0$.

To describe the evolution of the spins during the Hahn-echo sequence, we make the assumption that the spins-resonator system is in the weak-cooperativity regime and we neglect transverse relaxation (also called decoherence or T_2 processes in ch. 3). Similarly to ch. 3, the spin ensemble is divided in spin subsets (j) of detunings $\Delta_{(j)} = \omega_{s,(j)} - \omega_0$; for the sake of simplicity we assume here that the shape of the distribution is a Lorentzian :

$$\rho(\Delta) = \frac{w/2\pi}{\Delta^2 + w^2/4} \tag{5.1}$$

of linewidth w and central frequency ω_s. The spin evolution can be described in the following way. Starting from an equilibrium polarization p at time -2τ along the z-direction such that the collective spin operators mean-values are:

$$\begin{cases} \langle \hat{\mathcal{S}}_x(-2\tau - \varepsilon)\rangle &= 0 \\ \langle \hat{\mathcal{S}}_y(-2\tau - \varepsilon)\rangle &= 0 \\ \langle \hat{\mathcal{S}}_z(-2\tau - \varepsilon)\rangle &= -p \end{cases} \tag{5.2}$$

an ideal $\pi/2$ around the x-axis creates the transversal magnetization state:

$$\begin{cases} \langle \hat{\mathcal{S}}_x(-2\tau + \varepsilon)\rangle &= 0 \\ \langle \hat{\mathcal{S}}_y(-2\tau + \varepsilon)\rangle &= p \\ \langle \hat{\mathcal{S}}_z(-2\tau + \varepsilon)\rangle &= 0 \end{cases} \tag{5.3}$$

Due to the spin ensemble inhomogeneity, the transverse magnetization decays in a time $1/w$, but the refocusing π pulse applied at $t = -\tau$ ensures that rephasing occurs at time $t = 0$. As seen in 3.1.1, for each spin subset, one has:

$$\langle \hat{\mathcal{S}}_-^{(j)}(t)\rangle = -\frac{ip}{2} e^{-i\Delta_j t} \quad \text{for} \quad t \geqslant -\tau. \tag{5.4}$$

The collective spin operator $\langle \hat{\mathcal{S}}_-\rangle$ can be calculated from each spin contribution:

$$\langle \hat{\mathcal{S}}_-(t)\rangle = -\int \rho(\Delta) \frac{ip}{2} e^{-i\Delta_j t} = -\frac{ipN}{2} e^{-w|t|/2} \tag{5.5}$$

The relation between the intra-resonator field and $\langle \hat{\mathcal{S}}_-\rangle$ in the semi-classical approximation is given

by Eq. 3.44. If the cavity resonance is matched to the spin frequency $\omega_0 = \omega_s$, it follows that the output field of port 2 is given by:

$$\langle \hat{a}_{\text{out}} \rangle = \sqrt{\kappa_2}\langle \hat{a} \rangle = -\sqrt{\kappa_2} \int_\Delta \frac{2gi}{\kappa + 2i\Delta} f(\Delta) \langle \hat{\mathcal{S}}_-^{(j)} \rangle d\Delta \tag{5.6}$$

$$\langle \hat{a}_{\text{out}} \rangle = -\frac{\sqrt{\kappa_2} gpN}{\kappa + w} \times \begin{cases} e^{wt/2} & t < 0 \\ \frac{\kappa+w}{\kappa-w} e^{-wt/2} - \frac{2w}{\kappa-w} e^{-\kappa t/2} & t > 0 \end{cases} \tag{5.7}$$

Eq. 5.7 yields that the signal is emitted on the quadrature $\langle \hat{X}_{\text{out}} \rangle$ at resonance. Assuming that the detection is achieved by a linear amplifier of power G and noise temperature T_N followed by homodyne detection yielding the quadratures $I(t)$ and $Q(t)$, one can set the phase of the local oscillator so that the output field quadrature $\hat{X}_{\text{out}}$ corresponds to the I quadrature for instance. As seen in ch. 2, the echo is emitted on a mode characterized by an envelope function $u(t)$, normalized such as $\int u(t)^2 dt = 1$. To maximize the signal we choose $u(t) \propto \langle \hat{X}_{\text{out}}(t) \rangle$ and using Eq. 5.7, we obtain:

$$\langle \hat{X}_{\text{out}} \rangle^2 = \int \langle \hat{X}_{\text{out}}(t) \rangle^2 dt = \frac{2\kappa_2 g^2 p^2 N^2 (\kappa + 2w)}{(\kappa + w)^2 w \kappa} \tag{5.8}$$

As seen in ch. 2, the noise n arises from both the electromagnetic fluctuations at thermal equilibrium given by Boltzmann statistics $n_{\text{eq}} = \frac{1}{4}\coth(\hbar\omega/2k_BT)$, and the noise added by the amplifier $n_{\text{amp}} = \frac{1}{2}k_BT_N/\hbar\omega$. In addition, the spins may also contribute to n due to their incoherent spontaneous emission [153] into the detection waveguide. Their exact contribution n_{SE} depends on the spins state but an estimate is provided by $n_{\text{SE}} \approx \Gamma_p N/4$. Overall one can write:

$$n = n_{\text{eq}} + n_{\text{amp}} + n_{\text{SE}}. \tag{5.9}$$

Finally, the signal-to-noise for the detection of a single-echo is characterized by:

$$\text{SNR} = \frac{\langle \hat{\text{X}}_{\text{out}} \rangle}{\sqrt{n}} = \frac{2gpn}{\kappa + w} \sqrt{\frac{1}{w}} \sqrt{\frac{\kappa_2(\kappa + 2w)}{w\,\kappa}} \tag{5.10}$$

The sensitivity of the experiment can be defined as the number of spins detectable in a single-echo with a signal-to-noise ratio of 1 and is thus given by:

$$N_{\min} \underset{\text{SNR}=1}{=} \frac{\sqrt{n}}{gp} \sqrt{\frac{(\kappa + w)^2 w\kappa}{4\kappa_2(\kappa + 2w)}} \xrightarrow{\kappa \gg w, \kappa \approx \kappa_2} \frac{\sqrt{n}}{2gp} \sqrt{\frac{\kappa}{T_E}} \tag{5.11}$$

where we have simplified the expression by assuming conventional ESR limit with $\kappa \gg w$ and that the echo duration was set by the inhomogeneity of the line $T_E \approx 1/w$ as well as set $\kappa_2 \approx \kappa$.

Proposal for nanoscale sensitivity

For a conventional room-temperature spectrometer, where the resonators often have a three-dimensional geometry, Eq. 5.11 yields $N_{\min} = 10^{13}$ (see Table 5.1). This number results from the weak spin-photon coupling achieved in the usual three-dimensional ESR resonators as well as the low spin-polarization and large microwave noise inherent to room-temperature operation.

This figure of merit can be significantly improved by using micro-fabricated resonators [142, 143, 37, 15], as shown in Fig. 5.3, because the two-dimensional confinement of the microwave field at the spin location increases g by several orders of magnitude. Operation at lower temperatures also enhances considerably the sensitivity by increasing the spin polarization and allowing for the use of better amplifiers. Sigillito et al. reported $N_{\min} = 10^7$ with a spectrometer built around a thin-film superconducting resonator at 4 K and a HEMT amplifier ([15], see Table 5.1). The latter is

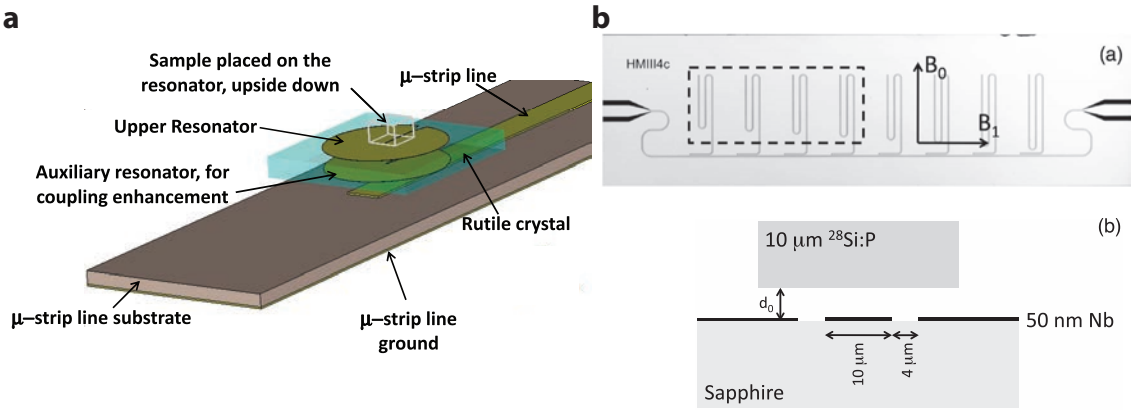

FIGURE 5.3: **Examples of micro-resonators** (**a**: extracted from [142], **b**: extracted from [37])

a commercially available low-noise amplifier operating at 4 K with reported noise temperatures down to $T_N = 1$ K[154].

To improve the sensitivity beyond this figure, our approach is to push these ideas even further. We will work at temperatures $T \ll \hbar\omega/k_B$, so that $n_{\text{eq}} = 1/4$, arising solely from the vacuum fluctuations of the field. In addition, we will use a JPA amplifier, for which $n_{\text{amp}} = 1/4$ in the case of phase-preserving amplification and $n_{\text{amp}} = 0$ in the case of phase-sensitive amplification. Working at X-band (7 GHz) and 20 mK, this results into a 2-orders of magnitude improvement on n compared to the state-of-the-art.

Operating with higher quality factors also increases the sensitivity since $N_{\min} \propto \sqrt{\kappa}$. Thin-film superconducting resonators can reach quality factors up to $10^5 - 10^6$, and if they are made out of Nb or NbTiN can withstand magnetic fields up to ≈ 1T (Nb, NbN [155, 156], NbTiN [157]). In our experiment, we will use aluminum which can withstand only small magnetic fields up to ≈ 10 mT, with $Q \approx 10^5$. Combined with a micro-resonator geometry allowing low-power and fast spin manipulation [15], this results in two orders of magnitude improvement on the sensitivity.

With these parameters, Eq. 5.11 predicts that a sensitivity $N_{\min} = 4 \times 10^2$ should be reached. While far from the sensitivities reached by the alternative methods discussed in 5.1.1, this would nevertheless represent an interesting development for inductively-detected ESR spectroscopy, going in the direction of "ESR at the nanoscale" while preserving its versatility and high-bandwidth. Possible applications include ESR spectroscopy of single cells, nanoparticles and nanodevices.

	T(K)	p	T_N(K)	n_I	$g/2\pi$ (Hz)	$Q = \omega_0/\kappa$	$N_{\min}$
Conventional spectrometer	300	7×10^{-4}	300	10^3	5×10^{-3}	2×10^3	10^{13}
Micro-resonator at 4 K [15]	4	8×10^{-2}	4	10	20	5×10^3	10^7
This work	0.02	1	0.35	1/4	50	1×10^5	4×10^2

TABLE 5.1: **Expected ESR sensitivities** for a conventional spectrometer, a micro-resonator operated at 4 K and the work reported here using Eq. 5.11. The frequency is assumed to be $\omega_0/2\pi = 7$ GHz and $T_E = 10\mu s$.

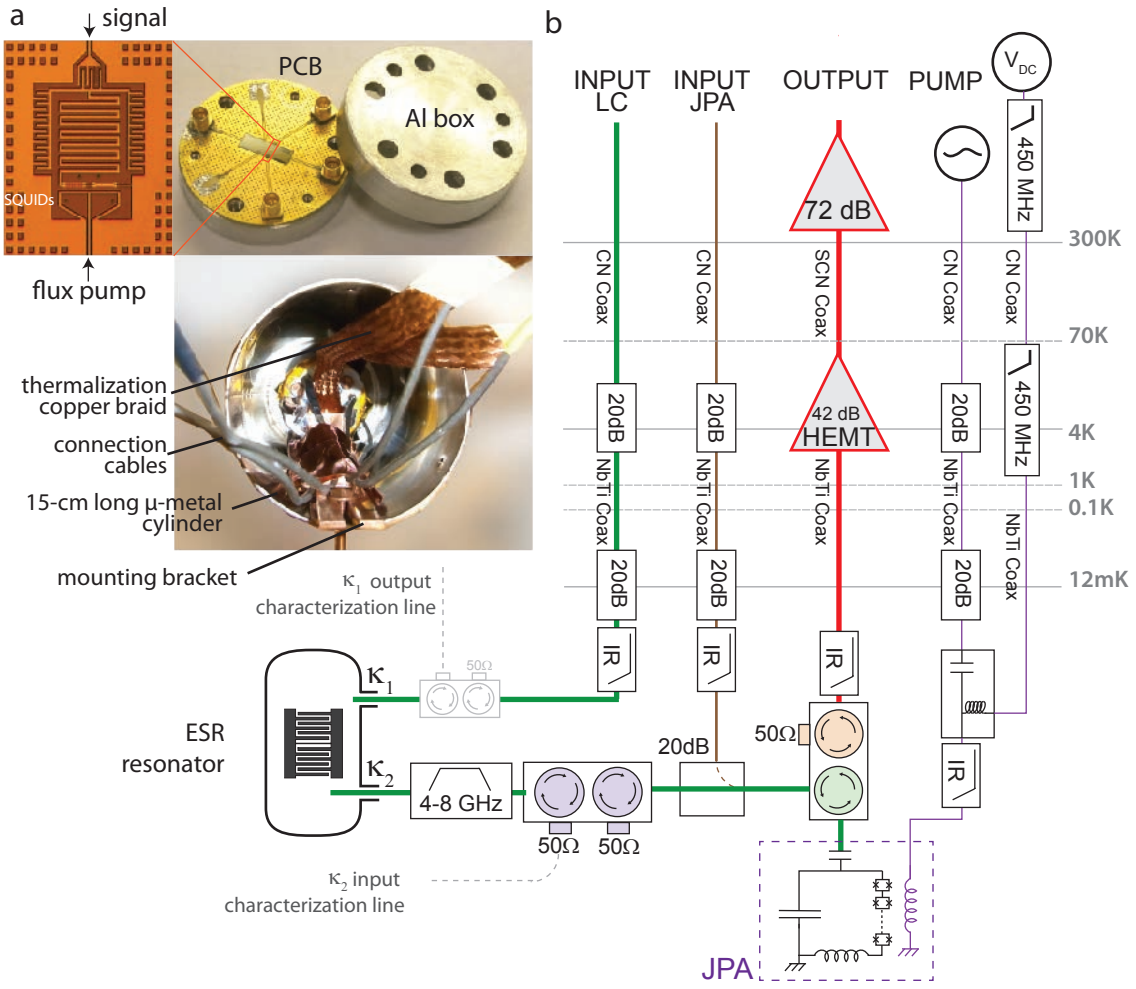

FIGURE 5.4: **ESR spectrometer at the quantum limit. a** Flux-pumped JPA design with its PCB and magnetic shielding. **b** Microwave setup connecting the room-temperature apparatus to the 12 mK experimental stage, on which are mounted both the ESR resonator and the JPA. The grey dashed elements indicate microwave lines added solely during the ESR resonator characterization.

5.2 Experimental setup

We describe in the following the experimental implementation of an ESR spectrometer with a quantum-limited sensitivity.

5.2.1 Low-temperature operation

The experiment is performed at 10 mK in a cryogen free dilution refrigerator fabricated by the company Cryoconcept. This refrigerator has five stages at different temperatures (70 K, 4 K, 1 K, 100 mK and 12 mK) separated by radiation shields. Both the ESR resonator and the JPA are anchored to the mixing chamber and thermalized at a temperature of 12 mK. The ESR resonator design and implementation are described in the following section. As seen in Fig. 5.4, the resonator is connected via its port 2 to the JPA described in ch. 2. A micrograph view of the JPA resonator with its geometrical inductance and capacitance and its SQUIDs array patterned on top of a silicon chip is

shown in Fig. 5.4a. The JPA chip is glued and bonded to a printed circuit board (PCB) inserted in an aluminum box to protect the SQUIDs from stray magnetic fields and ensure the stability of the JPA, (see Fig. 5.4a). Additional protection is provided by a two-layer mu-metal shielding (Cryoperm), the first one having the same shape as the aluminum box, and the second one being a 15-cm long cylinder at the bottom of which the JPA is placed.

The ESR measurements are performed via the microwave setup shown in Fig. 5.4b, with transmission lines linking the room-temperature measurement apparatus to the resonator and the JPA. To prevent heat transfer from higher to lower temperature stages, the transmission lines are made of CuNi (or S-CN) coaxial cables from room-temperature to 4 K and of NbTi superconducting cables from 4 K to 12 mK. An experimental challenge, which is encountered in all cQED experiments, is to prevent thermal or technical noise at microwave frequencies to reach the sample at 20 mK so that the microwave field at 20 mK is truly in its ground state, while still being able to measure the signal transmission.

For input lines (green and brown lines), the solution is to cool the microwave field along the transmission line by inserting attenuators at low temperatures. Consider a cable with a $50\ \Omega$ input impedance at room-temperature, yielding a number of propagating noise photons $n_{\rm th}(T) = k_B T/\hbar\omega = 900$; inserting an attenuator A thermalized at a temperature T_0 brings down the number of propagating noise photons to $n_{\rm th}/A$ while adding $n_{\rm th}(T_0) = \coth(\hbar\omega/2k_BT)$ thermal photons. Thus for the input lines shown in Fig. 5.4 attenuated by 20 dB at 4 K and by 20 dB at 20 mK, the number of propagating noise photons incoming onto the resonator is $n_{\rm th} = 0.2$. In addition, the asymmetry of the coupling antennas $\kappa_1 \ll \kappa_2$ ensures an additional attenuation (≈ 6 dB) leading to $n_{\rm th} = 0.05$. This figure could be improved by adding an extra 10 dB at 20 mK.

For the output lines (red lines) however the signal cannot be attenuated without degrading the signal-to-noise ratio of the measurement. To nevertheless protect the sample from thermal photons and noise photons emitted by the amplifiers, microwave circulators are placed at 20 mK. Used as shown in Fig. 5.4, they make it possible to let all the output signal propagate towards the amplifier at 4 K, whereas the noise coming from the opposite direction is channeled to a cold $50\ \Omega$ load that absorbs the noise. Commercial circulators have only 18 dB isolation, we thus use two circulators in series (green and orange in Fig. 5.4) to isolate the JPA from the HEMT noise. As the noise temperature of our HEMT is $T_H = 4.5$ K, the number of propagating noise photons incoming onto the JPA is estimated to $n_{\rm th} = 0.01$.

In order to characterize the JPA response without having to pass through the ESR resonator, an additional input microwave line (brown in Fig. 5.4) is coupled via a 20-dB directional coupler to the JPA input. The circulator shown in green in Fig. 5.4 is responsible for routing the signal outcoming from the ESR resonator to the JPA and from the JPA to the output line (red) in addition to providing thermal isolation. A double circulator (purple in Fig. 5.4) is inserted between the JPA and the ESR resonator to protect the ESR resonator from the JPA amplified noise and prevent interferences between the two devices.

The DC and AC bias lines needed to tune the JPA frequency and deliver the pump tone are shown in purple. The DC bias is provided by a stable voltage source (Yokogawa 7651) and is filtered at room-temperature and 4 K, where in addition a voltage divider ($\div 10$) is placed. The AC pump tone at $\omega_p \approx 2\omega_p$ (≈ 14 GHz in our experiment) is sent via a dedicated line attenuated by 20 dB at 4 K and 20 mK, like the input signal line. Pump tone leakage to the ESR resonator is suppressed by a 4-8 GHz bandpass filter.

Low-noise signal amplification is done in several steps, and relies on the fact that the dominant contribution comes essentially from the first amplifier of the chain, regardless of the noise of follow-up amplifiers. Indeed two amplifiers of gain G_1 and G_2 with noise temperature $T_{N,1}$ and $T_{N,2}$ are equivalent to an amplifier of gain G_1G_2 with noise temperature $T_1 + T_2/G_1$. In our case, the JPA provides ≈ 25 dB gain; it is followed at 4 K by a HEMT amplifier (LNF amplifier) that provides $G_H = 42$ dB with a noise temperature of $T_{N,\rm H} = 4.5$ K and finally at room-temperature by two

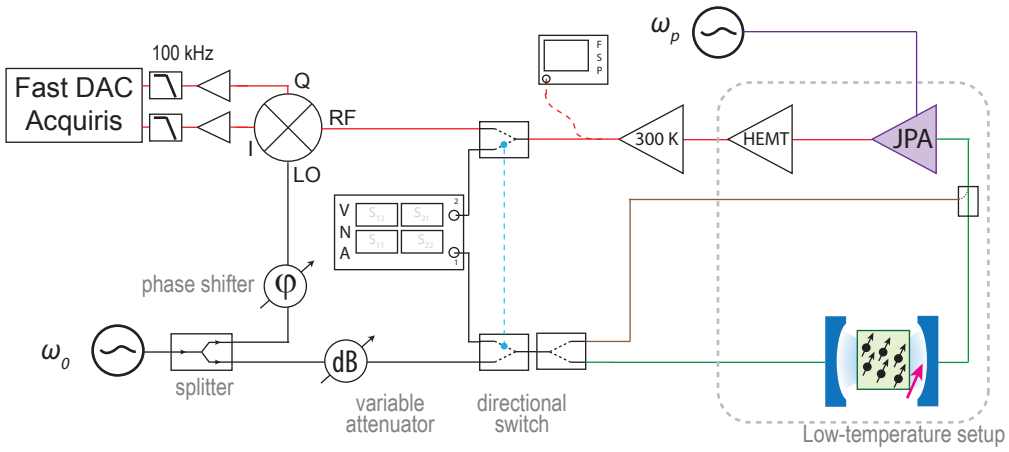

FIGURE 5.5: **Room-temperature setup.**

microwave amplifiers providing in series a total gain $G_{\mathrm{RT}} = 72$ dB with a noise temperature $T_{\mathrm{RT}} = 1000$ K, the overall noise temperature of the chain is:

$$T_N = T_{N,\mathrm{JPA}} + \frac{T_{N,\mathrm{H}}}{G_{\mathrm{JPA}}} + \frac{T_{\mathrm{RT}}}{G_{\mathrm{JPA}} G_{\mathrm{H}}} \tag{5.12}$$

In total, we see that the JPA contribution to the total noise figure of the amplification chain is close to 95%.

5.2.2 Room-temperature setup

The room-temperature microwave setup is depicted in Fig. 5.5. The ESR resonator and the JPA can be characterized either by a commercial Vector Network Analyzer (VNA), or direct homodyne demodulation followed by digitization with a rapid acquisition card. Microwave switches allow to use either the VNA or homodyne setup on-demand.

For homodyne detection, a microwave source provides both a coherent signal sent towards the ESR resonator or to the JPA as well as a continuous tone which serves as the local oscillator of an IQ mixer to demodulate the output signal. The resulting I and Q quadratures are then amplified and filtered in several stages before being recorded by a fast digitizer (Acqiris DC282) and transferred to a computer for processing. The phase of the homodyne detection is set manually via a tunable phase-shifter.

The microwave sources generating the JPA pump tone as well as the signal tone are synchronized via a 1-GHz-synchronization loop in addition to the 10-MHz-synchronization loop running through every instrument to improve phase stability even further, which is essential in particular for operating the JPA in the degenerate mode.

5.2.3 JPA characterization

Phase-preserving and phase-sensitive gain.

We first study the dependence of the JPA resonator frequency on the DC magnetic flux Φ that threads the SQUIDs loops. At $\Phi = 0$, the JPA reflexion coefficient has a constant amplitude with a 2π-phase shift (see Fig. 5.6a&b), yielding $\omega_{\mathrm{JPA}}/2\pi = 8.02$ GHz and $Q = 200$ (using Eq. 2.57). Passing current

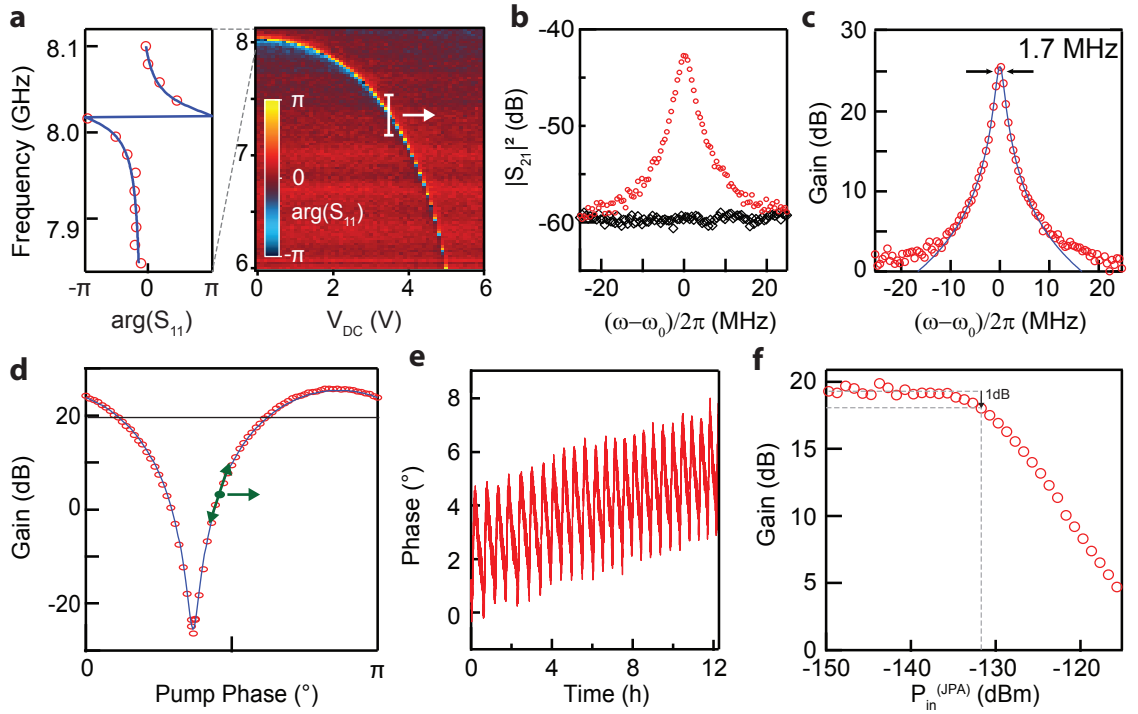

FIGURE 5.6: **Characterization of the flux-pumped JPA.** **a** Linear response of the JPA as a function of the flux threaded through the SQUID loop, controlled by V_{DC}. **b** Transmission with (red circles) and without JPA pump (black diamonds). **c** Phase-preserving gain in optimized settings. **d** Phase-sensitive gain. **e** Monitoring the phase-preserving gain set at $\phi = \pi/2$ overnight evidences a 8°phase stability. Fast oscillations are due to the lab air conditioner system. **f** Finite dynamic range of the JPA.

in the JPA flux line changes Φ and thus ω_{JPA}, as seen in Fig. 5.6a, which allows tuning the JPA to the desired frequency ω_0.

We set $\omega_0/2\pi \approx 7.3$ GHz. Turning on the JPA pump at $\omega_p \approx 2\omega_0$ with power P_{p}, the previously flat reflexion coefficient now shows some amplification (see Fig. 5.6b). Taking the ratio of the transmissions with the pump on and off yields a Lorentzian gain curve, with a measured gain of 17 dB for these operating conditions. Fine tuning of the parameters $(\omega_p, P_{\mathrm{p}}, \Phi)$ allows to increase the device gain up to 26 dB within a bandwidth of 1.7 MHz (see Fig. 5.6c).

Phase-sensitive amplification is measured by sending a continuous wave signal at ω_0 and setting $\omega_p = 2\omega_0$. Using the spectrum analyser, we record the output signal power with the JPA on and off, with the gain given as $G = P_{\mathrm{out}}/P_{\mathrm{out(JPAoff)}}$. Fig. 5.6d shows the dependence of G on the phase difference between the pump and signal tone, behaving as expected from Eq. 2.78 with deamplification for one quadrature and amplification by an extra 6 dB compared to the phase-preserving amplification for the other quadrature.

The phase-stability of the setup and of the JPA is probed by monitoring overnight the gain in degenerate mode. The pump phase is chosen so that the phase-preserving gain lies around $G \approx 0$, so that the gain is maximally sensitive to phase changes (see green arrow in Fig. 5.6d). Fig. 5.6e shows overall phase drifts of 8°, clearly due to temperature variations of the room-temperature cables and setup since 15 min oscillations synchronous to the air conditioner system can be seen. In the experiments, the gain is set to its maximal value, so that G is only quadratically sensitive to phase shifts; 8°drifts are then acceptable for our measurements.

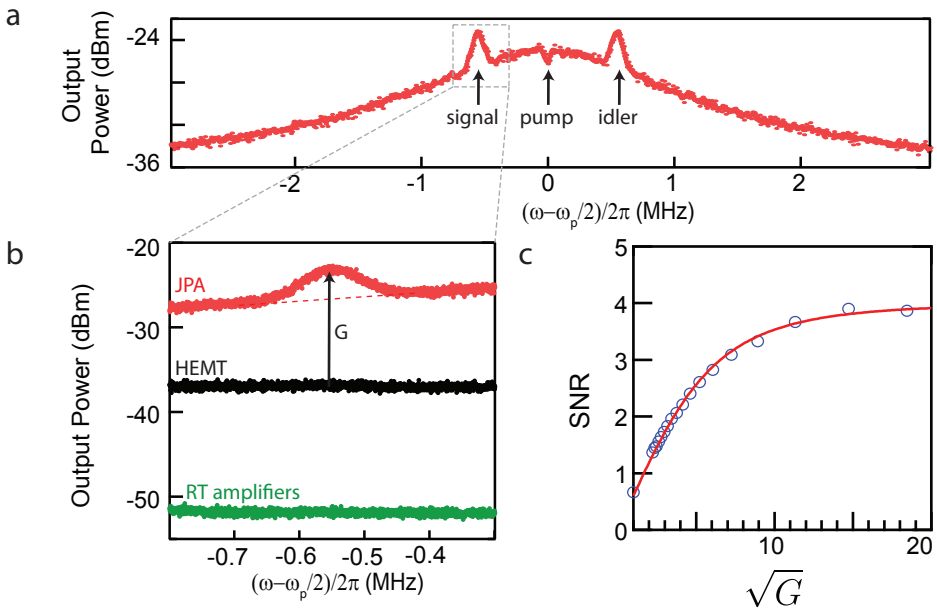

FIGURE 5.7: **SNR enhancement** brought by the JPA as measured by a spectrum analyser. **a** Output power spectrum with acquisition bandwidth 100 kHz for a coherent signal sent at ω while the JPA is pumped at $\omega_p \approx 2\omega$, evidencing signal and idler as well as the noise added by the JPA. **b** Zoom on the signal showing the rise of the noise level compared to amplification with the HEMT and compared to amplification with the room-temperature amplifiers. It evidences a reduction of the noise referred to the input of the amplification chain when turning on the JPA. **b** SNR as a function of the JPA gain.

Dynamic range

To measure the JPA dynamic range, we measure the gain as a function of the power of the incident signal in phase-preserving mode using the homodyne detection setup. Fig. 5.6f shows that the JPA provides a constant gain only for low input powers, with the 1 dB compression point lying at -132 dBm. Note that higher compression points have been obtained with different JPA designs and parameter choices [60, 52, 158]

Signal-to-noise ratio improvement

To characterize the signal-to-noise improvement brought by the JPA over the follow-up amplifiers, we perform measurements of the total output noise power in various configurations using a spectrum analyzer. With both JPA and HEMT switched off, we measure -52 dBm. Switching the HEMT on yields -43 dBm, indicating that the output noise is dominated by the HEMT noise and not by the room-temperature amplifiers. Then, switching the JPA on still yields a 13 dB increase in the noise, which confirms that the total output noise contribution is at 95% from the JPA, in agreement with our expectations based on Eq. 5.12.

A more precise characterization of the SNR enhancement is done in the following way. A continuous microwave signal at frequency ω_0 is sent to the JPA. Fig. 5.7a shows the corresponding output power spectrum (red curve) with both signal and idler mode visible. The JPA gain is given once again as $G = P_{\text{out}}/P_{\text{out(JPAoff)}}$ and is measured separately with a measurement bandwidth taken as small as possible to remove any contribution of the noise (in contrast to the data shown in Fig. 5.7a). The same experiment is then repeated without any input signal so as to obtain P_{n}, the noise power in

the desired measurement bandwidth, chosen here to be 100 kHz. The amplitude signal-to-noise ratio is then evaluated by $\mathrm{SNR} = \sqrt{\mathrm{P_{out}}/\mathrm{P_n}}$ and is shown in Fig. 5.7c.

The SNR can be related to the JPA gain in the following way. Consider the noise referred at the output of the JPA: when the JPA is off, the noise arises from the HEMT, the room-temperature amplifiers (see Eq. 5.12) and from the signal noise. We denote this contribution as n_{bg}. For a gain G, the JPA adds noise $(G-1)n$ where $n = n_{\mathrm{eq}} + n_{\mathrm{amp}}$. As the signal is amplified by $\sqrt{G}$, the SNR expressed at the output of the JPA dependent on G according to:

$$\mathrm{SNR} \propto \sqrt{\frac{\mathrm{G}}{(\mathrm{G}-1)n + n_{\mathrm{bg}}}} \tag{5.13}$$

Fig. 5.7c shows that the measured SNR follow this expected dependence. The fit does not allow us to determine independently n and n_{bg}; however we obtain their ratio, $n_{\mathrm{bg}}/n = 36$, as observed in similar setups [159].

Absolute calibration of the mean photon number in the ESR resonator was performed in a later run (see Appendix A) and yields $n_{\mathrm{th}} = 0.05 \pm 0.05$, which confirms that the dominant contribution of noise in the setup is of quantum origin.

5.3 Design of a superconducting ESR resonator with high quality factor and small mode volume

In the following, we describe the design of the high quality factor small-mode volume resonator needed to obtain a high sensitivity before describing its experimental implementation and characterization.

5.3.1 Design choices

Small mode volume

As explained in ch. 3, the spin-resonator coupling is given by:

$$g = \gamma_e |\langle \mathfrak{e}| \boldsymbol{\delta B}(\boldsymbol{r}).\hat{\boldsymbol{S}} |\mathfrak{g}\rangle|, \tag{5.14}$$

where $|\mathfrak{e}\rangle$ and $|\mathfrak{g}\rangle$ are the energy levels spanning the ESR transition to be probed and $\boldsymbol{\delta B}$ is generated by the current fluctuations δI in the resonator inductance. We have $\delta I = \omega_0 \sqrt{\hbar/(2Z_0)}$, Z_0 being the resonator impedance. Maximizing g thus requires minimizing Z_0 and bringing the spins as close as possible to the inductance.

We thus choose to implant bismuth atoms very close to the surface (more precisely between 20 and 150 nm). One could also adopt a flip-chip configuration, where the sample containing the spins is stacked on top of the microwave resonator patterned on a different chip, but generally an incompressible gap of several hundreds of nanometers subsists at the interface.

To minimize the resonator impedance, a **lumped-element geometry** is particularly suited since it can combine small inductors patterned in parallel with large **interdigitated capacitors** (see Fig. 5.8e); simulations indicate that impedances as low as $15\ \Omega$ can be reached. Even larger capacitances could be obtained by using conventional overlap capacitors, but they are in general more lossy than interdigitated capacitances [160].

High-quality factor

In our quest for a high-quality factor resonator, it is indeed important to **minimize the resonator internal losses**, of associated damping rate κ_{int}. The value reached for κ_{int} is also key to determine the choice of the coupling rates κ_2 and κ_1 since it is best to operate in the critical coupling regime. Indeed, using Eq. 5.11, the setup sensitivity N_{min} can be shown to be maximum when $\kappa_2 = \kappa_{\text{int}}$ (assuming $\kappa_1 \ll \kappa_2$).

Owing to intensive research in the superconducting qubits community, the origin of the internal losses of lumped-element interdigitated resonators are relatively well known. Resonators with internal quality factors in the 10^6 range have been obtained [161]. Four different physical phenomena leading to resonator internal losses have been identified : the motion of magnetic vortices trapped in the superconducting thin films [162], the presence of out-of-equilibrium quasi-particles (i.e., non-superconducting charge carriers) [163], dielectric losses in general [164], originating mostly from dirty interfaces and in particular from the substrate-metal interface which contributes the strongest [165], and finally radiation from the resonator [166]. The latter can be suppressed by enclosing the sample in a leak-tight metallic box, as shown in Fig. 5.8a [167]. The box is designed so that all its modes have frequencies well above the planar LC resonator frequency. The best quality factors are obtained with superconducting boxes since losses through the box walls surface resistivity are then minimized [168]. However in the context of ESR measurements which necessitate to apply magnetic fields, we chose to have the box made of oxygen-free-high-conductivity copper.

The coupling of the planar resonator to the measurement lines is obtained via **capacitive coupling to antennas** fed through holes drilled in the box (see Fig. 5.8a). The resulting coupling rates κ_1 and κ_2 are the sum of two contributions. The first one is a direct capacitive coupling of the resonator electrical dipole to the antenna while the second one is an evanescent coupling mediated via the first TE101 mode of the copper box (see Fig. 5.8c & d). As a result, the rates κ_1 and κ_2 are set by the position of each antenna relatively to the resonator as well as their coupling to the box mode.

To control κ_1 and κ_2, the frequency and the quality factor of the copper box TE101 mode thus has to be carefully designed. The box mode quality factor should be kept low so as to be well below its internal quality factor. The internal quality factor of an OFHC copper box was found to be ≈ 6000; we thus limit ourselves to $Q_{box} \leq 1000$. The larger the detuning between the LC resonator and the box TE101 mode, the weaker the coupling mediated by the box mode is. To obtain quality factors on the order of 10^5 for the LC with $\omega_{LC}/2\pi \sim 7.4$ GHz, we choose the dimensions of the box so that its lowest-frequency mode mode is at $\omega_{\text{TE101}}/2\pi = 8.9$ GHz.

To be able to adjust the coupling rates κ_1 and κ_2 to κ_{int} at each run, we soldered the antennas on SMA throughs which are then screwed in the cavity wall (see Fig. 5.8a). Depending on the insertion of the SMA through in the wall, the antenna's depth can be tuned over several millimeters, allowing to tune κ_1 and κ_2 by $\approx \times 50$.

Finally, the resonator is made in a 50-nm-thick aluminum film. We chose this metal because it is well-established that aluminum resonators can have quality factors reaching at least 10^6[161, 169, 170] and contrary to niobium films in particular, aluminum can be processed by lift-off techniques and removed by wet etchants which are harmless for the underlying silicon substrate. This is particularly important in our case given that the dopant atoms are very close to the surface.

Since Si:Bi spins have a large zero-field splitting, several of the ESR transitions can still be tuned at resonance with a static magnetic field below the 10 mT critical field of bulk aluminum provided that the resonator frequency lies within 200 MHz of ω_{ZFS}. In the future, to study the clock-transitions of bismuth located at larger magnetic field (see ch. 4) or other spin systems, materials sustaining higher fields while maintaining high-quality factors could be used.

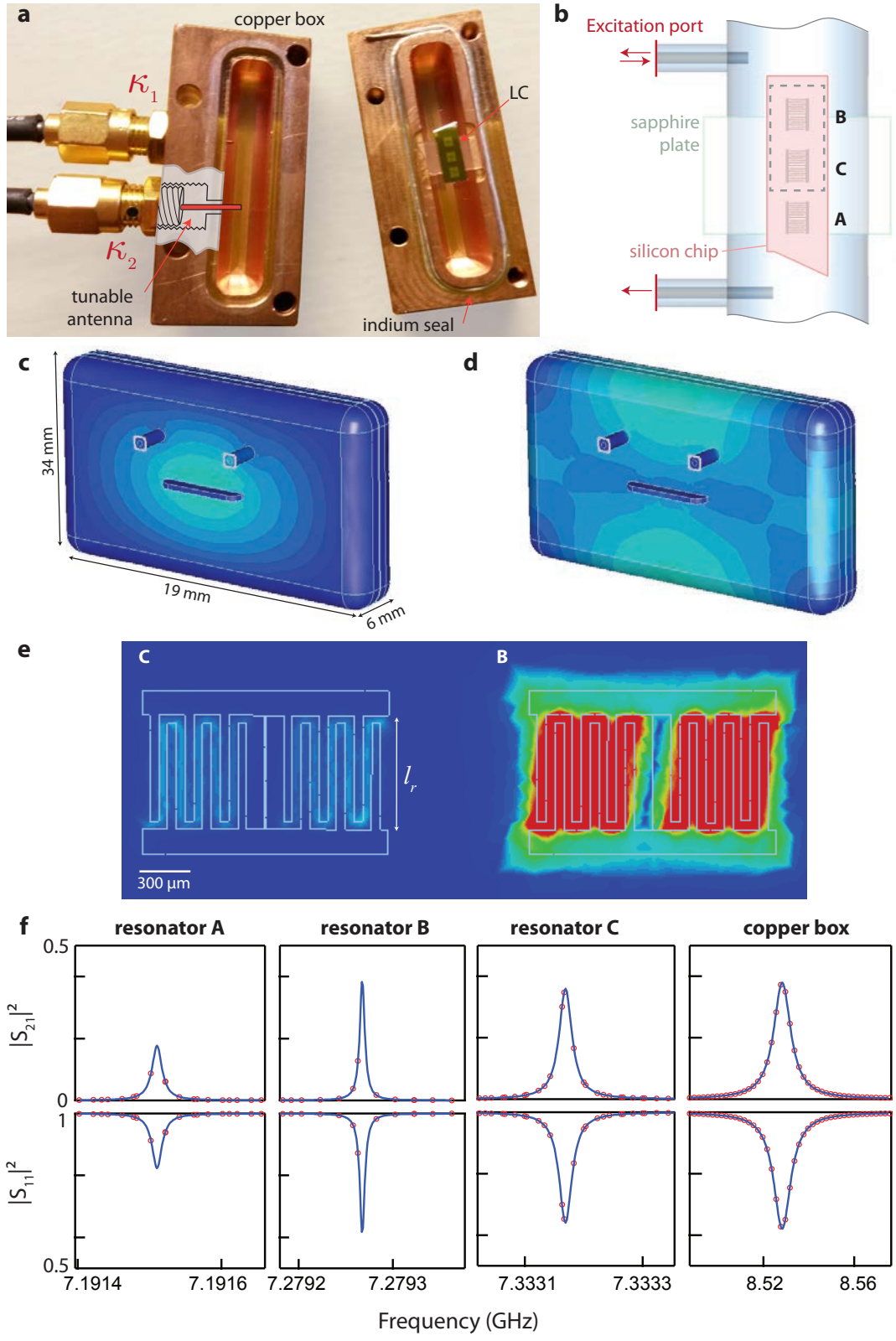

FIGURE 5.8: **Microwave simulations. a** Copper box with the LC oscillators coupled via tunable antennas mounted on SMA throughs. **b** CST model. **c** TE101 electrical mode. **d** TE101 magnetic mode. **e** Resonator B electrical mode. The crosstalk with resonator C is extremely limited. **f** Frequency domain response simulated with CST yielding ω_0, κ_1 and κ_2.

	Resonator A		Resonator B		Resonator C		Copper box	
l_r	730	µm	720	µm	710	µm		
$\omega_0/2\pi$	7.1915	GHz	7.2753	GHz	7.3332	GHz	8.52	GHz
$\kappa_1/2\pi$	0.77	kHz	0.7	kHz	2.6	kHz	0.96	MHz
$\kappa_2/2\pi$	16	kHz	5.8	kHz	24	kHz	8.1	MHz

TABLE 5.2: **Simulated resonators characteristics.**

5.3.2 Electromagnetic simulations

The resonator geometry and coupling to the measurement lines are designed using electromagnetic simulations realized with CST microwave studio. A modeling tool allows to reproduce the geometry of the copper sample holder (assuming perfect conductivity for the walls), the antennas, the substrate silicon chip (with relative dielectric constant $\varepsilon_r = 11.5$) as well as the superconducting resonator (modeled by a perfect electrical conductor of zero-thickness), as shown in Fig. 5.8b. As the resonator is made of 50-nm-thick aluminum and has lateral dimensions > 1 µm, kinetic inductance contribution is negligible [171] and is not included in the simulation. The sample holder and the resonator eigenmode frequencies can be determined in the software by exciting ports placed on the antennas and analyzing the frequency response, given as a S-parameters matrix.

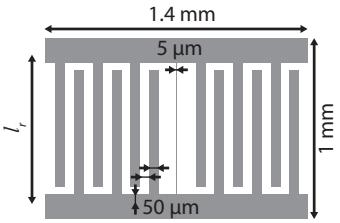

FIGURE 5.9: **Resonator layout**

The final geometry of the LC resonator is a 5-µm-wide inductive wire of length l_r in parallel with an interdigitated capacitance of 12 50-µm-wide fingers spaced by 50 µm (see Fig. 5.9). The width and spacing of the fingers is chosen to minimize the dielectric losses [172]. The whole structure fits in a rectangle of 1 mm by 1.4 mm. The bismuth implanted silicon sample at our disposal is 1-cm-long and 3-mm-wide, we can thus multiplex our measurements by placing 3 resonators of slightly different frequencies, obtained by choosing three different values of l_r: 710, 720 and 730 µm. The resonators are separated by 1 mm and visualizing the simulated microwave electrical field (see Fig. 5.8e) shows that there is very little cross-talk between them.

The simulated S-parameters are shown in Fig. 5.8f. Four resonances are visible, with the highest-frequency one being the box TE101 mode (see Fig. 5.8c & d) and the lowest three the planar resonators (see Fig. 5.8e). Fitting the simulated S-parameters for each resonator to the input-output formulas (see Eq. 2.56), their frequency and coupling rates $\kappa_1$and κ_2 are extracted and given in Table 5.2 , with all resonators reaching quality factors above 10^5.

5.3.3 Coupling to bismuth donor spins

To estimate the coupling constant of the resonator to spins, it is necessary to know the magnitude of the magnetic field vacuum fluctuations. We proceed in three steps, explained below in details. First we determine the resonator current fluctuations δI from CST simulations; then, we compute the geometrical distribution of this current across the resonator inductance; finally, using the COMSOL magnetic field solver, we compute the magnetic field. For this last step a magnetostatic solver is sufficient since the length scales that come into play are very much smaller than the wavelength.

To estimate δI, we use CST to determine the magnitude of the AC current $I_{\text{sim}} \cos(\omega_0 t)$ that flows through the resonator inductance for the simulated power $P_{\text{in}} = 0.5$ W. We find that $I_{\text{sim}} = 60$ A. Based on our knowledge of all the resonator κ_i (obtained from CST as explained above), we can

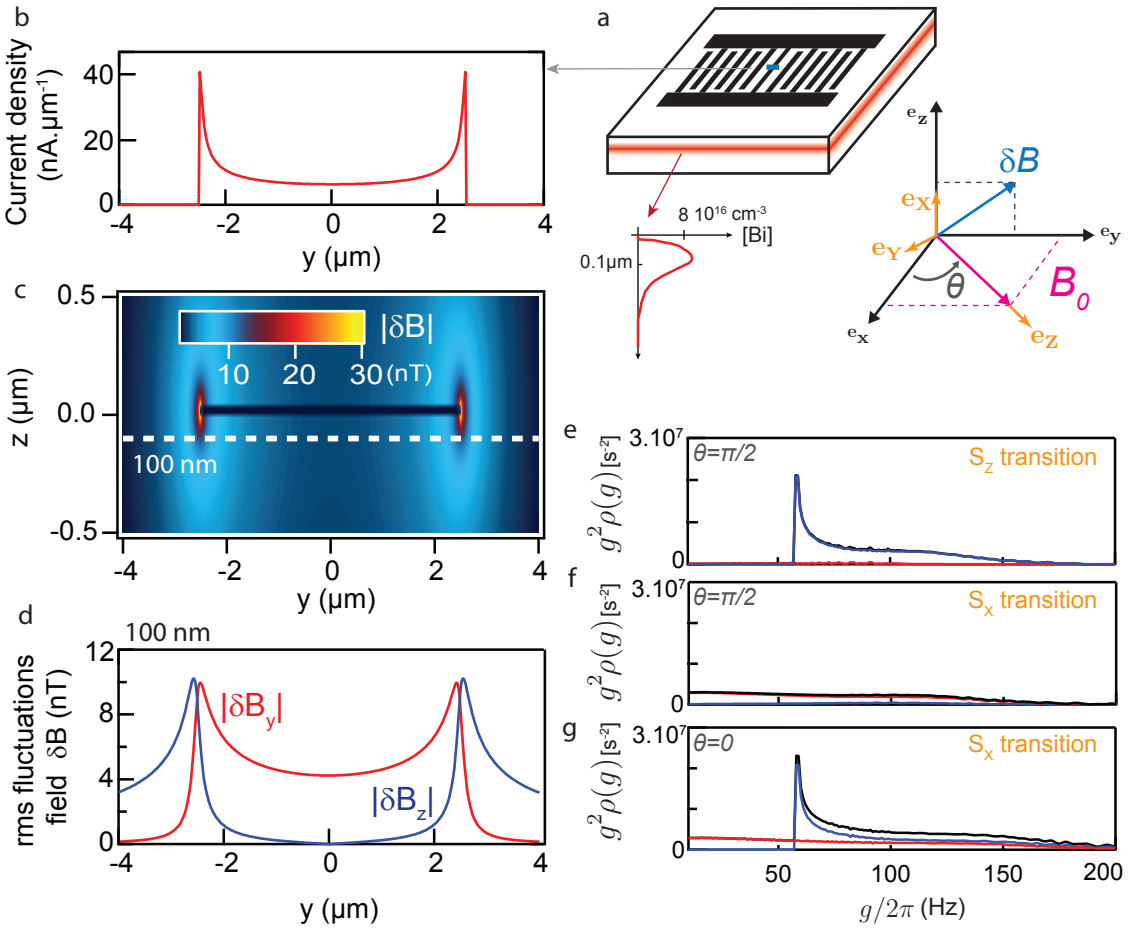

FIGURE 5.10: **Coupling between bismuth donor spin and LC resonator**. **a** LC resonator coupled to Bi donor spins with implanted profile of [137]; the directions correspond to the text. The spins are tuned to resonance via an in-plane static magnetic field $\boldsymbol{B}_0$ forming an angle θ with $\boldsymbol{e}_x$ and excited via an AC magnetic field $\boldsymbol{\delta B}$ orthogonal to the wire. **b** Spatial distribution of the current rms vacuum fluctuations flowing through the resonator, corresponding to an impedance of 44 Ω. **c** rms vacuum fluctuations of the magnetic field generated by the current density of panel **a**. **d** y (red) and z (blue) components for the vacuum fluctuations of the magnetic field at $z = -100$ nm. **e-g** Coupling strength distribution $\rho(g)$, plotted as $g^2\rho(g)$, extracted from magnetic field simulations and evaluated with $\gamma_e = 28$ GHz/T and $|\langle i|\hat{S}_k|j\rangle| = 0.5$ for a S_X transition with $\theta = 0$ (panel **g**) or $\pi/2$ (panel **f**) as well as for a S_Z transition with $\theta = \pi/2$ (panel **e**). Solid black line is the contribution from all spins whereas red (blue) line is the contribution from spins located under (outside) the wire with $|y| < 2.5$ μm ($|y| \geqslant 2.5$ μm).

derive the mean photon number corresponding to P_{in} using Eq. 2.55. This allows us to extract δI as:

$$\delta I = I_{\text{sim}}/2\sqrt{\bar{n}} = 49 \text{ nA} \tag{5.15}$$

corresponding to a resonator impedance $Z_0 = 44\ \Omega$.

The current distribution over the cross-section of a superconducting wire (see Fig. 5.10b) is given by the following formulas [173]:

$$\delta J(y) = \begin{cases} \delta J(0)\ [1-(2y/w_r)^2]^{-1/2} & \text{for } |y| \leqslant |w_r/2 - \lambda^2/(2b)| \\ \delta J(w_r/2)\exp[-(w_r/2-|y|)b/\lambda^2] & \text{for } |w_r/2-\lambda^2/(2b)| < |y| < w_r/2 \\ (1.165/\lambda)\ \sqrt{w_r b}\ \delta J(0) & \text{for } y = w_r/2 \end{cases} \tag{5.16}$$

In these expressions y is the wire transversal coordinate indicated in Fig. 5.10a, $w_r = 5$ µm is the wire width, $b = 50$ nm is its thickness and $\lambda = 90$ nm is the penetration depth of the aluminum film [174]. The normalization constant $\delta J(0)$ is determined by the condition $\int_{-w_r/2}^{w_r/2} \delta J(x)dx = \delta I$.

We finally use $\delta J(y)$ to compute $\boldsymbol{\delta B}_0(r)$, using the COMSOL magnetostatic solver. The result is shown in Fig. 5.10c. The field $\boldsymbol{\delta B}(\boldsymbol{r})$ is located in the plane perpendicular to the resonator wire axis ($\delta B_x(\boldsymbol{r}) = 0$), and importantly Fig. 5.10d shows that it is essentially along $\boldsymbol{y}$ for spins under the wire, and essentially along $\mathbf{z}$ for spins outside the wire.

In our experiment, the static magnetic field $\boldsymbol{B}_0$ is applied parallel to the surface (see Fig. 5.10a) along an axis $\boldsymbol{e}_Z$ that can be decomposed along the orientations defined in Fig. 5.10a as:

$$\boldsymbol{B}_0 = B_0 \boldsymbol{e}_Z = B_0\cos(\theta)\boldsymbol{e}_x + B_0\sin(\theta)\boldsymbol{e}_y \tag{5.17}$$

The field $\boldsymbol{\delta B}(\boldsymbol{r})$ can be decomposed in either basis:

$$\boldsymbol{\delta B}(\boldsymbol{r}) = \begin{pmatrix} 0 \\ \delta B_y \\ \delta B_z \end{pmatrix}_{(\boldsymbol{e}_x,\boldsymbol{e}_y,\boldsymbol{e}_z)} = \begin{pmatrix} \delta B_z \\ -\cos(\theta)\delta B_y \\ \sin(\theta)\delta B_y \end{pmatrix}_{(\boldsymbol{e}_X,\boldsymbol{e}_Y,\boldsymbol{e}_Z)} \tag{5.18}$$

For Eq. 5.14 applied to bismuth donors, the coupling constant for a spin located at $\boldsymbol{r} = (x, y, z)$ is thus:

$$g = \gamma_e \left| \begin{pmatrix} \delta B_z \\ -\cos(\theta)\delta B_y \\ \sin(\theta)\delta B_y \end{pmatrix} . \begin{pmatrix} \langle i|\hat{S}_X|j\rangle \\ \langle i|\hat{S}_Y|j\rangle \\ \langle i|\hat{S}_Z|j\rangle \end{pmatrix} \right| \tag{5.19}$$

where $|i\rangle$ and $|j\rangle$ are two of the twenty energy levels of bismuth donors. A bismuth donor in silicon possesses both $\hat{S}_x$ transitions probed by an AC magnetic field transverse to $\boldsymbol{B}_0$ and $\hat{S}_z$ transitions probed by an AC magnetic field parallel to $\boldsymbol{B}_0$ (see ch. 4). Eq. 5.19 can be simplified in both cases:

- For S_x transitions, as $|\langle i|\hat{S}_X|j\rangle| = |\langle i|\hat{S}_Y|j\rangle|$ and $|\langle i|\hat{S}_Z|j\rangle| = 0$, we have:

$$g \underset{S_X}{=} \gamma_e |\langle i|\hat{S}_X|j\rangle| \sqrt{\delta B_z^2 + (\cos\theta)^2 \delta B_y^2} \tag{5.20}$$

- For S_z transitions, as $|\langle i|\hat{S}_X|j\rangle| = |\langle i|\hat{S}_Y|j\rangle| = 0$, we have:

$$g \underset{S_Z}{=} \gamma_e |\langle i|\hat{S}_Z|j\rangle| \sin\theta\ \delta|B_y| \tag{5.21}$$

A spin located outside the wire ($|y| \geqslant w_r/2$) is probed by a microwave field essentially along $\boldsymbol{z}$ ($\delta B_y \approx 0$) and thus its coupling to the resonator is only possible for a S_X transition. In addition, the coupling does not depend on θ since $\boldsymbol{B}_0$ is in any case orthogonal to $\boldsymbol{\delta B}$.

In contrast, a spin located below the wire ($|y| \leqslant w_r/2$) is probed by a microwave field essentially along $\boldsymbol{y}$ ($\delta B_z \approx 0$). As a result, the coupling to a S_X transition is maximum when $\theta = 0$ and fully suppressed when $\theta = \pi/2$, whereas the coupling to a S_Z transition is suppressed when $\theta = 0$ but maximum for $\theta = \pi/2$.

The coupling distribution for both transition types is computed using the bismuth implantation profile and the $\boldsymbol{\delta B}(\boldsymbol{r})$ map and shown in Fig. 5.10e for a matrix element taken arbitrarily at 0.5 for easy comparison. We show in red the contribution from spins located under the wire ($|y| < w_r/2$) and in blue the contribution from spins located outside the wire.

5.3.4 Experimental implementation

Fabrication

To obtain a high internal quality factor resonator, dielectric losses should be minimized. Lossy dielectrics are found most notably at the metal-substrate interface; our fabrication process thus tries to keep it as clean as possible. In particular it has been demonstrated that oxygen plasma cleaning before metal deposition is essential to reduce the losses [175]:

- **Substrate cleaning**: 2 hours in a Piranha acid mixture at 80°C, followed by 5′ in acetone before rinsing with isopropanol and blowing dry.
- **Resist coating**: bi-layer MAA(200 nm) - PMMA(100 nm) with a 7-nm-thick aluminum layer deposited by metal evaporation for charge evacuation during the E-beam lithography.
- **E-beam lithography**: the entire pattern is drawn with a 25keV electron beam in 15′.
- **Resist development**: 30″ in MF-319 to remove the Al layer, before developing the resist with a 40″ dip in MIBK (dilution 2:1). Rinse in water and blow dry.
- **Mask cleaning**: 1′ in an oxygen plasma asher. The plasma parameters were chosen so that it corresponds to the etching of 6-nm of the PMMA layer.
- **Metal deposition:** 50 nm of Al are deposited via a Plassys evaporator at a rate of 1 nm/s.
- **Lift-off**: 5′ in acetone before rinsing in isopropanol and blowing dry.

Other solutions to reduce the contribution of TLS is to deeply etch the substrate using the metallic resonator as a mask [176]. Doing so removes the TLS lying underneath the edges of the metal where the electrical field is the strongest and thus where the TLS contribute the most. However such a solution would damage our substrate permanently.

Sample mounting and microwave setup

After fabrication, the chip is inserted in the copper box by gluing it to a sapphire plate with small amounts of vacuum grease. The sapphire plate is then glued in the copper box sample groove, also using vacuum grease (see Fig. 5.8a). The copper box is closed using an indium seal to ensure good electrical contact between both parts and reduce losses. Finally, the copper box is mounted in a couple of orthogonal Helmholtz coils that provide a 2D static magnetic field $\boldsymbol{B}_0$ (see Fig. 5.11) up to $10\ \mathrm{mT}$ each.

The final step to ensure a high-quality factor is to protect the superconducting thin films from losses occurring through out-of equilibrium quasi-particles and vortices. Low-pass filters containing infra-red absorptive material are put on each line to minimize the quasi-particles (see Fig. 5.4b). The Helmholtz coils are inserted in a 1-mm-thick cryoperm magnetic shielding to minimize stray

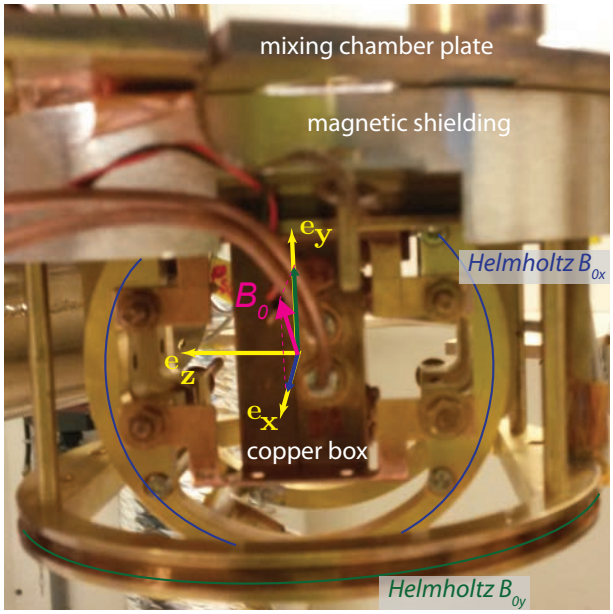

FIGURE 5.11: **LC within its sample holder mounted inside a couple of Helmholtz coils**

magnetic field which may introduce vortices in the film during cool down of the film through its critical temperature.(see Fig. 5.11).

Microwave characterization

The characterization of the LC resonators is carried out in two steps. In the first step, we use two extra microwave lines (see Fig. 5.4b) to measure all S-parameters and determine without ambiguity κ_1 and κ_2. The fit of the measured S_{21}, S_{11} and S_{22} to the input and output formulas given in Eqs. 2.57 & 2.56 is shown in Fig. 5.12 for resonator B and the extracted values for κ_1 and κ_2 are given in Table 5.3. The values are found to be approximately a factor 2 higher than estimated by the CST simulations (see Table 5.2), meaning that the antennas are inserted a little deeper in the copper box than in the simulation. Similar results are obtained for resonators A and C.

In what follows, we use the simplified setup shown in black in Fig. 5.4b, without the extra microwave lines used for measuring the complete resonator S-parameters. Using only the transmission from port 1 to port 2, we then can only determine the resonator frequency ω_0 and total damping rate κ; using the previously determined values of κ_1 and κ_2 yields κ_{int}. The measured values for ω_0, κ and κ_{int} determined in this setup and used in the following chapters are given in Table 5.3 for the three resonators. All resonators are in the critical coupling regime, with $Q_{\text{int}} \approx 2Q \approx 5 \times 10^5$.

Contrary to most usual ESR spectrometers, our ESR resonator has in addition a response in magnetic field. When ramping the parallel static magnetic field applied on the resonator by one of the Helmholtz coils (see Fig. 5.13), the resonator quality factor remains flat whereas the frequency of the resonator decreases quadratically by nearly 1 MHz due to the increase of the thin-film kinetic inductance, with in addition sudden jumps that we attribute to magnetic vortices entering the film. We measured the critical field of the Al resonators to be ≈ 14 mT for a parallel magnetic field. The dependence of the resonator in B_0 thus requires us to systematically fit the resonator transmission at each B_0 to determinate its frequency.

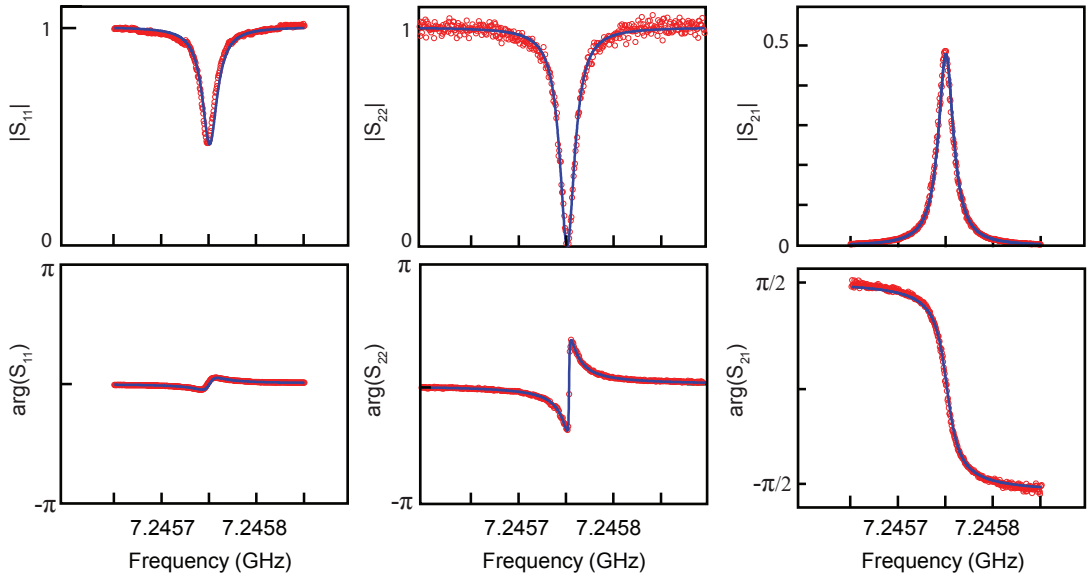

FIGURE 5.12: **Characterization of ω_0, κ_1 and κ_2** for resonator B.by measuring S_{21}, S_{11} and S_{22} with the VNA.

	Resonator A	Resonator B	Resonator C
$\omega_0/2\pi$	7.14 GHz	7.246 GHz	7.305 GHz
$\kappa_1/2\pi$	2.1 kHz	2.1 kHz	5.7 kHz
$\kappa_2/2\pi$	31 kHz	9.2 kHz	50 kHz
Q	1.4×10^5	3.2×10^5	1.1×10^5
Q_{int}	4.0×10^5	6.4×10^5	6.8×10^5

TABLE 5.3: **Measured ESR resonator characteristics** with coupling values agreeing within a factor 2 to the simulated values. The copper box mode cannot be measured since at 20 mK its frequency lies outside the circulator range.

Internal losses

We have investigated experimentally the mechanisms at the origin of Q_{int} in our experiment. If the dielectric losses are dominant due to TLS lying at the metal-substrate interface, the internal quality factor is expected to be significantly lower when measured for powers corresponding to intra-resonator photon number $\bar{n} \sim 1$ than at high-powers when the TLS are saturated. We indeed measure a factor 2 reduction of Q_{int} at low powers (see Fig. 5.14a), indicating that dielectric losses contribute for half of the total internal losses.

Fig. 5.14b shows that Q_{int} can be improved if a non-zero magnetic field is applied while the Al film is undergoing its metal to superconductor transition. This indicates that there is a small residual magnetic field orthogonal to the field which creates vortices in the film; its compensation thus reduces the number of vortices and improves Q_{int} [162].

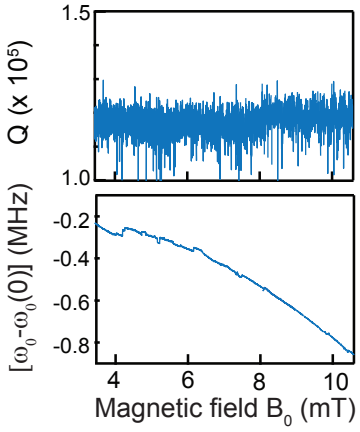

FIGURE 5.13: **Resonator A response to an applied magnetic field parallel to the resonator wire**

To conclude, future improvements of Q_{int} will take place by simultaneously reducing dielectric losses, improving the magnetic shielding and removing any

magnetic material close by the cavity and increasing the infra-red filtering.

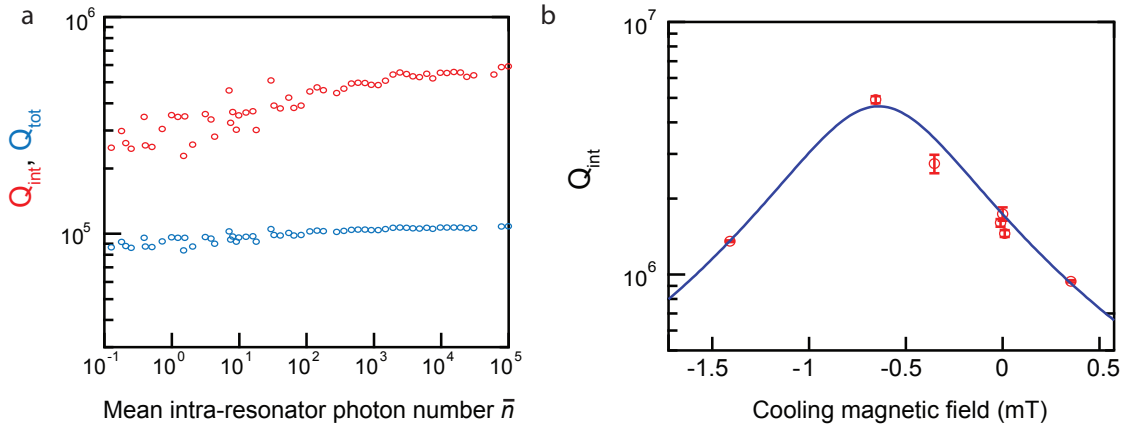

FIGURE 5.14: **Internal quality factor dependence** on **a** the intra-resonator photon number, indicating that dielectric losses contribute for half of the internal losses; **b** Parallel magnetic field applied during the Al transition to superconductor using one of the Helmholtz coils. A possible misalignement of the mechanical parts probably gives rise to a small orthogonal component of unknown amplitude responsible for the compensation of the stray magnetic field. The blue line is a polynomial fit to $\omega_0/Q_{\rm int}$.

Chapter 6

ESR spectroscopy of Bismuth donors in silicon

In this chapter, we characterize the Si:Bi spins using our setup. The sample we are using was already studied by Weis et al.[137] with a conventional ESR spectrometer at 25 K (see 4.6). We first detail the experimental implementation of Hahn-echo pulse sequences in our setup, before presenting results on Si:Bi. Last, we measure the Si:Bi relaxation times.

6.1 Hahn-echo detected ESR

In all that follows, the spin signal is obtained by spin echoes generated via Hahn-echo sequences $\pi/2 - \tau - \pi - \tau$. We briefly outline here the main experimental specificities of our home-made high quality factor low-temperature spectrometer.

6.1.1 Experimental techniques

Pulse generation

The first requirement is to be able to send microwave drive pulses to the spins with a sufficient on/off ratio. The microwave setup of Fig. 5.5 modified to generate microwave pulses is shown in Fig. 6.1. The pulses are shaped by microwave switches with an on/off ratio of 80 dB, in series with the microwave source internal switch, which only allows square-shaped pulses to be sent. The relative phases of the pulses are set by the analog phase modulation of the microwave source. All the control pulses are generated by an arbitrary waveform generator (AWG5014 from Tektronix).

Two pulses of different powers can be generated using two switches in parallel, each in series with a variable attenuator. By proper calibration of the microwave lines in our setup, we can estimate the power incident on the ESR resonator P_{in} with an accuracy of $1\ \mathrm{dB}$. In this setup we can deliver pulses of power P_{in} up to $-50\ \mathrm{dBm}$.

Echo acquisition

The transmitted pulses and the echo signals are demodulated at ω_0 and their I and Q quadratures are detected using the setup shown in Fig. 5.5. To suppress residual DC offsets and drifts on the I and Q channel, every pulse sequence is repeated twice with opposite phases on the excitation pulse $R_{\pm\theta}$. This phase cycling protocol yields two echo signals with opposite phases taken in the same conditions. The DC offset is then removed by taking the difference between the two time-traces acquired on each sequence. The acquisition by the digitizer is also triggered by the AWG.

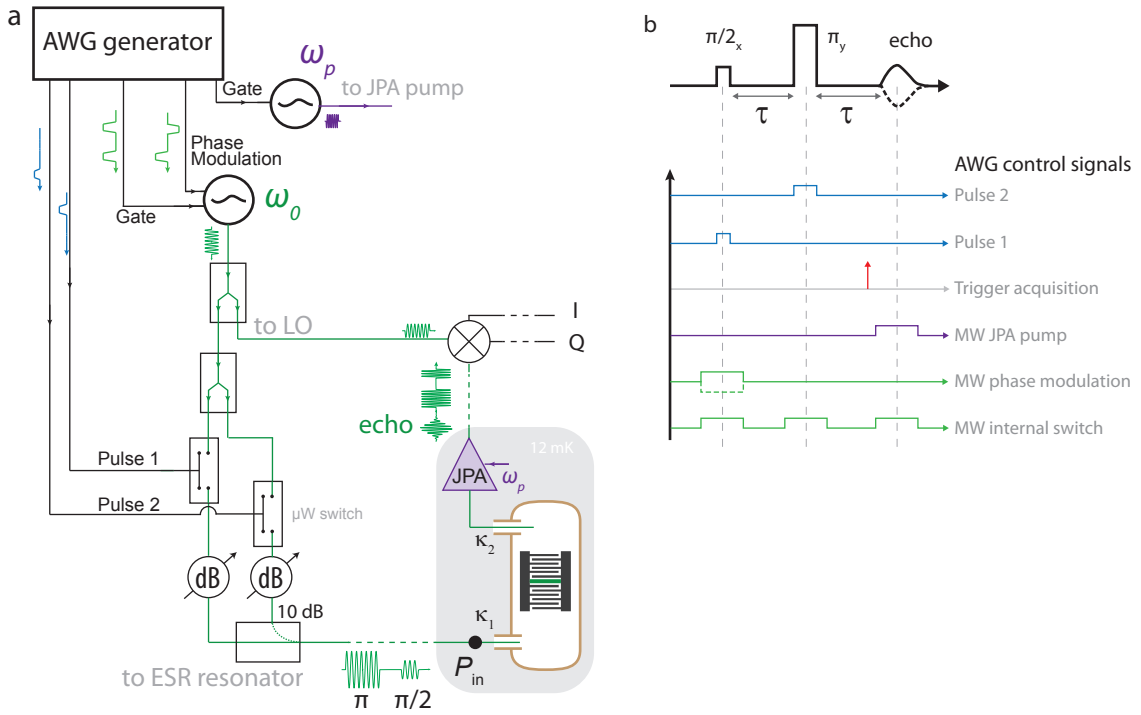

FIGURE 6.1: **Pulsed ESR implementation. a** Two independent microwave pulses can be generated via two microwave switches in parallel, each being in series with a tunable attenuator to control the pulse input power P_{in} referred to port 1 of the resonator. The pulses' phases are set via phase modulation of the microwave source. All signals are controlled via an AWG generator. **b** Control signals for a Hahn-echo sequence. The JPA is switched on only during the echo emission.

We also switch the JPA on only during the echo emission by pulsing the pump signal via the microwave source internal switch. This is done to minimize the cryostat heating due to the pump signal. The JPA is set for most of the data shown in the following chapter in phase-preserving mode with a gain $G \approx 20$ dB. To ensure that the idler mode is properly filtered out, we take $\omega_p/2 - \omega_0 = 500$ kHz and we set the detection bandwidth to be 100 kHz.

6.1.2 Hahn-echo sequence

Before moving on to the ESR spectroscopy, we first examine a single Hahn-echo sequence acquired with resonator B. The transition $|9\rangle \leftrightarrow |10\rangle$ is tuned at resonance by applying a magnetic field $\boldsymbol{B}_0 \approx 5$ mT. A $\pi/2$ pulse of power P_{in} and duration $t_\pi/2 = 2.5$ μs followed $\tau = 300$ μs later by a π pulse of same power P_{in} but of duration $t_\pi = 5$ μs leads to the emission of an echo at time 2τ. The calibration of the power P_{in} for the $\pi/2$ and π pulses is realized by performing Rabi oscillations, as will be explained in the following.

Fig. 6.2 shows the recorded amplitude for such a sequence. The output amplitude shows the two drive pulses, followed after a time 2τ by an echo emitted by the spins. The drive pulse shape, far from being square as the input pulse, appears asymmetric with a long-time exponential decay, due to filtering by the resonator. The echo shape, of duration $T_E \approx 50$ μs, is also not Gaussian, due to the convolution of the spin response with the drive pulses and the resonator filtering. The I and Q quadratures of the echo are shown in the inset of Fig. 6.2, evidencing that the echo lies on a single quadrature. In the following, we quantify the echo signal using either its integrated amplitude A_e

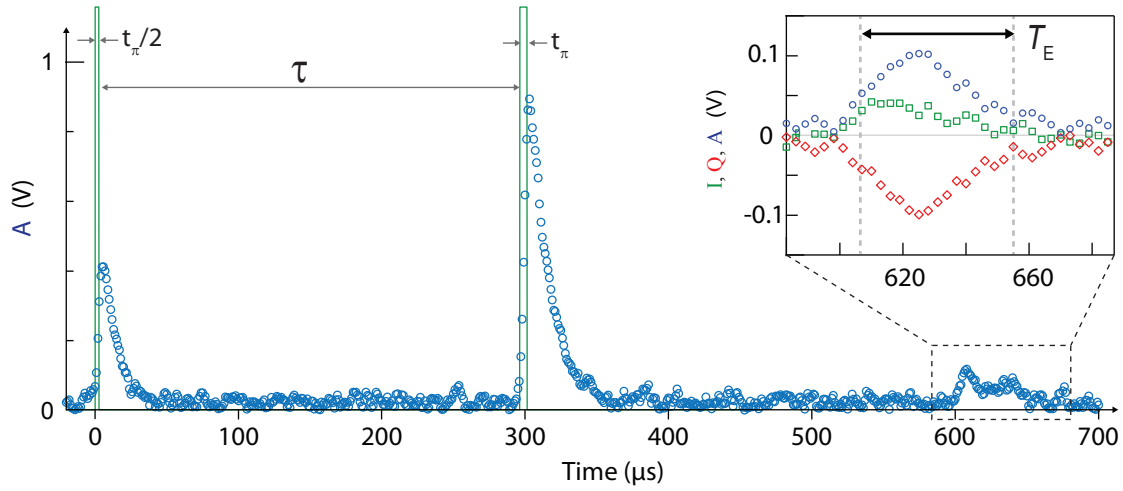

FIGURE 6.2: **Hahn-echo sequence.** Recorded amplitude, showing the $\pi/2$ and π pulses (green lines indicates the microwave switch control pulses) with their long ESR resonator-induced decay. At time 2τ, an echo of duration T_E is detected, with its quadratures I and Q and amplitude shown in inset. (The data in the inset is different from the blue points by a factor 3 in the averaging.). Data taken with resonator B at $B_0 = 5.13$ mT, with JPA off to avoid its saturation by the control pulses.

or its integrated quadrature A_Q defined as:

$$A_e = \frac{1}{T_E}\int_0^{T_E} A(t)\mathrm{d}t \tag{6.1}$$

$$A_Q = \frac{1}{T_E}\int_0^{T_E} \tilde{I}(t)\mathrm{d}t \tag{6.2}$$

where $\tilde{I}(t)$ is either the I(or Q) quadrature if the demodulation local oscillator phase was set so that the echo is emitted solely on I (or Q). It may also be the result of a post-acquisition numerical rotation: $\tilde{I}(t) = I(t)\cos\varphi + Q(t)\sin\varphi$, where φ is chosen so that all signal lies on $\tilde{I}(t)$.

6.1.3 Rabi oscillations

To calibrate drive pulses, we measure Hahn-echo detected Rabi oscillations. For that, we apply a Hahn-echo sequence in which the tipping angle θ_p of the refocusing pulse is varied, either by sweeping t_p or P_{in} (see Fig. 6.3a). This results in the appearance of oscillations in the echo integrated signal, as shown in Fig. 6.3b-d.

Indeed, consider the same spin ensemble as in 5.1.2, divided in spin subsets whose frequency is distributed according to a distribution $\rho(\Delta)$. An ideal $\pi/2$ applied around the x-axis at time $t = -2\tau$ creates a transversal magnetization state aligned on the y-axis (see Eq. 5.3). The evolution of each spin subset (j) of detuning Δ_j at times $-2\tau \leqslant t < -\tau$ is:

$$\begin{cases} \langle \hat{\mathcal{S}}_x^{(j)}(t)\rangle &= p\sin(\Delta_j(t+2\tau)) \\ \langle \hat{\mathcal{S}}_y^{(j)}(t)\rangle &= p\cos(\Delta_j(t+2\tau)) \\ \langle \hat{\mathcal{S}}_z^{(j)}(t)\rangle &= 0 \end{cases} \tag{6.3}$$

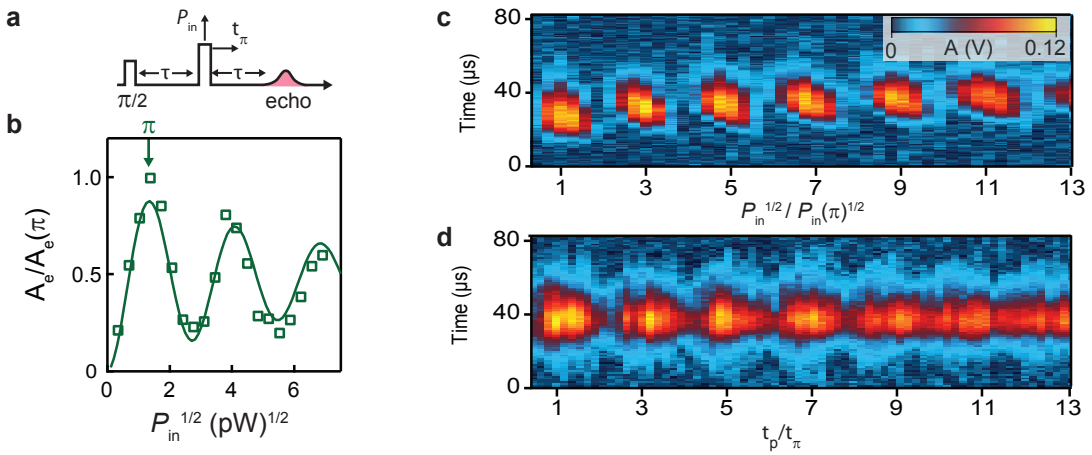

FIGURE 6.3: **Rabi oscillations. a** Rabi oscillations can be performed by varying either the amplitude or the duration of the refocusing pulse. **b** They lead to the appearance of oscillations in the integrated echo amplitude A_e (red shade in **a**) whose well-defined frequency yields g (see text). Data was acquired with $t_{\pi/2} = 2.5$ µs and $t_p = 5$ µs. **c** Rabi oscillations performed by sweeping $P_{\rm in}$ leading to long-subsisting Rabi oscillations whereas Rabi oscillations performed by sweeping t_p (**d**) vanishes due to bandwidth mismatches. All data were acquired with resonator B at $B_0 = 5.13$ mT and $\theta = 0$.

Applying a pulse of tipping angle θ_p around the y-axis at time $t = -\tau$ leads to the following evolution at times $t \geqslant -\tau$ for each spin subset:

$$\begin{cases} \langle \hat{\mathcal{S}}_x^{(j)}(t) \rangle &= p \sin(\Delta_j (t + 2\tau)) \cos\theta_p \\ \langle \hat{\mathcal{S}}_y^{(j)}(t) \rangle &= p \cos(\Delta_j (t + 2\tau)) \\ \langle \hat{\mathcal{S}}_z^{(j)}(t) \rangle &= p \sin(\Delta_j (t + 2\tau)) \sin\theta_p \end{cases} \tag{6.4}$$

Assuming that the tipping angle is identical for all spin subsets, one can show that the transverse magnetization at time $t = 0$ is:

$$\begin{cases} \langle \hat{\mathcal{S}}_x(0) \rangle &= \frac{p}{2}(1 + \cos\theta_p) \sum_j \sin(2\Delta_j \tau) \\ \langle \hat{\mathcal{S}}_y(0) \rangle &= \frac{p}{2}(1 - \cos\theta_p) + \frac{p}{2}(1 + \cos\theta_p) \sum_j \cos(2\Delta_j \tau) \end{cases} \tag{6.5}$$

If $2\tau \gg T_2^*$, the sums $\sum_j \sin(2\Delta_j \tau)$ and $\sum_j \cos(2\Delta_j \tau)$ average to zero and as a result the spin echo signal is proportional only to:

$$A_e \propto \frac{p}{2}(1 - \cos\theta_p) \tag{6.6}$$

which describes the oscillations pattern that can be seen directly in the integrated echo signal (see Fig. 6.3a), allowing to determine the set of parameters $P_{\rm in}$ and t_p corresponding to a π pulse.

Link between θ_p and g

The precise relation between the tipping angle θ_p, the incident power $P_{\rm in}$ and the spin-resonator coupling constant g can be worked out by considering the action of the intra-resonator field on the spins. For a coherent square pulse of duration t_p applied at time $t = 0$ at resonance on port 1 of the ESR resonator, the intra-resonator field evolution is given using Eq. 2.52 by:

$$\langle \hat{a}(t) \rangle = \begin{cases} 0 & \text{for} \quad t < 0 \\ \sqrt{\bar{n}}(1 - e^{-\kappa t/2}) & \text{for} \quad 0 \leqslant t < t_p \\ \sqrt{\bar{n}}(1 - e^{-\kappa t_p/2}) e^{-\kappa(t - t_p)/2} & \text{for} \quad t \geqslant t_p \end{cases} \tag{6.7}$$

(see Fig. 6.2 & 6.4), where $\bar{n}$ is the steady-state intra-resonator photon number linked to P_{in} by $\bar{n} = 4\kappa_1 P_{\text{in}}/(\hbar\omega_0\kappa^2)$ (see Eq. 2.53). The integrated field amplitude is:

$$\int_t \langle \hat{a}(t)\rangle dt = \sqrt{\bar{n}} t_p \tag{6.8}$$

The resulting action of the excitation microwave field $\hat{\boldsymbol{B}}_1 = \boldsymbol{\delta B}(\hat{a} + \hat{a}^\dagger)$ on the spins is given using Eqs. 3.41-3.44. In the semi-classical limit, for spins at resonance the rotation induced by a coherent drive is given by $\omega_1(t) = 2g\langle \hat{a}(t)\rangle$. As a result, the spins undergo a Rabi oscillation of angle:

$$\theta_p = \int_t \omega_1(t) = 2g\sqrt{\bar{n}} t_p. \tag{6.9}$$

Fig. 6.3a shows very well-defined oscillations taken with resonator B , which show that $\theta_p = \pi$ is obtained for $t_p = 5$ µs with $P_{\text{in}} = 1.9 \pm 0.2$ pW. Using the relation between P_{in} and $\bar{n}$ and the measured damping rates values given in Table 5.3, we can estimate $g/2\pi = 50$ Hz $\pm$ 7 Hz, a value in good agreement with the estimate given in 5.3.3. The precision on g is set by the 1 dB accuracy on P_{in}.

In addition, the fact that well-defined oscillations are observed is a first clear indication that the spins are coupled with a narrow g distribution to the resonator. Otherwise, each spin subset of coupling g_j would experience a different tipping angle $\theta_{p,j}$. The measured Rabi oscillations would then be a sum of oscillations largely spread in frequency and would thus lead to their averaging for large tipping angles.

$$A_e \propto \frac{p}{2}\sum_j (1 - \cos\theta_p^{(j)}) \to \frac{p}{2} \tag{6.10}$$

Bandwidth issues

So far we have considered only spins at resonance. However, we will see below that in our experiment the ESR linewidth is considerably broader than the resonator linewidth. As a result, the pulse, whose bandwidth is eventually limited by the resonator, excites only a fraction of the spins. Indeed, the power response function $\mathcal{R}(\omega)$ of a pulse of length t_p incident on a resonator with bandwidth κ at resonance is expressed as:

$$\mathcal{R}(\omega) = \left[2\frac{\sin(t_p(\omega-\omega_0)/2)}{t_p(\omega-\omega_0)}\right]^2 \times \mathcal{R}_{cav}(\omega) = \left[2\frac{\sin(t_p(\omega-\omega_0)/2)}{t_p(\omega-\omega_0)}\right]^2 \times \frac{1}{1+4\left(\frac{\omega-\omega_0}{\kappa}\right)^2} \tag{6.11}$$

For pulses of length $t_p \gg 2/\kappa$, the excitation linewidth is set by the pulse length $\Delta\omega/2\pi \approx 1.2/t_p$, whereas when $t_p \ll 2/\kappa$ the linewidth is set by κ (see Fig. 6.4a & b). On the latter case, the spins excitation profile would have the same bandwidth were they a linear system. For large tipping angles such an approximation is impossible, since the Rabi frequency varies in $\Omega_R = \sqrt{(\omega-\omega_0)^2 + \Omega_{R,0}^2}$ that makes an angle θ in the x-z plane, with $\tan\theta = (\omega-\omega_0)/\Omega_{R,0}$ (see ch. 3). Therefore, the larger is $\Omega_{R,0}$, the weaker is the tipping angle inaccuracy for spins whose frequency lies within the resonator bandwidth. The exact excitation profiles can be computed using the Bloch equations and are shown in Fig. 6.4c for a π tipping angle and considering different ratios of $t_p\kappa$. Their bandwidths appear similar to the corresponding pulse bandwidth and scale with the Rabi frequency $\Omega_{R,0}$, or equivalently with the power $P_{\text{in}}^{1/2}$.

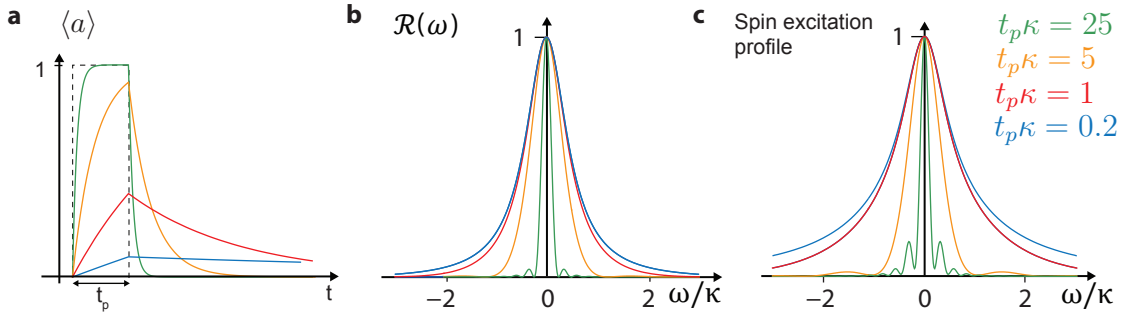

FIGURE 6.4: **Pulse bandwidths. a** Normalized temporal and **b** spectral response for a square pulse of duration t_p incident on a resonator of bandwidth κ. **c** Spin excitation profile for a π pulse applied with different values of the ratio $t_p\kappa$.

In principle, the refocusing pulse bandwidth of the Hahn-echo sequence should exceed the excitation pulse bandwidth for the refocusing to be efficient. Otherwise, the spins whose frequency lies within the excitation pulse bandwidth and therefore contribute to the echo signal are refocused by different tipping angles leading to an averaging in the measured echo signal. This is illustrated in Fig. 6.3b-c, where Rabi oscillations are performed by sweeping either the pulse power P_{in} or the refocusing pulse length t_p. The Rabi oscillations performed by sweeping t_p appear less robust than those performed by sweeping P_{in} with less oscillations being visible, due to their weaker Rabi frequency. In the following we mainly use short pulses sequences with $t_p\kappa \sim 1$ such as shown in Fig. 6.2.

6.2 Strain-broadened transitions

Several ESR transitions can be tuned at resonance with the three resonators patterned on the Si:Bi chip with a magnetic field B_0 below the aluminum bulk critical field. The corresponding B_0 and matrix elements for all three resonators are given in Table. 6.1. We recall that, as explained earlier, an interesting feature of bismuth donor spins is that they possess both S_x transitions that can be probed with a $\boldsymbol{B}_1$ field perpendicular to $\boldsymbol{B}_0$ and S_z transitions that are probed via a $\boldsymbol{B}_1$ field parallel to $\boldsymbol{B}_0$. In the following, we present spectroscopic measurements of these transitions.

		Resonator C		Resonator B		Resonator A	
Transitions	Type	B_0 (mT)	Mat. El.	B_0 (mT)	Mat. El.	B_0 (mT)	Mat. El.
$\|9\rangle \leftrightarrow \|10\rangle$	S_x	2.84	0.47	5.18	0.47	9.24	0.47
$\|9\rangle \leftrightarrow \|11\rangle$	S_z	3.20	0.30	5.85	0.30		
$\|8\rangle \leftrightarrow \|11\rangle^*$	S_x	3.67	0.42	6.71	0.42		
$\|8\rangle \leftrightarrow \|12\rangle$	S_z	4.30	0.41	7.88	0.41		
$\|7\rangle \leftrightarrow \|12\rangle^*$	S_x	5.19	0.37	9.56	0.37		
$\|7\rangle \leftrightarrow \|13\rangle$	S_z	6.56	0.46				
$\|6\rangle \leftrightarrow \|13\rangle^*$	S_x	9.00	0.32				

TABLE 6.1: **Expected ESR transitions** below Al critical field for resonators A, B, C. Transitions $|i\rangle \leftrightarrow |j\rangle$ noted with (*) are doubly-degenerate with the corresponding transition $|i+1\rangle \leftrightarrow |j+1\rangle$ (see ch. 4). In the table and in all the text, we denote them using the transition $|i\rangle \leftrightarrow |j\rangle$. Since the sum of both matrix elements is 0.5, only the matrix element corresponding to $|i\rangle \leftrightarrow |j\rangle$ is given.

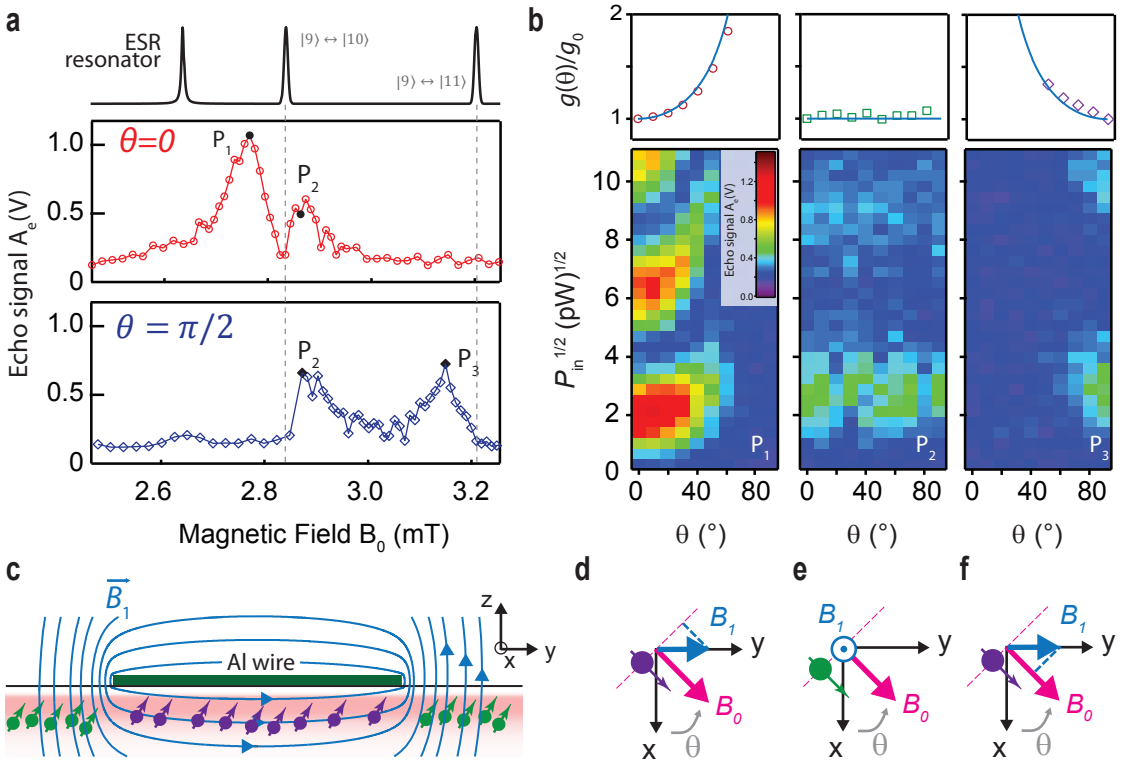

FIGURE 6.5: **First S_x and S_z ESR transitions** for resonator C. **a** Frequency and power compensated echo-detected field sweep for resonator C with $\theta = 0$ and $\theta = \pi/2$. The black line on top indicates the resonator linewidth as well as the transition linewidth measured by Weis et al. [137]. **b** Rabi oscillations as a function of θ at magnetic fields P_1, P_2 and P_3 indicated with black points in panel **a**. The color axis is the averaged echo amplitude A_e. Above the color-plots are extracted the ratio $g(\theta)/g_0$ (circles, squares and diamond) from the Rabi oscillations, where g_0 is taken to be $g(\theta = 0)$ for P_1 and P_2 but $g(\theta = \pi/2)$ for P_3. The solid lines give the expected variation (see text). **c**. Schematic of $\boldsymbol{B}_1$ for spins located under and outside the Al wire. **d-f** Schematic depicting the relative orientations of $\boldsymbol{B}_1$ and $\boldsymbol{B}_0$ as a function of θ while probing peak P_1 (panel **d**), peak P_2 (panel **e**) and peak P_3 (panel **f**).

6.2.1 Doublet-shaped transitions

We start with the measurements performed using resonator C, whose frequency is closest to the zero-field splitting. Using a Hahn-echo sequence such as shown in Fig. 6.2, we record the echo signal A_e as a function of B_0. Applying a magnetic field parallel to the superconducting resonator increases the film kinetic inductance which decreases the resonator frequency as seen in ch. 5. As a consequence, at each B_0, the resonator transmission is measured, fitted, and the microwave source adjusted to this frequency, using an automated routine; after that the echo sequence is run as explained earlier. The power of the excitation and refocusing pulses are calibrated via Rabi oscillations to ensure they correspond to $\pi/2$ and π pulses for each B_0. We also set the repetition rate well below the spin energy relaxation rate.

Fig. 6.5a shows the data for $\theta = 0$ around the magnetic field $B_0 = 2.84$ mT expected for the first encountered S_x transition $|9\rangle \xleftrightarrow{S_x} |10\rangle$. The line appears much broader than observed by Weis et al. [137] with its FWHM linewidth being $\Delta B_0 = 200\ \mu\text{T} \gg 12.2\ \mu\text{T}$. It is also considerably broader than the ESR resonator linewidth (which corresponds to $\approx 3\ \mu$T in magnetic field units). In addition, the line appears to be split: two well-defined asymmetric peaks appear on each side of the expected B_0 field. Such a line splitting has never been reported so far in Si:Bi samples, most remarkably

in measurements performed on the exact same sample in a conventional ESR spectrometer. We denote P_1 (P_2) the low-field (high-field) peak, and we discuss the origin of this doublet shape in the following.

To complement these data, we perform the exact same measurements but with $\theta = \pi/2$, (pink curve in Fig. 6.5a). P_1 is seen to be fully suppressed, whereas P_2 remains unchanged. The spins contributing to P_1 are thus not excited anymore when B_0 is orthogonal to the wire, while P_2 spins are probed identically. In addition, a new peak (noted P_3) is visible, at a magnetic field B_0 close to the one expected for the $|9\rangle \xleftrightarrow{S_z} |11\rangle$ transition, with a linewidth similar to the other peaks but remarkably without visible splitting.

To account for these experimental facts, our hypothesis is that the peaks P_1 and P_3 arise from spins located under the Al wire, probed by an excitation field $\boldsymbol{B}_1$ mainly aligned on y (see Fig. 6.5c). When $\theta = 0$, $\boldsymbol{B}_0$ is orthogonal to $\boldsymbol{B}_1$ (see Fig. 6.5d) and thus the spins can only contribute to $|9\rangle \xleftrightarrow{S_x} |10\rangle$ (i.e. P_1); in reverse when $\theta = \pi/2$, $\boldsymbol{B}_0$ is parallel to $\boldsymbol{B}_1$ (see Fig. 6.5f) and thus the spins can only contribute to $|9\rangle \xleftrightarrow{S_z} |11\rangle$ (i.e. P_3). In contrast, spins located outside the wire are probed via an excitation field $\boldsymbol{B}_1$ mainly aligned on z (see Fig. 6.5c), and thus whatever the orientation of $\boldsymbol{B}_0$ they systematically contribute to $|9\rangle \xleftrightarrow{S_x} |10\rangle$ (i.e. P_2) but never to the $|9\rangle \xleftrightarrow{S_z} |11\rangle$ transition.

In order to test this hypothesis, we measure the Rabi oscillation frequency for varying angles θ. As explained in ch. 5, we expect different angular dependence of g (see Eqs. 5.20 & 5.21) on θ:

- for a S_x transition, for spins located under the wire as $g(\theta) \propto \cos(\theta)$
- for a S_x transition, for spins located outside the wire as $g(\theta) = g(0)$
- for a S_z transition, for spins located under the wire as $g(\theta) \propto \sin(\theta)$.

and thus the Rabi-oscillations frequency should follow the expected $1/g(\theta)$ dependence. Fig. 6.5b shows the results. Very different angular dependences are indeed observed for the 3 peaks. On the P_1 peak, a $1/\cos\theta$ dependence is found, while P_3 has a $1/\sin\theta$ dependence and P_2 does not depend on θ; this confirms our hypothesis for the peaks identification.

6.2.2 Rabi frequency dependence on B_0

According to our previous discussion, there appears to be a correlation between the spins Larmor frequency and their spatial location with respect to the resonator. Further insight in this direction is obtained by doing systematic measurements of the Rabi frequency as a function of B_0 along the spectroscopy peaks. Fig. 6.6 shows the Rabi oscillations performed for transition $|9\rangle \xleftrightarrow{S_x} |10\rangle$ for resonator B with $\theta = 0$: the recovered echo amplitude A_e is color-coded and plotted as a function of the refocusing power P_{in} and the magnetic field B_0. The overall amplitude of the oscillations (shown in the top panel of Fig. 6.6) resembles the lineshape already observed with resonator C, showing two very asymmetric peaks. The most remarkable feature however is the fact that the frequency of the Rabi oscillations (see Fig. 6.6) shows a pronounced and non-trivial dependence on B_0.

Our interpretation of the observed dependence of g on B_0 is based on the fact that g is proportional to the amplitude of the $\boldsymbol{B}_1$ field generated by the resonator, which itself depends on the spatial position relative to the resonator wire (see for instance Fig. 5.10 in ch. 5). As already discussed for the explanation of the two-peak structure of the line, we are thus led to the conclusion that the spin Larmor frequency is somehow correlated to their location relative to the resonator wire. From our knowledge of $\boldsymbol{B}_1(\boldsymbol{r})$, we can go further and actually assess that within the P_1 peak, "low-field" spins are located closer to the wire edge where $\boldsymbol{B}_1$ is strongest (i.e. $|y|$ just below $w_r/2$) whereas "high-field" spins are located in the middle of the wire (i.e. $|y| \ll w_r/2$); for the P_2 peak on the

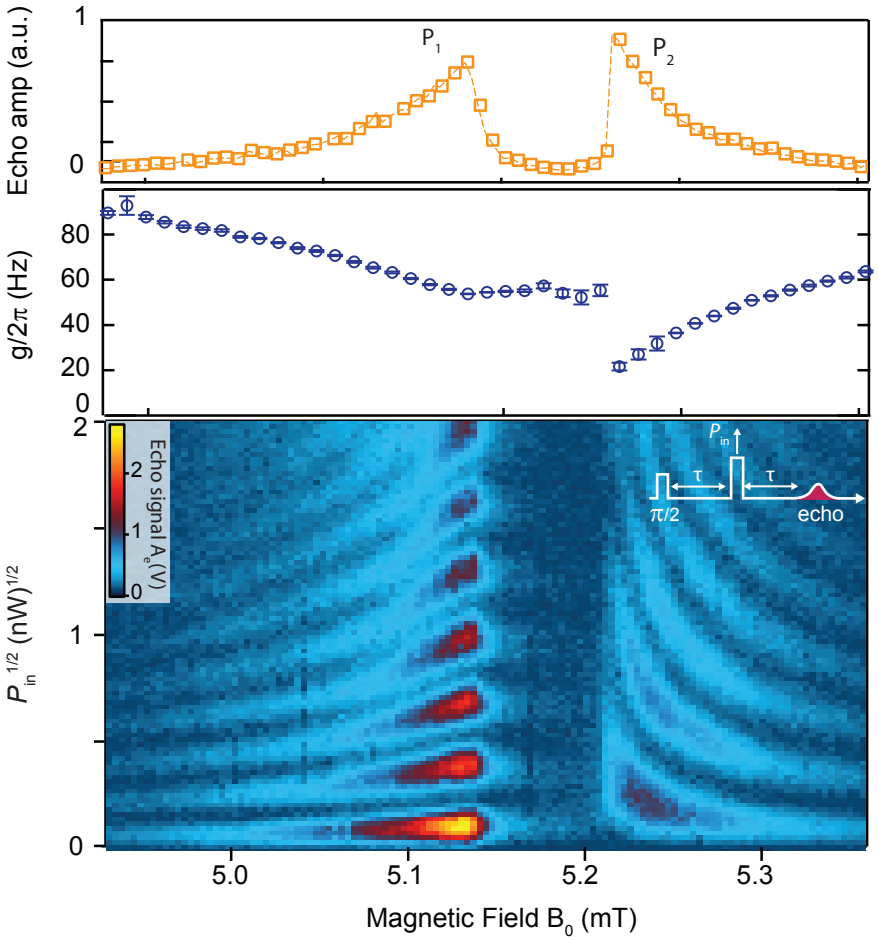

FIGURE 6.6: **Rabi oscillations as a function of $\boldsymbol{B}_0$** for transition $|9\rangle \overset{S_x}{\longleftrightarrow} |10\rangle$ taken with resonator B and $\theta = 0$. The amplitude of the refocusing pulse in the Hahn-echo sequence is varied to reveal oscillations in the integrated echo signal A_e. The frequency of the oscillations allows to extract the spin-resonator coupling $g(B_0)$. On top is shown the frequency and power compensated ESR spectrum, evidencing the same doublet-shape than resonator C.

other hand, "low-field" spins are located far from the wire where $\boldsymbol{B}_1$ becomes vanishingly small (i.e. $|y| \gg w_r/2$) whereas "high-field" spins are closer to the wire edge (i.e. $|y|$ just above $w_r/2$).

Thus the physical mechanism that explains the line broadening causes the spins located near the edge of the aluminum wire to be far offset from their expected Larmor frequency, with positive detuning for the spins lying below the edge of the wire ($|y| < w_r/2$), and negative detunings for the spins located on the side of the edge of the wire ($|y| > w_r/2$). Spins located either far from the wire or underneath its center lie closer in frequency to the expected ESR transition.

While we have not yet provided an explanation for the underlying physical mechanism causing this effect, we can already note a beneficial consequence for our experiments. Since the resonator line is much narrower than the overall spin distribution, we can effectively choose to drive and measure ensembles of spins with very different couplings to the resonator simply by changing B_0. In particular, we can work with ensembles of spins with a coupling constant to the resonator that is much better defined than in the absence of the line broadening mechanism, where the Rabi oscillation pattern would in fact be an average over all Rabi frequencies observed in Fig. 6.6 and thus lead to much less precise Rabi angles.

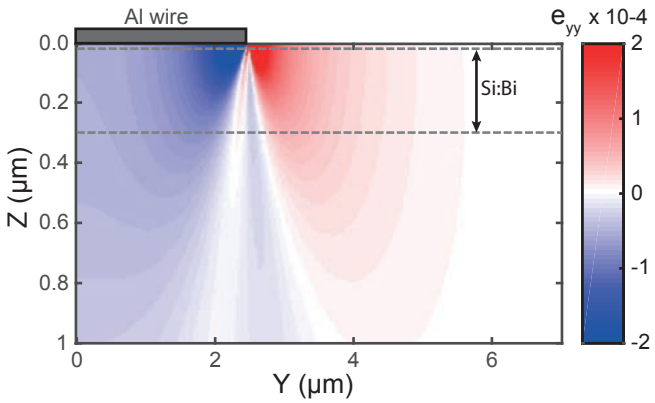

FIGURE 6.7: **Induced strain.** Diagonal strain tensor component ε_{yy} experienced by the donors as a result of thermal expansion coefficient mismatch between silicon and the aluminum inductive wire, obtained via finite element simulation realized with COMSOL Multiphysics.

6.2.3 Induced strain, a likely suspect

Clearly, the physical mechanism responsible for these phenomena has to be linked to the presence of the aluminum wire on top of the substrate. A thorough and quantitative analysis was performed by J. Pla and will be reported in [177]; as it is not the main topic of this thesis we will only briefly summarize its main conclusions in the following.

The mechanisms at the origin of the broadening could be either:

- **Magnetic field inhomogeneities:** B_0 could have a spatial dependence originating from its expulsion from the superconducting thin films forming the resonator, due to the Meissner effect. However such inhomogeneities would be proportional to the applied magnetic field. As a similar or even slightly narrower linewidth is measured for resonator B and C for the $|9\rangle \xleftrightarrow{S_x} |10\rangle$ transition, this mechanism can be ruled out.
- **Built-in electric fields:** the aluminum/silicon interface beneath the resonator forms a Schottky barrier which could lead to frequency shifts of the donor spin resonance. However induced electrical fields would only induce a Stark shift of the hyperfine interaction or electron γ_e-factor, altering only quadratically the spin frequency. As we observe simultaneously positive and negative detunings, we can also rule out this mechanism.
- **Induced strain**. As aluminum and silicon have different coefficients of thermal expansion, cooling the device from room-temperature to 20 mK induces strain in the silicon. As discussed in ch. 4, strain can induced both hyperfine interaction shift as well as quadrupolar effects. While we can rule out broadening due to the hyperfine interaction, quadrupolar interaction is a likely candidate that can provide both positive and negative detunings [111] as observed in our experiment.

We thus retain only the latter hypothesis. Through finite elements simulations, the strain in the vicinity of the wire at 20 mK can be computed as shown in Fig. 6.7. The subsequent modification of the donor wave-functions A_1, E and T_2 is computed using an effective mass theory model [109]. As explained in ch. 4, the modification of the fully symmetric A_1 ground state reduces the hyperfine coupling $A(\varepsilon) \leqslant A(0)$, but from the simulations only a small shift of the order of 0.8 μT is estimated.

The quadrupolar interaction, while zero in absence of stress, arises via the mixing of A_1 with the non-symmetric E_{xyz} state that induces a non-zero electrical field gradient (EFG). Linking the quadrupolar factor $\boldsymbol{Q}$ involved in the quadrupolar Hamiltonian (see Eq. 4.28) to the EFG accurately is non-trivial, due to the very complex structure of the donor and is the object of a detailed discussion in [177]. In

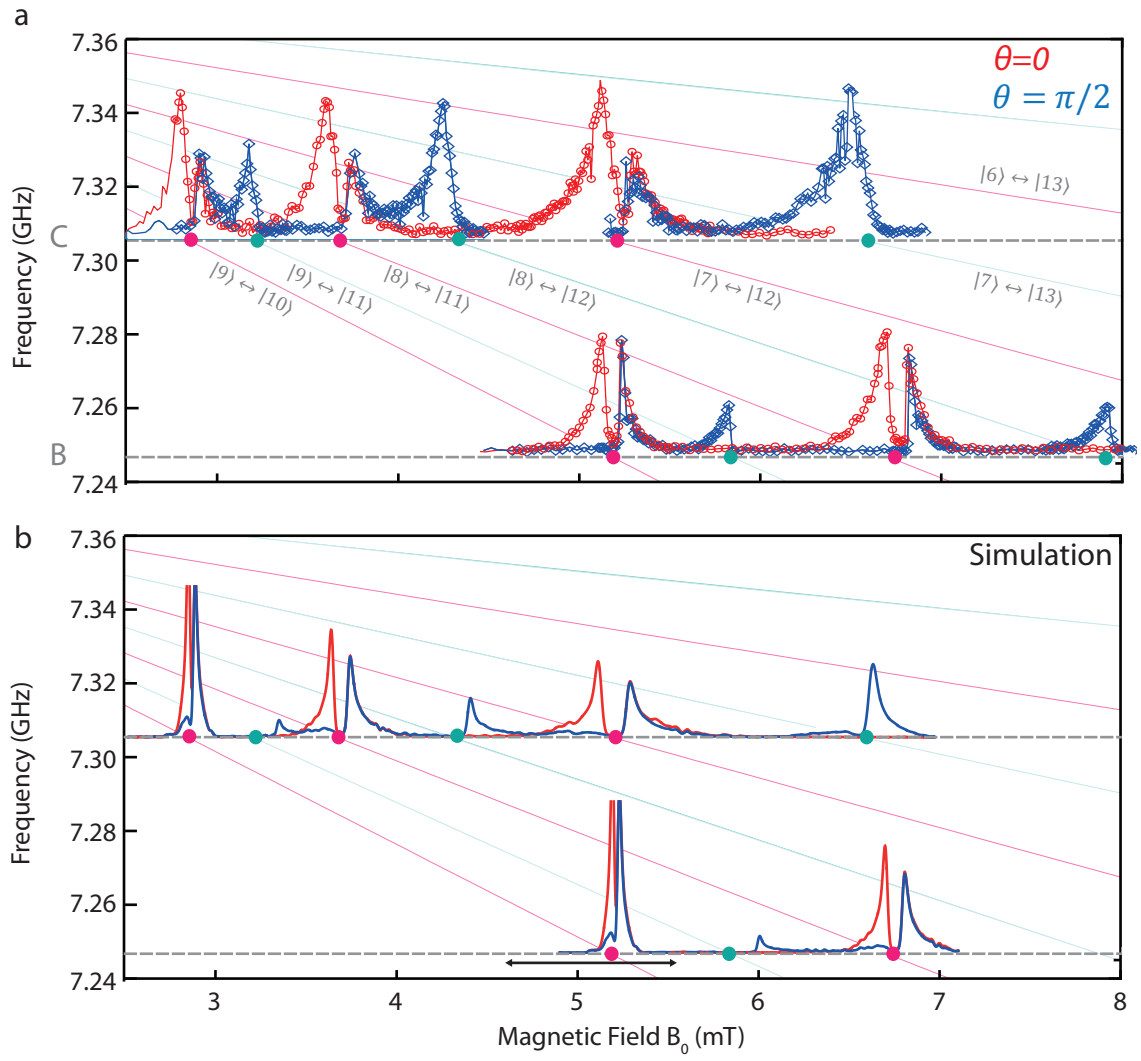

FIGURE 6.8: **Measured and simulated field ESR spectroscopy** for resonator B and C. Top (bottom) panel corresponds to the frequency and power compensated echo-detected field sweep while the bottom panel corresponds to simulations described in the main text (extracted from [177]). Dashed grey lines indicate the resonator frequencies, while the light green (purple) lines indicate the $S_x(S_z)$ transitions, with the notations of Table. 6.1 given in grey. Resonator A is not shown, but similar results are obtained for transition $|9\rangle \overset{S_x}{\longleftrightarrow} |10\rangle$.

particular, a significant part of the imprecision arises from the Sternheimer anti-shielding effect [178]. This phenomenon describes the re-arrangement of the inner electron shells in response to an external EFG, with a resulting enhancement of the total EFG experienced by the nucleus. $\boldsymbol{Q}$ is thus multiplied by a factor that can be considerable ($\approx \times 46$ for Bi^{5+} ions [179]) but that is undetermined up to now for Si:Bi donors. In the following an extra proportional correction on $\boldsymbol{Q}$ is added as a fitting parameter to include this effect. Once the quadrupolar Hamiltonian is estimated (see Eq. 4.28), the expected transition shift can be computed by adding the quadrupolar term to the Si:Bi Hamiltonian of Eq. 4.8.

At each point (x, y, z) of the sample relative to the wire, one can thus estimate via the strain simulation the expected ESR spectrum. The global expected ESR spectrum can thus be modeled by summing all spins contributions, weighted according to the implantation profile of the bismuth

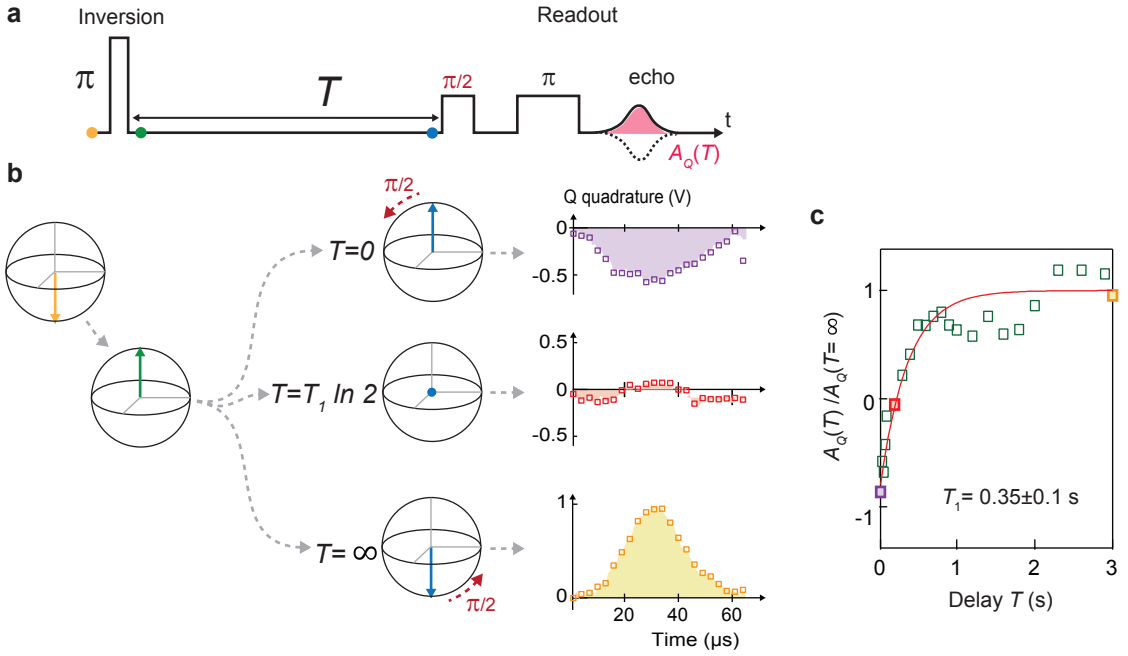

FIGURE 6.9: **Inversion recovery. a** The sequence consists in sending a large bandwidth π pulse to invert the spins. After a delay T, the remaining polarization is measured via a Hahn-echo sequence. **b** At very short times ($T = 0$), the echo measured on a single quadrature (Q for instance) has the opposite sign than at times $T \gg T_1$. **c** The integrated quadrature signal A_Q as a function of the delay T is well-fit by an exponential (red solid line) yielding $T_1 = 0.35$ s.

atoms extracted by SIMS (see Fig. 4.12) and to the coupling constant g extracted from the simulation of the $\boldsymbol{\delta B}$ excitation field.

The results of the full ESR spectroscopy of resonators B and C as well as the simulated ESR lineshapes is shown in Fig. 6.8. While the model fails to account precisely for the peak broadening and the asymmetry of the S_z transitions, it does capture most of the features of the ESR spectroscopy, such as the S_x peak splitting and the θ-dependence. The best match between experimental data and simulations required a correction factor of 400, it would be very interesting to test this determination using other configurations. Nevertheless, we can conclude that quadrupolar effects due to strain induced in the silicon by the aluminum wire is a very likely mechanism for the overall peak broadenings observed in our experiment.

6.3 Relaxation times

We now characterize the relaxation and coherence times of the sample. For this purpose, we concentrate on the transition $|9\rangle \overset{S_x}{\longleftrightarrow} |10\rangle$ tuned at resonance with resonator B by applying $B_0 = 5.13$ mT and $\theta = 0$.

6.3.1 Energy relaxation

We first measure the energy relaxation time T_1 using inversion-recovery [5] as described in Fig. 6.9. Starting from thermal equilibrium, a 5-µs-long π pulse is sent at resonance to invert the spin polarization, after which the magnetization decays by T_1 processes back to thermal equilibrium. To

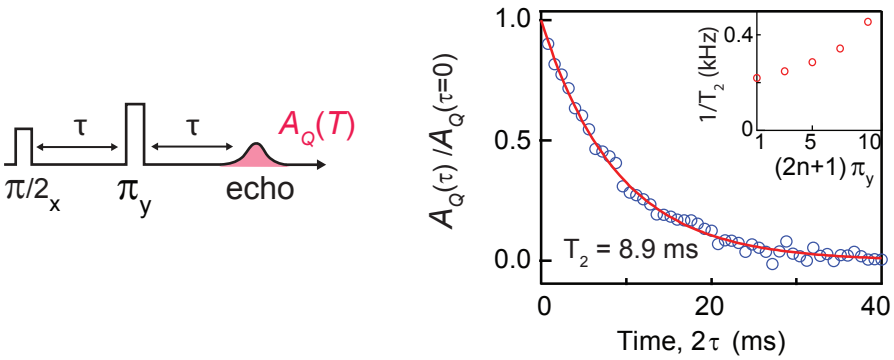

FIGURE 6.10: **Decoherence times.** As the total time 2τ between the initial $\pi/2$ pulse and the echo is increased, the recovered quadrature signal $A_Q(\tau)$ decays with an exponential behavior (red curve is a fit), yielding a spin coherence time $T_2 = 8.9$ ms. When the bandwidth of the refocusing pulse is increased, the decoherence time T_2 decreases (see inset), indicating that the decoherence mechanism is partly due to instantaneous diffusion.

readout the remaining polarization after a time T, we employ once again a Hahn-echo sequence, with a shorter bandwidth than the excitation pulse ($t_\pi = 100$ µs). At times $T \gg T_1$, the measured spins have relaxed back to equilibrium, and thus a steady-state echo is recorded, yielding $A_Q(T = \infty)$. At time $T = 0$, the polarization is fully inverted, thus the $\pi/2$ pulse of the Hahn-echo sequence projects the magnetization vector on the opposite direction compared to the steady-state situation so that the echo signal $A_Q(T = 0)$ has the opposite sign than $A_Q(T = \infty)$. The T_1 relaxation is thus observed by measuring the decay from $A_Q(T = 0)$ to $A_Q(T = \infty)$. For resonator B at $B_0 = 5.13$ mT and $\theta = 0$, the decay is exponential with a characteristic time $T_1 = 0.35$ s, as shown in Fig. 6.9c.

The shortness of this measured time compared to the values obtained in the literature at even higher temperatures (see 4.4.1) is due to the Purcell effect induced by the high quality factor resonator, as will be explained in ch. 8.

6.3.2 Coherence times

As already explained in ch. 4, the decoherence time T_2 is characterized in ESR measurements by sweeping the delay time 2τ between the initial $\pi/2$ pulse and the echo emission. Fig. 6.10 shows such a measurement for resonator B at $B_0 = 5.13$ mT and $\theta = 0$, well fitted by an exponential decay of characteristic time $T_2 = 8.9$ ms. Whereas this value is characteristic of the long coherence times readily obtained for donors in isotopically purified silicon samples, it is nevertheless surprisingly long given the sample concentration. Indeed, measurements performed by Weis et al. [137] on the same sample report $T_2 = 500$ µs, more than an order of magnitude shorter than the data in Fig. 6.10.

Our interpretation of this discrepancy is as follows. In Weis et al. measurements, T_2 was shown to be limited by instantaneous diffusion, caused by the unwanted spin flips of the neighboring Si:Bi donors upon the application of the refocusing π pulse. In our experiment however, due to the strain-induced line broadening discussed earlier and to the narrow resonator bandwidth, the π pulses address only a small subset of the entire spin ensemble, which could lead to much less pronounced instantaneous diffusion effects thus explaining the longer T_2 measured. In order to test this idea, we have performed T_2 measurements using higher refocusing pulse powers, leading to higher Rabi frequencies and thus larger number of spins being flipped. As qualitatively expected, we see a reduction in T_2 (see inset of Fig. 6.10), which we have however not attempted to account for quantitatively. To conclude, it seems likely that our measured coherence time is at least partly limited by instantaneous diffusion, as is often the case for measurements on ensembles of donors [126, 124].

Chapter 7

Spectrometer sensitivity

In this chapter, we estimate the sensitivity $N_{\min}$ of our spectrometer defined as the number of spins that can be detected with a single Hahn-echo for a signal-to-noise ratio of 1. We first determine the number of spins contributing to the signal, and we measure the SNR of an echo; this yields a sensitivity of 2000 spins detectable with SNR$= 1$ in a single echo sequence. We also demonstrate how CPMG sequences can be used to enhance further the sensitivity by a factor ≈ 10.

7.1 Determining the number of spins

We define the number of spins contributing to the echo signal N_{spins} as the number of spins excited by the $\pi/2$ pulse. We estimate N_{spins} using resonator B and concentrating on the low-field peak of transition $|9\rangle \leftrightarrow |10\rangle$ tuned at resonance with $B_0 = 5.13$ mT by two methods detailed in the following.

7.1.1 Direct counting of the donors

A first method to evaluate the number of spins consists in using our knowledge of the bismuth atoms implantation profile to count the number of atoms in the detection volume. Let us call N_{tot} the number of spins contributing to the low-field peak of transitions $|9\rangle \leftrightarrow |10\rangle$. As the resonator linewidth is considerably smaller than the ESR linewidth (see Fig. 7.1), only a small fraction of the spins $N_{\text{spins}} = \xi N_{\text{tot}}$ contributes effectively to the signal. The $\pi/2$ pulse of the Hahn-echo sequence shown in Fig. 6.2 being 5 µs long, we make the assumption that it excites spins with a frequency response similar to the resonator response (see 6.1.3) and thus ξ is approximately given by:

$$\xi = \int \rho_{\text{LC}}(\omega)\rho_{\text{ESR}}(\omega)d\omega \tag{7.1}$$

where $\rho_{\text{LC}}(\omega) = 1/(1 + 4(\omega - \omega_0)^2/\kappa^2)$ is the ESR resonator spectral response and $\rho_{\text{ESR}}(\omega)$ is the spins density profile.

To determine $\rho_{\text{ESR}}(\omega)$, we use the measured spin-echo line and more precisely we will focus on the low-field peak (P_1) which has the advantage of corresponding to a well-defined detection volume: the spins located exactly below the resonator wire. The measured spin-echo amplitude $A_e(B_0)$ does not provide directly the spin density ρ_{ESR}, because, as explained earlier, the spin-resonator coupling is B_0-dependent, which leads to a slight distortion of the curve since the detected signal is itself proportional to g. Thus, ρ_{ESR} is proportional to $A_e(B_0)/g(B_0)$. B_0 is converted to ω units using the the $|9\rangle \leftrightarrow |10\rangle$ transition frequency dependence on B_0. The spectrum computed using the ESR data acquired for resonator B and normalized using $\int \rho_{\text{ESR}}(\omega)d\omega = 1$ is shown in Fig. 7.1a. At

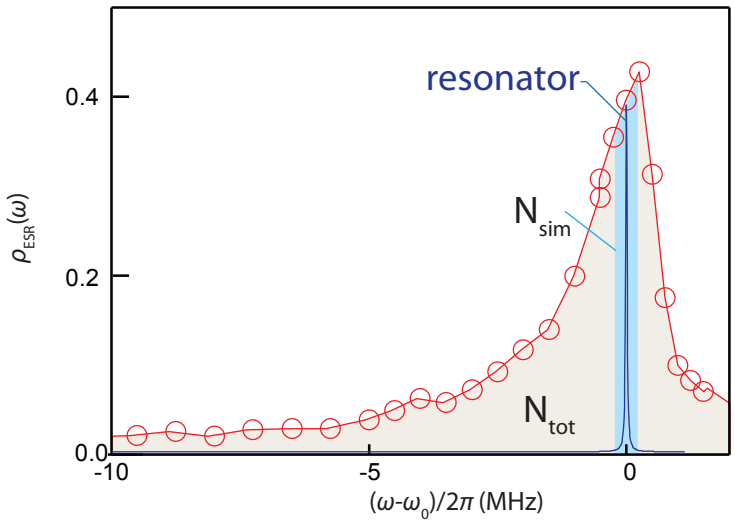

FIGURE 7.1: **Estimation of the number of spins.** The spin density profile $\rho_{\mathrm{ESR}}(\omega)$ (red circles) is extracted from measuring $A_e(B_0)$ and $g(B_0)$ to be compared to the resonator bandwidth (dark blue). The grey shade indicates N_{tot} the total number of spins comprising the low-field peak of transition $|9\rangle \leftrightarrow |10\rangle$ and the blue shade indicates N_{num} the number of spins comprising the spin ensemble numerical model.

field $B_0 = 5.13$ mT, using the resonator linewidth determined in Table 5.3, we find from Eq. 7.1 $\xi \approx 1.6 \times 10^{-2}$.

To go further we need to evaluate the total number of spins N_{tot}. We estimate N_{tot} using the implantation profile [Bi](z) measured by SIMS by Weis et al. (see section 4.6 and [137]) by:

$$N_{\mathrm{tot}} = \frac{1}{9} w_r l_r \int_z [\mathrm{Bi}](\mathrm{z})\mathrm{dz} \tag{7.2}$$

where w_r and l_r are the wire dimensions. A factor $1/9$ is added since we are probing via the transition $|9\rangle \leftrightarrow |10\rangle$ only one of the 9 ground states of Si:Bi that we assume to be equally populated at 20 mK. We find $N_{\mathrm{tot}} = 4.7 \times 10^6$.

This estimate can be refined by considering that the number of spins may be less than the number of implanted atoms for the following reasons. First, as explained in ch. 4, only 60% of the implanted atoms become converted as donors following the post-implant annealing, as measured by Weis et al. [137].

Second, the aluminum thin-film deposited directly on top of the silicon substrate can give rise to a Schottky barrier in which donors may be ionized (see Fig. 7.2). The difference in the work function of aluminum and silicon causes a band-bending responsible for the ionization of the donors over an area called the depletion region. A simple model to estimate the depth of the depletion region is to make the full-depletion assumption[180]. In this model, the donors are assumed to be ionized on a depth z_d and neutral for $z \geqslant z_d$:

$$\begin{cases} N_D^+(z) = & [\mathrm{Bi}](\mathrm{z}), & z \leqslant z_d \\ N_D^+(z) = & 0 & z > z_d \end{cases} \tag{7.3}$$

where $N_D^+(z)$ is the number of ionized donors. To determine z_d, one has then to solve the Poisson equation:

$$-\frac{d^2\phi}{\mathrm{dx}^2} = \rho/\varepsilon_{\mathrm{Si}} \tag{7.4}$$

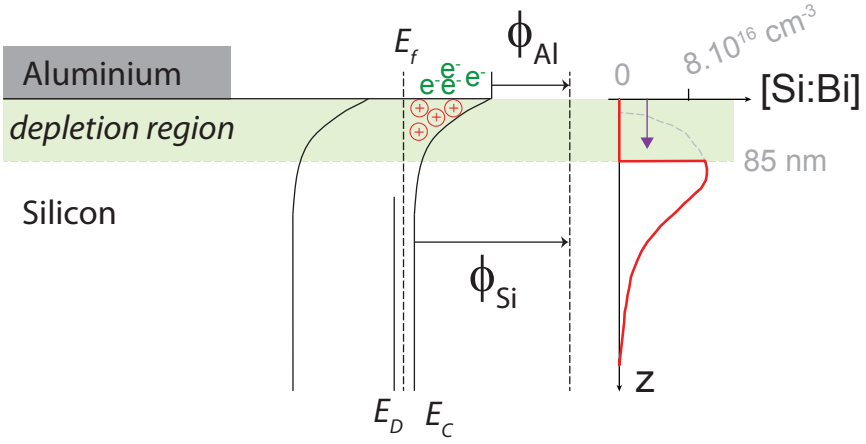

FIGURE 7.2: **Schottky barrier** at the aluminum-silicon interface. A bending of the valence and conduction band of silicon is observed due to the work function difference $\phi_{\mathrm{Al}} - \phi_{\mathrm{Si}}$ between aluminum and silicon. It is responsible for the ionization of the donors in the *depletion region* of depth 85 nm in our sample.

with $\rho(z) = eN_D^+(z)$, taking as boundary condition that the electrical field $\mathcal{E} = -\frac{d\phi}{\mathrm{dz}}$ is zero for $z \geqslant z_d$. Solving numerically $\phi(z_d) - \phi(0) = \phi_{\mathrm{Si}} - \phi_{\mathrm{Al}}$ yields $z_d \approx 85$ nm for $\phi_{\mathrm{Si}} - \phi_{\mathrm{Al}} = 0.5$ V [181]. Re-evaluating [Bi](z) using this estimate and taking into account the limited yield, we obtain $N_{\mathrm{tot}} \approx 1.5 \times 10^6$ and thus:

$$N_{\mathrm{spins}} = 2.4 \times 10^4 \tag{7.5}$$

7.1.2 Estimate based on numerical simulations

To determine more accurately N_{spins}, we simulate numerically a Hahn-echo sequence and extract the number of spins excited by the $\pi/2$ pulse, using the model described in ch. 3 and [77, 78, 182]. The spin ensemble is divided into $\mathcal{M}$ sub-ensembles where each subset (m) contains N_m spins with subset-dependent coupling constant g_m and detuning to the resonator $\Delta_m = \omega_m - \omega_0$. The spin-resonator dynamics can then be simulated by integrating numerically the equations of motion (see Eqs. 3.41-3.44) for the resonator field and the spins collective components of all of the sub-ensembles. We use for this purpose a Matlab code developed by our collaborator Brian Julsgaard.

As input to the simulation, we use the relaxation and decoherence times measured experimentally. An important point for our sensitivity analysis is to determine precisely the size N_m of each subset. For this purpose, we use the numerical simulations to reproduce the time-dependent absorption of a microwave pulse, whose rich features are better suited than a simple echo sequence to assess the model accuracy.

Modeling

While in our experiment strain induces a correlation between a spin frequency and its spatial position and thus its coupling to the resonator (see ch. 5), we make the assumption that the spectral window and thus spatial window probed by the resonator is narrow enough to neglect this correlation. The spin-ensemble is then simply modeled by the joint distribution of a coupling constant distribution $\rho(g_i)$ and a spin detuning distribution $\rho(\Delta_j)$ of total number of bins $M_g \times M_\Delta$. The two-dimensional distribution is weighted so that the sum of all the sub-ensembles (i, j) contains $\sum_{i=1}^{M_g} \sum_{j=1}^{M_\Delta} N_{i,j} = N_{\mathrm{num}}$ spins.

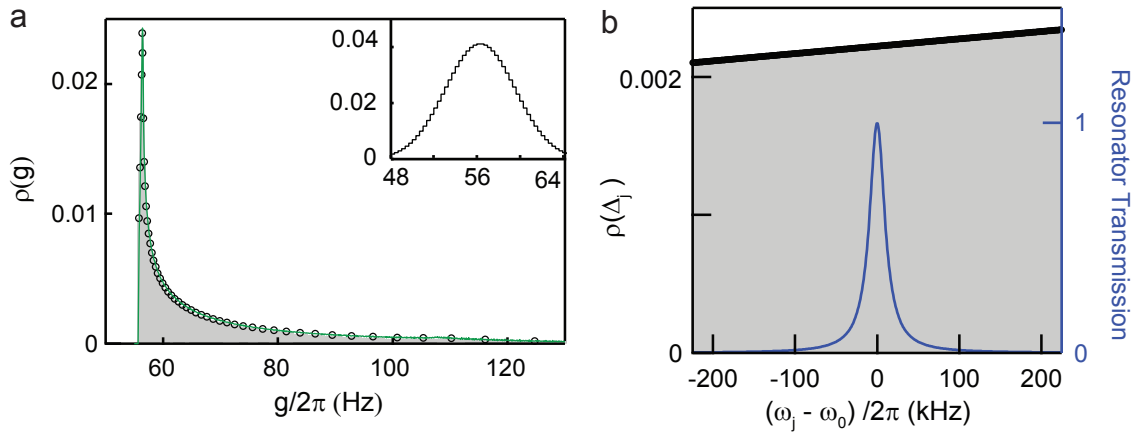

FIGURE 7.3: **Spin ensemble modeling a** Coupling constant distribution extracted from $\boldsymbol{\delta B}(\boldsymbol{r})$ simulations for $|y| < w_r/2$ weighted by the ionized spin concentration z-profile and normalized to unity (red line). The black circles show the discrete distribution used in the simulation, with $M_g = 50$. In inset is shown the equivalent Gaussian distribution. **b** Tilted square distribution used in the simulation, with $M_\Delta = 450$. The blue line indicates the resonator linewidth.

Determining the coupling constant distribution As the measurements we would like to reproduce were performed with the magnetic field B_0 aligned along the wire, on the low-field peak P_1 of the transition $|9\rangle \leftrightarrow |10\rangle$, the g distribution is extracted, similarly to section 6.1.3, from the simulation of $\boldsymbol{\delta B}(\boldsymbol{r})$ for spins under the wire ($|y| < w_r/2$) with a S_x transition matrix element $\langle 9|\hat{S}_x|10\rangle = 0.47$, taking into account the ionized spin concentration profile. The peak of the distribution now lies at $g/2\pi = 56$ Hz, close to the value determined experimentally by Rabi oscillations (see Fig. 6.3). We choose a discrete distribution with irregularly spaced $M_g = 50$ bins, as shown in Fig. 7.3a.

Simulations done in this chapter use this as-extracted distribution. Note that later on, in ch. 9, we simulate the spin-echo at two different magnetic fields within P_1 and thus probe spin subsets with different Larmor frequency that have a different mean coupling constant g_0 (see ch. 6). To capture the difference in g when modeling the two different spin subsets, we simplify the as-extracted distribution in a Gaussian distribution centered on g_0 with a width Δg that is phenomenologically adjusted.

Determining the spin frequency distribution Simulating sequences as long as 1 ms requires a small bin size for the spin frequency distribution; we choose 1 bin per 1 kHz, over a 450 kHz range. The resonator linewidth being two orders of magnitude smaller than the spin linewidth, the zero-order approximation would be to assume a square spin frequency distribution. We nevertheless introduce a tilted square distribution to take into account more precisely the shape of the line, as shown in Fig. 7.3b. The relative slope is derived from $\rho_{\mathrm{ESR}}(\omega)$.

Spin-decoherence rate and energy relaxation rate Spin decoherence is treated by including both a spin dephasing rate $\gamma_\perp = 1/T_2$ and a spin energy decay rate $\gamma_\parallel = 1/T_1$. We use the experimental measured coherence time $T_2 = 9$ ms (see Fig. 6.10). The energy relaxation rate, on the other hand, is due to Purcell relaxation (as will be explained ch. 8). As a result, spins detuned from the cavity have a longer relaxation rate. This is captured by defining for each sub-ensemble:

$$\gamma_\parallel^{(i,j)} = \kappa \frac{g_i^2}{\Delta_j^2 + \frac{\kappa}{4}}. \tag{7.6}$$

Since $\gamma_\perp \gg \gamma_\parallel$, the introduction of $\gamma_\parallel$ is only important for describing the initial state of the ensemble. Indeed, every experimental sequence is repeated several times at rate $\gamma_{\rm rep}$ (with $\gamma_{\rm rep}^{-1}$ ≈3 to 10 s) and the results are then averaged. This waiting time $\gamma_{\rm rep}^{-1}$ is long enough compared to T_1 to be neglected for spins at resonance, however detuned spins have a longer T_1 and thus do not fully relax between two consecutive sequences, contributing less to the signal than spins at resonance. To take into account this effect, we define an effective initial polarization $S_z^{(i,j)}(t=0)$ for a sub-ensemble depending on its relaxation time:

$$\mathcal{S}_z^{(i,j)}(t=0) = -N_{i,j} \times \left(1 - e^{-\gamma_\parallel^{(i,j)}/\gamma_{\rm rep}}\right) \tag{7.7}$$

Resonator and drive parameters The ESR resonators parameters κ_1, κ_2, $\kappa_{\rm int}$ and ω_0 are taken equal to the measured values (see Table 5.3). We make the assumption that all drives pulses are sent at resonance. The incident power $P_{\rm in}$ is assumed identical to the value determined experimentally within a 1-dB-error margin.

Absolute calibration of the spin density

The only free parameter in the model is thus the absolute scaling factor $N_{\rm num}$, whose exact determination is crucial to estimate the number of spins excited during the Hahn-echo sequence. To calibrate $N_{\rm num}$, we measure the time-dependent absorption by the spins of a 500-µs-long pulse of power $P_{\rm in}$, as shown in Fig. 7.4a. The data are shown in Fig. 7.4b for unsaturated spins, and in **Fig.8.4c** for saturated spins. When the spins are not saturated, the transmitted pulse shows two prominent features that should be precisely reproduced by the simulations: the Rabi oscillation transients at the beginning, which are characterized by an oscillation frequency Ω_R, a decay time and an initial amplitude, and the FID of the spins which gives rise to the emission of a microwave signal even after the resonator field has decayed (see Fig. 7.4a). For comparison, and to provide the scaling factor between numerical and experimental data, the transmission of a second pulse P sent right after a strong microwave saturating pulse is also recorded. The sequence is acquired 1000 times with a repetition time $\gamma_{\rm rep}^{-1} = 5$ s.

We perform a numerical simulation of this experiment using the model described above. We find that for the as-extracted g-distribution, $N_{\rm num} = 2.0 \times 10^5$ gives a good agreement with the FID decay as well as the Rabi oscillations amplitude. To obtain the accurate Rabi oscillation frequency, we had to scale $P_{\rm in}$ by a factor 1.1. By adjusting only those two independent parameters, the spin absorption data is quantitatively reproduced (solid colored lines in Fig. 7.4b&c), which validates the model to estimate the number of spins contributing to the signal[1].

Comparison with the atom-counting estimate We can use the absolute scaling determined numerically to evaluate the total number of spins $N_{\rm tot}$ that contribute to the low-field ESR peak P_1. As the absolute scaling $N_{\rm num}$ is evaluated for spins lying in a bandwidth $\Delta\omega/2\pi = 450$ kHz (see Fig. 7.1), we have:

$$N_{\rm num} = N_{\rm tot} \int_{-\Delta\omega/2}^{\Delta\omega/2} \rho_{\rm ESR}(\omega) d\omega \tag{7.8}$$

where $\rho_{\rm ESR}(\omega)$ is the spins spectrum determined from the ESR spectroscopy as explained in section . We find $N_{\rm tot} = 1.2 \times 10^6$, a value in very good agreement with the estimate $N_{\rm tot} = 1.5 \times 10^6$ given by the "atom-counting" method.

[1] In the case of a Gaussian g-distribution, the parameters $g/2\pi = 56$ Hz, $\Delta g = 1.5$ Hz and $N_{\rm num} = 1.8 \times 10^5$ with $\epsilon = 0.85$ gives a less but still correct agreement to the experimental data, with the Rabi oscillations damping not being entirely captured (dashed line in Fig. 7.4b)

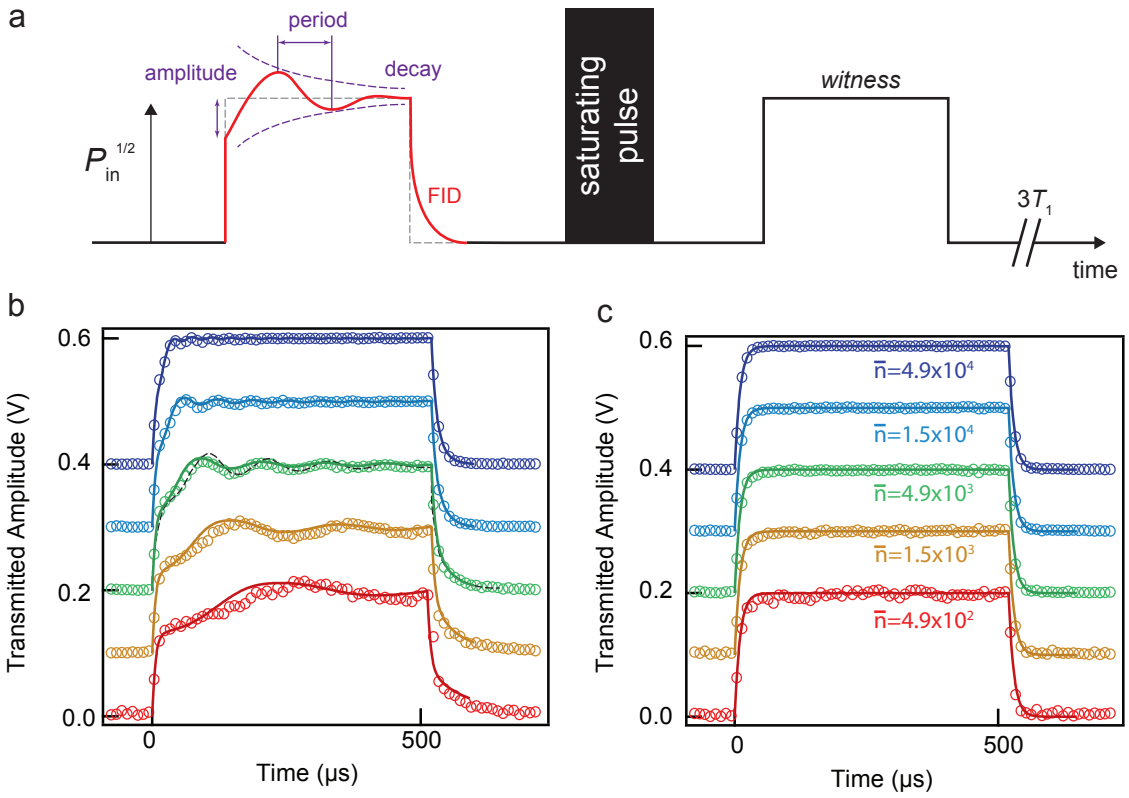

FIGURE 7.4: **Time-dependent absorption. a** Experimental sequence consisting of a first 500-µs-long pulse at power $P_{\rm in}$, followed by a strong microwave pulse immediately followed by a second 500-µs-long at same power $P_{\rm in}$ to remove the spins contribution. **b-c** Absorbed and saturated pulses taken with average number of photons $\bar{n}$ for the intra-resonator field, rescaled to the same amplitude as for the curve corresponding to $\bar{n} = 4.9 \times 10^3$(green) with additional offsets and averaged 1000 times. Open circles: data. Solid-lines: numerical fit with as-extracted g-distribution. Black dashed line: numerical fit with Gaussian g-distribution.

Reproducing a Hahn-echo sequence

We now simulate the full echo-sequence, keeping exactly the same model parameters. The input power of the simulated $\pi/2$ and π pulses are calibrated by simulating Rabi oscillations. We find that in the simulation the π pulse power is only 1 dB away from the experimental one, which further confirms the validity of our model.

The spin echo sequence was acquired with the JPA off, in order to avoid its saturation by the drive pulses. The output amplitude is scaled by comparing the theoretical and experimental decay of the two excitation pulses. With only this adjustment factor the simulated echo is found to be in quantitative agreement with the experimental data as shown in Fig. 7.5.

To evaluate the number of spins excited during the spin-echo sequence, we extract from the simulation the time-dependent mean spin polarization $\langle \hat{S}_z \rangle$, as shown in Fig. 7.5. We consider more particularly that the quantity $\langle \hat{S}_z(t > \pi/2) \rangle - \langle \hat{S}_z(t = 0) \rangle$ is a direct estimate if the number of spins excited by the Hahn-echo sequence. We find[2] $N_{\rm spins} = 1.2 \times 10^4$, confirming our previous estimate of $\xi \approx 1.6 \times 10^{-2}$. We thus come to the conclusion that $N_{\rm spins}$ participate to the echo shown in Fig. 7.5.

[2]Using the Gaussian g-distribution, we find a similar number $N_{\rm spins} = 1.1 \times 10^4$

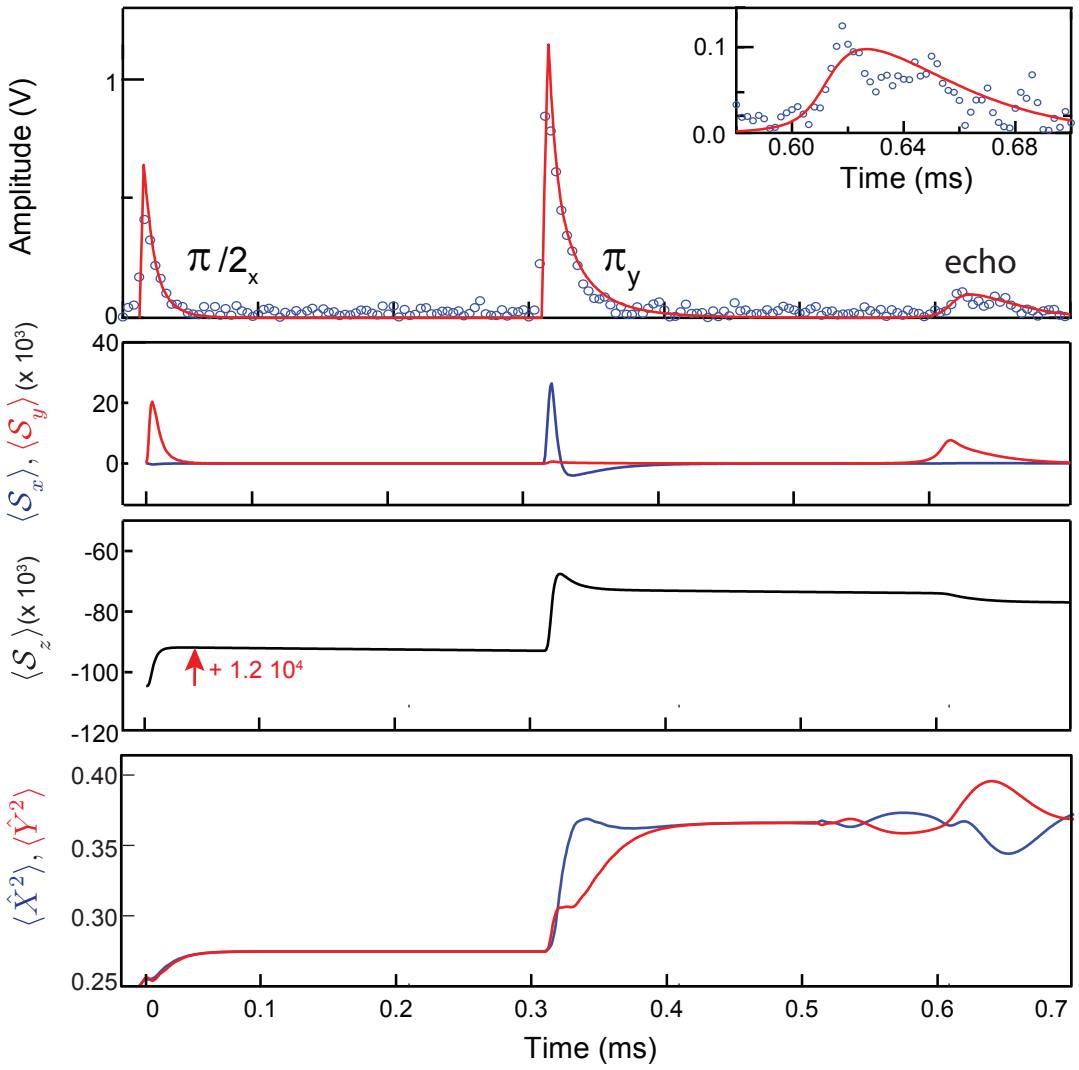

FIGURE 7.5: **Hahn-echo sequence simulation**. (Top) The simulated Hahn-echo sequence (red lines) lies on top of the recorded experimental echo sequence (blue points) taken without JPA to avoid any saturation effect and reproduces quantitatively the data. (Middle panels) Collective spin components $\langle \mathcal{S}_k \rangle = \sum_m \langle \mathcal{S}_k^{(m)} \rangle$ extracted from the simulation. The component $\langle \mathcal{S}_z \rangle$ is used to determine the number of spins N_{spins} excited during the $\pi/2$ pulse. (Bottom) Resonator field quadrature variances evidencing that 30% extra-noise is added during the spin-echo sequence due to spin spontaneous emission.

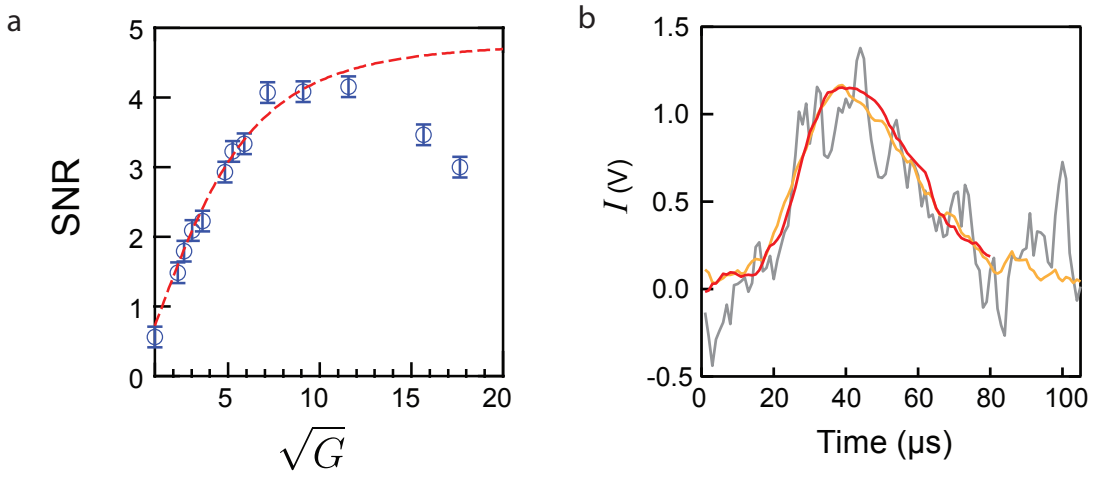

FIGURE 7.6: **Single-echo signal-to-noise ratio**. **a** Echo SNR dependence on JPA gain (blue circles), with error bars given in the text. Red-dashed line shows the JPA's SNR for a coherent signal, rescaled to these data, showing that the spin-echo signal-to-noise increases as expected from the earlier characterization of the JPA, until saturation. **b** Echo signal $I(t)$ averaged 10 times without JPA (grey), with JPA in non-degenerate mode (orange), with JPA in degenerate mode (red). The grey ($\times 38$, SNR=2 ± 0.5) and orange curve ($\times 2.2$, SNR=14 ± 1) were rescaled to the red (SNR=22 ± 3) for easy comparison.

7.2 Characterization of the sensitivity

7.2.1 Single-echo signal-to-noise ratio

To obtain the setup sensitivity, we also need to characterize the SNR of a single echo. We study the SNR for various JPA gains, using the homodyne detection setup and the JPA in phase-preserving mode. We evaluate separately the signal and the noise by the following procedure. First, we choose the local oscillator phase so that the echo lies entirely on the I quadrature. We then average 10 spin-echo signals yielding the averaged time-traces $I(t)$ from which we compute the signal using only a simple top-hat integration window such that:

$$\mathcal{S} = \frac{1}{T_E} \int_0^{T_E} \bar{I}(t) dt. \tag{7.9}$$

The noise is determined from 500 traces of the same duration acquired without any echo being triggered (microwave drive pulses turned off) as:

$$\mathcal{N}^2 = \frac{1}{T_E} \int_0^{T_E} \overline{I^2}(t) dt. \tag{7.10}$$

As shown in Fig. 7.6a, the resulting SNR$= \mathcal{S}/\mathcal{N}$ follows the same dependence on the JPA gain as determined using only the JPA. For the JPA in phase-preserving mode, at the optimal SNR value, the single-echo SNR (orange curve in Fig. 7.6b) is increased by a factor $\approx \times 7$ compared to a single-echo acquired with only the HEMT (grey curve in Fig. 7.6b) and reaches SNR$= 4$.

We now use the JPA in phase-sensitive (degenerate) mode, with the pump phase chosen so that the I quadrature which is aligned with the echo is amplified. As the gain increases by 6 dB while only increasing the noise power by 3 dB, the SNR is expected to increase by a factor $\sqrt{2}$ compared to the non-degenerate mode of the JPA. We find experimentally a factor 1.7, probably due to the fact that when the JPA is operated in phase-preserving gain, the necessity to filter the idler requires working

slightly detuned from the top of the JPA gain curve and thus the gain improves by a little more than 6 dB when shifting to phase-sensitive operation.

Summing up, the best absolute SNR reached is 7 ± 1 (red curve in Fig. 7.6b) a factor $\approx \times 11$ better than without JPA. The sensitivity of the spectrometer is thus:

$$N_{\min} = \frac{N_{\text{spins}}}{\text{SNR}} = 1.7 \times 10^3 \tag{7.11}$$

spins detected in a single-echo with a SNR unity. As T_1 was measured to be 0.3 s (see Fig. 6.9) in these conditions, the SNR determination was done with the repetition rate set at $\gamma_{\text{rep}}^{-1} = 3T_1 = 1$ s and thus the overall absolute sensitivity of the spectrometer is 1.7×10^3 spins/$\sqrt{\text{Hz}}$.

Spins spontaneous emission noise

The interest of determining separately the noise from the signal is to be able to determine more accurately the noise by accumulating more data, since every point can be acquired without having to wait $3T_1$. The statistical uncertainty of the SNR thus comes solely from the signal with $\varepsilon_{\text{SNR}} = 1/\sqrt{10}$ for the above determination.

However such a determination neglects any noise emitted by the spins such as the spontaneous emission noise n_{SE}. To evaluate nevertheless this contribution, we perform once again numerical simulations but include this time the quantum noise evaluation using the methods of [182]. The numerical results are shown in Fig. 7.5 and predict an excess noise of $\approx$ 30 % during the echo emission, that would scale down the measured SNR to 5.5 ± 1. Taking into account the fact that this noise is proportional to the number of spins N_{spins}(this assumption was checked numerically) being excited, the sensitivity reached with a SNR unity can be estimated to be $N_{\min} = 1.8 \times 10^3$ or equivalently 1.8×10^3 spins/$\sqrt{\text{Hz}}$.

Comparison to theoretical estimate

This experimentally determined sensitivity is in semi-quantitative agreement with the theoretical estimate of section 5.1.2, which predicted $N_{\min} = 400$ for our parameters (see Eq. 5.11). The gain of four-orders of magnitude compared to the state-of-the-art is consistent with the improvements made on the spectrometer setup. Working at low-temperatures yields a complete polarization of the spin ensemble, giving a factor 12 enhancement, but also permit to cool-down the microwave field to its ground state. With a detection made by a JPA in phase-sensitive mode, the quantum fluctuations are thus the dominant noise source, giving a factor ≈ 10 improvement on $N_{\min}$. Finally the choice of a high-quality factor resonator, together with its small mode volume, gives a factor 20 improvement.

The remaining discrepancy between the theoretical estimate and our experimental determination can be traced to various origins. First, the derivation of section 5.1.2 assumed that $\kappa \gg w$ and that the drive pulses were ideal; this is not the case in our experiment as explained earlier. Then, our experiment suffers from microwave losses (resonator internal losses, circulators and filters insertion loss, ...). In addition, our JPA is not perfect; in particular the contribution of the follow-up amplifiers to the total output noise is not negligible. Finally, in the experiment the signal was defined with a square time integration window (see Eq. 7.9), instead of the optimal output mode choice defined as in Eq. 5.8.

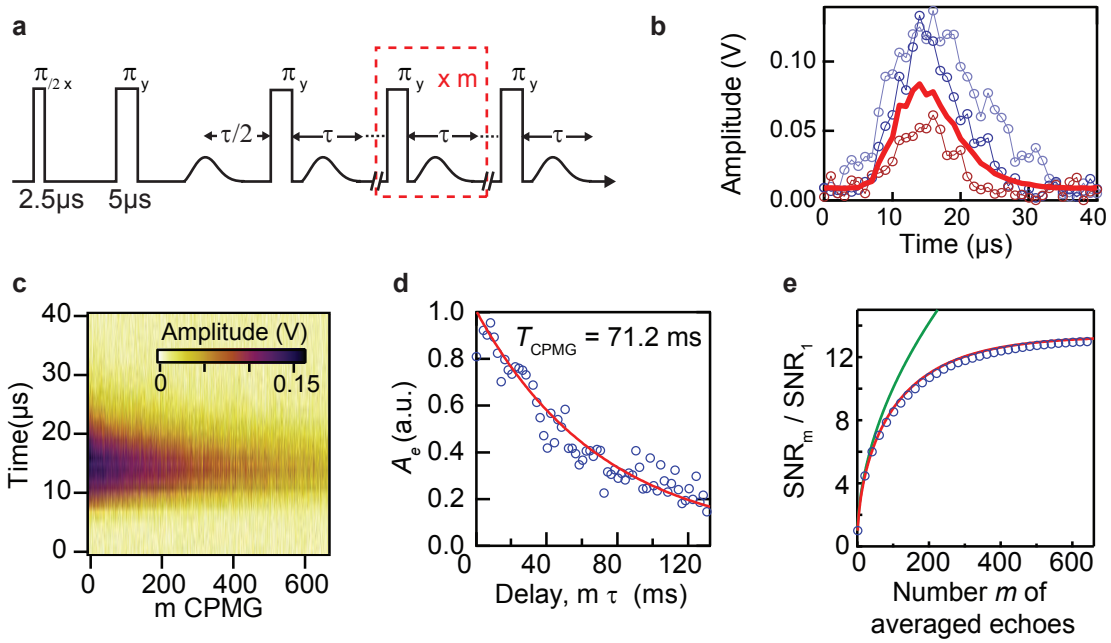

FIGURE 7.7: **CPMG sequence. a** A spin-echo generated by any pulsed ESR experiment can be refocused by a train of m π pulses with axis of rotation oriented along the echo phase direction. **b** Three time-traces (circles) of echoes $m_i = 1$ (light blue), $m_i = 100$ (dark blue) and $m_i = 600$ (dark red). Solid line shows the average over $m = 650$ echoes. **c** Color-plot giving the damping of echo m_i up to $m = 650$. **d** Decay of the echo integrated amplitude as a function of the time elapsed between the initial $\pi/2$ pulse and the echo (circle), well fit to an exponential of characteristic time $T_{\text{CPMG}} = 71.2$ ms. **e** Experimentally determined SNR enhancement obtained by averaging m echoes as a function of the number m of echoes in the CPMG sequence (blue circles), showing a 12-fold improvement. In the absence of decoherence the SNR should follow a $\sqrt{m}$-law (green curve). With damping (red, see text and Eq. 7.13), the SNR levels off for higher m.

7.2.2 Sensitivity enhancement by CPMG echoes

The sensitivity can be further increased by using a Carr-Purcell-Meiboom-Gill (CPMG) sequence [183]. As shown in Fig. 7.7a, adding m π_y pulses after the initial echo generated by a $\pi_x - \tau - \pi_y - \tau$ Hahn-echo sequence allows to refocus the spins m more times and thus recover m extra-echoes within a single sequence; all the echoes can then be averaged out to improve the SNR. Fig. 7.7b-c shows that for our Si:Bi sample up to 650 echoes can be recovered. The echo signal is seen to decrease exponentially with a characteristic damping time $T_{\text{CPMG}} = 71$ ms, a value ten times bigger than the time T_2 measured in Fig.6.10.

In terms of sensitivity, the recovered echoes can simply be averaged to enhance the SNR. While averaging m times the same signal yields a $\sqrt{m}$-enhancement, the echo damping levels off the enhancement at high m. Indeed, consider the accumulation of m echoes emitted at a a period T damped at rate T_{CPMG} and acquired with the same noise $\mathcal{N}$. The best SNR is obtained by weighting each echo with an exponentially decreasing weight $w_i = \alpha e^{-iT/T_{\text{CPMG}}}$. The overall normalization factor α for each weight is found by expressing that $\mathcal{N}_{(m)} = \sqrt{\sum_i w_i^2 \mathcal{N}_{(1)}^2} = \mathcal{N}^{(1)}$ and thus

$$\alpha^2 \frac{1 - e^{-2\text{mT}/\text{T}_{\text{CPMG}}}}{1 - e^{-2T/T_{\text{CPMG}}}} = 1. \tag{7.12}$$

It then comes that the signal is expressed as $\mathcal{S}_{(m)} = \sum_i \mathcal{S}_{(1)} \alpha e^{-i2T/T_{\mathrm{CPMG}}}$ so that the SNR enhancement reads:

$$\frac{\mathrm{SNR}_m}{\mathrm{SNR}_1} = \sqrt{\frac{1 - e^{-2\mathrm{mT}/\mathrm{T_{CPMG}}}}{1 - e^{-2T/T_{\mathrm{CPMG}}}}} \underset{T \ll T_{\mathrm{CPMG}}}{\longrightarrow} \sqrt{\frac{2T}{T_{\mathrm{CPMG}}}(1 - e^{-2\mathrm{mT}/\mathrm{T_{CPMG}}})} \tag{7.13}$$

Eq. 7.13 yields that for small m, the SNR increases as $\sqrt{m}$ but is bounded at $T_{\mathrm{CPMG}}/2T$ for larger values. We applied this averaging method to our experiment, as shown in Fig. 7.7e, demonstrating a 12-fold improvement over the single-echo SNR. This has the direct consequence of improving the sensitivity to $N_{\mathrm{min}} = 150$. Moreover as this technique does not require waiting a time $3T_1$ between each echo, the absolute sensitivity is also improved to 150 spins/$\sqrt{\mathrm{Hz}}$.

The sensitivity could be further increased if the CPMG damping was reduced, by for example using more complicated sequences alternating $\pi_{\pm y}$ and $\pi_{\pm x}$ such as the CPMG XY-8 sequence[184] up to the point where it becomes limited either by spin decoherence, or by pulse errors. We did not investigate such techniques in our ESR spectrometer.

7.3 Conclusion

The analysis above demonstrates that the combined use of low-temperatures, high-quality factors, small-mode volumes and quantum-limited amplifiers can dramatically enhance the sensitivity of an ESR experiment, with a 4-orders of magnitude enhancement compared to the state-of-the-art. This experiment places ESR in a new regime where the noise is no longer limited by thermal or technical noise but by the quantum fluctuations of the electromagnetic field.

The achieved sensitivity for our resonator detection volume of ~ 0.02 nl already enables ESR experiments at the nanoscale. More versatility could easily be obtained by patterning the resonator out of superconductors able to sustain higher magnetic fields (such as niobium) which would thus allow to study a wider range of spin species. Applications include studying single cells, small molecular ensembles, nanoparticles and nanodevices.

Finally, the sensitivity can be improved even beyond the above results. While the spin polarization is now maximum, the other quantities entering into play in the sensitivity can still be improved. Indeed, the quality factor can yet be increased by a factor of 2 or 3 if the losses were reduced to the current state-of-the-art $Q_{\mathrm{int}} > 10^6$. A straightforward enhancement could also come from the spin-photon coupling. While we reached $g/2\pi \sim 50$ Hz with a 5 µm wide wire, nano-fabrication techniques easily allow to scale down the wire transverse dimensions by a factor 100, which would yield an enhancement of the same factor on g and thus allow to improve the sensitivity up to the level of being able to detect only a few spins. Last, even if quantum fluctuations have become the primary noise source in our experiment, decreasing the noise beyond the standard quantum limit is possible with the use of squeezed quantum states as we will see in ch. 9.

Part III

The Purcell effect applied to spins

Chapter 8

Controlling spin relaxation with a cavity

> Coupling with the radiation is hopelessly inadequate as a relaxation mechanism
>
> *A. Abragam*, on nuclear spins [4].

Understanding and controlling spin relaxation is essential in applications such as spintronics, quantum information processing and magnetic resonance imaging. The energy relaxation time T_1 describes the return to equilibrium and has to be sufficiently long to permit coherent spin manipulation since $T_2 \leqslant 2T_1$. However a too long T_1 can become a major bottleneck, since the return to equilibrium will be prohibitively long and limit the repetition rate of an experiment, directly impacting factors such as the achievable sensitivity. An ideal situation would be to have the ability to re-initialize the spins on-demand while having a long T_1 to preserve the spin coherence. This can be achieved in particular systems by an active reset. For example,NV centers have a state-selective optical transition allowing to establish a spin polarization higher than 90% under laser illumination [185]. Coupling to the environment via other degrees of freedom can also reset the system: a neutral phosphorus donor in silicon can be initialized via its charge state when coupled to a single-electron transistor [122] or by selective Auger photo-ionization when coupled to a donor bound exciton [133].

For other spin systems, such active re-initialization schemes may not be available. This is particularly an issue at ultra-low temperature since the spin-lattice relaxation times can become very long due to the vanishing phonon density (see 4.4.1). For instance, T_1 reaches up to thousands of seconds for phosphorus donors at 1.2 K[16]. To shorten the spin relaxation times a number of in-situ methods have been developed such as chemical doping [186] and gamma irradiation [187]. Nevertheless such methods are not tunable and a too fast T_1 relaxation will ultimately affect the coherence time T_2. In short, for systems without an active reset, an efficient, universal and tunable initialization method for spin systems is still lacking.

In all listed spin relaxation phenomena, spontaneous emission of radiation is usually quickly dismissed as a possible spin relaxation mechanism due to the very weak coupling of spins to their electromagnetic environment. However, Purcell realized in 1946 that the spontaneous emission rate can be dramatically enhanced by placing the quantum system in a resonant cavity [188]. This effect has since then be used to control the lifetime of atoms [28] and semi-conducting heterostructures [29] coupled to microwave or optical cavities and is essential for the realization of high-efficiency single-photon sources [30]. In this chapter, we apply this idea to spins in solid to provide an on-demand re-initialization scheme. We first review cavity-enhanced spontaneous emission implementations before demonstrating experimentally the Purcell effect for bismuth donors in silicon. The last part will discuss how this effect can be harnessed to control in-situ the spin relaxation.

8.1 Cavity-enhanced spontaneous emission

As we have seen in ch. 3, spontaneous emission of radiation is due to the coupling of a two-level-system (TLS) to the quantum fluctuations of the electromagnetic field. If the TLS is in free space, an infinity of electromagnetic modes are available for the photon emission, resulting in an irreversible incoherent process. E. Purcell predicted in 1946 that by placing the TLS inside a cavity [188], spontaneous emission can be greatly inhibited or enhanced due to the modification of the mode density. This effect is captured by the so-called Purcell rate whose expression was derived in ch. 3 (see Eq. 3.37) and is a founding concept of the field of cavity Quantum Electrodynamics[189]. In his pioneering article of 1946, Purcell considered a nuclear spin embedded in a resonant structure, such as the resonant RLC circuit used in NMR. Because nuclear spin spontaneous emission occurs at a negligible rate due to the very weak coupling of the spin to the vacuum fluctuations, the first experimental observation was done instead with atoms in a microwave cavity [28].

Even if we have already derived the Purcell formula using the formalism of CQED in ch. 3, it is interesting to derive it here using other arguments to understand why it has not be observed up to now for spins. We thus first derive the theoretical expressions for spontaneous emission rates both for an electrical and a magnetic dipole before succintly recalling the Purcell effect. We review its experimental realizations in systems with an electrical dipole and then consider its application to spins.

8.1.1 Spontaneous emission into free space

The rate of spontaneous emission into free space Γ_0 can be derived using the Weisskopf-Wigner approximation, as explained for instance in [190]. Consider a spin with an energy splitting $\hbar\omega_s$ between its ground $|\mathfrak{g}\rangle$ and excited $|\mathfrak{e}\rangle$ state. As we have seen in ch. 3, its interacting Hamiltonian with the electromagnetic radiation is $\hat{H}_{\text{int}} = -\hat{\boldsymbol{\mu}} \cdot \hat{\boldsymbol{B}}(t)$. In the Heisenberg picture, the free-space quantized magnetic field is the sum of the quantized field of each mode of wavevector $\mathbf{k}$ and polarization state λ, $\hat{\boldsymbol{B}} = \sum_{\boldsymbol{k}\lambda} \hat{\boldsymbol{B}}_{\boldsymbol{k}\lambda}$ with $\hat{\boldsymbol{B}}_{\boldsymbol{k},\lambda}$ being [38]:

$$\hat{\boldsymbol{B}}_{\boldsymbol{k}\lambda} = i\sqrt{\frac{\mu_0\hbar\omega_k}{2V}}\boldsymbol{e}_{\boldsymbol{k}\lambda}\left(\hat{a}_{\boldsymbol{k}\lambda}e^{-i\omega_k t} - h.c.\right) \tag{8.1}$$

where $\boldsymbol{e}_{\boldsymbol{k}\lambda}$ are the two unit polarization vectors and V the quantization volume. We assume implicitly in this expression that the electromagnetic field is slowly varying at the spin location so that we can realize the dipole approximation $e^{i\boldsymbol{k}\cdot\boldsymbol{r}} \approx 1$. Following the same steps than in 3.2.1 for each mode $(\boldsymbol{k}, \lambda)$, the interaction Hamiltonian in the interaction picture after the rotating wave approximation is:

$$\hat{H}_{\text{int}} = \hbar\sum_{\boldsymbol{k}\lambda}(g_{\boldsymbol{k}\lambda}\hat{\sigma}_+\hat{a}_{\boldsymbol{k}\lambda}e^{-i(\omega_k-\omega_s)t} + h.c.) \tag{8.2}$$

where the coupling strength for each mode is now $g_{\boldsymbol{k}\lambda} = \langle\mathfrak{e} \mid \boldsymbol{\mu}\cdot\boldsymbol{e}_{\boldsymbol{k}\lambda} \mid \mathfrak{g}\rangle\sqrt{\mu_0\omega_k/(2\hbar V)}$. We next assume that at time $t = 0$, the spin is in its excited state while the elecromagnetic field is in its ground state, so that the overall state of the system is written:

$$|\Psi(t)\rangle = c_{\mathfrak{e},0}|\mathfrak{e},0\rangle + c_{\mathfrak{g},\boldsymbol{k}\lambda}|\mathfrak{g},1_{\boldsymbol{k}\lambda}\rangle \tag{8.3}$$

with $c_{\mathfrak{e},0}(0) = 1$ and $c_{\mathfrak{g},\boldsymbol{k}\lambda}$. Using the Schrödinger equation $|\dot{\Psi}(t)\rangle = -\frac{i\hat{H}_{\text{int}}}{\hbar}|\Psi(t)\rangle$, one can show that the evolution of the coefficient $c_{\mathfrak{e},0}$ is given by the following differential-integral equation:

$$\dot{c}_{\mathfrak{e},0} = -\sum_{\boldsymbol{k}\lambda}|g_{\boldsymbol{k}\lambda}|^2\int_0^t e^{-i(\omega_k-\omega_s)(t-t')}c_{\mathfrak{e},0}(t')dt' \tag{8.4}$$

	Nuclear spin $1/2$[188]	**Electronic spin** $1/2$[5]	**Sodium atom** [28] $\lvert 23S\rangle \leftrightarrow \lvert 22P\rangle$
$\omega_0/2\pi$	10 MHz	7 GHz	340 GHz
Interaction	$\mu = \mu_N$	$\mu = \hbar\gamma_e S$, $\gamma_e = 28$ GHz/T	$d = 570D$
Γ_0 (s^{-1})	3×10^{-28}	1×10^{-12}	145
Γ_1 at $T = 4$ K (s^{-1})	5×10^{-24}	2.4×10^{-11}	150
Γ_1 at $T = 300$K (s^{-1})	4×10^{-22}	2×10^{-9}	6×10^3

TABLE 8.1: Spontaneous emission rate at zero, helium and room temperature for various systems emitting microwave radiation in free space. μ_N is the nuclear magneton, γ_e the electron gyromagnetic ratio.

The sum over the wavevectors may be replaced by an integral over $\boldsymbol{k}$-space, spanned by spherical coordinates with the z-axis aligned on $\boldsymbol{\mu}$ so that $\boldsymbol{\mu}.\boldsymbol{k} = dk\cos\theta$:

$$\dot{c}_{\mathfrak{e},0} = \int_{\omega=0}^{\infty} \rho(\omega)d\omega \int_{\theta=0}^{\pi}\int_{\varphi=0}^{2\pi} \sin\theta\, d\theta\, d\varphi \sum_{\lambda} |g_{\omega\lambda}|^2 \int_0^t e^{-i(\omega-\omega_s)(t-t')} c_{\mathfrak{e},0}(t')dt' \tag{8.5}$$

with the mode density $\rho(\omega)$ being $\frac{\omega^2 V}{8\pi^3 c^3}$. In this coordinate system, one can show that $|g_{\omega\lambda}|^2$ simplifies to $\tilde{\mu}^2\sin^2(\theta)\mu_0\omega_k/(2\hbar V)$ where $\tilde{\mu} = |\langle \mathfrak{e} \mid \mu \mid \mathfrak{g}\rangle|$. Next, as $c_{\mathfrak{e},0}(t)$ is expected to decay at a rate $\sim \Gamma_0$ much smaller than the frequency ω, $\int_0^\infty e^{-i(\omega-\omega_s)(t-t')}c_{\mathfrak{e},0}(t')dt'$ can be approximated as $\approx \pi\delta(\omega-\omega_s)c_{\mathfrak{e},0}(t)$, doing the so-called Weisskopf-Wigner approximation [190]. Performing the integration over θ, ϕ and ω, Eq. 8.5 thus yields:

$$\dot{c}_{\mathfrak{e},0} = -\frac{\mu_0\tilde{\mu}^2\omega_s^3}{6\pi\hbar c^3} c_{\mathfrak{e},0}(t) \tag{8.6}$$

Identifying the decay rate in Eq. 8.6 to $\Gamma_0/2$, we find the usual expression of Γ_0 for a magnetic dipole into free space [4]:

$$\Gamma_0^{(\mathrm{magn})} = \frac{\mu_0\tilde{\mu}^2\omega_s^3}{3\pi\hbar c^3} \tag{8.7}$$

The derivation for an electrical dipole $\boldsymbol{d}$ is similar: the interacting Hamiltonian is given by $\hat{H}_{\mathrm{int}} = -\hat{\boldsymbol{d}}\cdot\hat{\boldsymbol{E}}(t)$ and the free-space quantized electrical field $\hat{\boldsymbol{E}}$ is linked to $\hat{\boldsymbol{B}}$ by $\boldsymbol{E}_{\boldsymbol{k},\lambda} = \boldsymbol{B}_{\boldsymbol{k},\lambda}\times\boldsymbol{e}_k/\sqrt{\mu_0\varepsilon_0}$. Following the same steps, we obtain:

$$\Gamma_0^{(\mathrm{elec})} = \frac{\tilde{d}^2\omega_s^3}{3\pi\varepsilon_0\hbar c^3} \tag{8.8}$$

Interestingly, if we consider a Bohr magneton μ_B and the dipole created by two elementary charges separated by a Bohr radius $d \sim ea_0$ the ratio of their spontaneous emission is $\Gamma_0^{(\mathrm{elec})}/\Gamma_0^{(\mathrm{magn})} = \frac{c^2d^2}{\mu^2} = \frac{1}{\alpha^2}$ where α is the fine structure constant, confirming that an electrical dipole is naturally more strongly coupled to the field than a magnetic dipole.

These rates are derived under the assumption that there are no thermal photons populating the electromagnetic field. If it is at thermal equilibrium at a temperature T, its thermal photon occupancy is $n_{\mathrm{th}}(T)$ (see Eq. 2.10). As we have seen in ch. 3 (see Eq. 3.45), the resulting relaxation rate is modified to $\Gamma_1(T) = (2n_{\mathrm{th}}(T)+1)\Gamma_0$. Due to the ω_s^3 dependence and to the strength difference between electric and magnetic dipole transitions, the spontaneous emission rates at 4 K and 300 K for a Rydberg atom, an electronic spin, and a nuclear spin range from easily detectable values to the age of the universe, as shown in Table 8.1.

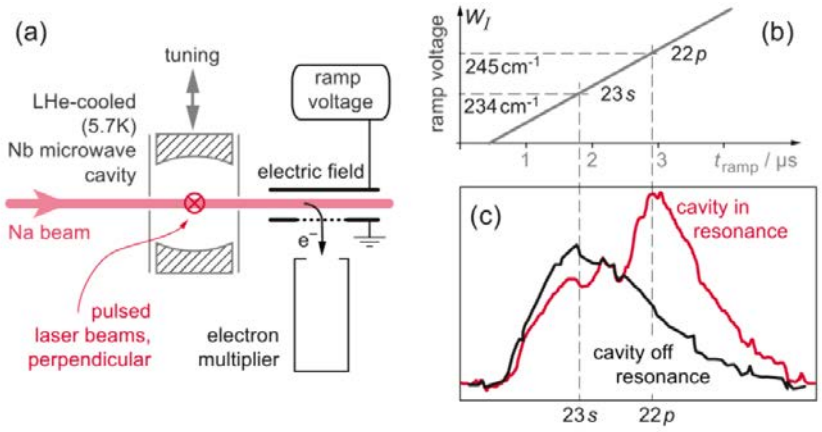

FIGURE 8.1: **Experimental evidence of the Purcell effect with Rydberg atoms [28]. a** Setup schematic. **b** Ramp voltage tuning to detect $|23S\rangle$ or $|22P\rangle$ levels. **c** Experimental signal showing the signal measured when the cavity is off resonance (black) and on resonance (red). Figures extracted from [28, 192]

8.1.2 The Purcell effect

The Purcell effect dramatically enhances the spontaneous emission of a TLS since the resonant structure in which it is embedded has a mode density peaked at ω_0 which can be orders of magnitude larger than the vacuum mode density. It can also inhibit the spontaneous emission when the cavity is non resonant with the two-level system and acts as a filter [191]. In ch. 3, using cavity QED formalism, we have shown that the cavity-enhanced spontaneous emission rate was (see Eq. 3.37):

$$\Gamma_p(\Delta) = \kappa \frac{g^2}{\Delta^2 + \kappa^2/4} \tag{8.9}$$

where κ is the cavity emission rate, Δ the detuning between the cavity and the TLS, and g the coupling constant. Instead of this formula, the Purcell effect is usually given by a parameter called the "Purcell factor" defined by $\eta_P = \Gamma_p(\Delta = 0)/\Gamma_0$ and expressed as a function of a quantity called the resonator mode volume, defined as $V_{\text{eff}} = \int_V |f(\boldsymbol{r})|^2 d\boldsymbol{r}$ with $f(\boldsymbol{r})$ a dimensionless function proportional to the field mode amplitude at location $\boldsymbol{r}$ with maximal value 1. Eq. 8.9 gives $\Gamma_p(\Delta = 0) = 4g^2/\kappa$, where the coupling constant can be expressed as $g^2 = \tilde{\mu}^2 \mu_0 \omega_s / 2\hbar V_{\text{eff}}$. Using Eq. 8.7, we then obtain that:

$$\eta_p = \frac{3}{4\pi^2} \frac{Q\lambda^3}{V_{\text{eff}}} \tag{8.10}$$

where $\lambda = 2\pi c/\omega_s$, which precisely corresponds to the original Purcell formula [4]. At radio frequencies, the Purcell factor can be very large. For a nuclear (electronic) spin inside an usual NMR(ESR) cavity (Q = 1000, $V_{\text{eff}} = 1\text{mm}^3$), it is as large as $\eta_P = 8 \times 10^{12} (2 \times 10^4)$. Nevertheless, due to the very weak values of the spontaneous emission rate in these systems, even the Purcell-enhanced spontaneous emission remains usually negligibly small. In the optical domain, the achievable Purcell factors are closer to unity because the cavity dimensions are usually larger than the emission wavelength. However since relaxation times are already limited by spontaneous emission in free space, the Purcell effect is readily observable.

8.1.3 Experimental realizations

The first experimental evidence of the Purcell effect came from the optical domain with observed intensity and rate alterations in the fluorescence of dye molecules deposited on a thin dielectric

layer over a metal substrate with both magnetic and electric dipoles [193]. A more quantitative test of Purcell-enhanced relaxation was performed with sodium Rydberg atoms flying through a microwave Fabry-Pérot cavity in 1983 in the Haroche group [28], see Fig. 8.1a. The transition labelled $|23S\rangle \leftrightarrow |22P\rangle$ occuring at 340 GHz is tuned to resonance with a superconducting cavity of quality factor $Q \sim 10^6$. The experiment is realized at 4 K where the thermal occupation of the intra-cavity field is below 2% and the spontaneous emisison rate into free space is $\Gamma_1 = 150\ \mathrm{s}^{-1}$ due to the large electrical dipole of the targeted transition. The sodium atoms are prepared in the $|23S\rangle$ state and fly through the cavity one by one before being detected via state ionization. By sweeping the voltage applied on the condenser plates realizing the ionization, the probabilities for the atoms to be in the states $|23S\rangle$ or $|22P\rangle$ are detected at different times, Fig. 8.1b. When the cavity is resonant with the transition, the Purcell effect increases the probability for the atom to decay to $|22P\rangle$ during the time the atom spends in the mode. Thus a larger signal is detected at the corresponding $|22P\rangle$ voltage when the cavity is tuned at resonance, see Fig. 8.1c. The measured spontaneous emission rate enhancement was in good agreement with the expected Purcell factor $\eta_P = 530$. Purcell-inhibition was demonstrated a few years later also in the microwave domain with a single electron in a Penning trap [194] and with Rydberg atoms [195]. Those results were the first experimental milestones in the development of CQED.

Following this, cavity-enhanced and inhibited spontaneous emission were observed for systems emitting radiation in the near-infrared and optical domains: caesium [196] and ytterbium [197] atoms as well as dye molecules [198]. This last experiment pioneered the control of spontaneous emission with microcavities, where the cavity characteristic size is comparable to the wavelength of emission. Microcavities made out of semiconducting heterostructures [199] were then used to control spontaneous emission of free excitons in GaAs quantum wells [29, 200] and later on of quantum dots in InAs [30]. It made possible the development of ultra-bright single photon sources by placing a single emitter in a nanostructure to increase both the spontaneous emission rate and the collection efficiency. Various structures have been developed over the last fifteen years for quantum-dots and optical defects based photon sources: micro-pillars [30], micro-disks [201], photonics crystals [202, 203], as well as plasmonic structures such as gold particles [204].

8.1.4 Spontaneous emission with spins

Due to the very weak coupling of their magnetic dipole to vacuum fluctuations, spins have never reached a regime where their dominant relaxation mechanism was spontaneous emission – even though they are indeed placed in a cavity used for detection in magnetic resonance. Nevertheless

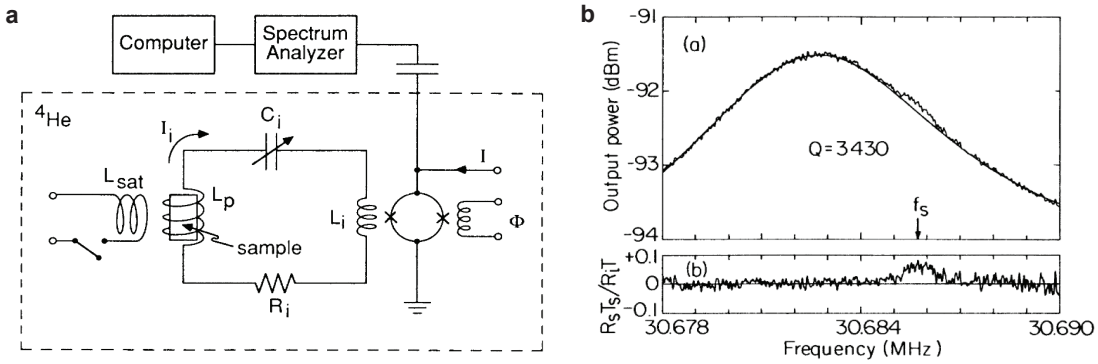

FIGURE 8.2: **Nuclear spin noise. a** A sample of $NaClO_3$ is embedded in a LCcircuit linked to a SQUID amplifier. **b** Output power spectrum of the resonator showing the spin spontaneous emission noise. Figures extracted from [187, 153].

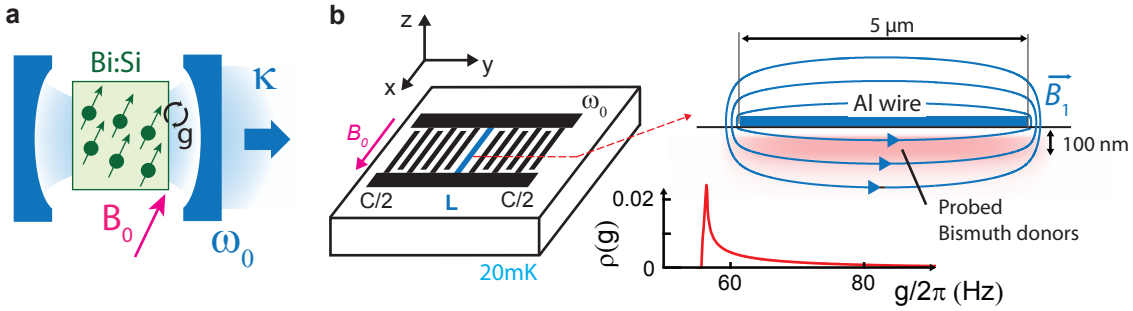

FIGURE 8.3: **Experimental scheme. a** To implement the Purcell effect, an ensemble of bismuth donors in silicon is embedded in a cavity. **b** The cavity is implemented by a LC lumped element resonator (see Fig. 5.9), whose inductive wire couples to the spins with a coupling constant distribution peaked at 56 Hz.

in 1985, Sleator et al. were able to detect the spontaneous emission of nuclear spins [187, 153]. A sample of $NaClO_3$ containing ^{35}Cl nuclei is embedded in a resonator of frequency 30 MHz and quality factor $Q = 1000$, Fig. 8.2a, yielding $\eta_P = 10^{11}$ and a corresponding enhanced spontaneous emission rate $\Gamma_p = 10^{-16}\mathrm{s}^{-1}$. Even in the absence of any external radiofrequency drive, the nuclear spins spontaneous emission results in voltage fluctuations in the readout circuit. When starting from a saturated spin ensemble where $N_{\mathrm{spins}}/2$ spins are in their excited state, the power emitted by spontaneous emission is $\hbar\omega_s\Gamma_p N_{\mathrm{spins}}/2$. Due to the large number of spins $N = 10^{21}$ in the experiment, this power was large enough to be detected as an added bump in the resonator output power spectrum, see Fig. 8.2b. Nevertheless the associated radiative relaxation rate $T_1 \approx 3000$ years remained significantly larger than the non-radiative dominant relaxation times estimated to be on the order of days in the experiment.

8.2 Experimental implementation for electronic spins

Here we reach the regime in which the Purcell effect is so strong that spontaneous emission becomes an efficient relaxation mechanism for the spins to return back to equilibrium [27]. Our experiment is suited to operate in this regime since on one hand Si:Bi are expected to have long phonon-limited relaxation times at 20 mK (of order 10^5 s, see ch. 4). On the other hand, the steps undertaken in the previous chapters to increase the ESR sensitivity, namely a small resonator mode volume and a high quality factor, result in a large Purcell factor[1] $\eta_P \approx 1 \times 10^{13}$ that lead to spontaneous emission times on the order of seconds; thus making it possibly the dominant spin relaxation mechanism.

8.2.1 Cavity-spin system

The cavity is implemented by the aluminum superconducting resonators deposited at the surface of the bismuth implanted sample, designed and characterized in ch. 5. In this section, we only use resonators B and C, whose quality factors are in the 10^5 range (see Table 8.2). The quantum fluctuations $\delta\boldsymbol{B}$ of the resonator field are responsible for the Purcell-enhanced spontaneous emission. Without any intra-cavity thermal state, the cavity-enhanced spontaneous emission rate is simply given by the Purcell formula at resonance $\Gamma_p(\Delta = 0) = 4g^2/\kappa$.

When a thermal state is present, the steady-state polarization of the ensemble is reduced and the relaxation rate is increased by $2n_{\mathrm{th}} + 1$ (see Eq. 3.45). Considering our setup and the microwave lines

[1] We consider $Q = 10^5$, $\omega_0/2\pi = 7.3$ GHz. To evaluate V_{eff}, we use the microwave fields simulations of Fig. 5.10 to determine $f(\boldsymbol{r})$ and we obtain $V_{\mathrm{eff}} = 5 \times 10^4$ μm^3 $= 0.05$ pL.

	$\omega_0/2\pi$ GHz	Q	$\boldsymbol{B}_0$ mT	$P_{\rm in}(\pi)$ pW	κ_1 s^{-1}	$\bar{n}(\pi)$	$g/2\pi$ Hz	T_1 s
B	7.246	3.2×10^5	5.13	1.9	5.8×10^4	1.0×10^6	50 ± 7	0.26 ± 0.08
C	7.305	1.1×10^5	2.78	4.6	3.1×10^5	7.4×10^5	58 ± 7	0.75 ± 0.15

TABLE 8.2: **Experimental values for resonators B & C.** Resonator X, with frequency ω_0 and quality factor Q is resonant with transition $|9\rangle \leftrightarrow |10\rangle$ at magnetic field $\boldsymbol{B}_0$. From Rabi oscillations, the input power of a π pulse of duration 5μs can be determined. Knowledge of Q and κ_1 the input coupling rate allow to link $P_{\rm in}$ to $\bar{n}$ the intra-cavity mean photon number for a π pulse and to the spin-resonator coupling constant g_0. The Purcell formula allows to estimate the expected enhanced spontaneous emission time at resonance.

shielding (see ch. 5), we expect $n_{\rm th} = 0.05$ and additional measurements (described in Appendix A) confirms $n_{\rm th} = 0.05 \pm 0.05$. We can therefore expect T_1 values given by:

$$T_1 = \Gamma_p^{-1}(0)/(2n_{\rm th} + 1) \tag{8.11}$$

The experiments are realised on the low-field peak of the transition $|9\rangle \leftrightarrow |10\rangle$, with the applied magnetic field $\boldsymbol{B}_0$ aligned along the wire ($\theta = 0$), see Table 8.2. As explained in ch. 6, this peak originates from spins located under the wire. An estimate of the spin-coupling constant over this spin sub-ensemble yields a distribution sharply peaked on $g/2\pi = 56 \pm 1$ Hz, (see Fig. 8.3b and 5.3.3).

8.2.2 Experimental estimate of g

Rabi oscillations can be performed to obtain an independent estimate of g, see Fig. 8.4c. As explained in 6.1.3, their frequency $\Omega_R = 2g\sqrt{\bar{n}}$ directly yields g upon knowledge of the incident power $P_{\rm in}$ and the measured input and output coupling rates. The precision of this determination is limited by

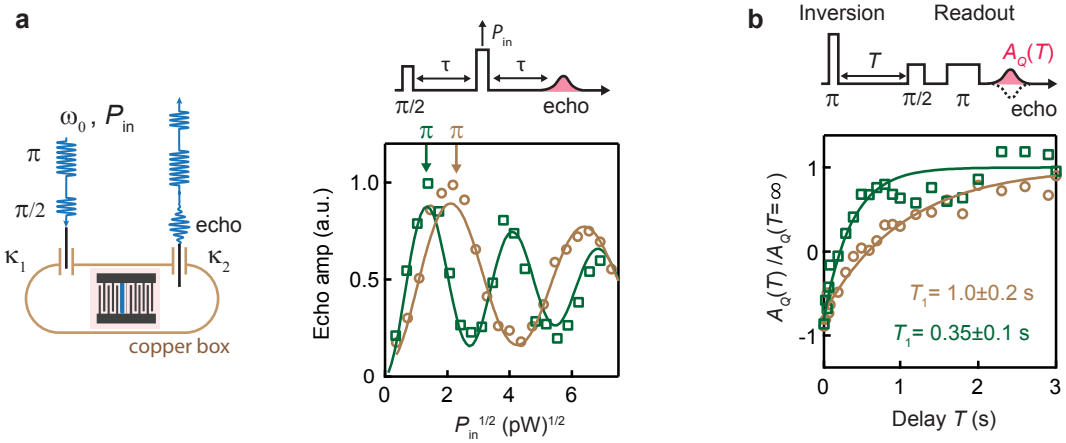

FIGURE 8.4: **Purcell-limited T_1. a-b** Data obtained with the static field $\boldsymbol{B}_0$ parallel to the inductor ($\theta = 0$). The symbols represent data for resonator B (green squares) and resonator C (brown circles) **a** Rabi oscillations are driven by varying the cavity input power of the refocusing π pulse (5 µs-long) applied $\tau = 300$ µs after the first $\pi/2$ pulse. Solid lines are exponentially damped sinusoidal fits. **b** The inversion-recovery sequence is used to measure the spin relaxation time T_1 (see 6.3.1). Solid lines are exponential fits to the data with time constant T_1. The uncertainty is given by the standard deviation of the exponential fit parameters.

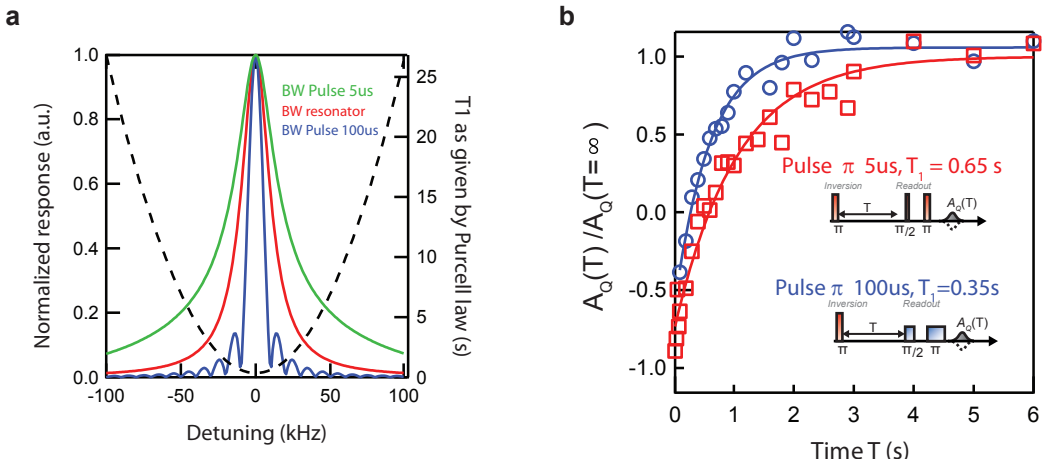

FIGURE 8.5: $T_1(\Delta = 0)$ **bandwidth. a** Bandwidths (left axis) of resonator B(green) and applied readout sequences with pulses of 5 µs (green) and 100 µs (blue) resulting in an averaging effect on the measured T_1 (right axis). **b** Comparison of T_1 measured with readout pulses of 5 µs (red squares) and 100 µs (blue circles). The spin energy relaxation time T_1 being of order 1 s, we choose a repetition rate $\gamma_{\rm rep}$ =0.04 Hz sufficiently low to allow full relaxation of the spins in-between successive inversion recovery sequences.

the accuracy on $P_{\rm in}$ which we estimate to be of 30%. The values obtained for resonators B and C (see Table 8.2) are in good agreement with the numerical estimate.

From the experimental determination of g, the measured resonator quality factors and $n_{\rm th}$, the expected spontaneous emission rate at resonance can be estimated to be $T_1 = 0.26 \pm 0.08$ s for resonator B and $T_1 = 0.74 \pm 0.15$ s for resonator C, see Table 8.2. We can also evaluate the spin-ensemble cooperativity (see Eq. 3.51) to evaluate the relevance of collective radiation effects. Using the numerical simulations of ch. 7 we find $C_B = 0.26$ and $C_C = 0.09$. Since both are below 1, we thus expect that spins will relax independently from each other, with an exponential decay at rate Γ_P.

8.2.3 T_1 at resonance

As explained in section 6.3.1, T_1 is measured by the inversion-recovery sequence shown in Fig. 8.4c, consisting in a π pulse followed after a varying delay T by a spin-echo readout sequence. The resulting echo signal $A_Q(T)$ comes from all spins whose frequency lies in the readout sequence pulse bandwidth. To avoid an averaging effect on the measured T_1 arising from its dependence on Δ, the detection bandwidth has to be small (see 6.1.3). For the narrowest bandwidth $\kappa/2\pi = 23$ kHz of resonator B, Fig. 8.5a shows that pulses of 5 µs are heavily filtered by the resonator and have a bandwidth of 40 kHz whereas 100 µs-long pulses have a reduced bandwidth of ≈ 10 kHz. In the case of 100 µs-long pulses, only spins with $|\Delta|/2\pi \leq 5$ kHz contribute to the signal, corresponding to a negligible dispersion of 5% for the Purcell relaxation times. Indeed, as illustrated in Fig. 8.5b, no averaging effect is observed for a T_1 measured with 100 µs-long pulses whereas a T_1 acquired with 5-µs–long pulses is 50% longer. Therefore we chose to use 100 µs-long readout pulses although the inversion pulse bandwidth is chosen to be large ($t_\pi = 5$ µs) in order to maximize the inversion efficiency.

The relaxation curves measured for resonators B and C are shown in Fig. 8.4c and are well fitted by exponential decays. The extracted characteristic times yield $T_1 = 0.35 \pm 0.1$ s for resonator B and $T_1 = 1.0 \pm 0.2$ s for resonator C. This is in close agreement with the predicted values (see Table 8.2). Resonators B and C have a factor 3 difference in their quality factor, a factor that we retrieve in their

relaxation times. From these results we can infer that cavity-enhanced emission is the dominant spin relaxation mechanism in our experiment.

8.3 Controlling spin relaxation

We now show how the Purcell effect can provide a method to tune T_1 in-situ and on-demand. Indeed, the Purcell rate depends on three quantities that can be tuned experimentally:

- **the cavity quality factor** Q. At resonance, the Purcell rate is proportional to Q. This is evidenced in our experiment by the dependence of the relaxation times measured at resonance for resonators B and C on their quality factors. A dynamic control of the quality factor could be achieved by using Josephson junction devices [205, 206]. We have not explored this option.
- **the spin-cavity coupling constant** g**.** At resonance, the Purcell rate is proportional to g^2. In our experiment, due to the strain applied by the aluminum wire on the silicon substrate, we can access different subsets of spins coupled at different strengths to the resonator to probe this dependence (see 6.2.2). In our setup, the coupling constant can also be altered in-situ by changing the angle between the static field $\boldsymbol{B}_0$ and the microwave field $\delta\boldsymbol{B}$, as will be shown below.
- **the spin-cavity detuning** Δ. The Purcell rate is strongly dependent on the spin-cavity detuning which can be controlled by changing $\boldsymbol{B}_0$.

8.3.1 Tuning T_1 via the spin-cavity coupling g_0

Purcell-limited T_1 dependence on B_0

In our experiment, the spin frequency spread $\Delta\omega$ is much larger than the resonator bandwidth κ. By applying various magnetic fields $\boldsymbol{B}_0$, different spin subsets are brought to resonance. Since the line inhomogeneity is due to the strain applied by the aluminum (see ch. 6), the spin frequency is correlated to their spatial position with respect to the wire, which is also correlated to the spatial dependence of $\delta\boldsymbol{B}(\boldsymbol{r})$ and thus to g. We evidenced this effect in 6.2.2 via the magnetic field $\boldsymbol{B}_0$ dependence of the Rabi oscillations frequency (see Fig. 8.6a). From this measurement, we estimate g with values ranging from 20 to 90 Hz for B_0 ranging from 4.9 to 5.4 mT for resonator B.

We measure T_1 relaxation times with an inversion recovery sequence at various magnetic fields $\boldsymbol{B}_0$ on a range covering the entire spin frequency distribution (see Fig. 8.6b). As anticipated, we find a strong dependence of T_1 on $\boldsymbol{B}_0$, with values ranging from 1 to 8 s. To verify that T_1 scales as g^{-2}, we plot $(T_{1,i}/T_{1,0})$ as a function of $(g_i/g_0)^{-2}$ with $T_{1,0} = T_1(5.13\ \mathrm{mT})$ and $g_0 = g(5.13\ \mathrm{mT})$ and $T_{1,i}$ and g_i the values at different magnetic fields. The corresponding experimental data shown in Fig. 8.6c demonstrate quantitatively that within the experimental errors bars T_1 depends linearly on g^{-2} as expected from the Purcell law.

If we focus on a single magnetic field $B_0 = 5.13$ mT, we note that $T_{1,0} = 1.4 \pm 0.2$ s which is a factor 2 longer than expected for an estimated $g_0/2\pi = 56$ Hz and a thermal photon occupancy $n_{\mathrm{th}} = 0.05$. Two factors can explain this error. First, the measured quality factor was by mistake not determined at the single-photon limit and thus could be wrong by a factor 2 (see 5.3.4). Secondly, g is determined with two uncertainties: the input power P_{in} is known only at 1 dB precision and in

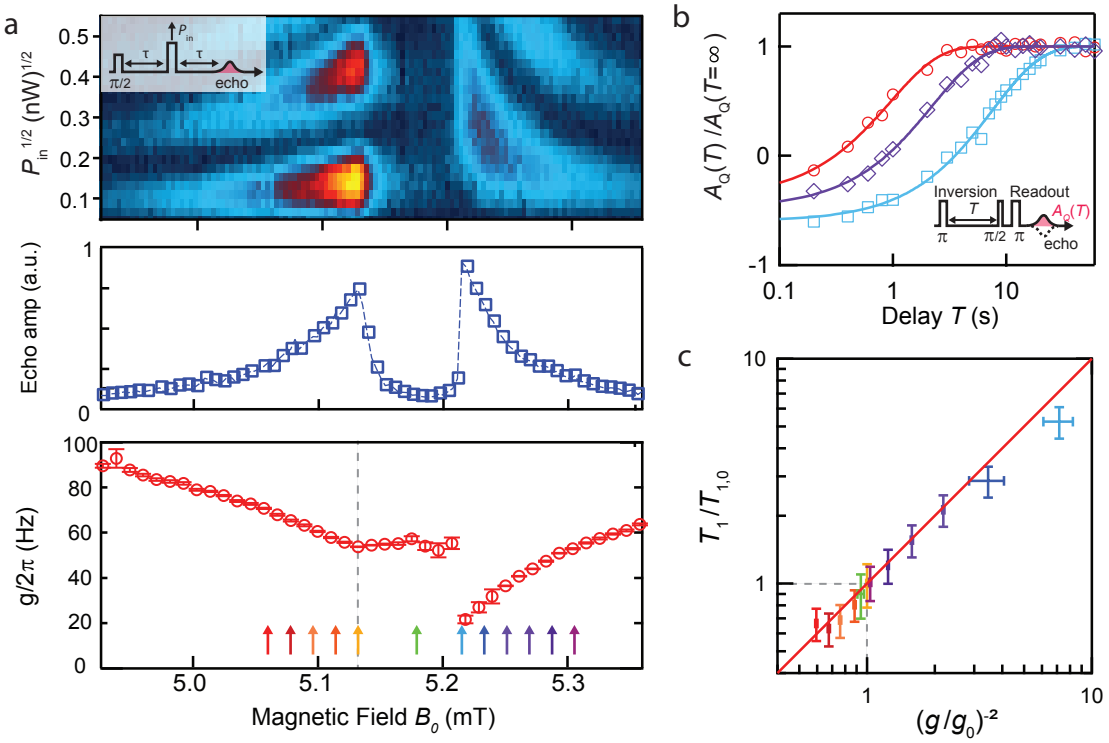

FIGURE 8.6: **Dependence of Purcell relaxation on spin-cavity coupling** $g_0(B_0)$. **a** (top) Rabi oscillations as a function of the magnetic field. (middle) Hahn-echo magnetic field sweep (botttom) Coupling constant distribution extracted from Rabi oscillations, with uncertainty solely estimated from the fit (neglecting the 30% uncertainty from the knowledge of the attenuation of the line). **b** T_1-relaxation measured by inversion-recovery as a function of $\boldsymbol{B}_0$. For clarity, only three values of $\boldsymbol{B}_0$ are shown: 5.06 mT (red circles), 5.29 mT (purple diamonds) and 5.22 mT (blue squares). **c** Measured $T_1/T_{1,0}$ as a function of measured coupling constant $(g/g_0)^{-2}$, as evaluated from the Rabi oscillations (filled circles, color corresponds to $\boldsymbol{B}_0$, with arrows on **a**). The index 0 denotes data taken for $B_0 = 5.13$ mT (grey dashed line on **a**). The uncertainties are determined from the σ-values extracted from the T_1 and Rabi oscillations fits. The solid red line is the demarcation y=x. All data was collected with resonator B, with $Q = 1.05 \times 10^5$ and $\theta = 0$.

this particular run the couplings κ_1 and κ_2 for each resonator were not determined, leading us to rely on assumptions[2] to estimate the intra-cavity photon number $\bar{n}$.

In spite of this remaining uncertainty, we can still harness the linear dependence of T_1 on g^2 to control T_1: here we show that we can access values of T_1 ranging over one order of magnitude. We note that the spatial dependence of T_1 could be evidenced more straightforwardly if the spin ensemble was attached to the tip of a scanning probe, and could be displaced with respect to the resonator.

[2]Compared to the couplings presented in Table 8.2, the chip was oriented differently and resonators B & A have reversed positions with respect to the input and output antennas whereas resonator C had the same spatial position. Assuming a posteriori that the losses were identical for each resonator, we can estimate $\kappa_{\text{int}} = 3.1 \times 10^5 s^{-1}$ by supposing the couplings for resonator C are identical to Table 8.2. Then by assuming resonator B has the same asymmetry in coupling as resonator A had, we can evaluate $\kappa_1 = 9.4 \times 10^3 s^{-1}$ and are able to determine the intra-cavity photon number $\bar{n}$ and thus determine $g_0/2\pi = 56$ Hz.

Purcell-limited T_1 dependence on θ

Our 2D coil magnet offers another method to control g in-situ. The experimental 2D-coils setup allows to tilt $\boldsymbol{B}_0$ within the resonator plane with an angle θ with respect to the resonator wire. As a consequence of the spin system isotropy, the spin quantization axis is always aligned along $\boldsymbol{B}_0$. The particular sub-ensemble of spins lying under the wire is excited by a field $\boldsymbol{B}_1$ mainly parallel to the surface, with only a small out-of-plane component. By tuning θ, the quantization axis can be tuned from being perpendicular to $\boldsymbol{B}_1$, a geometry that maximizes the coupling to the resonator, to being parallel to $\boldsymbol{B}_1$ which leads to a vanishing coupling to the field. This θ-dependence of g_0 is captured in the following relation (see Eq. 5.20):

$$[g(\theta)]^2 = g_y^2 \cos^2(\theta) + g_z^2 \tag{8.12}$$

where $g_z \propto \delta B_z$ and $g_y \propto \delta B_y$, see Fig. 8.7a. To experimentally test this expected θ-dependence, we perform Rabi-oscillations at varying angles θ, as shown in Fig. 8.7b. We performed this experiment on resonator C using the $|9\rangle \leftrightarrow |10\rangle$ transition. The frequency of the Rabi oscillations is decreasing as a function of θ, which indicates decreasing values of $g(\theta)$, as seen in Fig. 8.7c. For large angles θ, the coupling becomes too small to detect a signal, explaining the disappearance of the Rabi oscillations. A fit of $g(\theta)$ with Eq. 8.12 yields $g_y/2\pi = 55$ Hz and $g_z/2\pi$ =17 Hz.

T_1 relaxation curves as a function of θ are then measured with an inversion recovery sequence (see Fig. 8.7d). Smaller values of T_1 are measured for larger θ as expected from the reduced coupling of the spin to the microwave field. Plotting $1/T_1(\theta)$ versus $\cos^2(\theta)$ shows a linear dependence (see Fig. 8.7e). It follows the theory line given by the Purcell relation evaluated with the $g(\theta)$-fit from Fig. 8.7c (red solid line) and the measured quality factor for resonator C (given in Table 8.2).

Here, we have been able to control the relaxation time T_1 by a factor 3 by tuning the spin-cavity coupling constant. Larger tuning factors could be obtained with a better $\boldsymbol{B}_1$ homogeneity over the probed spin ensemble, which would allow to better align $\boldsymbol{B}_1$ on $\boldsymbol{B}_0$ and thus to suppress completely the spin-microwave coupling.

8.3.2 Tuning T_1 via the spin-resonator detuning

Experimental protocol

According to Eq 8.9, T_1 should strongly depend on the spin-cavity detuning if it is indeed limited by the Purcell effect. To test this effect we introduce in the T_1 measurement sequence a magnetic field pulse of amplitude $\boldsymbol{B}_\Delta$ and of duration T between the spin excitation and the readout spin-echo sequence (see Fig. 8.9a), which results in a temporary detuning Δ of the spins given by $\Delta = \frac{d\omega_s}{\mathrm{dB}}\boldsymbol{B}_\Delta$. As the spins are detuned from the resonator during this waiting period they have a smaller Purcell decay rate leading to a reduced polarization decay during the time T. The decay of the echo signal amplitude A_Q as a function of T yields the detuned spins energy relaxation time.

The magnetic field pulse $\boldsymbol{B}_\Delta$ is implemented by applying a current pulse on one of the Helmholtz coils used to apply the static field $\boldsymbol{B_0}$, see Fig. 8.8a. The pulse is output by a pulse generator with $50\,\Omega$ output impedance placed in parallel to the DC supply of one of the Helmholtz coils. To calibrate the additional magnetic field pulse, the generator is used in continuous mode to realize a field sweep echo spectroscopy yielding directly the voltage to B_0 conversion factor, as seen in Fig. 8.8b. Note that pulsing only one of the two coils also slightly modifies θ by less than 4^o, which we neglect in the following. The response time is determined to be on the order of 1 s by measuring the response to a step pulse via the spin echo signal, see Fig. 8.8c.

To generate the magnetic field pulse, we use a square voltage biasing pulse, which generates a magnetic field $\boldsymbol{B}_\Delta$ with transient exponential rising and falling periods t_up and t_d (Fig. 8.9, red).

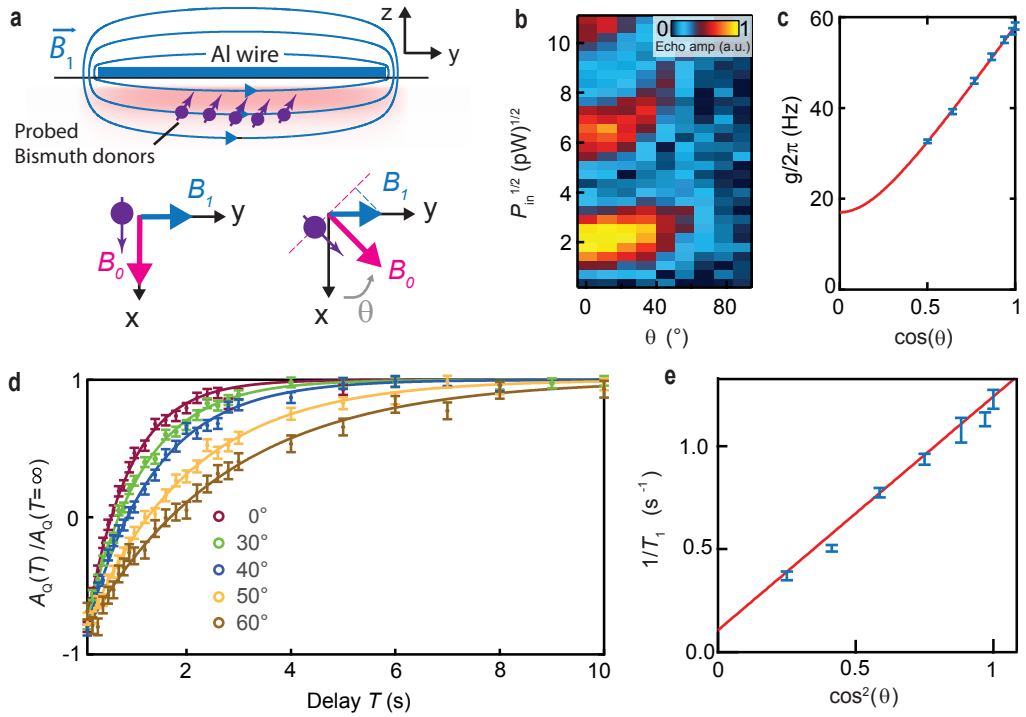

FIGURE 8.7: **Dependence of Purcell relaxation on spin-cavity coupling** $g(\theta)$.**a** Schematic: the probed spins (red shade) are aligned with respect to $\boldsymbol{B_0}$ and probed by the microwave field generated by the wire, whose direction for the concerned spins is along **y**. **b** Rabi oscillations measured as a function of $\boldsymbol{B}_0$ field orientation θ; the colour scale indicates the echo amplitude in arbitrary units. **c** The Rabi oscillations in **a** are used to extract the spin-cavity coupling strength g (blue symbols, error bars are determined by the 30% uncertainty on P_{in}). These data are fit to Eq 8.12 (red line); the non-zero value of $g(\pi/2)$ is due to the finite out-of-plane component of the microwave magnetic field. **d** Inversion recovery measurements (error bars indicate the standard deviation of a measured echo) for different values of θ confirm that the relaxation time T_1 shown in panel **e** (error bars are estimates of the standard deviation of the fit) varies as $g^2(\theta)$. The red solid line in **e** is the Purcell rate predicted using the $g(\theta)$ dependence fitted from panel **c**. All data were collected using resonator C at $\boldsymbol{B}_0 = 2.8$ mT, with characteristics given in Table 8.2.

To take into account the slow coil response, buffer delays of 1 s are added after ramping the coil voltages up and down. The relaxation rate given by the Purcell effect will take values ranging from $T_1(0)^{-1}$ to $\Gamma_p = T_1(0)^{-1} \times \frac{1}{1+4(\Delta/\kappa)^2}$ with soft transitions (Fig. 8.9, green). Those soft transitions will cause additional unwanted decays of the spin polarization (Fig. 8.9, purple). The overall decay for the polarisation during the pulse may then be written as:

$$p(t) = \begin{cases} 0 & \text{for} \quad \mathrm{t} = 0 \\ 1 - e^{-\int_0^t \Gamma_p[\Delta(t')]\mathrm{dt}'} & \text{for} \quad 0 < \mathrm{t} \leqslant \mathrm{t_{up}} \\ 1 - e^{-\int_0^{t_{\mathrm{up}}} \Gamma_p[\Delta(t')]\mathrm{dt}'} \times e^{-\Gamma_p(\Delta)(t-t_{\mathrm{up}})} & \text{for} \quad \mathrm{t_{up}} < \mathrm{t} \leqslant \mathrm{t_{up}} + \mathrm{T} \\ 1 - e^{-\int_0^{t_{\mathrm{up}}} \Gamma_p[\Delta(t')]\mathrm{dt}'} \times e^{-\Gamma_p(\Delta)T} \times e^{-\int_{t_{\mathrm{up}}+\mathrm{T}}^{t} \Gamma_p[\Delta(t')]\mathrm{dt}'} & \text{for} \quad \mathrm{t_{up}} + \mathrm{T} < \mathrm{t} \\ 1 & t = \infty \end{cases}$$

The polarisation measured with the spin-echo sequence can be expressed without knowledge of t_{up} and t_{down} by writing $p_m(T) = p_m(\infty) - [p_m(\infty) - p_m(0)]e^{-\Gamma_p(\Delta)T}$ since $p_m(T = \infty) = 1$. The readout echo signal $A_{\mathrm{Q}}(T)$ being directly proportional to the polarization, it will decay as $A_Q(T) = A_Q(\infty) - [A_Q(\infty) - A_Q(0)]e^{-\Gamma_p(\Delta)T}$ and gives the expected exponential decay to be measured. The quantity $e^{-\Gamma_p(\Delta)T}$ is accessed by computing $[A_{\mathrm{Q}}(T) - A_{\mathrm{Q}}(\infty)] \,/\, [A_{\mathrm{Q}}(0) - A_Q(\infty)]$.

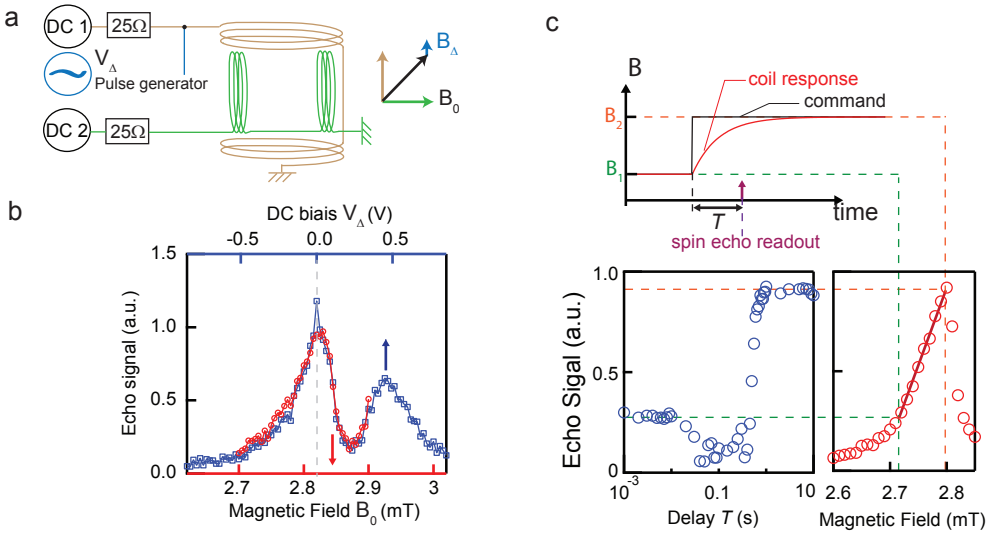

FIGURE 8.8: **Coil calibration**. **a** A comparison between the lineshape obtained by sweeping the output of the pulse generator used in DC mode (blue points) with $B_0 = 2.82$ mT to the lineshape obtained by sweeping the DC coil bias (red points) yield the calibration of the magnetic field pulse. **b** (top panel) The time response of the coil is probed by reading out the spin echo signal for various delay times T (left panel) after a step command pulse rising the magnetic field from B_1 to B_2. At very short times $T \ll 0.01$ s, an echo signal corresponding to the steady state $A(B_1)$ (right panel) is measured whereas for longer times $T >1$ s the echo signal corresponds to the steady-state $A(B_2)$ signal. In-between, due to the transient of the pulse, the readout does not occur at the same magnetic field as the excitation and thus we measure an echo signal less than the steady-state situation. From this a transient time of 1 s is inferred for the coils.

For the experiment to be successful, the loss of polarization during the buffer times should be limited: $A_Q(T = 0)$ should be significantly smaller than $A_Q(T = \infty)$. This signal loss is minimized by purposely increasing the T_1 at resonance, thanks to its angular dependence demonstrated earlier. We set $\theta = \pi/4$ and work on transition $|9\rangle \leftrightarrow |10\rangle$ with resonator C so that $T_1(\Delta = 0) = 1.68$ s. For values of Δ ranging from 0.3 MHz to 4 MHz, $A_Q(0)/A_Q(\infty)$ varies from 0.2 to 0.5 since the coil response time is now on the order of $T_1(0)^{-1}$, which leaves enough signal for the T_1 measurements.

Spectral spin diffusion

Inversion recovery is not an ideal method to observe the long relaxation times we expect. Indeed, when the spin linewidth is broader ($\sim \times 20$) than the excitation bandwidth and the thermalization time is very long, one can observe polarization mixing mechanisms [207, 4], spectral and spatial spin diffusion being the most relevant to our case as the system is only constituted from one species. For $\Delta/2\pi = (\omega_s - \omega_0)/2\pi = 3.8$MHz $> \Delta\omega$, an inversion recovery sequence including a detuning pulse (see Fig. 8.10a) yields a double exponential relaxation (Fig. 8.10d, green), which we attribute to the existence of a spectral spin diffusion mechanism.

One way to prevent spectral spin diffusion is to suppress any polarization gradient along the spin line by saturating the spins first to reach an incoherent mixed state with the population evenly shared between excited and ground states [5]. This is difficult to achieve in our experiment since the spin linewidth $\Delta\omega$ is 20 times larger than the resonator bandwidth. The simplest saturation recovery scheme (Fig. 8.10b) consists of sending a strong microwave tone at resonance, but a T_1-relaxation measured with this scheme still yields a double-exponential decay (Fig. 8.10d, orange), with time

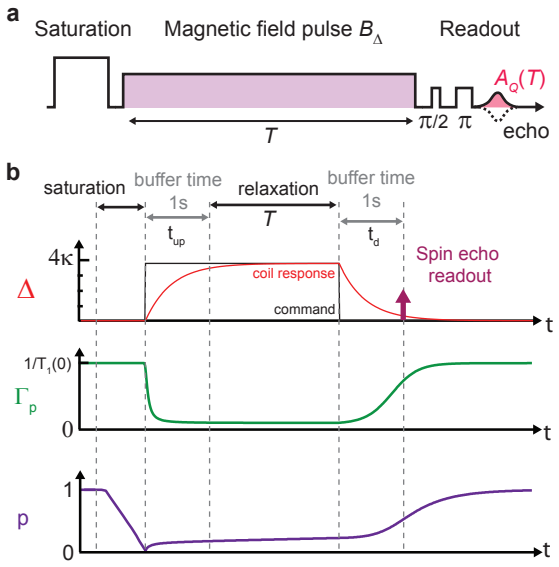

FIGURE 8.9: **T_1 (Δ) measurement sequence**. **a** Saturation recovery sequence. The spins are saturated before being detuned by an amount Δ for a time T. A Hahn echo sequence reads out the subsequent spin polarization. **b** Illustration of the evolution of the polarization during the sequence.

constants similar to the inversion recovery case. This implies that the saturation of the line is still partial. To improve the saturation, one can sweep the magnetic field during the saturation pulse so as to bring different subsets of the spin line to resonance and realize a full saturation. The adopted sweep scheme is shown on Fig. 8.10c. The corresponding relaxation curve now fits well to a simple exponential decay (Fig. 8.10d, blue), indicating the suppression of the spin diffusion effect.

One can further check the quality of the saturation by measuring the polarization across the full spin linewidth immediately after saturation. To realize such scans (Fig. 8.10e), we apply the relevant saturation pulse at ω_0, then apply a magnetic field pulse $B_\Delta = (\omega_s - \omega_0)/\gamma_e$ to measure the echo signal $A_Q(\omega_s)$ at a different frequency ω_s. When no saturation pulse is applied, the measured echo signal $A_{Q0}(\omega_s)$ gives the full polarization $-\langle S_z(\omega_s)\rangle = +1$ (black curve) and shows the natural spin linewidth. With an excitation pulse, the polarization is $-\langle S_z(\omega_s)\rangle = A_Q(\omega_s)/A_{Q0}(\omega_s)$, where $A_Q(\omega_s)$ is the measured echo signal. Thus $-\langle S_z(\omega_s)\rangle = -1$ indicates a full inversion, $\langle S_z(\omega_s)\rangle = 0$ saturation and $-\langle S_z(\omega_s)\rangle = +1$ return to thermal equilibrium. The green, orange and blue curves are taken after respectively a π pulse **(a)** and a saturation without field sweep **(b)** and with field sweep **(c)**. At resonance, one expects a change of S_z from -1 to +1 for a π pulse and from -1 to 0 for a saturation pulse. Due to the coil transient time, all three curves show partial relaxation. If the saturation was optimal and no partial relaxation was occurring, one should observe $S_z = 0$ for all detunings Δ. Among the three sequences studied here, scheme **(c)** is the closest to saturating the line. For scheme **(b)** the spin saturation bandwidth is of ≈ 250 kHz and for the inversion scheme **(a)** the bandwidth ≈ 82 kHz is set by the resonator. This confirms that only in scheme **c** can spin diffusion be fully suppressed as confirmed by the observed simple exponential decay and we therefore use it to measure the Δ-dependent relaxation rates.

Experimental Δ-dependent relaxation

The magnetic field pulse is followed by a spin-echo sequence to readout the polarization of the ensemble; the echo signal amplitude A_Q as a function of T yields the spins energy relaxation time while they are detuned by Δ.

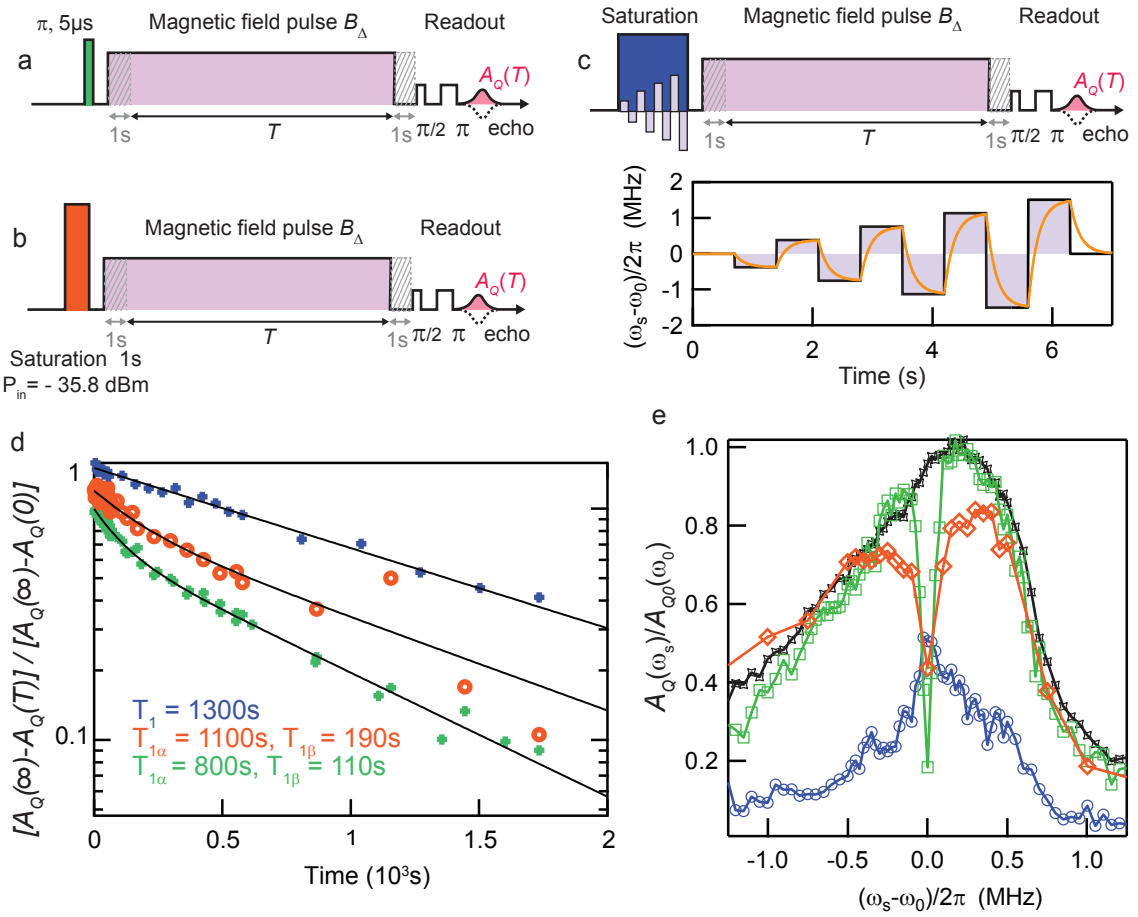

FIGURE 8.10: **Spectral spin diffusion**. **a-c** T_1 measurement sequence when spins are detuned from the cavity by applying a magnetic field B_Δ, providing a detuning $\Delta = \omega_s - \omega_0 = 2\pi\gamma_{\text{eff}} B_\Delta$, with $\gamma_{\text{eff}} = df/dB(B_0)$. **a** uses a $\pi = 5\,\mu$s pulse to realize a so-called inversion recovery sequence, **b** and **c** are saturation recovery sequences: **b** uses a 1-s-long strong microwave pulse sent at cavity resonance whereas **c** has in addition a magnetic field scan shown on the bottom part. Depicted in orange is the expected magnetic field profile due to the the coil filtering, assuming the coil to be an order-1 low-pass filter of bandwidth 1-Hz. **d** T_1 measurements for sequence **a** (green), **b** (orange), **c** (blue) for $\Delta/2\pi = 3.8\,$MHz. Fits (black lines): **a** & **b** have a double exponential decay whereas **c** is a simple exponential. We attribute this double-exponential decay to spin diffusion. **e** Spectral profiles of excitation pulses **a** (green), **b** (orange) & **c** (blue). The sequence is as follows: send the excitation pulse, detune the spins and measure $A_Q(\omega_s)$. Black line is the reference profile without any excitation pulse, yielding reference $\langle S_z(\omega_s)\rangle = -A_{Q0}(\omega_s)/A_{Q0}(\omega_s)$. When an excitation pulse is sent, one can access $\langle S_z(\omega_s)\rangle = -A_Q(\omega_s)/A_{Q0}(\omega_s)$. Note that neither the π profile or the saturation profile reach either the full inversion +1 or full saturation 0 at resonance. This is an artefact due to the coil transient time.

As evident in Fig. 8.11b, we find that the decay of the echo signal is well fit by a single exponential with a decay time increasing with $|\Delta|$. The extracted $T_1(\Delta)$ curve (see Fig. 8.11c) shows a remarkable increase of T_1 by up to 3 orders of magnitude when the spins are detuned away from resonance, until it becomes limited by a non-radiative energy decay mechanism. The error bars come from the accuracy of the relaxation rates fits.

The global fit shown on Fig. 8.11c is obtained by using equation $T_1(\Delta)^{-1} = \Gamma_p + \Gamma_{\text{NR}}$ which may be expressed as:

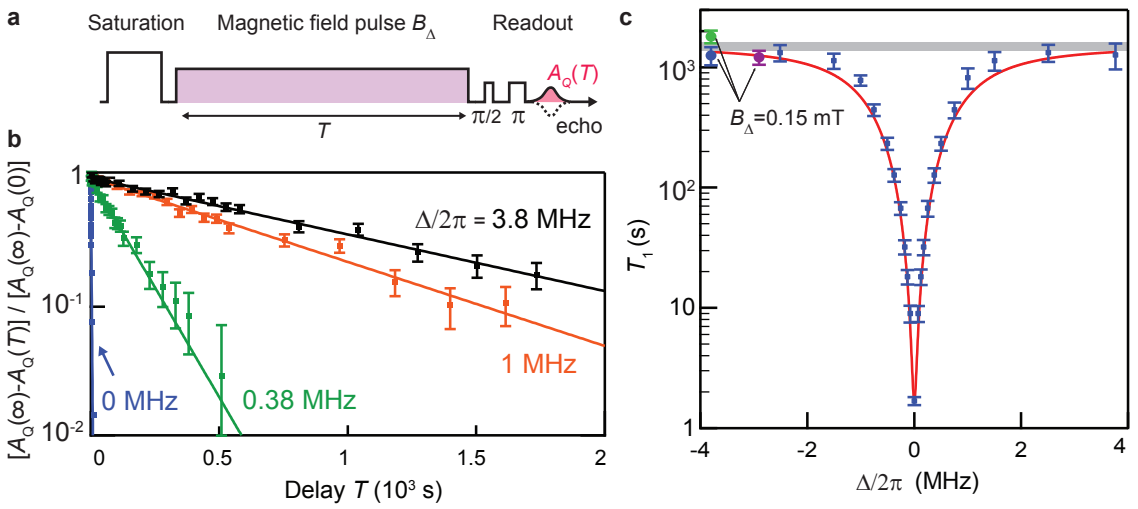

FIGURE 8.11: **Controlling Purcell relaxation by spin-cavity detuning**. **a** In-between their saturation (see Figure 8.10c) and subsequent readout, the spins are detuned from the cavity by $\Delta = \frac{d\omega_s}{dB} B_\Delta$ by applying a magnetic field pulse of amplitude B_Δ, with $\frac{1}{2\pi}\frac{d\omega_s}{dB} \simeq 25$ GHz/T for this transition and magnetic field. **b** Measured spin polarisation decays (dots) for four different detunings, well fit (lines) to exponential decays, with relaxation time constants T_1 increasing with the detuning (Error bars: single-shot standard deviation (s.d.), n=2001). **c** Measured T_1 as a function of detuning Δ, error bars are fit s.d. estimates, using resonator C and with $\theta = \pi/4$. Blue points correspond to data acquired on the left peak of transition $|9\rangle \leftrightarrow |10\rangle$ (spins under the wire), the green point, to data acquired on the right peak of transition $|9\rangle \leftrightarrow |10\rangle$ (spins outside the wire) and the purple point, to data acquired on the left peak of transition $|8\rangle \leftrightarrow |11\rangle$(spins under the wire). The solid red line is a fit to the blue data points with $(\Gamma_p(\Delta) + \Gamma_{\rm NR})^{-1}$, yielding $\Gamma_{\rm NR}^{-1} = 1500 \pm 100$ s, grey area. These measurements are taken using resonator C and with $\theta = \pi/4$, which results in $T_1 = 1.68$ s at $\Delta = 0$. In this experiment done in a separate run, the quality factor of resonator C dropped from $Q = 1.07 \times 10^5$ to $Q = 8.9 \times 10^4$ due to slightly higher losses, yielding the resonator bandwidth $\kappa/2\pi = 82$ kHz.

$$T_1(0)^{-1}\left(1 + 4\left(\frac{\Delta}{\kappa}\right)^2\right)^{-1} + \Gamma_{\rm NR} \tag{8.13}$$

so that it involves only experimentally determined quantities. Indeed, κ is precisely determined by measuring the quality factor of the resonator[3] at low power; $T_1(0)$ is determined accurately by an inversion recovery sequence, and Δ has been determined by the precise calibration of the coil pulse. The only remaining free parameter in the fit is thus $\Gamma_{\rm NR}$, yielding $\Gamma_{\rm NR}^{-1} = 1500 \pm 100$ s.

Non-radiative decay

We now discuss the possible non-radiative decay mechanisms in light of what is known about the relaxation of bismuth donors in silicon, as explained in ch. 4 (see 4.4.1). At the low temperatures of our experiment, direct phonon relaxation should be the dominant process. As explained earlier, Si:Bi energy levels are in general highly hybridized electro-nuclear spin states; as a result, their phonon relaxation rates in general involve complex combinations of T_S (electronic spin flip: $\Delta m_s = \pm 1$, $\Delta m_i = 0$) and T_X ($\Delta m_s = \pm 1$, $\Delta m_i = \mp 1$) processes. However, the $|9\rangle \leftrightarrow |10\rangle$ transition is somewhat special from that respect, as the T_X process is impossible and only the T_S process can contribute, which simplifies the discussion. In 4.4.1, we have derived by comparison to data on

[3] In this experiment done in a separate run, the quality factor of resonator C dropped from $Q = 1.07 \times 10^5$ (given in Table 8.2) to $Q = 8.9 \times 10^4$ due to slightly higher losses, yielding the resonator bandwidth $\kappa/2\pi = 82$ kHz.

Si:P donors that a T_s relaxation time on the order of 10^5 s is expected at zero-temperature, which turns out to be much larger than the 1500 s measured in our experiment. This seems to indicate that phonon relaxation is not likely to explain Γ_{NR}. In addition, for transition $|8\rangle \leftrightarrow |11\rangle$, as level $|11\rangle$ can relax to two ground states $|7\rangle$ and $|9\rangle$ with a different admixture of T_x and T_s processes, a different relaxation rate would likely be expected, instead of what we have measured the same non-radiative decay time (purple point shown in Fig. 8.11c). Note that another signature would also be a minor dependence on strain, on the order of a factor unity. We can test this by measuring the non-radiative decay for spins located outside the wire where the strain is different than under the wire. The measured decay $\Gamma_{\mathrm{NR}}^{-1} = 1800 \pm 200$ s (green point) is only slightly different than the value $\Gamma_{\mathrm{NR}}^{-1} = 1500 \pm 100$ s measured for spins under the wire (blue point), with a too large uncertainty for the test to be conclusive.

We next discuss whether charge hopping (see 4.4.1) could explain our measured Γ_{NR}. Indeed, interestingly, for similar concentrations of Si:P as our sample concentration in Si:Bi, Feher et al. showed that T_1 at 1.25 K is decreased by several orders of magnitude compared to its low-concentration value [16]. They have attributed the effect to the activation of a spin exchange mechanism by the formation of clusters of Si:P donors at higher concentrations. It is difficult to estimate if this effect is relevant in our experiment since on one hand Si:Bi is a deeper and more confined donor than Si:P and thus the threshold concentration should be higher than for Si:P. On the other hand, charge hopping is enhanced in presence of ionized donors [16], as is the case in the experiment since the donors are partially ionized nearby the wire due to the Schottky barrier created in contact with the aluminum (see Fig. 7.2). Charge hopping thus appears as one of the possible candidates to explain our data.

Last, as we have seen above with the imperfections of the inversion recovery sequence, spin diffusion mechanisms can occur. In the case of Γ_{NR}, the mechanism would not be spectral spin diffusion but spatial spin diffusion. The spins outside the detection volume of the resonator remain polarized even after the microwave saturation and thus a polarization transfer to the saturated probed ensemble of spins located near the wire could take place, appearing in the measurement as a spin relaxation process. One very naive way of estimating this process is by using the measurements we have realized for spectral spin diffusion, as the underlying mechanism is identical. In our experiment, due to strain applied by the aluminum, the spatial and spectral distribution are linked: the $\Delta\omega/2\pi = 2$ MHz broad linewidth of the left side peak of transition $|9\rangle \leftrightarrow |10\rangle$ corresponds approximately to spins under the wire which occupy a volume of width 5 μm. With a π-pulse of bandwidth 100 kHz, the spectral spin diffusion process takes place approximately in 100 s. Thus, if we were to saturate a spectral range of $\Delta\omega/2\pi = 2$ MHz one would roughly expect spin diffusion to occur on a timescale of 2000 s, which is indeed of the same order of magnitude as $\Gamma_{\mathrm{NR}}^{-1}$.

To conclude, the lack of measured values for bismuth in conditions similar to our experiment, the in-built strain and consequent broad spin linewidth as well as the ionized donors present in our experiment make the identification of the non-radiative decay mechanism quite difficult. Given the above discussion, we tentatively attribute this non-radiative decay to charge hopping spin relaxation, and(or) to spin diffusion.

8.4 Conclusion

We have brought three independent experimental demonstrations that T_1 in our experiment is limited by spontaneous emission. T_1 at resonance was found to quantitatively match the Purcell formula; T_1 was found to linearly depend on g^{-2}; and T_1 was changed by 3 orders of magnitude by changing the spin-resonator detuning by only 2 MHz, again in quantitative agreement with Purcell formula. This Purcell relaxation could be used as an efficient method to re-initialize any spin in its ground state on-demand, which could be particularly useful in particular in Quantum Information Processing. The Purcell effect could also be used for dynamic nuclear polarization

in magnetic resonance[208, 209]. In such schemes, the polarization of a nuclear state is built by cross relaxation on a electron-nuclear flip-flop transition. Cavity-induced relaxation would be an alternative to existing relaxation mechanisms or enhance the relaxation rate of this transition to improve the efficiency of the nuclear polarization.

Even if our experiment takes place at low magnetic fields and low temperatures, such limits are not intrinsic to this scheme and the Purcell effect could be observed with a variety of other spin systems. Larger magnetic fields are possible if one uses superconductors with higher critical fields than aluminum. Resonators of high intrinsic quality factors have been demonstrated in a variety of materials (Nb, NbN[155, 156], NbTiN[157]) up to 1 T. On the other hand, temperature is important beyond the need for high quality factors. Spontaneous emission ensures relaxation to thermal equilibrium; low temperatures are required at the frequencies (7 GHz) used in this work for thermal equilibrium to correspond to a spin polarization higher than 99%. This limit could be lifted either by working at higher frequencies or at the price of reduced spin polarization. Note that operation at higher temperatures could make other relaxation mechanisms more efficient, reducing effectively the interest of cavity-enhanced spontaneous emission.

On a more fundamental level, it is interesting to note that we reach here for the first time a regime where the vacuum fluctuations of the microwave field can have a marked effect on spin dynamics. In many systems (Rydberg atoms, quantum dots, ...), the observation of the Purcell-enhanced relaxation of individual emitters was the first step towards the application of the full range of concepts and ideas of cavity QED (strong coupling, ...), and it is tempting to assume that it will be the case as well for spins in solids [189]. To pursue this aim, a higher Purcell rate could be achieved by increasing the coupling of the spins to the microwave cavity. The wire dimensions could be reduced by a factor 50, yielding an increase of g by the same factor and accessible T_1 below the millisecond range. In addition to permitting faster repetition rates and a higher sensitivity, this would considerably enhance the cooperativity and allow to reach the regime of high cooperativity needed to observe coherent interactions between cavity and spin [70].

Part IV

Squeezing-enhanced magnetic resonance

Chapter 9

Squeezing-enhanced magnetic resonance

Quantum mechanics, through the Heisenberg uncertainty principle, imposes a minimum amount of noise in a measurement. When this limit is set by the vacuum fluctuations of the electromagnetic field, the measurement is said to be performed at the standard quantum limit. Such performance is routinely reached for optical measurements, and more recently for microwave measurements thanks to the use of JPAs, as shown for example in ch. 7 for ESR measurements.

The standard quantum limit however is not as fundamental as the Heisenberg limits and can be overcome through the use of squeezed states for example. For these field states, whose properties were discovered in the 1970s by Stoler [210] and Yuen [211], the noise on one quadrature is reduced below the vacuum level, whereas the other one is correspondingly more noisy as required by Heisenberg uncertainty principle. In the optical frequency domain, where squeezing factors on the order of 12 dB are now produced [212], squeezed states were first proposed by Caves [18] and recently implemented [213, 31] to enhance the sensitivity of gravitational waves interferometric detectors. They have also been used for increasing the sensitivity of a number of other experiments, such as atomic absorption spectroscopy [214], atom-based magnetometry [32] and particle tracking of living systems [215]. In the microwave domain, while squeezed states were generated as early as 1989[12], it is only through more recent developments in cQED than a sufficient amount of squeezing was observed [216] to realize fundamental studies of light-matter interaction [217, 34] and enhanced sensing of a mechanical resonators [35].

In this chapter, squeezed microwave states are used for enhancing the sensitivity of ESR measurements. We review briefly the applications of squeezed states before explaining how they can be harnessed to enhance the sensitivity of an ESR experiment. We finally demonstrate the generation of squeezed states via the flux-pumped JPA presented in ch. 5 and their use in our ESR spectroscopy setup.

9.1 Squeezing-enhanced measurements

9.1.1 State-of-the-art

Squeezing for enhanced measurement sensitivity

The noise reduction provided by a squeezed state can be harnessed to increase the sensitivity of a measurement [40]. Depending on the purpose, several schemes have been put forward [218]. A pioneering proposal due to Caves [18] suggests to use squeezed vacuum at one of the ports of an optical interferometer, in order to enhance the sensitivity of phase detection. A prominent motivation is the application of this idea to gravitational wave detectors. In this scheme, a Michelson

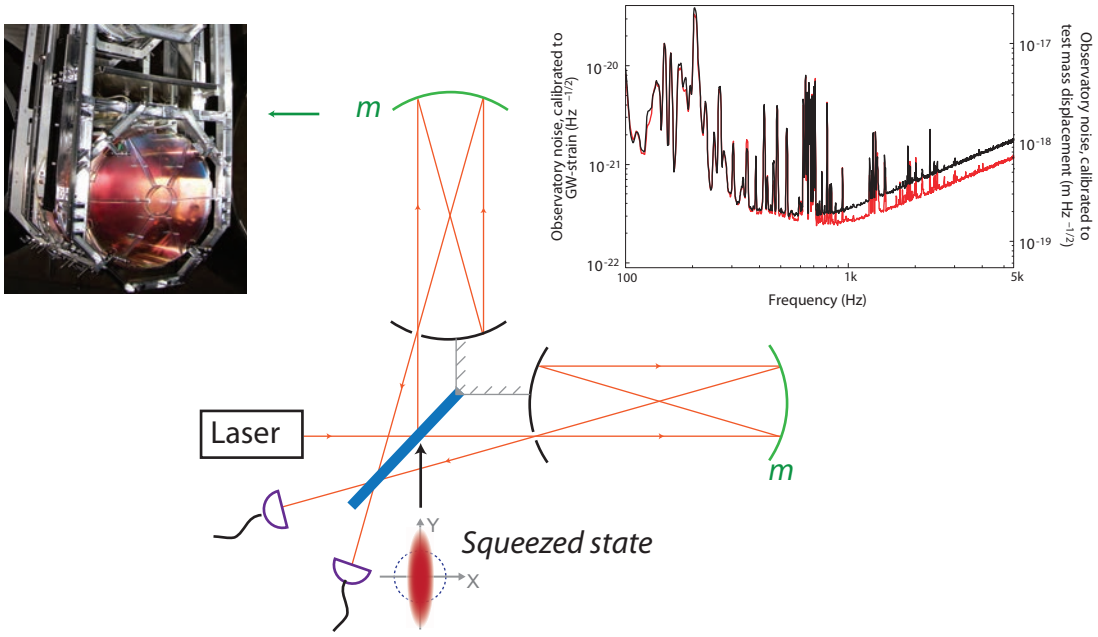

FIGURE 9.1: **Squeezing-enhanced interferometric gravitational detector.** Schematic of Caves proposal (adapted from [18]) where a squeezed state sent on the dark port of the beam-splitter (in blue) can enhance the detection of the floating mirrors displacement (green, see picture on the left for LIGO implementation). (right) Demonstration of squeezing enhanced detector sensitivity on the GEO600 instrument. [213]

interferometer is used to detect the relative displacement of two heavy masses m as depicted in Fig. 9.1. A laser beam, split in two via a beam splitter, bounces a number of times in each arm between two reflecting mirrors, one being fixed while the other is attached to a mass m. Detecting the light outcoming of each arm via photo-detectors thus yields information on the relative mass displacement. To understand where the usefulness of squeezed states arises, it is important to realize that the beam-splitter used to separate the laser in two coherent lights beams is actually a four-port device, connecting two input modes to two output modes. The first input port is used for the incoming light, while the second input port sees the vacuum state. Caves showed that the sensitivity of the measurement is heavily linked to the vacuum fluctuations arising at this second port [18]. Replacing the vacuum state by a squeezed vacuum state could thus improve the sensitivity of the measurement, as was shown recently by the LIGO collaboration with ≈ 2.5 dB enhancement over a large frequency range (see Fig. 9.1).

The use of squeezed-states for interferometric measurements generally relies on decreasing the vacuum fluctuations at the dark port of a beam-splitter [19]. The general strategy in all measurement is to adopt a scheme that combines the measured signal to the squeezed-state reduced vacuum fluctuations without signal degradation. An interesting device in this context is the asymmetric beam-splitter (known as directional coupler in microwave engineering), which allows to produce arbitrarily displaced squeezed states with preserved noise reduction. In atomic-absorption microscopy [214], atom-based magnetometry [32] and particle tracking of living systems [215], a displaced squeezed state is created via such an asymmetric beam-splitter to probe the system of interest and improve the measurement sensitivity. Similarly, for enhanced mechanical resonator sensing [35], a displaced microwave squeezed state is produced via a 20-dB coupler to probe the opto-mechanical system. More complex schemes also exist, such as the two-modes squeezing proposed for enhanced superconducting qubits readout [219, 220].

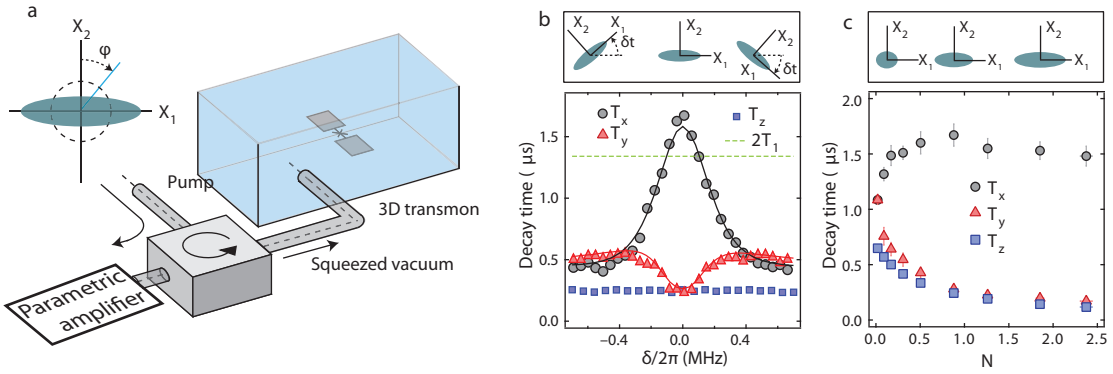

FIGURE 9.2: **Radiative decays in squeezed vacuum.** Adapted from [217]. A squeezed-vacuum generated by a JPA is shined on a transmon (panel **a**) whose longitudinal and transversal radiative lifetime are modified according to Gardiner's theory (panels **b** & **c**).

Squeezing effects in light-matter interaction

When a squeezed state field is incident on a two-level-system, Gardiner showed that the damping rates of the TLS are largely modified in presence of squeezing [221]. Consider a TLS described by the Pauli operators $\hat{\sigma}_i$ irradiated with a broad-band incident squeezed-state of parameters N and M given in ch. 2. If the TLS decay is radiatively limited with a decay time γ in absence of squeezing, Gardiner showed that the equations of motion for $\langle\hat{\sigma}_x\rangle$, $\langle\hat{\sigma}_y\rangle$ and $\langle\hat{\sigma}_z\rangle$ become in presence of squeezing [221]:

$$\langle\dot{\hat{\sigma}}_x\rangle = -\gamma\left(N+M+\tfrac{1}{2}\right)\langle\hat{\sigma}_x\rangle \tag{9.1}$$

$$\langle\dot{\hat{\sigma}}_y\rangle = -\gamma\left(N-M+\tfrac{1}{2}\right)\langle\hat{\sigma}_y\rangle \tag{9.2}$$

$$\langle\dot{\hat{\sigma}}_z\rangle = -\gamma(2N+1)\langle\hat{\sigma}_z\rangle - \gamma \tag{9.3}$$

The consequences are dramatic for the transverse decay rates γ_x and γ_y since they are respectively enhanced and inhibited by the same ratios than the amplified and squeezed quadratures. In the same time, the longitudinal decay rate γ_z is increased by a factor $2N+1$, with a reduced steady-state polarization $1/(2N+1)$, as would be the case if a thermal state with the same mean photon number N was impinging on the TLS. These variations on the TLS fluorescence were recently observed experimentally employing superconducting qubits [217, 34], as shown in Fig. 9.2.

9.1.2 Squeezed states for magnetic resonance

To understand how squeezed states can be harnessed to improve the sensitivity of an ESR measurement beyond the vacuum fluctuations limit, consider the scheme depicted in Fig 9.3a. It is very similar to the setup described in earlier chapters: a sample containing an ensemble of spins is embedded inside a microwave resonator of frequency ω_0 and cooled to millikelvin temperatures so that the electromagnetic field reaches its ground state. By applying a static magnetic field $\boldsymbol{B}_0$, the spins can be tuned to resonance with the ESR resonator. The latter is coupled with rate κ_c to a single measurement line supporting incoming ($\hat{a}_{\text{in}}$) and outgoing ($\hat{a}_{\text{out}}$) field modes. After application of a $\pi/2-\tau-\pi$ sequence to the spins, an echo is emitted at time 2τ in the output measurement line. The echo is then amplified and detected at frequency ω_0 by homodyne detection with a local oscillator phase chosen so that the echo lies only on one of the two field quadratures I and Q, for instance I.

As explained in ch. 5, the use of a JPA operated in phase-sensitive mode in the detection chain ensures that a major part of the noise detected on the I quadrature arises from the fluctuations of

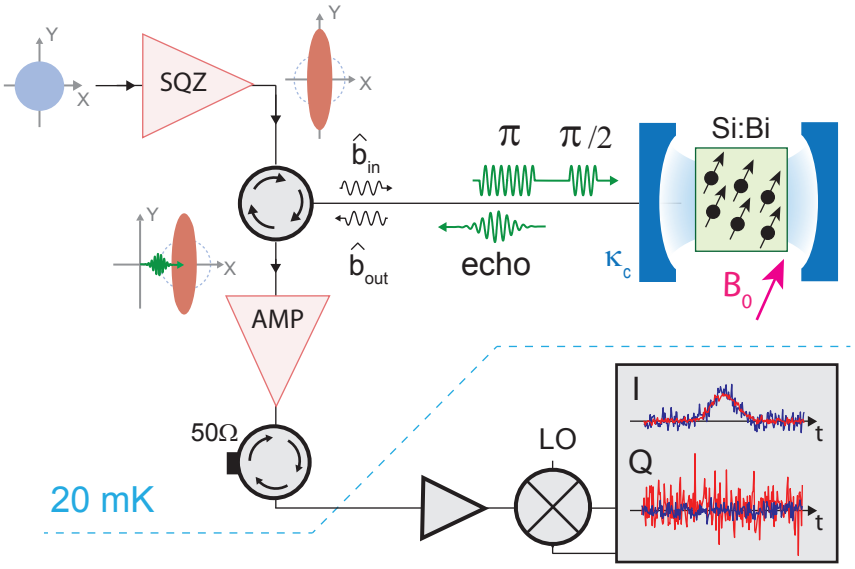

FIGURE 9.3: **Proposal for squeezing enhanced ESR.** A squeezed vacuum state is shined onto the cavity with frequency ω_0 containing the spins to be detected, which are tuned into resonance at ω_0 by a dc magnetic field $\boldsymbol{B}_0$. The spins are subjected to a Hahn echo sequence $(\pi/2 - \tau - \pi - \tau)$, leading to the emission of an echo in the detection waveguide. This echo is noiselessly amplified by a JPA followed by amplification at higher temperatures and homodyne demodulation. With the squeezed quadrature aligned along the echo emission quadrature, the SNR is improved beyond shot-noise.

the JPA input field $\hat{a}_{\text{out}}$. These fluctuations can be seen as the fluctuations of the $\hat{a}_{\text{in}}$ mode reflected by the resonator into the output mode. If the input field is cooled to the vacuum state, the detected noise reaches the quantum limit. If $\hat{a}_{\text{in}}$ is instead prepared in a squeezed-state whose squeezed quadrature is aligned on the echo emission quadrature, the noise on the detected quadrature can then be expected to be below the quantum limit (see Fig 9.3a), whereas the other quadrature on the other hand, which has no spin signal at all, has increased noise. This results in an enhanced sensitivity for the echo detection.

Note that this argument is valid only if:

- the echo just acts as a displacement operator on the squeezed state without impacting its noise properties
- the squeezed state does not affect the average spin-echo signal.

Such a vision is valid for a weakly coupled spin ensemble. A more quantitative treatment can be done by considering the spins-resonator coupling similarly to what is done in ch. 7. The following derivation is the fruit of a collaboration with Aarhus University, with Alexander Holm-Kiilerich and Klaus Mølmer, and we give in the following only the main ideas.

We recall first the resonator field equation of motion (see Eq 2.49):

$$\dot{\hat{a}}(t) = -i[\hat{a}, \hat{H}_{\text{sys}}] - \frac{\kappa}{2}\hat{a}(t) + \sqrt{\kappa}\hat{a}_{\text{in}}(t) \tag{9.4}$$

where $\hat{H}_{\text{sys}}$ is the Tavis-Cummings Hamiltonian of Eq. 3.46. We consider the simple case where the spin-cavity coupling is identical for each spin j so that $g_j = g$. We treat the spin-echo sequence similarly to ch. 7, with the spins brought to the equator of the Bloch sphere by the initial $\pi/2$ pulse at $t = -2\tau$. Inhomogeneous broadening leads to the acquisition for each spin of a phase

$\varphi_j = \Delta_j(t+2\tau)$, refocused by the π pulse applied at time $t=-\tau$ which then leads to the echo signal at time $t=0$.

We shall now describe the spin lowering and raising operators as oscillator annihilation $\hat{s}_j^\dagger$ and creation $\hat{s}_j$ operators obeying $[\hat{s}_j, \hat{s}_k^\dagger] = \delta_{k,j}$ following the so-called Holstein-Primakov approximation [71, 222, 223, 224], valid when each spin of the ensemble is only weakly excited. Eq. 9.4 now yields:

$$\dot{\hat{a}}(t) = -ig\sum_j \hat{s}_j - \frac{\kappa}{2}\hat{a}(t) + \sqrt{\kappa}\hat{a}_{\rm in}(t) \tag{9.5}$$

Following a similar treatment that the derivations of Eqs. 3.41-3.44, the spin equations of motion are:

$$\dot{\hat{s}}_j = -(\gamma + i\Delta_j)\hat{s}_j - ig\hat{a} + \sqrt{2\gamma}F_j(t) + \alpha e^{-i\Delta_j\tau}\delta(t+\tau) \tag{9.6}$$

where the term $\alpha e^{-i\Delta_j\tau}\delta(t+\tau)$ describes the spins initial coherent excitation giving rise to the echo and $F_j(t)$ is the quantum Langevin noise term associated to spin relaxation at the rate γ, with a zero mean-value. Fourier transforming both equations[1] yields:

$$-i\omega\hat{a}(\omega) = -\tfrac{\kappa}{2}\hat{a}(\omega) - ig\sum_j \hat{s}_j(\omega) + \sqrt{\kappa}\hat{a}_{\rm in} \tag{9.7}$$

$$-i\omega\hat{s}_j(\omega) = -(\gamma+i\Delta_j)\hat{s}_j(\omega) - ig\hat{a}(\omega) + \alpha e^{-i\Delta_j\tau} + \sqrt{2\gamma}\tilde{F}_j(\omega) \tag{9.8}$$

These equations can be solved, which yields:

$$\hat{a}(\omega) = \frac{-ig\sum_j \frac{\alpha e^{-i\Delta_j\tau}}{\gamma+i\Delta_j-i\omega} - ig\sum_j \frac{\sqrt{2\gamma}\tilde{F}_j(\omega)}{\gamma+i\Delta_j-i\omega} + \sqrt{\kappa}\hat{a}_{\rm in}(\omega)}{\frac{\kappa}{2} - i\omega + g^2\sum_j \frac{1}{\gamma+i\Delta_j-i\omega}} \tag{9.9}$$

To simplify this equation, we consider a Lorentzian distribution of width w: $\rho(\Delta) = \frac{w/2\pi}{\Delta^2+w^2/4}$. Replacing the sum by an integral, the denominator of Eq. 9.9 simplifies in:

$$\frac{\kappa}{2} - i\omega + g^2\frac{wN_{\rm spins}}{\omega^2+w^{2/4}} \tag{9.10}$$

In the case of a spin ensemble such that is cooperativity $C = \frac{2g_{\rm ens}^2}{\kappa w} \ll 1$, the term $g^2\frac{wN_{\rm spins}}{\omega^2+w^{2/4}}$ can be neglected. Using the input-output equation $\hat{a}_{\rm in} + \hat{a}_{\rm out} = \sqrt{\kappa}\hat{a}$ (neglecting any internal losses), we can now express the output field as:

$$\hat{a}_{\rm out}(\omega) = -i\frac{g\sqrt{\kappa}}{\kappa/2-i\omega}\int_\Delta \rho(\Delta)\frac{\alpha e^{-i\Delta\tau}d\Delta}{\gamma+i\Delta-i\omega} - \frac{ig\sqrt{\kappa}}{\kappa/2-i\omega}\tilde{F}_{\rm tot}(\omega) + \frac{\kappa+2i\omega}{\kappa-2i\omega}\hat{a}_{\rm in}(\omega) \tag{9.11}$$

where we have defined the total spin noise Langevin term as $\tilde{F}_{\rm tot}(\omega) = \int_\Delta \rho(\Delta)\frac{\sqrt{2\gamma}\tilde{F}(\omega,\Delta)d\Delta}{\gamma+i\Delta-i\omega}$. The first term, being the only one with a non-zero expectation value, describes the emission of the echo signal into the measurement line. In the weak coupling limit, the spin noise term is also smaller than the third term which describes the input field quantum fluctuations.

Eq. 9.11 confirms our earlier qualitative argument: the expectation value of the output field is the echo signal unaffected by the quantum statistics of the input field $a_{\rm in}$; but its fluctuations are governed by the input field, be it in the vacuum or in a squeezed state. We stress that throughout the derivation we have used the weak coupling condition $C \ll 1$. Properly expressing the enhancement of the SNR gained by having an incoming squeezed-state during the echo emission requires reverting to the time-domain and choosing a mode filter function, as explained in ch. 5. Nonetheless, Eq 9.11

[1] The chosen convention in this manuscript is : $\tilde{f}(\omega) = \int dt e^{i\omega t} f(t)$ and $f(t) = \frac{1}{2\pi}\int {\rm dt e^{-i\omega t}\tilde{f}}(\omega)$.

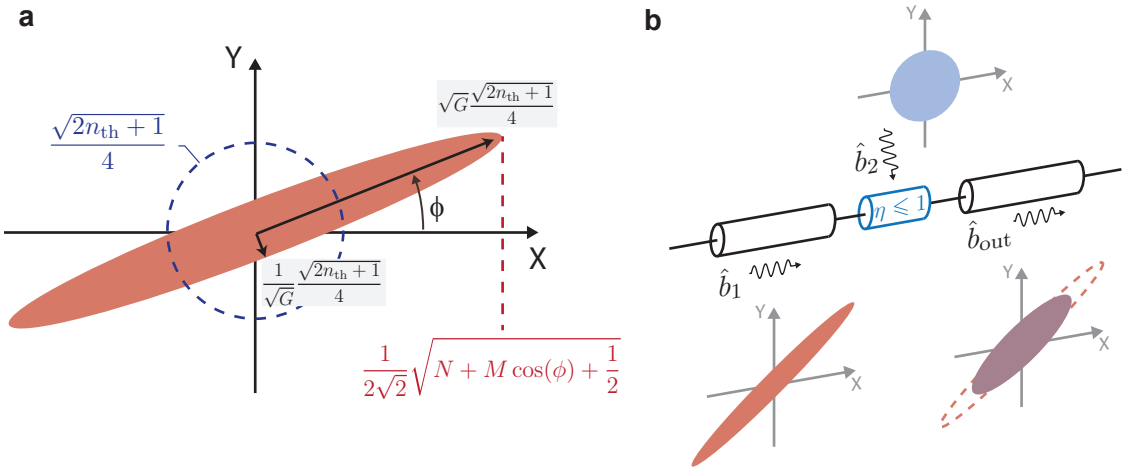

FIGURE 9.4: **Squeezed vacuum. a** Squeezed state produced by a phase-sensitive amplifier of power gain G whose input is a thermal state of occupancy $n_{\rm th}$, fully characterized either by G and n_th or by the numbers N and M defined in Eqs. 2.17 & 2.18. **b** Attenuation of a squeezed state.

is sufficient to evidence that an input field with a quadrature squeezed by a factor η_S is expected to enhance of the SNR by a factor $\sqrt{\eta_S}$.

9.2 Detecting and characterizing microwave squeezed states

9.2.1 Microwave squeezed-states

At microwave frequencies, a squeezed vacuum state can be generated by a parametric amplifier used in phase-sensitive mode, as explained in ch. 2. If the parametric amplifier input field is a thermal vacuum state of occupancy $n_{\rm th}$, we recall that for a gain G the squeezed state variances are (see Fig. 9.4a):

$$\langle \Delta \hat{X}_\phi^2 \rangle = \frac{(2n_{\rm th}+1)G^{-1}}{4} \tag{9.12}$$

$$\langle \Delta \hat{Y}_\phi^2 \rangle = \frac{(2n_{\rm th}+1)G}{4}. \tag{9.13}$$

where $\hat{X}_\phi$ and $\hat{Y}_\phi$ are respectively the deamplified and amplified quadratures, relative to the choice of the phase ϕ of the JPA pump tone compared to the detection quadratures $\hat{X}$ and $\hat{Y}$.

Microwave squeezed states are well-known to be fragile, and in particular are susceptible to losses encountered during their propagation. Attenuation by a factor η is generally modeled as the action of a beam-splitter of finite transmission η, with the vacuum at the other port (see Fig. 9.4b). The relations linking the input and output fields of a beam-splitter is:

$$\hat{b}_{\rm out} = \eta \hat{b}_1 + (1-\eta)\hat{b}_2. \tag{9.14}$$

If on the port $\hat{b}_2$ is impinging a thermal state of occupancy $n_{\rm th}$ identical to the squeezed state $\langle \Delta \hat{X}_2^2 \rangle = (2n_{\rm th}+1)//4$, then the outcoming squeezed state has a reduced degree of squeezing:

$$\langle \Delta \hat{X}_{\phi,\rm out}^2 \rangle / \langle \Delta \hat{X}_2^2 \rangle = G^{-1}\eta + (1-\eta) < G^{-1}\eta \tag{9.15}$$

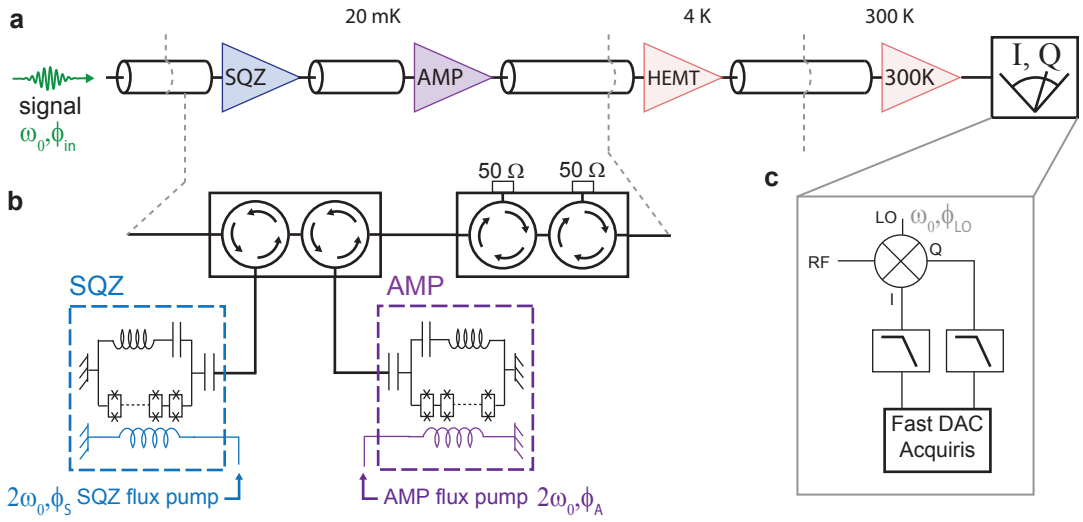

FIGURE 9.5: **Experimental setup for SQZ characterization. a** Two JPAs are mounted in series: the first generates a squeezed vacuum state while the second ensures its noiseless detection **b** Circuit view of (panel **a**). **c** The detection is performed via homodyne detection. The bandwidth of the filters preceding the acquisition card was chosen significantly smaller than the JPAs bandwidths ($\times 10$).

9.2.2 Characterization of the flux-pumped JPA as a squeezing generator

To generate a microwave squeezed-state, we use the flux-pumped JPA presented in ch. 2 and characterized in ch. 5. We first characterize the squeezed vacuum generated by the JPA with a simplified setup that does not include the ESR resonator nor the spins (see Fig. 9.5a), very similar to the one used in [216]. A second JPA device, noted SQZ, is operated in phase-sensitive mode to generate a squeezed vacuum state (blue device), whose squeezed quadrature is set by its pump tone phase ϕ_s. To characterize the emitted radiation noise properties of this state, we use the same amplification chain described and characterized in ch. 5, comprising the same JPA device, noted AMP (purple device) in the following, followed by amplification at 4 K and 300 K.

Using the AMP in phase-sensitive mode ensures noiseless amplification on one quadrature set by its pump phase ϕ_A (see ch. 2) . Using homodyne detection, with a local oscillator phase ϕ_{LO} chosen so that the amplified quadrature corresponds to the I quadrature, one can relate the quantum fluctuations of the input AMP field quadrature $\hat{X}_{\phi_A,\mathrm{in}}$ to the I quadrature noise $\langle \Delta I^2 \rangle$, see ch. 2.

When the SQZ pump is turned on with no incident signal, a squeezed vacuum state is generated at the AMP input, replacing the vacuum state. If the relative pump phase $\phi_S - \phi_A = \pi/2$, the squeezed quadrature is aligned on the amplification quadrature and thus I quadrature noise can be expected to be below the quantum limit. For all phase settings, the noise is related to the variance of the squeezed state by Eq. 2.14.

SQZ characterization

We first characterize the SQZ as explained earlier for the JPA, with the flux-tunability of its resonance frequency and its average phase-dependent gain. Applying the same voltage to both flux-lines at the same time, the reflexion coefficient shows the SQZ and AMP 2π phase shifts associated to their respective resonance frequencies (see Fig. 9.6a). In the remainder of this chapter, we choose their DC bias so that $\omega_0/2\pi \approx 7.3$ GHz (grey dashed line in Fig. 9.6a).

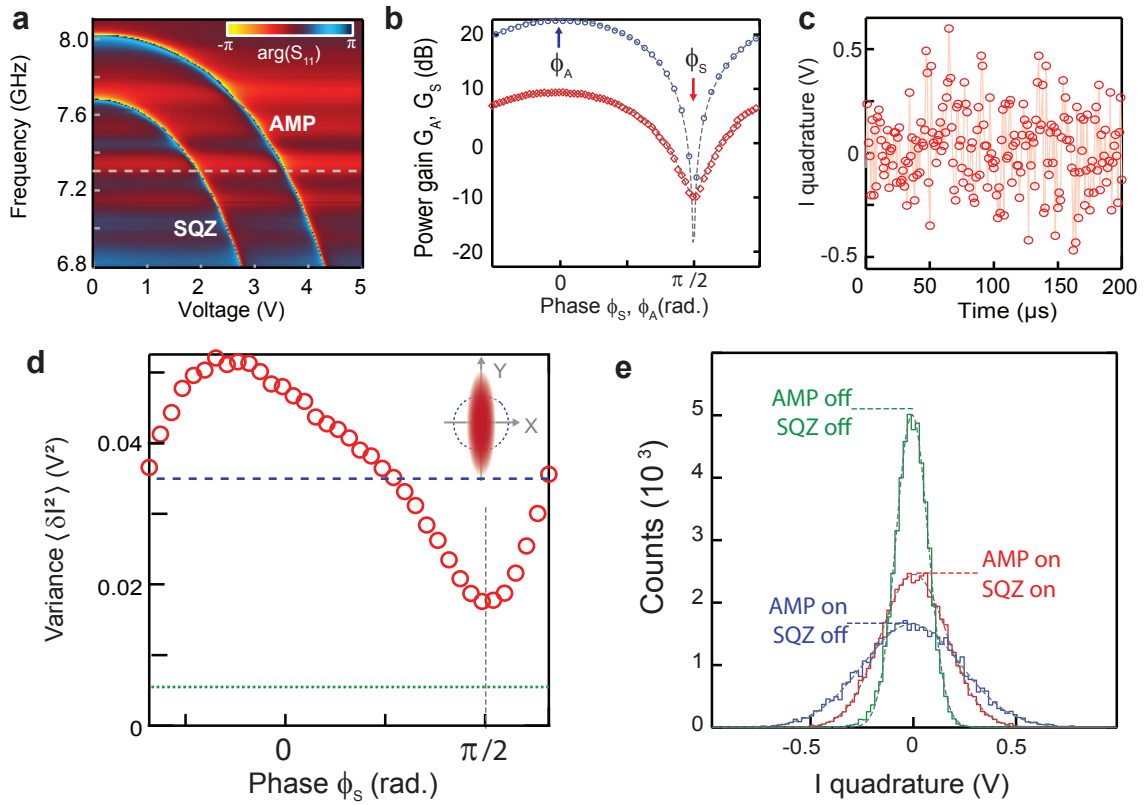

FIGURE 9.6: **Squeezed vacuum characterization. a** DC flux-bias sweep. **b** SQZ and JPA phase-sensitive gains **c** Typical time trace recorded on the I quadrature allowing to extract the noise variance (panel **d**) as a function of the SQZ phase ϕ_S and noise histogram (panel **e**) when $\phi_S - \phi_A = \pi/2$.

In addition, the phase-sensitive gains of both JPAs G_A and G_S are calibrated by measuring the amplification of an input signal depending on its relative phase to the pump tone (see Fig. 9.6b).

Noise reduction characterization

We now wish to observe the noise reduction brought by the generated squeezed state. Time traces of $I(t)$ and $Q(t)$ are obtained by digitizing the homodyne signal outputs. Without any input signal, white noise traces such as shown in Fig. 9.6c are recorded and characterized either via their variance $\langle \Delta I^2 \rangle$ or a noise histogram. Similarly to ch. 2, we set the detection bandwidth to be significantly smaller (300 kHz) than the JPA devices bandwidth (see Fig. 9.5c).

When the SQZ is on, $\langle \Delta I^2 \rangle$ is seen to depend on ϕ_S (see Fig. 9.6d) as expected from Eq. 2.14. It can be reduced below the value measured in absence of squeezing, as shown by a narrower histogram (see Fig. 9.6e). The total noise reduction is given by:

$$\eta_{\text{tot}} = \frac{\min_{\phi_S}[\langle \Delta I^2 \rangle_{\text{on}}]}{\langle \Delta I^2 \rangle_{\text{off}}} \tag{9.16}$$

and reaches $\eta_{\text{tot}} = -3.4$ dB (see Fig. 9.6d). One can also characterize the degree of squeezing η_S achieved experimentally by subtracting the background noise $\langle \Delta I^2 \rangle_{\text{bg}}$:

$$\eta_S = \frac{\min_{\phi_S}[\langle \Delta I^2 \rangle_{\text{on}}] - \langle \Delta I^2 \rangle_{\text{bg}}}{\langle \Delta I^2 \rangle_{\text{off}} - \langle \Delta I^2 \rangle_{\text{bg}}} \tag{9.17}$$

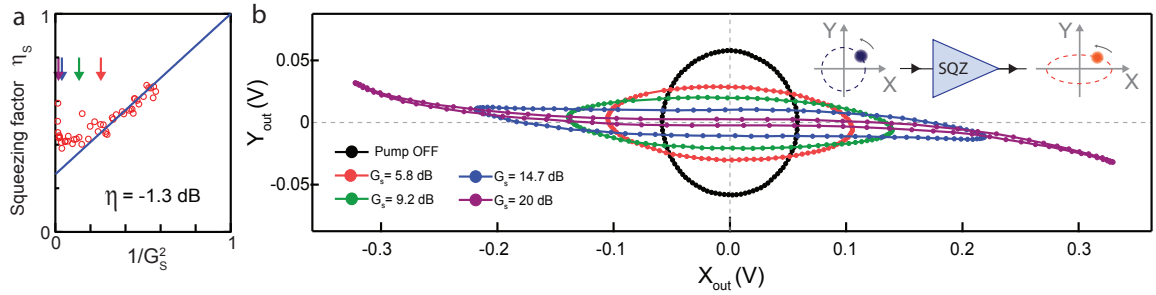

FIGURE 9.7: **Squeezed vacuum distortion**. **a** Squeezing factor η_S as a function of G_S^{-1}, allowing to extract the setup microwave losses η by a linear fit. **b** Squeezed vacuum distortion at high gains. The data is acquired by varying the phase of a small input coherent signal and measuring the averaged output field quadratures. The corresponding measured squeezing factors are indicated by the arrows in panel **a**.

The background noise is measured by switching both SQZ and JPA off and is mainly set by the noise of the HEMT amplifier, as shown in ch. 5. For the data shown in Fig. 9.6d, $\eta_S = -4.1$ dB.

Limitations to squeezing

The data shown in Fig. 9.6d correspond to the maximum amount of squeezing obtained, far from the 20 dB squeezing that one could naively expect from Eq.2.14, and we will now explain why. Repeating the experiment for several SQZ gains settings, we notice that the degree of squeezing is systematically smaller than the deamplification factor $\eta_S \leqslant G_S^{-1}$, as shown in Fig. 9.7a. At low gains, η_S depends linearly on G_S^{-1}, as expected from Eq. 9.15 for degradation due to attenuation. Fitting the linear dependence according to Eq. 9.15 yields a total microwave attenuation of $\eta = -1.3$ dB. This value is compatible with the setup of Fig. 9.5b, where losses are mainly set by the circulator insertion losses (2×0.4 dB), the 1-m-long copper coaxial cables linking SQZ and AMP (≈ 0.3 dB) and the on-chip losses (≈ 0.1 dB).

At high gains, a departure from linearity is observed, with an increase of η_S that we attribute to non-linearity induced in the SQZ resonator by the Josephson junctions used to modulate the resonator frequency (see ch. 2 and [55]). To confirm this hypothesis, we measure the output quadratures $\langle \hat{X}_{\text{out}} \rangle$ and $\langle \hat{Y}_{\text{out}} \rangle$ of a small input signal amplified by the SQZ in phase-sensitive mode as a function of its input phase (see Fig 9.7b). When the phase runs from 0 to 2π, plotting $\langle \hat{Y}_{\text{out}} \rangle$ versus $\langle \hat{X}_{\text{out}} \rangle$ emulates the shape of the produced squeezed vacuum. When the SQZ is off, a perfect circle is observed. As long as the squeezing factor varies linearly as a function of G_S^{-1}, the squeezed vacuum is ellipsoidal as expected (red curve). For higher gains, a progressive distortion of the ellipse (green, blue and purple curves) is observed which eventually leads to the increase of η_S. In the following, we thus choose moderate values of G_s which lead to the maximum η_S.

Noise reduction optimization

The total noise reduction factor η_{tot} is smaller than η_S because the total output noise is not only due to the amplified quantum noise, but also contains a small "background" contribution from the HEMT. This contribution can be minimized by working at high AMP gains. However, as shown in ch. 5, the AMP eventually saturates at high intra-resonator photon number, once again due to the non-linearity induced by the Josephson junctions. We have experimentally observed that even a weakly distorted squeezed state impinging on the AMP can lead to its saturation for high G_A. The best achievable η_{tot} thus results from an exhaustive simultaneous optimization of G_A and G_S.

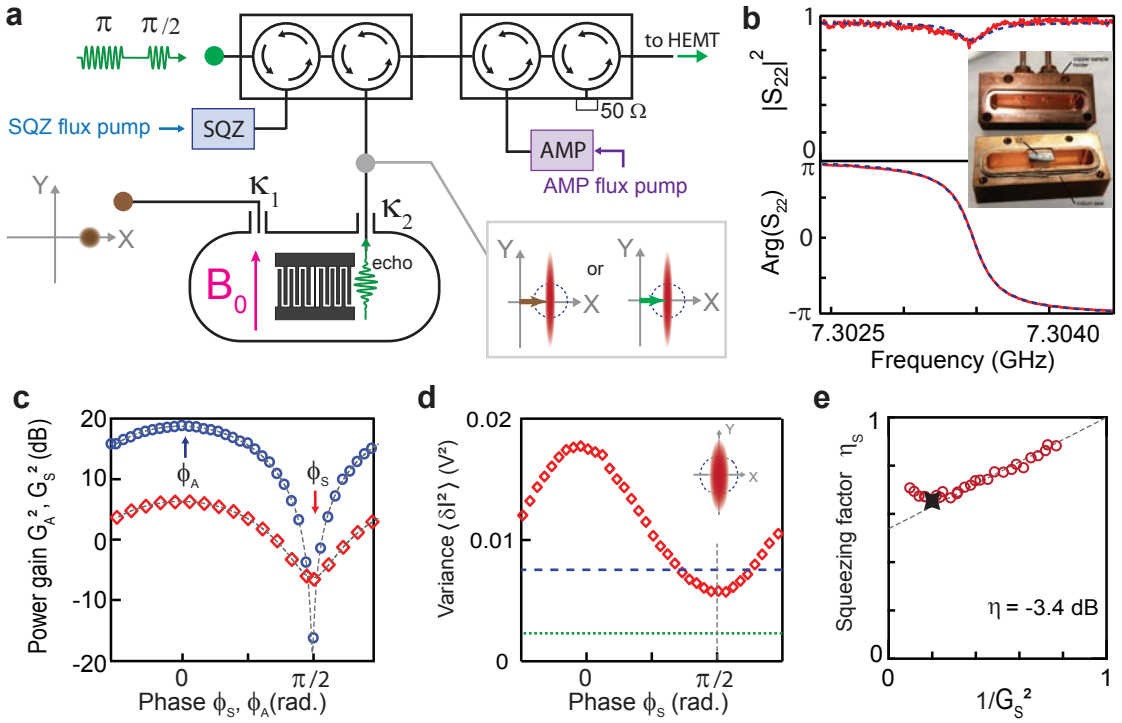

FIGURE 9.8: **Squeezed vacuum generation for an ESR resonator**. **a** Setup including an ESR resonator. The port 1 is used to send coherent signals mimicking the echo emission. **b** The antennas 1 and 2 are chosen to minimize the losses in reflexion on port 2. **c-e** Squeezed vacuum characterization with an ESR resonator

The data shown in Fig. 9.6c-d are taken at the best settings found. It is comparable to other values obtained with different JPAs designs in similar setups: -4.9 dB [216], and -3.1 dB [34].

9.2.3 Noise reduction below the quantum limit with an ESR resonator

Having thus characterized the squeezed state noise reduction and determined its limitations, we include the ESR resonator in the setup. We place the ESR resonator between SQZ and AMP, as depicted in Fig. 9.8a, so that the squeezed vacuum is sent on its second port, coupled to the input line with rate κ_2. We use the same sample and resonators as in the previous chapters. We choose to perform all the following measurements with resonator C ($\omega_0/2\pi = 7.305$ GHz). As explained above, any losses in the setup matter and we have to minimize the resonator internal losses. For that purpose, we voluntarily largely over-couple the resonator via its port 2, with $\kappa_2 \gg \kappa_1 + \kappa_{\text{int}}$ and $\kappa_{\text{int}} \gg \kappa_1$. The length of the coupling antennas is adjusted as shown in Fig. 9.8b to obtain $\kappa_1 = 3 \times 10^3 s^{-1}$, $\kappa_2 = 1.6 \times 10^6 s^{-1}$ and $\kappa_{\text{int}} = 6 \times 10^4 s^{-1}$, values fitted from the measurement of the full resonator scattering matrix. The losses in reflexion are thus $\left|\frac{\kappa_2-\kappa_1-\kappa_{\text{int}}}{\kappa_2+\kappa_1+\kappa_{\text{int}}}\right|^2 = -0.7$ dB (see Fig. 9.8b).

The same optimization procedure described above is used to determine the best operating point for SQZ and AMP with the spins detuned from resonance. For $G_S = 6$ dB and $G_A = 18$ dB, we find $\eta_S = -1.8$ dB and $\eta_{\text{tot}} = 0.77$ (see Fig. 9.8c-d). Exploiting the linear dependence of η_S as a function of G_S^{-1}(see Fig. 9.8e), the losses between SQZ and AMP are estimated to $\eta = -3.4$ dB. This figure is compatible with the higher complexity of the setup (comprising now 4 circulators, 2-m-long coaxial cables, the JPA devices and the ESR resonator).

To ensure that the squeezed quadrature variance $\langle \hat{X}^2 \rangle_{\phi_S=0}$ is reduced below the vacuum fluctuations level $\langle \hat{X}_0^2 \rangle = \frac{1}{4}$, an absolute calibration of the unsqueezed field is needed. This calibration was carried out by Philippe Campagne-Ibarcq using a transmon qubit, and is described in Appendix A. It yields $n_{\mathrm{th}} = 0.05 \pm 0.05$. As seen in ch. 2, the thermal vacuum fluctuations level is given by $\langle \hat{X}_{\mathrm{th}}^2 \rangle = \frac{2n_{\mathrm{th}}+1}{4}$ and thus the squeezed quadrature variance is reduced below the vacuum fluctuations level by a factor:

$$\frac{\langle \hat{X}^2 \rangle_{\phi_S=\pi/2}}{\langle \hat{X}_0^2 \rangle} = \eta_S \frac{\langle \hat{X}_{\mathrm{th}}^2 \rangle}{\langle \hat{X}_0^2 \rangle} = \eta_S (2n_{\mathrm{th}} + 1) \tag{9.18}$$

Given that $\eta_S = 0.66$, we conclude that the field fluctuations are 0.73 ± 0.06 times the vacuum fluctuations, thus reaching the regime of true quantum squeezing. It is comparable to other values reached in the literature: for example Mallet et al. achieved a squeezing of 0.68 ± 0.09 times the vacuum fluctuations [216].

9.2.4 Detection of displaced squeezed states

Finally, to validate our experimental setup and parameters, we simulate the echo emission by sending a small coherent pulse through port 1 of the ESR resonator, as depicted in Fig. 9.9a. The phase of the input pulse is set so that the detected signal lies entirely on the I quadrature, corresponding also to the squeezed quadrature. The detected field amplitude with SQZ on and off for different input powers is shown in Fig. 9.9a. For moderate signal amplitude, the noise histogram shows the same noise reduction $\eta_{\mathrm{tot}} = 0.77$ as without a coherent signal (Fig. 9.9b), as expected.

However for larger input signals, the SQZ on amplitude is a few percents lower than the SQZ off one. We explain this signal degradation once again by the saturation of the JPA devices caused by its Josephson junctions, as already shown in Fig. 9.7. Here, the non-linearity manifests itself in a slightly different way: the output signal phase becomes dependent on the input field amplitude.

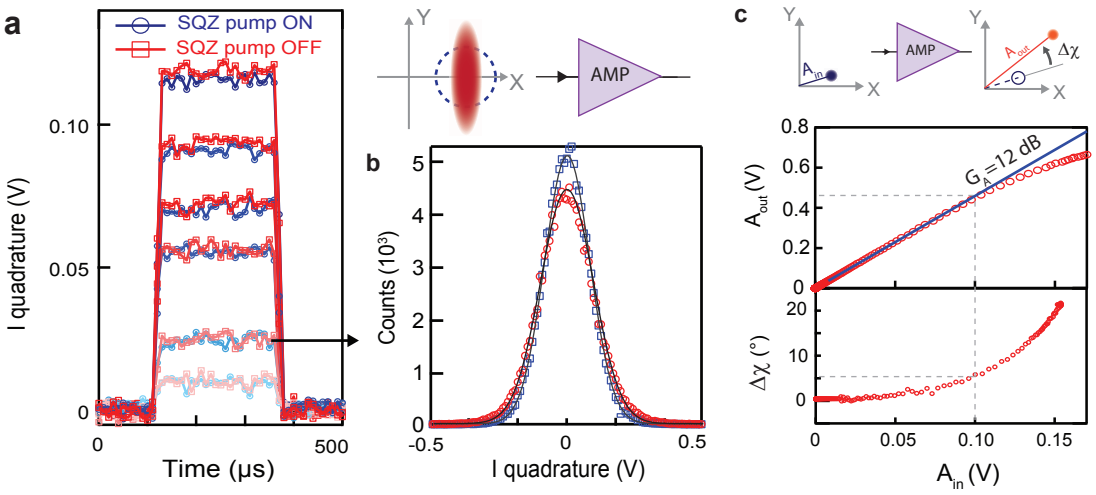

FIGURE 9.9: **Displaced squeezed vacuum state. a** Coherent pulses of varying powers sent through port 1 are measured with (red) and without squeezing (blue). For low powers, the expected noise reduction is observed (panel **b**) but at large powers, the output amplitude is reduced when the SQZ is switched on. **c** The effect is explained by the saturation of the AMP, with an important phase deviation due to the Josephson junctions non-linearities.

The amplitude fluctuations of the displaced squeezed state being larger than the ones of a coherent state of same average amplitude causes the observed difference. To avoid this detrimental effect in our experiment we thus intentionally choose to limit the spin-echo amplitude, as explained below.

9.3 An ESR signal emitted in squeezed vacuum

9.3.1 Squeezing-enhanced ESR: proof-of-principle

We now proceed to the demonstration of squeezing-enhanced ESR detection. For this experiment, we use the lowest-frequency spin transition $|9\rangle \leftrightarrow |10\rangle$ and first characterize the spin-echo with SQZ off. A Hahn-echo field sweep is shown in Fig. 9.10.

The spin-resonance is found at the expected field $B_0 \approx 2.8$ mT; however its shape is significantly different from the one reported in previous chapters. In particular, the double-peak structure is barely visible. This is due to a combination of several factors. The Purcell relaxation time $T_1^{-1} = (2n_{\rm th}+1)(4g^2/\kappa)$ is now one order of magnitude longer due to the lower resonator quality factor used. As explained in ch. 8, T_1 is longest on the upper field peak, where it now reaches ≈ 70 s, thus necessitating a repetition time of ≈ 300 s to measure the whole spin resonance without distortion. For practical reasons, we decided to perform this measurement with a shorter repetition time 15 s, which leaves the low-field peak undistorted but strongly reduces the upper-field peak. To minimize the amplitude of the emitted echo signal for the reasons explained earlier, we set $B_0 = 2.6$ mT, on the "tails" of the low-field peak.

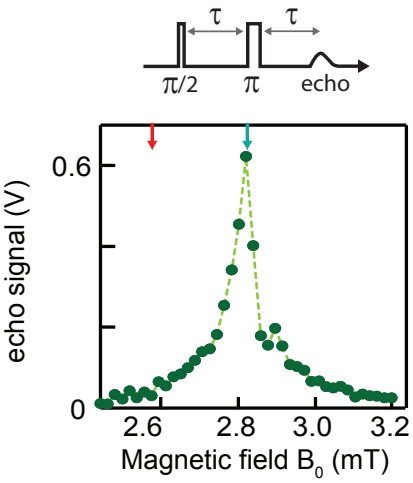

FIGURE 9.10: **Hahn-echo field sweep** with calibrated $\pi/2$ and π pulses.

The experiment consists in repeating a spin-echo sequence ($R_\theta - \tau - \pi - \tau -$ echo) with the SQZ on and off. To limit the spin-echo amplitude even further, we choose a Rabi angle $R_\theta \approx \pi/3$ for the excitation pulse instead of a $\pi/2$ pulse. The SQZ pump is switched on during a time window of 200 µs around the expected echo emission at $t = 2\tau$ (see Fig. 9.11a-b). The phase of the excitation pulse is set such that the echo signal lies entirely on the I quadrature, on which is also aligned the squeezed quadrature.

To minimize setup drifts during the six-hour-long acquisition, we alternate echos acquired with SQZ on and off and we use phase-cycling as shown in Fig. 9.11b. We acquire $N_{\rm avg} = 2500$ echos with SQZ on and 2500 SQZ off. The quadrature voltage $I(t)$ is digitized at a sampling rate of 1 pt/µs with an acquisition bandwidth of 300 kHz. The data is recorded on a time window $T = 200$ µs centered on the echo. The waiting time between each echo sequence is taken to be $T_{\rm rep} \approx 5T_1 = 5$ s. Time traces of the digitized $I(t)$ quadrature are shown in Fig. 9.11c with the echo barely visible in single-shots traces. The averaged signals are computed as:

$$\bar{I}_{\rm ON}(t) = \sum_{i=1}^{N_{\rm avg}} \frac{I_{(1),i}(t) - I_{(2),i}(t)}{2} \text{ and } \bar{I}_{\rm OFF}(t) = \sum_{i=1}^{N_{\rm avg}} \frac{I_{(3),i}(t) - I_{(4),i}(t)}{2} \tag{9.19}$$

where subscripts (j) are indicated in Fig. 9.11b. As can be seen in Fig. 9.11c, the averaged echoes for SQZ on and off are identical, showing that JPA saturation effects have been indeed avoided.

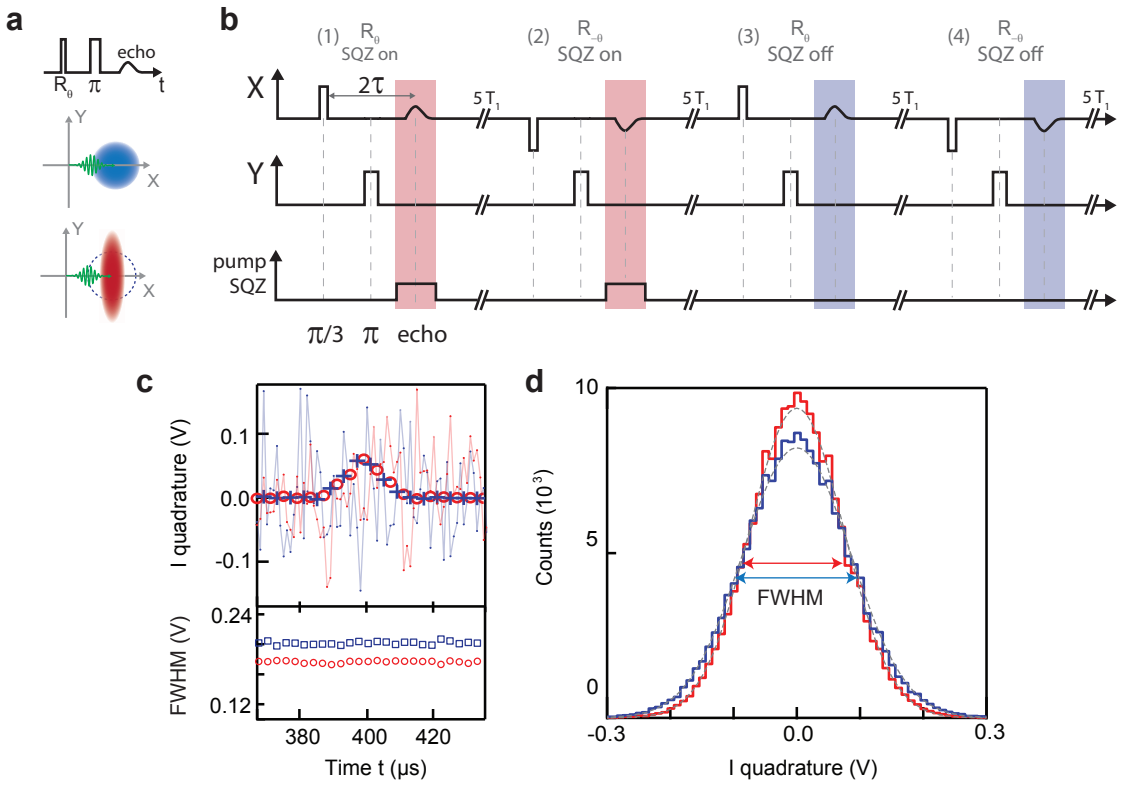

FIGURE 9.11: **Squeezing enhanced echo emission. a-b** Acquisition sequence representing the detected field quadratures. The excitation pulse R_θ followed by a π pulse $\tau = 200$ µs later triggers the emission of an echo at time 2τ. The SQZ is turned on just during the echo emission. The sequence is acquired four times to use phase-cycling and compared echo with SQZ on and off. **c** (top) Echo signal with SQZ on (red) and off (blue). Dash-dotted lines show the single-shot signal. (bottom) Full-width half maximum for identical time stamps. **d** Noise histograms of the I quadrature measured during the echo emission, with SQZ on (red curve) and on (blue curve), fitted with Gaussian distribution (grey dashed lines).

Noise histograms in Fig. 9.11d are computed from the bins $\{I_{(1),i}(t) - \bar{I}_{\mathrm{ON}}(t), \forall i, \forall t\} \cup \{I_{(2),i}(t) + \bar{I}_{\mathrm{ON}}(t), \forall i, \forall t\}$ when the SQZ is on and $\{I_{(3),i}(t) - \bar{I}_{\mathrm{OFF}}(t), \forall i, \forall t\} \cup \{I_{(4),i}(t) + \bar{I}_{\mathrm{OFF}}(t), \forall i, \forall t\}$ and are very close to the ones displayed obtained in Fig. 9.9b for a displaced vacuum squeezed state. In particular the same noise reduction factor of $\eta_{\mathrm{tot}} = 0.77$ is observed. To ensure the echo emission is not affecting the noise properties, we have also computed the noise histograms and variances keeping only identical stamping times t and found no variations (see Fig. 9.11c).

To compute the SNR for both echoes, we use the same procedure explained in ch. 5 where the mode filter function u is chosen to be the echo signal $u(t) \propto [I_{\mathrm{ON}}(t) + I_{\mathrm{OFF}}(t)]/2$. For each echo (j) of each sequence i, we can thus evaluate the signal and noise quantities as $\langle I_{(j),i} \rangle$ and $\langle \Delta I^2_{(j),i} \rangle$. Averaging over all recorded echoes yields the noise and echo signal shown in Table 9.1, demonstrating a rms noise reduction by 11%. Repeating the same procedure for the tophat u function of width 20 µs centered on the echo used in ch. 7 yields similar results.

9.3.2 Absolute sensitivity

Similarly to the analysis done in ch. 7, the number of spins contributing to the signal N_{spins} can de determined by numerical simulations. In ch. 7, the spin distribution at the peak of the spin

$u(t)$	Echo shape			Tophat function		
SQZ	$\langle I \rangle$	$\sqrt{\langle \Delta I^2 \rangle}$	SNR	$\langle I \rangle$	$\sqrt{\langle \Delta I^2 \rangle}$	SNR
OFF	0.179	0.202	0.886	0.161	0.202	0.797
ON	0.177	0.181	0.973	0.160	0.181	0.884
ON/OFF ratio	0.988	0.897	1.10	0.992	0.894	1.11

TABLE 9.1: **Squeezing-enhanced SNR for the echo signal**

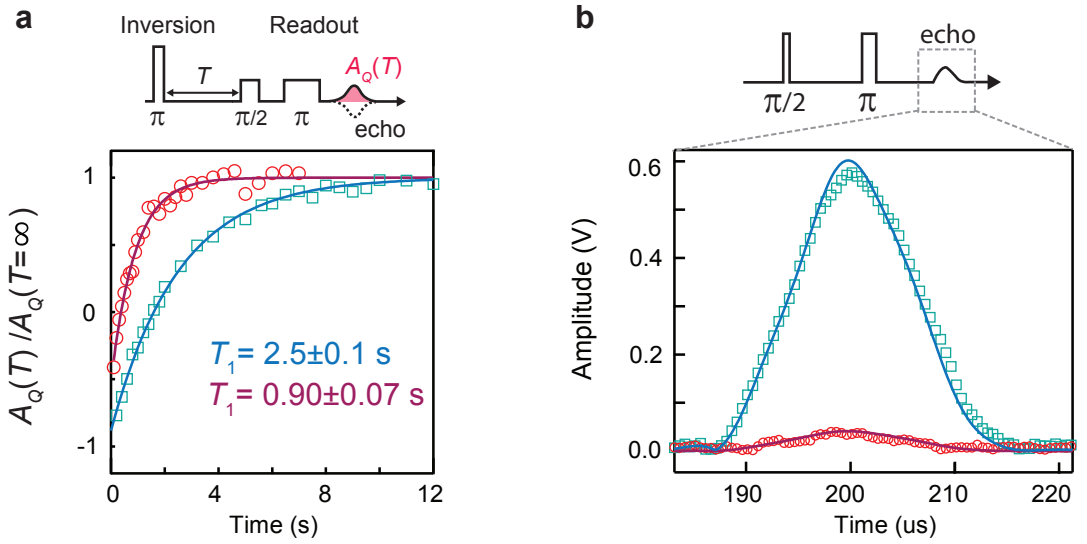

FIGURE 9.12: **Number of spins characterization**. **a** Spin relaxation times measured using inversion recovery at $B_0 = 2.6$ mT (red circles) and $B_0 = 2.8$ mT (blue squares), well fit by exponential decays (solid lines) allowing to extract g to perform numerical simulations. **b** Echo time traces for $B_0 = 2.6$ mT (red circles) and $B_0 = 2.8$ mT (blue squares), reproduced via numerical simulations (solid lines).

line ($B_0 = 2.8$ mT) was found to be adequately modeled with a Gaussian distribution of g with mean value $g_0/2\pi = 56$ Hz and FWHM $\Delta g/2\pi = 1.5$ Hz, as well as a square distribution of the spin detuning of width largely exceeding the resonator bandwidth. Repeating the numerical simulations for resonator B parameters, we find the number of excited spins at $B_0 = 2.8$ mT to be $N_{\text{spins}}(2.8\text{mT}) = 1.2 \times 10^5$.

As discussed in ch. 6, g depends on the magnetic field B_0 due to the strain exerted by the aluminum wire on the silicon introducing a correlation between the spin spectral distribution and the spin spatial distribution (see Fig. 6.6 for example). We estimate the difference in g between 2.6 and 2.8 mT by comparing T_1 at these two fields. As shown in Fig. 9.12a, we find $T_1(2.6\text{ mT}) = 0.9$ s and $T_1(2.8\text{ mT}) = 2.5$ s, implying that $g_0(2.6\text{ mT})/g_0(2.8\text{ mT}) = 1.7$. Calibrating g by comparing the Rabi oscillation frequency for same input power yields the same factor (not shown). Running once again the numerical simulations with $g_0(2.6\text{ mT})/2\pi = 93$ Hz to simulate the echo emission at $B_0 = 2.6$ mT, we find that $N_{\text{spins}}(2.6\text{ mT}) = 4.7 \times 10^3$ reproduces the experimental echo amplitude (see Fig. 9.12b). Associated to the SNR estimation above, this analysis yields a minimal number of detectable spins in one echo sequence $N_{\text{min}} = 1.3 \times 10^4$ with SQZ off, improved to 1.1×10^4 with the SQZ turned on. It corresponds equivalently to a reduction of the acquisition time by 24%.

Note that determining g using the Purcell relation with the experimentally determined n_{th} and κ yields the value $g(2.8\text{ mT})/2\pi = 65$ Hz, 10% larger than estimated in ch. 6. We attribute this difference to the better determination of κ due to the fact that we are now operating in the over-coupled regime where κ_{int} has a minor contribution. In the previous measurements, κ_{int} may have been under-estimated by a measurement at too high power that saturates the TLS lying at

the metal-substrate interface and thus neglects their contribution to the resonator internal losses; a measurement of κ_{int} at input powers corresponding to intra-cavity fields close to 1 photon would have been preferable (see Fig. 5.14). With this newly determined value of g, the sensitivity reported in ch. 7 becomes $1500\ \text{spins}/\sqrt{\text{Hz}}$ instead of 1700.

9.3.3 Theoretical limit of a squeezing-enhanced ESR spectrometer

In our experiment, the achieved gain in sensitivity is limited by the finite degree of squeezing, due to the technical issues detailed in section 9.2.2 (JPA non-linearity and microwave losses along the squeezed-state propagation path). It is however interesting to discuss which would be the achievable enhancement if ideal squeezing could be achieved, and propagation losses suppressed. In other words, what is the theoretical achievable sensitivity of this scheme in the absence of technical imperfections ?

Squeezing backaction on spin dynamics

A first unavoidable and so far overlooked limitation is the impact that quantum squeezing can have on spin dynamics. As already explained in 9.1.1, it was predicted by Gardiner [221] and recently observed [217, 34] that the radiative damping rates of a TLS are modified in the presence of squeezing. As described by Eq. 9.3, shining a quantum squeezed state characterized by N and M (see Eq. 9.3) modifies the spin dynamics in the following ways:

- the radiative relaxation rate is increased by $(2N+1)$ with the steady-state polarization being reduced by the same factor.
- the radiative decoherence time is also impacted.

To measure these effects in our experiment, we compare the spin coherence and relaxation times with and without squeezing. T_2 is found to be unchanged by the squeezing, as shown in Fig. 9.13a, which is understandable by the fact that it is limited by non-radiative processes (see ch. 6). In contrast, we measure $T_1 = 0.45$ s with SQZ on whereas $T_1 = 0.9$ s with SQZ off as already mentioned. This factor 2 reduction is explained by the fact that contrary to T_2, T_1 is limited by a radiative process (spontaneous emission via the resonator) and is thus affected by squeezing according to Gardiner's theory. In addition, both measurements evidence a steady-state polarization reduction by the same factor 2, again consistent with Gardiner's theory. Interestingly, these observations provide us with an independent characterization of the degree of squeezing of the field inside the ESR resonator, in contrast with previous measurements which offer information of the squeezed state at the input of the AMP. We find $2N+1 = 2.0$, yielding a larger degree of squeezing for the intra-cavity field than for the field at the AMP input, qualitatively consistent with the additional losses occasioned by the field propagation from the cavity to the AMP. Using Eq 9.13 with $n_{\text{th}} = 0.1$, we find $\eta_S = -4.8$ dB for the intra-cavity field, compatible with previous measurements. We can thus estimate the losses between the resonator and the SQZ to be $\eta_1 = -0.5$ dB and the losses between the resonator and the AMP $\eta_2 = -2.9$ dB. These asymmetric loss factors are somewhat surprising considering our microwave setup; however we note that the relation between N and η_S is valid only for a perfectly ellipsoidal squeezed state, which is probably not the case in our experiment.

Squeezing-induced spin de-polarization is a major concern for the experiment, as it reduces the spin-echo signal by a factor 2, which would cause the signal-to-noise ratio to be in fact lower with SQZ on than with SQZ off ! In our experiment, this effect was avoided by switching the squeezing on only during the echo emission. This was possible because of the very large difference between the duration of the echo ($\approx 20\mu$s) and the timescale on which the spin become de-polarized, which is given by $T_1/(1+2N) = 0.45$ s. However this strategy would not hold for larger degree of squeezing, if the depolarization time becomes comparable to the echo emission time.

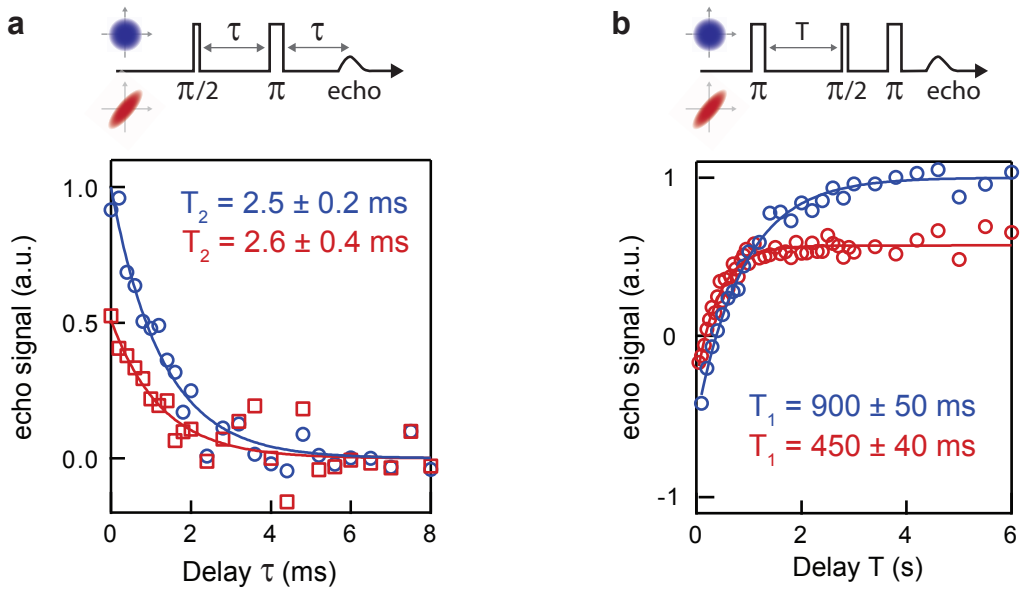

FIGURE 9.13: **Influence of squeezing on spin coherence times**. Coherence time T_2 measured with a Hahn-echo sequence (panel **a**) and energy relaxation time T_1 measured with inversion-recovery (panel **b**) for SQZ off (blue curves) and on (red curves). Solid lines are exponential fits. Both measurements evidence a reduced steady-state polarization in presence of squeezing.

Spin spontaneous emission noise

Another effect limiting the efficiency of the scheme is the presence of extra-noise in the output field due to spontaneous emission of the spins, as measured by Sleator et al. [153]. We can evaluate both experimentally and numerically this noise for our parameters. Experimentally, its contribution can be estimated by comparing the detected noise $\langle \Delta I^2 \rangle_{\text{AMP on}} - \langle \Delta I^2 \rangle_{\text{bg}}$ when the spins are in their ground state (reached after relaxing for $5T_1$) to the noise after inversion by a π pulse. We were unable to measure a statistically significant difference to the level of 2%. Numerically, we use the code developed by Brian Julsgaard and Kaus Mølmer [77] to compute the resonator operators second-moments using the spins distribution given in section 9.3.2 and find the spontaneous emission noise to be 0.16% of the vacuum fluctuations noise. The spin-noise contribution is thus negligible in our experiment. However if larger degree of squeezing could be achieved, this contribution would become significant and thus again limit the achievable sensitivity.

Squeezing enhancement in weak cooperativity regime

To conclude on the application of squeezing for magnetic resonance, we quantify in the following the enhancement brought by the squeezing depending on the experiment parameters. The discussion is limited to the case of weak cooperativity $C \ll 1$, which corresponds to the situation encountered in ESR experiments.

We call $E = N_{\text{min}}^{(\text{off})} / N_{\text{min}}^{(\text{on})}$ the ratio of the achieved sensitivity without squeezing to the sensitivity with squeezing. To express the sensitivity with SQZ on, we consider separately the signal and noise terms for a Lorentzian spin distribution of width w, a valid approximation for $C \ll 1$ (see

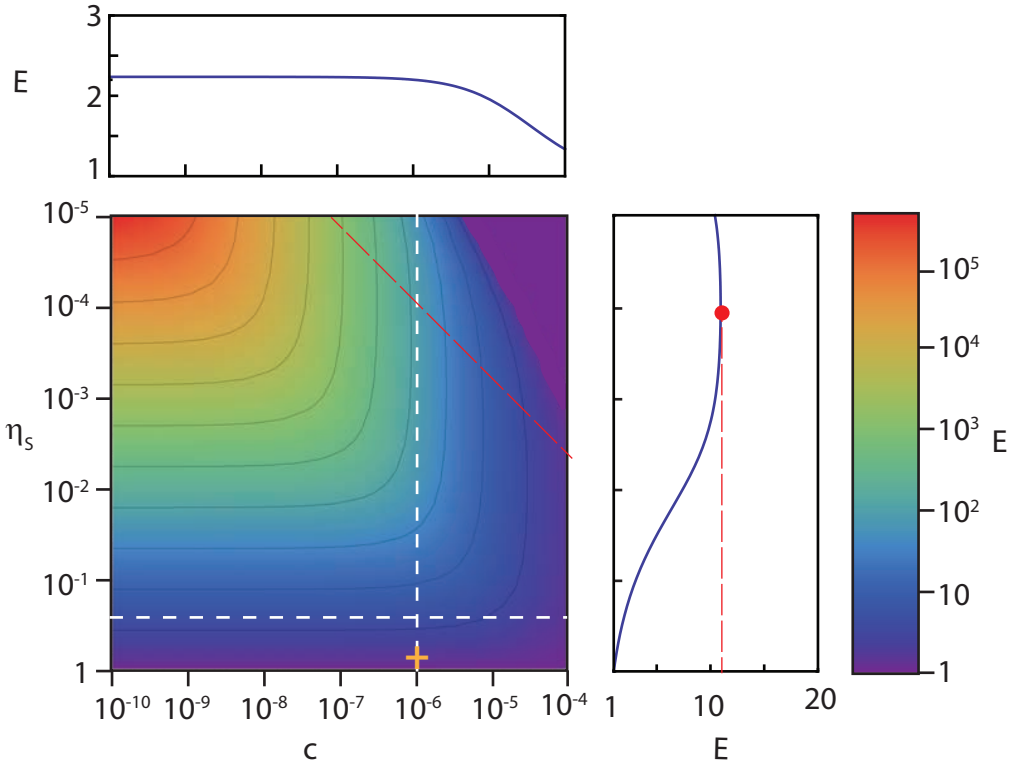

FIGURE 9.14: **Gain in ESR sensitivity with squeezing.** Color plot represents the theoretical gain in sensitivity brought by shining a squeezed state of parameter η_S on the resonator during the echo emission, for spins coupled with a single-spin cooperativity $c = 4g^2T_E/\kappa$. The top and right plots are line-cuts at the white dashed lines. Orange cross is the experiment operating point. The red long dashed line give the best E as a function of c, $E_{\max \eta_S}(c)$. The free parameters T_E, τ, N_{spins} values needed to perform the analysis are taken similar to the experiment.

section 9.1.2). We neglect for the moment the ESR resonator losses, assuming $\kappa_{\text{int}} = \kappa_1 = 0$. We also assume $n_{\text{th}} = 0$ for simplicity.

From Eq. 5.7, assuming $w \ll \kappa$, in absence of squeezing, the amplitude of an echo emitted at $t = 0$ is given by:

$$\langle \hat{a}_{\text{out}}(t) \rangle = -\frac{\sqrt{\kappa} g p N_{\text{spins}}}{\kappa + w} e^{-w|t|/2} \tag{9.20}$$

We assume the dominant effect of squeezing on the echo signal to be the squeezing-induced depolarization. To take into account this effect, we introduce a time dependent function $p(t)$ describing the fraction of spins contribution to the echo. From its initial value $p(0) = p_0$, p decays exponentially under the energy relaxation process after the refocusing π pulse at a rate $\Gamma_1 = \Gamma_P$ without squeezing and at rate $\Gamma_1 = \Gamma_P(2N + 1)$ when squeezing is turned on during the echo emission window ΔT. We then compute the quantity $\langle \hat{a}_{\text{out}}(t) \rangle$ using Eq. 2.43 with u being defined as a tophat function of width ΔT around the echo emission time. To take into account the spin spontaneous emission noise, we assume $\langle \hat{X}^2_{\text{out}} \rangle$ to be given by:

$$\langle \hat{X}^2_{\text{out}} \rangle = \frac{1}{4\eta_S} + n_{\text{SE}} \tag{9.21}$$

with n_{SE} evaluated as $\int_t u(t)\Gamma_1(t)p(t)\frac{N_{\text{spins}}}{2}$. For this analysis, the interesting parameters are η_S

the degree of squeezing, 2τ the sequence duration, T_E the echo width, $c = 4g^2/\kappa$ the single-spin cooperativity and N_{spins}. We then evaluate numerically E as a function of c and η_S from the expressions derived for $\langle \hat{X}^2_{\mathrm{out}} \rangle$ and $\langle \hat{X}_{\mathrm{out}} \rangle$ (see Fig. 9.14). τ and T_E are chosen similar to the experiment, and N_{spins} sufficiently small to ensure $C = cN_{\mathrm{spins}} \ll 1$.

For small c, as the spontaneous emission and the squeezing back-action are negligible, $E = \sqrt{\eta_s}$ as expected. For larger values of c, their contribution becomes non-negligible, and the achievable gain in sensitivity can be shown to be limited by:

$$E_{\max \eta_S}(c) \underset{c \ll 1}{\sim} 1/\sqrt{2cN_{\mathrm{spins}}} = 1/\sqrt{2C} \tag{9.22}$$

given at an optimal squeezing degree. At a given η_S, as $n_{\mathrm{SE}} \propto c$, E decreases from $\sqrt{\eta_S}$ to 1 for increasing c values.

Squeezing and resonator losses

We now come back to the impact of losses in the ESR resonator. In practice, there is an upper bound to the internal quality factor achievable for the resonator $Q_{\mathrm{int}} = \omega_0/\kappa_{\mathrm{int}}$ and thus to maximize the enhancement brought by the squeezing, one should minimize the losses in reflection and thus pick a large coupling rate $\kappa_2 = \alpha\kappa_{\mathrm{int}}$ so as to maximize $\eta = \left(\frac{1-\alpha}{1+\alpha}\right)^2$. However in case of a radiatively limited energy relaxation time, one would also like to minimize the repetition time and thus have a small coupling rate $\kappa = (1+\alpha)\kappa_{\mathrm{int}}$.

This is a non-trivial optimization problem with optimization conditions that depends on the context of the experiment:

- If the bandwidth κ has to be kept large, for instance to excite the whole spin linewidth ($\kappa \gg w$) or to implement fast-manipulating pulses, then its optimization compared to κ_{int} is unnecessary. The best enhancement brought by squeezing is then described by the previous analysis, keeping in mind that η_S will be eventually limited by the resonator losses.
- If on the contrary no physical constraint exists on the choice of the resonator linewidth, then κ should be optimized in such a way as to maximize the experimental sensitivity. We address this optimization problem in the following.

We assume that the squeezing is always broadband compared to the ESR resonator. As the signal-to-noise ratio scales like the square root of the number of repeated experimental sequences, to take into account the impact of κ on the emission efficiency, the noise reduction efficiency and the repetition rate, the quantity that should be optimized is the absolute sensitivity $\mathcal{H} = N^{(on)}_{\mathrm{min}}/\sqrt{\Gamma_1}$ with SQZ on. In the case where $w \ll \kappa$, we can distinguish several different limits:

- **Without squeezing and $\boldsymbol{\Gamma_1 \gg \Gamma_P}$**, then using Eq. 5.11 we get $\mathcal{H}_1 = \frac{\sqrt{nw}}{2gp\sqrt{\Gamma_1}} \frac{\kappa}{\sqrt{\kappa_2}} \propto \frac{(1+\alpha)}{\alpha^{1/2}}$.

  The minimum of $\mathcal{H}$ is thus reached for $\alpha = 1$, i.e. a critically-coupled resonator.

- **Without squeezing and $\boldsymbol{\Gamma_1 = \Gamma_P}$**, then $\mathcal{H}_2 = \frac{\sqrt{nw}}{4g^2p} \frac{\kappa^{3/2}}{\sqrt{\kappa_2}} \propto \frac{(1+\alpha)^{3/2}}{\alpha^{1/2}}$.

  The optimum is reached for $\alpha = 1/2$, once again close to critical-coupling.

- **With squeezing and $\boldsymbol{\Gamma_1 \gg \Gamma_P}$**: There is no back-action from the squeezing on the spins. Thus in $\mathcal{H}_1$ only $n = 1/4$ should be replaced by $n = \frac{1}{4}(\eta/\eta_S + 1 - \eta) + n_{\mathrm{SE}}$. The quantity to optimize is then: $\mathcal{H}_3 \propto \left[\left(4n_{\mathrm{SE}} + 1 - \frac{(\alpha-1)^2}{(\alpha+1)^2}\right) \frac{(1+\alpha)^2}{\alpha}\right]^{1/2}$ and thus the best choice is again $\alpha \sim 1$.

- **With squeezing and $\boldsymbol{\Gamma_1 = \Gamma_P}$.** In this case, one should take into account the squeezing back-action for the spins and use the above model. The sensitivity $N_{\min}(\eta_S, c)$ is rescaled by $\sqrt{1+1/\alpha}\, N_{\min}(\eta_s, c)$ in presence of losses. Knowing the intrinsic $c_{\rm int} = 4g^2 T_E/\kappa_{\rm int}$, one can optimize the choice of κ_2. For a given α, the cooperativity is expressed as $c = c_{\rm int}/(1+\alpha)$ and the best achievable squeezing is $1-\eta(\alpha)$. The optimal choice of α given $c_{\rm int}$ is thus to minimize $\mathcal{H}(\alpha, c_{\rm int}) = \sqrt{1+\alpha}\, N_{\min}^{(\rm on)}(c_{\rm int}/(1+\alpha), 1-\eta(\alpha))$.

  For our experimental parameters, this optimization yields $\kappa_2 = 0.25\, \kappa_{\rm int}$.

From this analysis, it appears that in most operating limits, the best choice is a critically coupled ESR resonator. In that case, the resonator internal losses will unavoidably limit the noise reduction obtained by squeezing to at most 3 dB, implying that squeezing factors above 10 dB would be irrelevant for this application. As already stated, this conclusion is only valid if the resonator linewidth can be chosen without any physical constraint (such as a finite spin linewidth, or pulse bandwidth), in which case larger enhancement factors can be theoretically reached as discussed in the previous paragraph.

9.4 Conclusion

We realized in this chapter a proof-of-concept demonstration that squeezed states can be used to enhance the sensitivity of a magnetic resonance experiment and reduce the acquisition time. The rms noise reduction achieved in our experiment is limited to 12%, due to a number of technical issues. We note that intensive research in cQED aims at improving JPA devices [60] and developing lossless circulators [225, 226], which will be directly applicable to our scheme, with the perspective of gaining one order of magnitude on the acquisition time.

Without improving the efficiency of the restitution of the energy stored by the spins by the first excitation pulse, by using CPMG sequences for example, further spectrometer sensitivity improvements will then come from increases in the resonator-spin coupling constant, or smaller resonator internal losses. We also note that other types of non-classical states could be useful for enhanced magnetic resonance: Fock states, Schrödinger-cat states [227], which are readily generated using circuit QED tools, are also known for their potential applications in quantum metrology. Further work should aim at assessing their usefulness for magnetic resonance. Moreover, more elaborate analysis than just measuring the variance could be useful, as was recently demonstrated in atomic spin squeezing [228]. In a broad perspective, our results indicate that the whole arsenal of quantum metrology deserves to be examined in view of its potential application in magnetic resonance.

Chapter 10

Conclusion and future directions

10.1 Magnetic resonance with quantum microwaves

In this thesis, we have reported three experiments in which we perform magnetic resonance spectroscopy in a novel regime where the microwave field, just like the spins, requires a quantum-mechanical description.

So far, the microwave signals detected during ESR experiments had always been treated classically, since the detected noise largely exceeded the field quantum fluctuations. In ch. 7, we demonstrated that thanks to the use of low-temperatures and of a quantum-limited amplifier, the spectrometer output noise could arise mainly from these quantum fluctuations. Combining this quantum-limited sensitivity with high-quality-factor and small-mode-volume resonators, we demonstrated an unprecedented sensitivity for our home-built ESR spectrometer of 1700 spins/$\sqrt{\text{Hz}}$ using Si:Bi spins. Using a CPMG sequence, we decreased this number to 150 spins/$\sqrt{\text{Hz}}$.

Entering the regime of quantum-limited noise opens the door to the use of quantum optics techniques to increase the measurement sensitivity beyond the quantum-limit. In ch. 9, we realized a proof-of-concept experiment where we used squeezed vacuum states to reduce the total spectrometer output noise power by 25%. This translates into a 12% enhancement on the sensitivity or equivalently a 25% reduction in the acquisition time.

Besides being relevant for the spectrometer output noise, quantum microwave fluctuations can also have a strong impact on the spin dynamics. In usual ESR experiments, the coupling constant between each spin and the microwave field is too small for the effect to be relevant. However, we showed in ch. 8 that for a spin placed at resonance in a high-quality-factor small-mode-volume resonator, the spin energy relaxation could be made faster via spontaneous emission of microwave photons. While the non-radiative relaxation time of Si:Bi spins was measured to be on the order of 20 minutes, the Purcell effect decreased T_1 to a few seconds. More generally, cavity-enhanced spin relaxation can be used as a fast spin initialization method in several ESR experiments. For future applications in quantum information, T_1 can be controlled on-demand by changing the spin-resonator coupling or detuning. This provides a new way to combine long intrinsic T_1 times with fast repetition rates.

10.2 Future research directions

The experimental results reported in this thesis open new possibilities both for magnetic resonance and for quantum information.

Beyond proof-of-concept quantum ESR

Our experimental setup reached record spin sensitivity, but with a very specific setup, since we measured implanted donors in silicon, and we use superconducting resonators, amplifiers, at ultra-low-temperatures, and with applied magnetic fields below 10 mT. An interesting research direction is to use our setup to measure "real-world" samples with comparable sensitivites.

A first point to note is that in order to detect a wider range of spin species, higher magnetic fields are required. A first objective would be to extend the setup to apply 0.2-0.3 T, which would enable to perform X-band ESR measurements. Such magnetic fields could be applied to the resonator without degrading its quality factor if the superconducting film had a higher critical field. Recently, resonators made out of superconductors such as nobium, nobium nitride [155, 156] and nobium titanium nitride [157] have demonstrated high quality factors up to 1 T. Further improvements can be expected since it is a subject of intense research in the cQED community, with the perspective of realizing hybrid devices combining superconducting qubits and for instance semiconducting nanowires [229], electrostatically quantum dots [230, 231] or Si:P spins [232].

Although we have used implanted donors in silicon, which are a well-known model spin system, other non-implanted spins could also be studied. The difficulty lies in having the spins a few tens of nanometers away from the resonator wire without using implantation. Some spins, such as the well-known organic compound 2,2-diphenyl-1-picrylhydrazyl (DPPH), widely used as a field and signal calibration marker in ESR spectrometers [233] or the stable free radical 1,3-bisdiphenylene-2-phenylallyl (BDPA), can be mixed with glassing mixtures and could be drop-cast on the chip [234] or vapor-deposited [235]. Measuring low-concentrated samples of these radicals would already be a proof-of-concept that our technique can be generalized.

Another topic where our experimental setup could be improved is the JPA. While the devices used in this work suffered from limited bandwidth and dynamic range, recently developed devices have reached much higher dynamic ranges (-100 dBm) and considerably larger bandwidths (1 GHz) [60]. Cascaded with HEMT amplifiers which have now demonstrated noise temperature of 1 K [154], they could provide quantum-limited amplification without restricting the bandwidth or output power level of the ESR spectrometer.

Low-temperatures are required both for having high spin polarization at gigaHertz frequencies and ensuring that the microwave field is in its ground state. Commercial spectrometers already operate at 4 K, where the use of frequencies > 100 GHz could allow for quantum-limited ESR. Keeping an operating temperatures of 20 mK would permit working at similar frequencies than used in this thesis and use lower magnetic fields than required for operation at 100 GHz.

Cavity-assisted dynamic nuclear polarization

Another promising research direction is to explore the applications of Purcell-enhanced spin relaxation to magnetic resonance. In particular, it seems interesting to envision how it could be applied to Dynamical Nuclear Polarization (DNP) schemes [208, 209]. In such schemes, the polarization of a nuclear state is built by cross-relaxation on a electron-nuclear flip-flop transition. Cavity-enhanced relaxation could be an alternative to existing relaxation mechanisms or enhance the relaxation rate of this transition to improve the efficiency of the nuclear polarization.

To give an example of implementation of cavity-assisted DNP, we briefly discuss preliminary results obtained using our setup. As shown in Fig. 10.1, our goal was to transfer population from Si:Bi state $|8\rangle$ into $|9\rangle$, using cavity-enhanced relaxation. The scheme consists in exciting the $|8\rangle \leftrightarrow |11\rangle$ transition with the $|9\rangle \leftrightarrow |11\rangle$ transition tuned at the resonator frequency so that spins undergo Purcell-enhanced relaxation. The population in $|9\rangle$ is finally probed by measuring spin-echoes on the $|9\rangle \leftrightarrow |10\rangle$ transition. Fig. 10.1b shows the echo signal as a function of the resonator detuning to

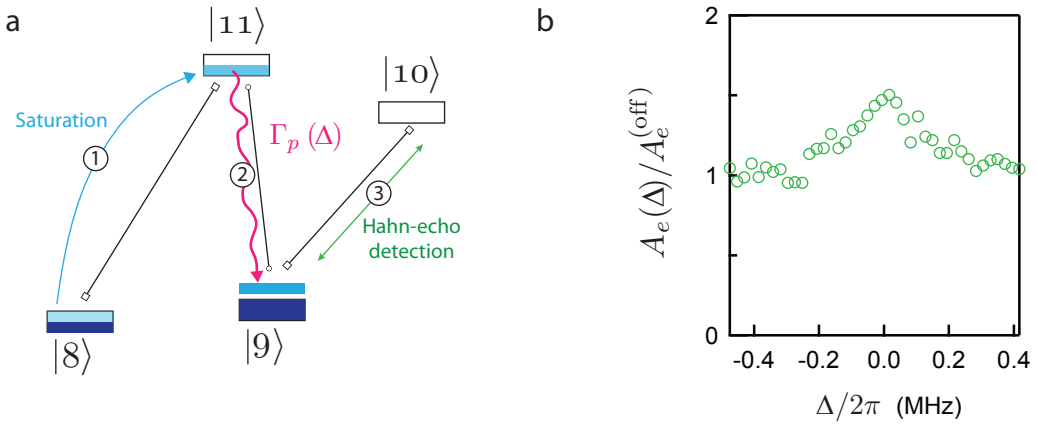

FIGURE 10.1: **Cavity-assisted DNP using Si:Bi spins.** **a** Working at $\theta = 45\,^{\circ}$, transitions $|8\rangle \leftrightarrow |11\rangle$, $|9\rangle \leftrightarrow |11\rangle$ and $|9\rangle \leftrightarrow |10\rangle$ are allowed. To transfer population from $|8\rangle$ to $|9\rangle$, a saturation pulse is first applied on $|8\rangle \leftrightarrow |11\rangle$. The population stored in $|11\rangle$ then relaxes via the Purcell effect down to $|9\rangle$. **b** Measuring the echo signal on transition $|9\rangle \leftrightarrow |10\rangle$ shows that when the Purcell relaxation is tuned at resonance, the echo signal is increased by 50%.

$|9\rangle \leftrightarrow |11\rangle$. When it is at resonance, the Purcell rate is maximized and activates the transfer to $|9\rangle$. Our results demonstrate a cavity-assisted hyperpolarization of $\approx 50\%$ in $|9\rangle$.

Higher degrees of polarization are difficult to obtain in our setup. First, our device geometry with its high quality factor does not allow to apply strong off-resonant pulses. This problem is avoided in the above scheme by pulsing the magnetic field in order to bring the various transitions successively in resonance with the resonator. However the slow response of the Helmholtz coils causes a partial decay via the Purcell effect of any population stored in an excited state and thus limits the pumping scheme efficiency. These issues could be solved with for example either a fast-tunable coil or a frequency-tunable resonator, or an ENDOR-type cavity enabling the application of rf pulses to control the nuclear states in addition to microwave pulses.

Beyond these technical considerations, the experiment described here is only one example for using cavity-enhanced relaxation in DNP schemes. Depending on the spin systems, many others schemes could be realized, provided that the relaxation transition can be sufficiently coupled to the cavity microwave field to obtain Purcell-enhanced spontaneous emission.

Single-spin inductive detection

A third promising perspective is to enhance the sensitivity of our setup even further. Indeed, when the spin relaxation is set by cavity-enhanced relaxation, the absolute sensitivity is given by $N_{\min}\sqrt{\Gamma_p}$ and thus scales as g^2 instead of g. As explained in this thesis, g is proportional to the magnetic field quantum fluctuations; reducing the lateral dimensions of our inductance wire by two orders of magnitude (down to 50 nm, see Fig. 10.2) would thus increase g by the same amount. Reaching such a coupling strength would put the detection of a single spin within reach.

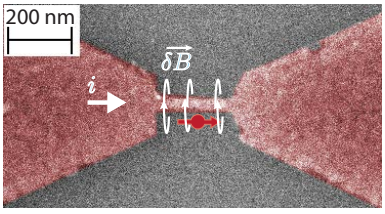

FIGURE 10.2: **Al nanowire constriction for single-spin sensitivity**

This goal is actively pursued in the group. Once achieved, such exquisite sensitivity will enable for example the detection of single magnetic entities, for instance individual molecular magnets.

For quantum information purposes, achieving a ratio $g/\kappa \lesssim 0.1$ would allow the electronic spin to interact strongly with incoming microwave photons. Applied to spin systems having both electronic and nuclear spins coupled by hyperfine interaction, such as Si:Bi spins or NV centers in diamond, the efficient detection of the electron spin opens the way to detection of the nuclear spin state. Indeed, the coupling between electronic and nuclear spin yields ESR transitions whose frequencies are nuclear spin state dependent, as seen in ch. 4 for Si:Bi spins. If only one of these transitions is coupled to the resonator, its efficient readout would then permit to non-destructively measure the nuclear spin state.

This enables in turn measurement-based entanglement schemes. Consider two spins coupled to two resonators. If each nuclear spin state readout yields the same result when the spins are prepared in the same state, then the simultaneous readout of both nuclear spins will not distinguish one spin from the other, resulting into the creation of an entangled state. Such a scheme would be the microwave transposition of the heralded entanglement scheme demonstrated on NV centers using optical readout [236].

Si:Bi spins for quantum memories

Finally, we note that Si:Bi spins have specific properties which make them particularly well suited for quantum memory implementation [71]. In this thesis we have already showed that they can be readily coupled to superconducting resonators and that they have long coherence times. Additional interesting features include the electrical control of the donor spin frequency, which has been demonstrated only for Si:P so far [237].

In quantum memory proposals [78], the state of a superconducting qubit is stored in a spin ensemble, mediated by an intermediate superconducting resonator. This requires that the spin ensemble is strongly coupled to the resonator so that it can absorb efficiently the microwave field. Strong collective coupling requires largely concentrated samples, which in general translates into lower spin coherence times due to dipolar interactions, thus shortening possible storage times. The key asset of Si:Bi is that seconds-long coherence times are possible even in highly concentrated samples at the clock transitions. Memory reset could be achieved using the Purcell effect, as demonstrated in this thesis.

Appendix A

Thermal occupancy calibration

Due to imperfect filtering of the microwave probe lines and to the refrigerator finite base temperature, one can never reach perfect electromagnetic vacuum. In this appendix, we describe the calibration procedure used to place an upper bound on the average excitation number of the input modes $\hat{b}_{\rm in}(\omega)$ around the ESR resonator resonance frequency (typically $|\omega - \omega_0| \leqslant \kappa_c$).

The method consists in replacing, in a separate cool-down of the refrigerator, the ESR resonator with a transmon superconducting qubit [238] coupled to a microwave readout resonator with resonance frequency ω_1. The resonator-qubit system is in the so-called *strong dispersive regime* of circuit QED in which photons in the resonator mode lead to dephasing of the qubit [239, 240]. Thus, by measuring the dephasing rate of the qubit beyond the effect of population relaxation $\gamma_\phi = \gamma_2 - \gamma_1/2$, where $\gamma_2 = 1/T_2$ and $\gamma_1 = 1/T_1$, one can place an upper bound on the thermal photon number $n_{\rm th}$ in the readout resonator, and then on the occupation of the traveling modes $\hat{b}_{\rm in}$.

Microwave setup and device

We calibrate the number of thermal photons using the squeezing experiment setup (see ch. 9) shown in Fig. A.1a. The ESR resonator is replaced by the following device, studied in [241]. On a sapphire chip, 4 lumped element microwave readout resonators, each one capacitively coupled to a transmon qubit (see Fig. A.1), are coupled to a single transmission feedline. In the following, we consider only the qubit-resonator system labeled *cell 2* (the other ones are well out of resonance). The feedline is connected to the setup depicted in Fig. A.1a at points A and B.

The readout resonator consists in an interdigitated capacitor made out of superconducting aluminum in parallel of an array of Josephson junctions (Fig. A.1). This array behaves as a non-linear inductor and was originally designed to allow for a single-shot readout of the attached qubit. This non-linearity is not relevant here and can anyway be neglected as the average photon number in the resonator is well below one. Note that the readout resonator has a slightly different frequency $\omega_1/2\pi = 7.62$ GHz than the ESR resonators, but we assume that the thermal equilibrium is similar so that $\langle \hat{b}^\dagger_{\rm in}(\omega)\hat{b}_{\rm in}(\omega)\rangle = \langle \hat{b}^\dagger_{\rm in}(\omega_1)b_{\rm in}(\omega_1)\rangle$ for all relevant values of ω. This assumption is reasonable given that $|\omega - \omega_1| \ll k_B T$, and the transmission of the microwave input lines is flat (± 0.5 dB variation) on this frequency range.

Note that in this geometry, the readout resonator thermal occupation is set by the average occupation of right propagating modes $\hat{b}_{\rm in}$ through A and left propagating modes $\hat{c}_{\rm in}$ through B (see Fig. A.1d). Internal losses of the readout resonator, that could act as a connexion to a fictitious cold reservoir, are shown to be negligible on Fig. A.3d. The blue input line connected at B in Fig. A.1a, which was originally designed to probe the ESR resonator in reflection on port 1, is less attenuated by 10 dB than the green line connected to A so that left propagating modes tend to increase the thermal

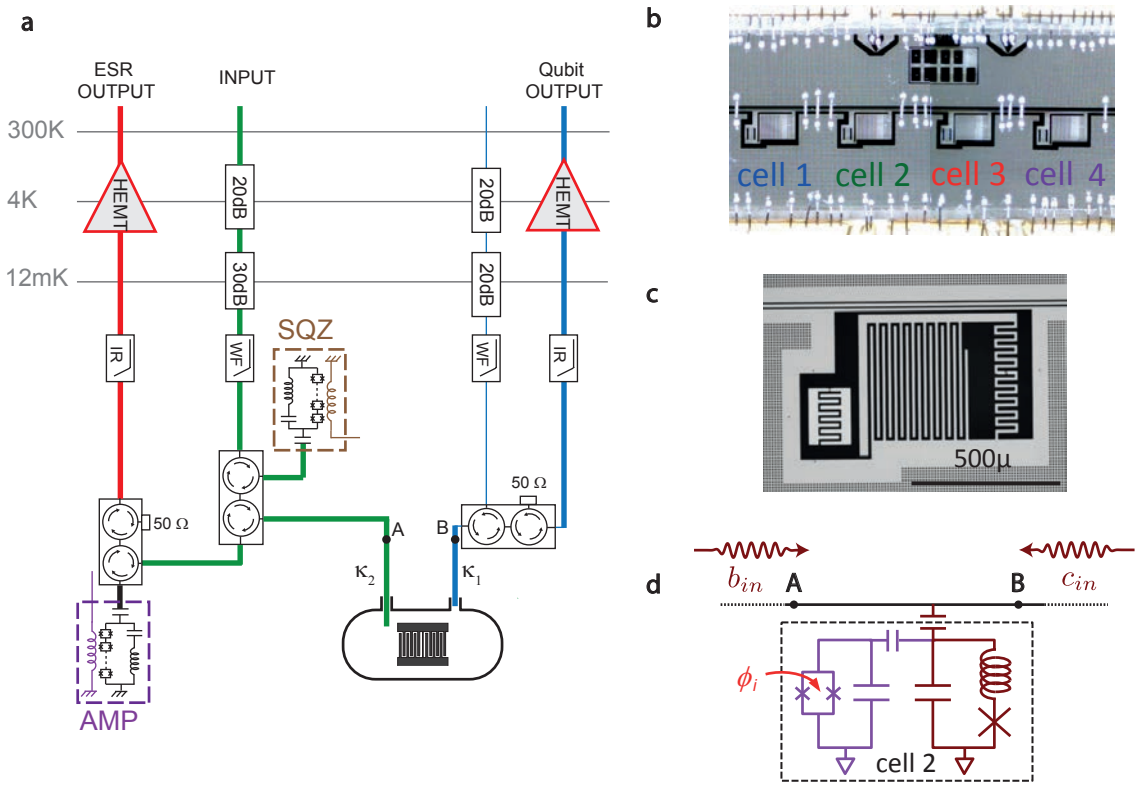

FIGURE A.1: **a** Microwave setup used during the squeezing experiment (see ch. 9) **b** Optical micrograph of the device used for estimating the number of thermally excited photons in $\hat{b}_{\text{in}}$. Four cells, each one composed of a transmon qubit with an attached readout resonator are probed with a single microwave feedline. **c** Zoom on one of the cells, showing the tunable transmon qubit (to the left) capacitively coupled to the readout resonator (to the right), itself capacitively coupled to the feedline (to the top). **d** Simplified electric circuit of the cell used for the calibration. The qubit contains a split Josephson junction and its resonance frequency can be tuned by threading the loop with a magnetic flux φ. The resonator, which contains an array of junctions, is slightly non linear. Thermal excitations in the resonator are due to both right and left traveling modes $\hat{b}_{\text{in}}$ and $\hat{c}_{\text{in}}$ in the feedline.

occupation of the readout resonator. This issue does not arise with the ESR resonator since the coupling rate through port 1 is negligible ($\kappa_1 \ll \kappa_2$). Thus, the calibration made here is conservative and the estimation of the thermal occupation of $\hat{b}_{\text{in}}$ should be considered as pessimistic.

The transmon qubit is made out of a smaller interdigitated capacitor in parallel with a split Josephson junction that allows to tune its resonance frequency. A DC magnetic field is then applied using a superconducting coil in order to operate the device at its *sweet spot*, where its frequency $\omega_q/2\pi = 6.23$ GHz does not depend on the magnetic field fluctuations at first order (see Fig. A.2).

The coupling rate of the qubit and readout resonator is much smaller than the detuning $\omega_1 - \omega_q$ so that the system is described by the dispersive hamiltonian [240]

$$H = \hbar\omega_1(\hat{a}^\dagger\hat{a} + \frac{1}{2}) + \hbar\omega_q\frac{\hat{\sigma}_z}{2} + \hbar\chi\hat{a}^\dagger\hat{a}\hat{\sigma}_z. \tag{A.1}$$

Here, $\hat{\sigma}_z$ is the Pauli operator of the qubit and χ is the qubit state dependent shift of the readout

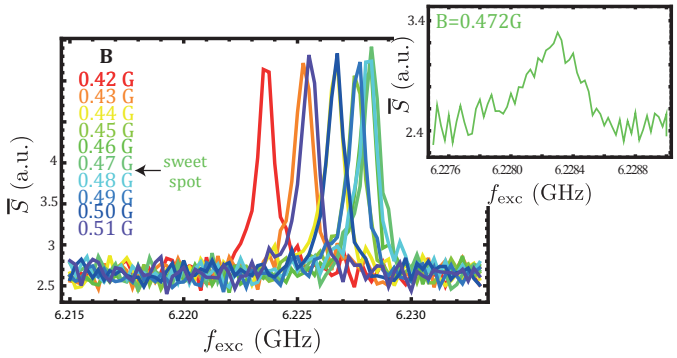

FIGURE A.2: **Two-tone spectroscopy** of the qubit. Starting from thermal equilibrium, the qubit is shined with a 5 µs-long saturating pulse (power -20 dBm referenced at refrigerator input) of frequency $f_{\rm exc}$ and then readout with an optimized pulse around $\omega_1/2\pi$ (see text and Fig. A.3). The integrated signal $\overline{S}$ reveals the qubit excited state occupation. One can vary the qubit resonance frequency by varying the amplitude of the applied B-field (encoded in color). **Inset:** desaturated qubit resonance (power -30 dBm at fridge input) at the sweet spot, showing that $\omega_q/2\pi = 6.228$ GHz.

resonator frequency, which provides us with a robust readout method of the transmon [242, 243]. Indeed, by probing the resonator with a microwave nearby its resonance frequency and integrating a quadrature of the transmitted field, one gets a signal $\overline{S}$ depending linearly on $\langle\hat{\sigma}_z\rangle$. In practice, the power, length and frequency of the readout pulse was empirically adjusted to optimize signal-to-noise ratio. It corresponds to few photons in the resonator (power 10 dB larger than for 1 photon characterization of the resonator on Fig A.3 d). Note that the JPA was turned off during all measurements.

Thermal photon characterization

Rigetti *et al.* computed the dephasing rate of a qubit induced by thermally excited photons in the readout resonator mode [244]. It reads

$$\gamma_{\rm phot} = \frac{\kappa}{2}\mathrm{Re}\Big\{\big((1+2i\frac{\chi}{\kappa})^2 + 8i\,n_{\rm th}\,\frac{\chi}{\kappa}\big)^{1/2} - 1\Big\}, \tag{A.2}$$

where κ is the photon exit rate from the readout resonator, and $n_{\rm th} = \langle a^\dagger a\rangle$ is the mean number of photons hosted by the resonator. Considering that $\gamma_{\rm phot} \leq \gamma_\phi = \gamma_2 - \gamma_1/2$, we now measure the qubit population and coherence relaxation rates γ_1 and γ_2 as well as all parameters entering the expression (A.2) in order to place an upper bound on $n_{\rm th}$.

By applying π and $\pi/2$ excitation pulses (calibrated by recording Rabi oscillations of the qubit), we first measure the qubit population relaxation rate $\gamma_1 = 0.41$ µs^{-1} (see Fig. A.3 a) and coherence relaxation rate $\gamma_2^* = 1.1$ µs^{-1} (see Fig. A.3 b). This last rate corresponds to a free-induction decay measurement, and includes the effect of low-frequency noise, such as second order perturbation of the fluctuations in the flux threading the qubit loop, along with high-frequency noise as induced by thermally induced photons in the readout resonator. A Hahn-echo measurement would rephase any low-frequency noise. As we measure $\gamma_{2,\rm echo} \simeq \gamma_2^*$ (see Fig. A.3 c), we can state that the dominant contribution is thermal dephasing ad thus the qubit pure dephasing rate is simply $\gamma_\phi = \gamma_2 - \gamma_1/2 = 0.9$ µs^{-1}.

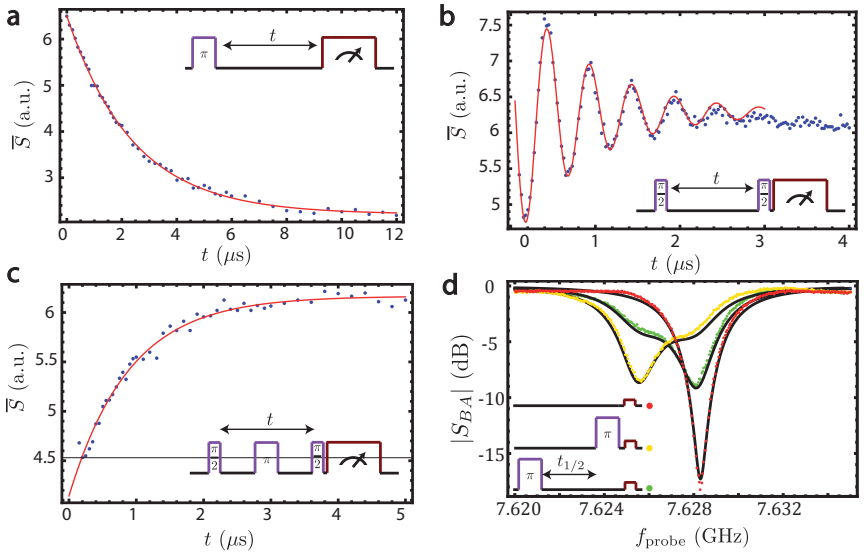

FIGURE A.3: **Qubit-resonator parameters characterization**. For each measurement, the pulse sequence is schematically represented at ω_q (in purple, all rotations around $\hat{\sigma}_y$ of the qubit) and at $\omega_{\mathrm{readout}} \simeq \omega_1$ (in brown). **a** Population relaxation measurement yielding $T_1 = 2.4$ µs, **b** Free induction decay measurement yielding $T_2^* = 0.9$ µs (excitation pulses at $\omega_q/2\pi + 2$ MHz). **c** Hahn-echo measurement yielding $T_{2,\mathrm{echo}} = 0.9$ µs. **d** Measured transmission coefficient S_{AB} when the qubit is at thermal equilibrium (red dots), right after an inverting π-pulse (yellow dots) and a qubit half-life later (green dots). Black lines: global fit with parameters $p_\pi = 0.66$, $\chi/2\pi = 1.48$ MHz and $\kappa_{\mathrm{int}}/\kappa_{\mathrm{c}} = 0.14$. For **a**, **b** and **c** the readout pulse power is empirically adjusted to optimize signal to noise ratio and the transmitted field is integrated over 5 µs. Only the quadrature $\overline{S}$ containing information on the qubit state is plotted. For **d** the readout pulse power is low enough that readout resonator non-linearity is neglected and the transmitted field is integrated over 0.2 µs in the stationary regime.

The last quantity needed to evaluate n_{th} is the anharmonicity χ. To have a precise estimate of its value, we detect the transmitted signal through the feedline for a probe pulse of low amplitude (linear regime of the readout resonator) and integrate the signal over 0.2 µs $\ll T_1$ in the stationary regime of the resonator (signal during ring-up is discarded in order to avoid distortion of the signal). The transmission coefficient from A to B then reads [245]

$$S_{BA}(\omega) = p\frac{\kappa_{\mathrm{int}} + 2i(\omega - \omega_{\mathrm{res}} - \chi)}{\kappa_{\mathrm{int}} + \kappa_{\mathrm{c}} + 2i(\omega - \omega_{\mathrm{res}} - \chi)} + (1-p)\frac{\kappa_{\mathrm{int}} + 2i(\omega - \omega_{\mathrm{res}} + \chi)}{\kappa_{\mathrm{int}} + \kappa_{\mathrm{c}} + 2i(\omega - \omega_{\mathrm{res}} + \chi)}, \tag{A.3}$$

where κ_{c} (resp. κ_{int}) is the resonator photon exit rate into the feedline (resp. due to internal losses) and $p = \langle 1 - \hat{\sigma}_z \rangle/2$ is the occupation of the ground state of the qubit. Note that the total photon exit rate from the resonator $\kappa = \kappa_{\mathrm{int}} + \kappa_{\mathrm{c}} = 2\pi \times 3.25$ MHz is determined independently by measuring the ringdown time of the resonator.

We record this transmission coefficient at thermal equilibrium ($p \simeq 1$, red dots on Fig. A.3d), after applying a π-pulse ($p = p_\pi$, yellow dots) and, for better precision, a duration $t_{1/2} = \ln 2\, T_1$ after the same pulse ($p = p_\pi/2$, green dots). If p_π can be roughly estimated given the drive pulse duration and delay before signal integration, it is difficult to predict accurately its value due to the reduction of T_1 in presence of a field in the readout resonator [246]. We rather estimate it along with the other parameters entering Eq. (A.3) by fitting these three curves altogether (black curves), which yields $p_\pi = 0.66$, $\chi/2\pi = 1.48$ MHz and $\kappa_{\mathrm{int}}/\kappa_{\mathrm{c}} = 0.14$. In this fit, we allow for a global scaling factor accounting for the attenuation in the lines, and a small offset in the transmitted field complex amplitude, attributed to impedance mismatch. From this calibration and using Eq. (A.2), we find for the readout resonator

$$n_{\mathrm{th}} = 0.5 \pm 0.5. \tag{A.4}$$

We thus conclude that the thermal occupancy of the transmission lines is also less than 0.1 and use this number throughout the experimental results presented in ch. 5-9, since all are acquired with only small changes in the microwave setup of Fig. A.1, with all probe lines having the same filtering. Improving this figure would certainly require increasing the attenuation of the input lines as well as adding extra-circulators on the output lines.

Bibliography

[1] I. I. Rabi, J. R. Zacharias, S. Millman, and P. Kusch. A new method of measuring nuclear magnetic moment. *Phys. Rev.*, 53:318–318, Feb 1938.

[2] F. Bloch, W. W. Hansen, and M. Packard. Nuclear induction. *Phys. Rev.*, 69:127–127, Feb 1946.

[3] E. M. Purcell, H. C. Torrey, and R. V. Pound. Resonance absorption by nuclear magnetic moments in a solid. *Phys. Rev.*, 69:37–38, Jan 1946.

[4] A. Abragam. *Principles of Nuclear Magnetism*. Oxford Science Publications, Clarendon Press, 1986.

[5] A. Schweiger and G. Jeschke. *Principles of Pulse Electron Paramagnetic Resonance*. Oxford University Press, 2001.

[6] M. Pellecchia, I. Bertini, D. Cowburn, C. Dalvit, E. Giralt, W. Jahnke, T. L. James, S. W. Homans, H. Kessler, C. Luchinat, B. Meyer, H. Oschkinat, J. Peng, H. Schwalbe, and Gregg Siegal. Perspectives on NMR in drug discovery: a technique comes of age. *Nat. Rev. Drug. Discov.*, 7(9):738–745, September 2008.

[7] R. M. Serra and I. S. Oliveira. Nuclear magnetic resonance quantum information processing. *Philos. T. Roy. Soc. A*, 370(1976):4615, 2012.

[8] H. Walther, B. T. H. Varcoe, B.-G. Englert, and T. Becker. Cavity quantum electrodynamics. *Reports on Progress in Physics*, 69(5):1325, 2006.

[9] A. Blais, R.-S. Huang, A. Wallraff, S. M. Girvin, and R. J. Schoelkopf. Cavity quantum electrodynamics for superconducting electrical circuits: An architecture for quantum computation. *Phys. Rev. A*, 69:062320, 2004.

[10] A. Wallraff, D. I. Schuster, A. Blais, L. Frunzio, R.-S. Huang, J. Majer, S. Kumar, S. M. Girvin, and R. J. Schoelkopf. Strong coupling of a single photon to a superconducting qubit using circuit quantum electrodynamics. *Nature*, 431:162, 2004.

[11] C. M. Caves. Quantum limits on noise in linear amplifiers. *Phys. Rev. D*, 26(8):1817–1839, October 1982.

[12] B. Yurke, L. R. Corruccini, P. G. Kaminsky, L. W. Rupp, A. D. Smith, A. H. Silver, R. W. Simon, and E. A. Whittaker. Observation of parametric amplification and deamplification in a Josephson parametric amplifier. *Phys. Rev. A*, 39(5):2519–2533, March 1989.

[13] N. Bergeal, F. Schackert, M. Metcalfe, R. Vijay, V. E. Manucharyan, L. Frunzio, D. E. Prober, R. J. Schoelkopf, S. M. Girvin, and M. H. Devoret. Phase-preserving amplification near the quantum limit with a Josephson ring modulator. *Nature*, 465(7294):64–68, May 2010.

[14] A. Bienfait, J. J. Pla, Y. Kubo, M. Stern, X. Zhou, C. C. Lo, C. D. Weis, T. Schenkel, M. L. W. Thewalt, D. Vion, D. Esteve, B. Julsgaard, K. Mølmer, J. J. L. Morton, and P. Bertet. Reaching the quantum limit of sensitivity in electron spin resonance. *Nat. Nanotechnol.*, 11(3):253–257, December 2015.

[15] A. J. Sigillito, H. Malissa, A. M. Tyryshkin, H. Riemann, N. V. Abrosimov, P. Becker, H.-J. Pohl, M. L. W. Thewalt, K. M. Itoh, J. J. L. Morton, A. A. Houck, D. I. Schuster, and S. A. Lyon. Fast,

low-power manipulation of spin ensembles in superconducting microresonators. *Appl. Phys. Lett.*, 104(22):222407, June 2014.

[16] G. Feher. Electron Spin Resonance Experiments on Donors in Silicon. I. Electronic Structure of Donors by the Electron Nuclear Double Resonance Technique. *Phys. Rev.*, 114(5):1219–1244, June 1959.

[17] A. Bienfait, J. J. Pla, Y. Kubo, X. Zhou, M. Stern, C. C. Lo, C. D. Weis, T. Schenkel, D. Vion, D. Esteve, J. J. L. Morton, and P. Bertet. Controlling spin relaxation with a cavity. *Nature*, 531(7592):74–77, 2016.

[18] C. M. Caves. Quantum-mechanical noise in an interferometer. *Phys. Rev. D*, 23(8):1693–1708, April 1981.

[19] P. Grangier, R. E. Slusher, B. Yurke, and A. LaPorta. Squeezed-light enhanced polarization interferometer. *Phys. Rev. Lett.*, 59(19):2153–2156, November 1987.

[20] Min Xiao, Ling-An Wu, and H. J. Kimble. Precision measurement beyond the shot-noise limit. *Phys. Rev. Lett.*, 59(3):278–281, July 1987.

[21] R. Vijay, D. H. Slichter, and I. Siddiqi. Observation of quantum jumps in a <superconducting artificial atom. *Phys. Rev. Lett.*, 106(11):110502, mar 2011.

[22] J.D. Teufel, T. Donner, M.A. Castellanos-Beltran, J.W. Harlow, and K.W. Lehnert. Nanomechanical motion measured with an imprecision below that at the standard quantum limit. *Nat. Nanotechnol.*, 4(12):820–823, 2009.

[23] J. Stehlik, Y.-Y. Liu, C. M. Quintana, C. Eichler, T. R. Hartke, and J. R. Petta. Fast Charge Sensing of a Cavity-Coupled Double Quantum Dot Using a Josephson Parametric Amplifier. *Appl. Phys. Lett.*, 4(1):014018, 2015.

[24] M. Hatridge, R. Vijay, D. H. Slichter, J. Clarke, and I. Siddiqi. Dispersive magnetometry with a quantum limited SQUID parametric amplifier. *Phys. Rev. B*, 83(13):134501, April 2011.

[25] G. Wolfowicz, A. M. Tyryshkin, R. E. George, H. Riemann, N. V. Abrosimov, P. Becker, H.-J. Pohl, M. L. W. Thewalt, S. A. Lyon, and J. J. L. Morton. Atomic clock transitions in silicon-based spin qubits. *Nat. Nanotechnol.*, 8(8):561–564, 2013.

[26] G. W. Morley, M. Warner, A. M. Stoneham, P. T. Greenland, J. van Tol, C. W. M. Kay, and G. Aeppli. The initialization and manipulation of quantum information stored in silicon by bismuth dopants. *Nat. Mater.*, 9(9):725–729, 2010.

[27] M. C. Butler and D. P. Weitekamp. Polarization of nuclear spins by a cold nanoscale resonator. *Phys. Rev. A*, 84(6):063407, December 2011.

[28] P. Goy, J. M. Raimond, M. Gross, and S. Haroche. Observation of Cavity-Enhanced Single-Atom Spontaneous Emission. *Phys. Rev. Lett.*, 50(24):1903–1906, June 1983.

[29] H. Yokoyama, K. Nishi, T. Anan, H. Yamada, S. D. Brorson, and E. P. Ippen. Enhanced spontaneous emission from GaAs quantum wells in monolithic microcavities. *Appl. Phys. Lett.*, 57(26):2814–2816, December 1990.

[30] J. M. Gérard, B. Sermage, B. Gayral, B. Legrand, E. Costard, and V. Thierry-Mieg. Enhanced spontaneous emission by quantum boxes in a monolithic optical microcavity. *Phys. Rev. Lett.*, 81(5):1110, 1998.

[31] Ligo Scientic Collaboration. Enhanced sensitivity of the LIGO gravitational wave detector by using squeezed states of light. *Nat Photon*, 7(8):613–619, August 2013.

[32] V. G. Lucivero, R. Jiménez-Martínez, J. Kong, and M. W. Mitchell. Squeezed-light spin noise spectroscopy. *Phys. Rev. A*, 93(5):053802, May 2016.

[33] B. Yurke. Squeezed-state generation using a Josephson parametric amplifier. *JOSA B*, 4(10):1551–1557, 1987.

[34] M. Toyli, D. W. Eddins, A. S. Boutin, S. Puri, D. Hover, V. Bolkhovsky, D. Oliver, W. A. Blais, and I. Siddiqi. Resonance Fluorescence from an Artificial Atom in Squeezed Vacuum. *Phys. Rev. X*, 6(3), July 2016.

[35] J. B. Clark, F. Lecocq, R. W. Simmonds, J. Aumentado, and J. D. Teufel. Observation of strong radiation pressure forces from squeezed light on a mechanical oscillator. *Nat. Phys.*, 3701, March 2016.

[36] T. Yoshimura, H. Yokoyama, S. Fujii, F. Takayama, K. Oikawa, and H. Kamada. In vivo EPR detection and imaging of endogenous nitric oxide in lipopolysaccharide-treated mice. *Nat. Biotechnol.*, 14(8):992–994, August 1996.

[37] H. Malissa, D. I. Schuster, A. M. Tyryshkin, A. A. Houck, and S. A. Lyon. Superconducting coplanar waveguide resonators for low temperature pulsed electron spin resonance spectroscopy. *Rev. Sci. Instrum.*, 84(2):025116, February 2013.

[38] C. Gerry and P. Knight. *Introductory Quantum Optics*. Cambridge University Press, Cambridge, UK; New York, 1st edition, November 2004.

[39] S. Haroche and J.-M. Raimond. *Exploring the Quantum*. Oxford University Press, 2006.

[40] V. Giovannetti, S. Lloyd, and L. Maccone. Quantum-Enhanced Measurements: Beating the Standard Quantum Limit. *Science*, 306(5700):1330–1336, November 2004.

[41] M. H. Devoret. Quantum Fluctuations in Electrical Circuits. *Elsevier*, page 351, 1997.

[42] B. Yurke and J. S. Denker. Quantum network theory. *Phys. Rev. A*, 29:1419–1437, 1984.

[43] A. A. Clerk, M. H. Devoret, S. M. Girvin, F. Marquardt, and R. J. Schoelkopf. Introduction to quantum noise, measurement, and amplification. *Rev. Mod. Phys.*, 82:1155, 2010.

[44] K. Kurokawa. Power waves and the scattering matrix. *IEEE T. Microw. Theory*, 13(2):194–202, Mar 1965.

[45] C. W. Gardiner and M. J. Collett. Input and output in damped quantum systems: Quantum stochastic differential equations and the master equation. *Phys. Rev. A*, 31:3761, 1985.

[46] H. A. Haus and J. A. Mullen. Quantum Noise in Linear Amplifiers. *Phys. Rev.*, 128(5):2407–2413, December 1962.

[47] F. Schackert. *A Practical Quantum-Limited Parametric Amplifier ased on the Josephson Ring Modulator*. PhD thesis, University of Yale, Yale, 2013.

[48] E. Flurin. *The Josephson Mixer, a Swiss army knife for microwave quantum optics*. PhD thesis, Ecole Normale Supérieure, Paris, December 2014.

[49] M. A. Castellanos Beltran. *Development of a Josephson parametric amplifier for the preparation and detection of nonclassical states of microwave fields*. PhD thesis, University of Colorado, 2010.

[50] C. Eichler, D. Bozyigit, C. Lang, M. Baur, L. Steffen, J. M. Fink, S. Filipp, and A. Wallraff. Observation of Two-Mode Squeezing in the Microwave Frequency Domain. *Phys. Rev. Lett.*, 107(11):113601, 2011.

[51] C. M. Wilson, T. Duty, M. Sandberg, F. Persson, V. Shumeiko, and P. Delsing. Photon Generation in an Electromagnetic Cavity with a Time-Dependent Boundary. *Phys. Rev. Lett.*, 105(23):233907, December 2010.

[52] J. Y. Mutus, T. C. White, E. Jeffrey, D. Sank, R. Barends, J. Bochmann, Yu Chen, Z. Chen, B. Chiaro, A. Dunsworth, J. Kelly, A. Megrant, C. Neill, P. J. J. O'Malley, P. Roushan,

A. Vainsencher, J. Wenner, I. Siddiqi, R. Vijay, A. N. Cleland, and John M. Martinis. Design and characterization of a lumped element single-ended superconducting microwave parametric amplifier with on-chip flux bias line. *Appl. Phys. Lett.*, 103(12):122602, September 2013.

[53] Z. R. Lin, K. Inomata, W. D. Oliver, K. Koshino, Y. Nakamura, J. S. Tsai, and T. Yamamoto. Single-shot readout of a superconducting flux qubit with a flux-driven Josephson parametric amplifier. *Appl. Phys. Lett.*, 103(13):132602, 2013.

[54] X. Zhou, V. Schmitt, P. Bertet, D. Vion, W. Wustmann, V. Shumeiko, and D. Esteve. High-gain weakly nonlinear flux-modulated Josephson parametric amplifier using a SQUID array. *Phys. Rev. B*, 89(21):214517, June 2014.

[55] W. Wustmann and V. Shumeiko. Parametric resonance in tunable superconducting cavities. *Phys. Rev. B*, 87(18):184501, May 2013.

[56] C. Eichler and A. Wallraff. Controlling the dynamic range of a Josephson parametric amplifier. *EPJ Quantum Technology*, 1(2), 2014.

[57] B. Josephson. Possible new effects in superconductive tunneling. *Physics Letters*, 1:251–253, 1962.

[58] J. Clarke. *The SQUID Handbook: Fundamentals and Technology of SQUIDs and SQUID Systems*. Wiley-VCH, 2005.

[59] L. D. Landau and E. M. Lifshitz. *Mechanics, Third Edition: Volume 1*. Butterworth-Heinemann, 3rd edition, 1976.

[60] C. Macklin, K. O'Brien, D. Hover, M. E. Schwartz, V. Bolkhovsky, X. Zhang, W. D. Oliver, and I. Siddiqi. A near–quantum-limited Josephson traveling-wave parametric amplifier. *Science*, 350(6258):307–310, October 2015.

[61] E. L. Hahn. Spin Echoes. *Phys. Rev.*, 80(4):580–594, November 1950.

[62] D. F. Walls and Gerard J. Milburn. *Quantum Optics*. Springer Science & Business Media, 2008.

[63] M. Fox. *Quantum Optics: An Introduction*. OUP Oxford, April 2006.

[64] B. Julsgaard and K. Mølmer. Measurement-induced two-qubit entanglement in a bad cavity: Fundamental and practical considerations. *Phys. Rev. A*, 85(3):032327, March 2012.

[65] J. Wang, H. M. Wiseman, and G. J. Milburn. Dynamical creation of entanglement by homodyne-mediated feedback. *Phys. Rev. A*, 71:042309, 2005.

[66] M. C. Butler. *Novel methods for force-detected nuclear magnetic resonance*. PhD thesis, California Institute of Technology, 2007.

[67] M. Tavis and F. W. Cummings. Exact Solution for an N-Molecule-Radiation-Field Hamiltonian. *Phys. Rev.*, 170:379, 1968.

[68] P. F. Herskind, A. Dantan, J. P. Marler, M. Albert, and M. Drewsen. Realization of collective strong coupling with ion Coulomb crystals in an optical cavity. *Nature Phys.*, 5:494, 2009.

[69] J. M. Fink, R. Bianchetti, M. Baur, M. Göppl, L. Steffen, S. Filipp, P. J. Leek, A. Blais, and A. Wallraff. Dressed Collective Qubit States and the Tavis-Cummings Model in Circuit QED. *Phys. Rev. Lett.*, 103(8):083601, August 2009.

[70] Y. Kubo, C. Grezes, A. Dewes, T. Umeda, J. Isoya, H. Sumiya, N. Morishita, H. Abe, S. Onoda, T. Ohshima, V. Jacques, A. Dréau, J.-F. Roch, I. Diniz, A. Auffeves, D. Vion, D. Esteve, and P. Bertet. Hybrid Quantum Circuit with a Superconducting Qubit Coupled to a Spin Ensemble. *Phys. Rev. Lett.*, 107:220501, 2011.

[71] C. Grezes. *Towards a spin-ensemble quantum memory for superconducting qubits*. PhD thesis, Université Pierre-et-Marie-Curie, 2014.

[72] R. H. Dicke. Coherence in spontaneous radiation processes. *Phys. Rev.*, 93:99, 1954.

[73] J. A. Mlynek, A. A. Abdumalikov, C. Eichler, and A. Wallraff. Observation of Dicke superradiance for two artificial atoms in a cavity with high decay rate. *Nat. Commun.*, 5(5186), 2014.

[74] G. Feher, J. P. Gordon, E. Buehler, E. A. Gere, and C. D. Thurmond. Spontaneous Emission of Radiation from an Electron Spin System. *Phys. Rev.*, 109(1):221–222, January 1958.

[75] V. V. Temnov and U. Woggon. Superradiance and Subradiance in an Inhomogeneously Broadened Ensemble of Two-Level Systems Coupled to a Low-Q Cavity. *Phys. Rev. Lett.*, 95:243602, 2005.

[76] C. J. Wood and D. G. Cory. Cavity cooling to the ground state of an ensemble quantum system. *Phys. Rev. A*, 93(2):023414, February 2016.

[77] C. Grezes, B. Julsgaard, Y. Kubo, M. Stern, T. Umeda, J. Isoya, H. Sumiya, S. Abe, S. Onoda, T. Ohshima, V. Jacques, J. Esteve, D. Vion, D. Esteve, K. Moelmer, and P. Bertet. Multimode Storage and Retrieval of Microwave Fields in a Spin Ensemble. *Phys. Rev. X*, 4:021049, 2014.

[78] B. Julsgaard, C. Grezes, P. Bertet, and K. Mølmer. Quantum Memory for Microwave Photons in an Inhomogeneously Broadened Spin Ensemble. *Phys. Rev. Lett.*, 110(25):250503, June 2013.

[79] A. Honig. Polarization of Arsenic Nuclei in a Silicon Semiconductor. *Phys. Rev.*, 96(1):234–235, October 1954.

[80] G. Feher, R. C. Fletcher, and E. A. Gere. Exchange Effects in Spin Resonance of Impurity Atoms in Silicon. *Phys. Rev.*, 100(6):1784–1786, December 1955.

[81] G. Feher and E. A. Gere. Electron Spin Resonance Experiments on Donors in Silicon. II. Electron Spin Relaxation Effects. *Phys. Rev.*, 114(5):1245–1256, June 1959.

[82] J. P. Gordon and K. D. Bowers. Microwave Spin Echoes from Donor Electrons in Silicon. *Phys. Rev. Lett.*, 1(10):368–370, November 1958.

[83] B. E. Kane. A silicon-based nuclear spin quantum computer. *Nature*, 393(6681):133–137, May 1998.

[84] M. H. Mohammady, G. W. Morley, and T. S. Monteiro. Bismuth Qubits in Silicon: The Role of EPR Cancellation Resonances. *Phys. Rev. Lett.*, 105(6):067602, August 2010.

[85] G. W. Morley, P. Lueders, M. H. Mohammady, S. J. Balian, G. Aeppli, C. W. M. Kay, W. M. Witzel, G. Jeschke, and T. S. Monteiro. Quantum control of hybrid nuclear–electronic qubits. *Nat. Mater.*, 12(2):103–107, December 2012.

[86] E. B. Hale and R. L. Mieher. Shallow Donor Electrons in Silicon. I. Hyperfine Interactions from ENDOR Measurements. *Phys. Rev.*, 184(3):739–750, August 1969.

[87] R. Kh. Zhukavin, K. A. Kovalevsky, V. V. Tsyplenkov, V. N. Shastin, S. G. Pavlov, H.-W. Hübers, H. Riemann, N. V. Abrosimov, and A. K. Ramdas. Spin-orbit coupling effect on bismuth donor lasing in stressed silicon. *Appl. Phys. Lett.*, 99(17):171108, October 2011.

[88] A. K. Ramdas and S. Rodriguez. Spectroscopy of the solid-state analogues of the hydrogen atom: donors and acceptors in semiconductors. *Rep. Prog. Phys.*, 44(12):1297, 1981.

[89] A. R. Stegner. *Shallow dopants in nanostructered and in isotopically*. PhD thesis, Technische Universität München, January 2011.

[90] A. Abragam and B. Bleaney. *Electron Paramagnetic Resonance of Transition Ions*. OUP Oxford, June 2012.

[91] G. Wolfowicz, J. J. L. Morton, and S. Benjamin. *Quantum control of donor spins in silicon and their environment*. PhD thesis, Oxford University, 2015.

[92] J. M. Luttinger and W. Kohn. Motion of Electrons and Holes in Perturbed Periodic Fields. *Phys. Rev.*, 97(4):869, 1955.

[93] P. Y. Yu and M. Cardona. *Fundamentals of Semiconductors*. Graduate Texts in Physics. Springer Berlin Heidelberg, Berlin, Heidelberg, 2010.

[94] D. K. Wilson and G. Feher. Electron Spin Resonance Experiments on Donors in Silicon. III. Investigation of Excited States by the Application of Uniaxial Stress and Their Importance in Relaxation Processes. *Phys. Rev.*, 124(4):1068–1083, November 1961.

[95] D. A. Neamen. *Semiconductor Physics And Devices: Basic Principles*. McGraw-Hill, New York, NY, 4th edition, January 2011.

[96] M. J. Calderón, B. Koiller, and S. Das Sarma. External field control of donor electron exchange at the Si / Si O 2 interface. *Phys. Rev. B*, 75(12):125311, March 2007.

[97] C. C. Lo, S. Simmons, R. Lo Nardo, C. D. Weis, A. M. Tyryshkin, J. Meijer, D. Rogalla, S. A. Lyon, J. Bokor, T. Schenkel, and J. J. L. Morton. Stark shift and field ionization of arsenic donors in 28Si-silicon-on-insulator structures. *Appl. Phys. Lett.*, 104(19):193502, May 2014.

[98] R. E. George, W. Witzel, H. Riemann, N. V. Abrosimov, N. Nötzel, M. L. W. Thewalt, and J. J. L. Morton. Electron Spin Coherence and Electron Nuclear Double Resonance of Bi Donors in Natural Si. *Phys. Rev. Lett.*, 105(6):067601, August 2010.

[99] S. J. Balian. *Quantum-Bath Decoherence of Hybrid Electron-Nuclear Spin Qubits*. PhD thesis, University College London, 2015.

[100] M. H. Mohammady, G. W. Morley, A. Nazir, and T. S. Monteiro. Analysis of quantum coherence in bismuth-doped silicon: A system of strongly coupled spin qubits. *Phys. Rev. B*, 85(9):094404, March 2012.

[101] D. Vion, A. Aassime, A. Cottet, P. Joyez, H. Pothier, C. Urbina, D. Esteve, and M. H. Devoret. Manipulating the Quantum State of an Electrical Circuit. *Science*, 296(5569):886–889, 2002.

[102] E. B. Hale and T. G. Castner Jr. Ground-State Wave Function of Shallow Donors in Uniaxially Stressed Silicon: Piezohyperfine Constants Determined by Electron-Nuclear Double Resonance. *Phys. Rev. B*, 1(12):4763, 1970.

[103] B. Koiller, Xuedong Hu, and S. Das Sarma. Strain effects on silicon donor exchange: Quantum computer architecture considerations. *Phys. Rev. B*, 66(11):115201, September 2002.

[104] H. Huebl, A. R. Stegner, M. Stutzmann, M. S. Brandt, G. Vogg, F. Bensch, E. Rauls, and U. Gerstmann. Phosphorus Donors in Highly Strained Silicon. *Phys. Rev. Lett.*, 97(16):166402, October 2006.

[105] M. Usman, C. D. Hill, R. Rahman, G. Klimeck, M. Y. Simmons, S. Rogge, and L. C. L. Hollenberg. Strain and electric field control of hyperfine interactions for donor spin qubits in silicon. *Phys. Rev. B*, 91(24), June 2015.

[106] L. Dreher, T. A. Hilker, A. Brandlmaier, S. T. B. Goennenwein, H. Huebl, M. Stutzmann, and M. S. Brandt. Electroelastic Hyperfine Tuning of Phosphorus Donors in Silicon. *Phys. Rev. Lett.*, 106(3):037601, January 2011.

[107] L. Dreher. *Spin Mechanics in Paramagnetic and Ferromagnetic*. PhD thesis, Verein zur Förderung des Walter-Schottky-Inst. der Techn. Univ. München, April 2013.

[108] G. P. Lansbergen, R. Rahman, C. J. Wellard, I. Woo, J. Caro, N. Collaert, S. Biesemans, G. Klimeck, L. C. L. Hollenberg, and S. Rogge. Gate-induced quantum-confinement transition of a single dopant atom in a silicon FinFET. *Nat. Phys.*, 4(8):656–661, August 2008.

[109] G. Pica, G. Wolfowicz, M. Urdampilleta, M. L. W. Thewalt, H. Riemann, N. V. Abrosimov, P. Becker, H.-J. Pohl, J. J. L. Morton, R. N. Bhatt, S. A. Lyon, and B. W. Lovett. Hyperfine Stark effect of shallow donors in silicon. *Phys. Rev. B*, 90(19):195204, November 2014.

[110] P. A. Mortemousque, S. Rosenius, G. Pica, D. P. Franke, T. Sekiguchi, A. Truong, M. P. Vlasenko, L. S. Vlasenko, M. S. Brandt, R. G. Elliman, and others. Quadrupole Shift of Nuclear Magnetic Resonance of Donors in Silicon at Low Magnetic Field. *arXiv preprint arXiv:1506.04028*, 2015.

[111] D. P. Franke, M. P. D. Pflüger, P.-A. Mortemousque, K. M. Itoh, and M. S. Brandt. Quadrupolar effects on nuclear spins of neutral arsenic donors in silicon. *Phys. Rev. B*, 93(16):161303, April 2016.

[112] C. P. Slichter. *Principles of Magnetic Resonance*. Springer Science & Business Media, March 1996.

[113] A. Abragam and J. Combrisson. Résonance paramagnétique des impuretés dans un semiconducteur. *Il Nuovo Cimento (1955-1965)*, 6(3):1197–1212, February 2008.

[114] A. Honig and E. Stupp. Electron Spin-Lattice Relaxation in Phosphorus-Doped Silicon. *Phys. Rev.*, 117(1):69–83, January 1960.

[115] T. G. Castner Jr. Direct measurement of the valley-orbit splitting of shallow donors in silicon. *Phys. Rev. Lett.*, 8(1):13, 1962.

[116] T. G. Castner Jr. Raman spin-lattice relaxation of shallow donors in silicon. *Phys. Rev.*, 130(1):58, 1963.

[117] T. G. Castner. Orbach spin-lattice relaxation of shallow donors in silicon. *Phys. Rev.*, 155(3):816, 1967.

[118] D. Pines, J. Bardeen, and C. P. Slichter. Nuclear Polarization and Impurity-State Spin Relaxation Processes in Silicon. *Phys. Rev.*, 106(3):489–498, May 1957.

[119] E. Abrahams. Donor Electron Spin Relaxation in Silicon. *Phys. Rev.*, 107(2):491–496, July 1957.

[120] L. M. Roth. g Factor and Donor Spin-Lattice Relaxation for Electrons in Germanium and Silicon. *Phys. Rev.*, 118(6):1534–1540, June 1960.

[121] H. Hasegawa. Spin-Lattice Relaxation of Shallow Donor States in Ge and Si through a Direct Phonon Process. *Phys. Rev.*, 118(6):1523–1534, June 1960.

[122] A. Morello, J. J. Pla, F. A. Zwanenburg, Kok W. Chan, Kuan Y. Tan, H. Huebl, M. Möttönen, C. D. Nugroho, Changyi Yang, J. A. van Donkelaar, and others. Single-shot readout of an electron spin in silicon. *Nature*, 467(7316):687–691, 2010.

[123] M. Belli, M. Fanciulli, and N. V. Abrosimov. Pulse electron spin resonance investigation of bismuth-doped silicon: Relaxation and electron spin echo envelope modulation. *Phys. Rev. B*, 83(23):235204, June 2011.

[124] G. Wolfowicz, S. Simmons, A. M. Tyryshkin, R. E. George, H. Riemann, N. V. Abrosimov, P. Becker, H.-J. Pohl, S. A. Lyon, M. L. W. Thewalt, and J. J. L. Morton. Decoherence mechanisms of 209Bi donor electron spins in isotopically pure 28Si. *Phys. Rev. B*, 86(24):245301, December 2012.

[125] N. F. Mott. On the Transition to Metallic Conduction in Semiconductors. *Can. J. Phys.*, 34(12A):1356–1368, December 1956.

[126] A. M. Tyryshkin, S. Tojo, J. J. L. Morton, H. Riemann, N. V. Abrosimov, P. Becker, H. Joachim Pohl, T. Schenkel, M. L. W. Thewalt, K. M. Itoh, and S. A. Lyon. Electron spin coherence exceeding seconds in high-purity silicon. *Nat. Mater.*, 11(2):143–147, February 2012.

[127] H. Y. Carr and E. M. Purcell. Effects of Diffusion on Free Precession in Nuclear Magnetic Resonance Experiments. *Phys. Rev.*, 94(3):630–638, May 1954.

[128] S. Meiboom and D. Gill. Modified Spin-Echo Method for Measuring Nuclear Relaxation Times. *Rev. Sci. Instrum.*, 29(8):688–691, August 1958.

[129] W.-L. Ma, G. Wolfowicz, Shu-Shen Li, J. J. L. Morton, and Ren-Bao Liu. Classical nature of nuclear spin noise near clock transitions of Bi donors in silicon. *Phys. Rev. B*, 92(16):161403, October 2015.

[130] A. Gruber, A. Dräbenstedt, C. Tietz, L. Fleury, J. Wrachtrup, and C. Von Borczyskowski. Scanning confocal optical microscopy and magnetic resonance on single defect centers. *Science*, 276(5321):2012–2014, 1997.

[131] A. Yang, M. Steger, D. Karaiskaj, M. L. W. Thewalt, M. Cardona, K. M. Itoh, H. Riemann, N. V. Abrosimov, M. F. Churbanov, A. V. Gusev, A. D. Bulanov, A. K. Kaliteevskii, O. N. Godisov, P. Becker, H.-J. Pohl, J. W. Ager, and E. E. Haller. Optical Detection and Ionization of Donors in Specific Electronic and Nuclear Spin States. *Phys. Rev. Lett.*, 97(22), November 2006.

[132] A. Yang, M. Steger, T. Sekiguchi, M. L. W. Thewalt, T. D. Ladd, K. M. Itoh, H. Riemann, N. V. Abrosimov, P. Becker, and H.-J. Pohl. Simultaneous Subsecond Hyperpolarization of the Nuclear and Electron Spins of Phosphorus in Silicon by Optical Pumping of Exciton Transitions. *Phys. Rev. Lett.*, 102(25):257401, June 2009.

[133] M. Steger, K. Saeedi, M. L. W. Thewalt, J. J. L. Morton, H. Riemann, N. V. Abrosimov, P. Becker, and H.-J. Pohl. Quantum Information Storage for over 180 s Using Donor Spins in a 28Si Semiconductor Vacuum. *Science*, 336(6086):1280–1283, 2012.

[134] T. Sekiguchi, M. Steger, K. Saeedi, M. L. W. Thewalt, H. Riemann, N. V. Abrosimov, and N. Nötzel. Hyperfine Structure and Nuclear Hyperpolarization Observed in the Bound Exciton Luminescence of Bi Donors in Natural Si. *Phys. Rev. Lett.*, 104(13):137402, April 2010.

[135] P. Becker, D. Schiel, H.-J. Pohl, A. K. Kaliteevski, O. N. Godisov, M. F. Churbanov, G. G. Devyatykh, A. V. Gusev, A. D. Bulanov, S. A. Adamchik, V. A. Gavva, I. D. Kovalev, N. V. Abrosimov, B. Hallmann-Seiffert, H. Riemann, S. Valkiers, P. Taylor, P. De Bièvre, and E. M. Dianov. Large-scale production of highly enriched ^{28} Si for the precise determination of the Avogadro constant. *Meas. Sci. Technol.*, 17(7):1854–1860, July 2006.

[136] P. Studer, S. R. Schofield, C. F. Hirjibehedin, and N. J. Curson. Studying atomic scale structural and electronic properties of ion implanted silicon samples using cross-sectional scanning tunneling microscopy. *Appl. Phys. Lett.*, 102(1):012107, 2013.

[137] C. D. Weis, C. C. Lo, V. Lang, A. M. Tyryshkin, R. E. George, K. M. Yu, J. Bokor, S. A. Lyon, J. J. L. Morton, and T. Schenkel. Electrical activation and electron spin resonance measurements of implanted bismuth in isotopically enriched silicon-28. *Appl. Phys. Lett.*, 100(17):172104, 2012.

[138] Y. Manassen, R. J. Hamers, J. E. Demuth, and A. J. Castellano Jr. Direct observation of the precession of individual paramagnetic spins on oxidized silicon surfaces. *Phys. Rev. Lett.*, 62(21):2531–2534, May 1989.

[139] D. Rugar, C. S. Yannoni, and J. A. Sidles. Mechanical detection of magnetic resonance. *Nature*, 360(6404):563–566, 1992.

[140] D. Rugar, R. Budakian, H. J. Mamin, and B. W. Chui. Single spin detection by magnetic resonance force microscopy. *Nature*, 430(6997):329–332, 2004.

[141] J. M. Taylor, P. Cappellaro, L. Childress, L. Jiang, P. R. Hemmer, A. Yacoby, R. Walsworth, and M. D. Lukin. High-sensitivity diamond magnetometer with nanoscale resolution. *Nat. Phys.*, 4:810, 2008.

[142] Y. Twig, E. Dikarov, W. D. Hutchison, and A. Blank. Note: High sensitivity pulsed electron spin resonance spectroscopy with induction detection. *Rev. Sci. Instrum.*, 82(7):076105, 2011.

[143] A. Blank, E. Dikarov, R. Shklyar, and Y. Twig. Induction-detection electron spin resonance with sensitivity of 1000 spins: En route to scalable quantum computations. *Physics Letters A*, 377(31):1937–1942, 2013.

[144] C. Durkan and M. E. Welland. Electronic spin detection in molecules using scanning-tunneling-microscopy-assisted electron-spin resonance. *Appl. Phys. Lett.*, 80(3):458, 2002.

[145] J. Wrachtrup, C. Von Borczyskowski, J. Bernard, M. Orritt, and R. Brown. Optical detection of magnetic resonance in a single molecule. *Nature*, 363:244–245, 1993.

[146] M. S. Grinolds, M. Warner, K. De Greve, Y. Dovzhenko, L. Thiel, R. L. Walsworth, S. Hong, P. Maletinsky, and A. Yacoby. Subnanometre resolution in three-dimensional magnetic resonance imaging of individual dark spins. *Nat. Nanotechnol.*, 9(4):279–284, 2014.

[147] J. Elzerman, R. Hanson, L. Willems van Beveren, B. Witkamp, L.M.K. Vandersypen, and L. Kouwenhoven. Single-shot read-out of an individual electron spin in a quantum dot. *Nature*, 430:431, 2004.

[148] M. Xiao, I. Martin, E. Yablonovitch, and H. W. Jiang. Electrical detection of the spin resonance of a single electron in a silicon field-effect transistor. *Nature*, 430(6998):435–439, July 2004.

[149] R. Vincent, S. Klyatskaya, M. Ruben, W. Wernsdorfer, and F. Balestro. Electronic read-out of a single nuclear spin using a molecular spin transistor. *Nature*, 488(7411):357–360, 2012.

[150] M. Veldhorst, J. C. C. Hwang, C. H. Yang, A. W. Leenstra, B. de Ronde, J. P. Dehollain, J. T. Muhonen, F. E. Hudson, K. M. Itoh, A. Morello, and A. S. Dzurak. An addressable quantum dot qubit with fault-tolerant control fidelity. *Nat. Nanotechnol.*, 9(12):1–10, 2014.

[151] J. J. Pla, K. Y. Tan, J. P. Dehollain, W. H. Lim, J. J. L. Morton, D. N. Jamieson, A. S. Dzurak, and A. Morello. A single-atom electron spin qubit in silicon. *Nature*, 489(7417):541–545, 2012.

[152] S. Thiele, F. Balestro, R. Ballou, S. Klyatskaya, M. Ruben, and . Wernsdorfer. Electrically driven nuclear spin resonance in single-molecule magnets. *Science*, 344(6188):1135–1138, 2014.

[153] T. Sleator, E. L. Hahn, C. Hilbert, and J. Clarke. Nuclear-spin noise and spontaneous emission. *Phys. Rev. B*, 36(4):1969–1980, August 1987.

[154] J. Schleeh, G. Alestig, J. Halonen, A. Malmros, B. Nilsson, P. A. Nilsson, J. P. Starski, N. Wadefalk, H. Zirath, and J. Grahn. Ultralow-Power Cryogenic InP HEMT With Minimum Noise Temperature of 1 K at 6 GHz. *IEEE Electr. Device L.*, 33(5):664–666, May 2012.

[155] S. E. de Graaf, D. Davidovikj, A. Adamyan, S. E. Kubatkin, and A. V. Danilov. Galvanically split superconducting microwave resonators for introducing internal voltage bias. *Appl. Phys. Lett.*, 104(5):052601, February 2014.

[156] I. Wisby, S. E. de Graaf, R. Gwilliam, A. Adamyan, S. E. Kubatkin, P. J. Meeson, A. Y. Tzalenchuk, and T. Lindström. Coupling of a locally implanted rare-earth ion ensemble to a superconducting micro-resonator. *Appl. Phys. Lett.*, 105(10):102601, 2014.

[157] N. Samkharadze, A. Bruno, P. Scarlino, G. Zheng, D. P. DiVincenzo, L. DiCarlo, and L. M. K. Vandersypen. High-Kinetic-Inductance Superconducting Nanowire Resonators for Circuit QED in a Magnetic Field. *Appl. Phys. Lett.*, 5(4):044004, April 2016.

[158] T. Roy, S. Kundu, M. Chand, A. M. Vadiraj, A. Ranadive, N. Nehra, M. P. Patankar, J. Aumentado, A. A. Clerk, and R. Vijay. Broadband parametric amplification with impedance engineering: Beyond the gain-bandwidth product. *Appl. Phys. Lett.*, 107(26):262601, December 2015.

[159] M. A. Castellanos-Beltran, K.D. Irwin, G. C. Hilton, L. R. Vale, and K. W. Lehnert. Amplification and squeezing of quantum noise with a tunable Josephson metamaterial. *Nat. Phys.*, 4(12):929–931, 2008.

[160] K. Cicak, D. Li, J. A. Strong, M. S. Allman, F. Altomare, A. J. Sirois, J. D. Whittaker, J. D. Teufel, and R. W. Simmonds. Low-loss superconducting resonant circuits using vacuum-gap-based microwave components. *Appl. Phys. Lett.*, 96(9):093502, 2010.

[161] A. Megrant, C. Neill, R. Barends, B. Chiaro, Yu Chen, L. Feigl, J. Kelly, Erik Lucero, Matteo Mariantoni, P. J. J. O'Malley, D. Sank, A. Vainsencher, J. Wenner, T. C. White, Y. Yin, J. Zhao, C. J. Palmstrom, John M. Martinis, and A. N. Cleland. Planar superconducting resonators with internal quality factors above one million. *Appl. Phys. Lett.*, 100:113510, 2012.

[162] C. Song, M. P. DeFeo, K. Yu, and B. L. T. Plourde. Reducing microwave loss in superconducting resonators due to trapped vortices. *Appl. Phys. Lett.*, 95(23):232501, 2009.

[163] R. Barends, J. Wenner, M. Lenander, Y. Chen, R. C. Bialczak, J. Kelly, E. Lucero, P. O'Malley, M. Mariantoni, D. Sank, H. Wang, T. C. White, Y. Yin, J. Zhao, A. N. Cleland, John M. Martinis, and J. J. A. Baselmans. Minimizing quasiparticle generation from stray infrared light in superconducting quantum circuits. *Appl. Phys. Lett.*, 99(11):113507, September 2011.

[164] Aaron D. O'Connell, M. Ansmann, R. C. Bialczak, M. Hofheinz, N. Katz, Erik Lucero, C. McKenney, M. Neeley, H. Wang, E. M. Weig, A. N. Cleland, and J. M. Martinis. Microwave dielectric loss at single photon energies and millikelvin temperatures. *Appl. Phys. Lett.*, 92(11):112903, 2008.

[165] D. S. Wisbey, J. Gao, M. R. Vissers, F. C. S. da Silva, J. S. Kline, L. Vale, and D. P. Pappas. Effect of metal/substrate interfaces on radio-frequency loss in superconducting coplanar waveguides. *J. Appl. Phys.*, 108(9):093918, November 2010.

[166] A. A. Houck, J. A. Schreier, B. R. Johnson, J. M. Chow, Jens Koch, J. M. Gambetta, D. I. Schuster, L. Frunzio, M. H. Devoret, S. M. Girvin, and R. J. Schoelkopf. Controlling the spontaneous emission of a superconducting transmon qubit. *Phys. Rev. Lett.*, 101:080502, Aug 2008.

[167] H. Paik, D. I. Schuster, L. S. Bishop, G. Kirchmair, G. Catelani, A. P. Sears, B. R. Johnson, M. J. Reagor, L. Frunzio, L. I. Glazman, S. M. Girvin, M. H. Devoret, and R. J. Schoelkopf. Observation of High Coherence in Josephson Junction Qubits Measured in a Three-Dimensional Circuit QED Architecture. *Phys. Rev. Lett.*, 107(24):240501, December 2011.

[168] M. Reagor, H. Paik, G. Catelani, L. Sun, C. Axline, E. Holland, I. M. Pop, N. A. Masluk, T. Brecht, L. Frunzio, M. H. Devoret, L. Glazman, and R. J. Schoelkopf. Reaching 10 ms single photon lifetimes for superconducting aluminum cavities. *Appl. Phys. Lett.*, 102(19):192604, 2013.

[169] C. Wang, C. Axline, Y. Y. Gao, T. Brecht, Y. Chu, L. Frunzio, M. H. Devoret, and R. J. Schoelkopf. Surface participation and dielectric loss in superconducting qubits. *Appl. Phys. Lett.*, 107(16):162601, October 2015.

[170] D. Ristè, S. Poletto, M.-Z. Huang, A. Bruno, V. Vesterinen, O.-P. Saira, and L. DiCarlo. Detecting bit-flip errors in a logical qubit using stabilizer measurements. *Nat. Commun.*, 6:6983, April 2015.

[171] J. W. C. De Vries. Temperature and thickness dependence of the resistivity of thin polycrystalline aluminium, cobalt, nickel, palladium, silver and gold films. *Thin Solid Films*, 167(1):25–32, December 1988.

[172] J. Wenner, R. Barends, R. C. Bialczak, Yu Chen, J. Kelly, Erik Lucero, Matteo Mariantoni, A. Megrant, P. J. J. O'Malley, D. Sank, A. Vainsencher, H. Wang, T. C. White, Y. Yin, J. Zhao, A. N. Cleland, and John M. Martinis. Surface loss simulations of superconducting coplanar waveguide resonators. *Appl. Phys. Lett.*, 99(11):113513, 2011.

[173] T. Van Duzer and C. Turner. *Superconductive Devices and Circuits*. Prentice Hall PTR, 1999.

[174] J. Romijn, T. M. Klapwijk, M. J. Renne, and J. E. Mooij. Critical pair-breaking current in superconducting aluminum strips far below tc. *Phys. Rev. B*, 26(7):3648–3655, October 1982.

[175] C. M. Quintana, A. Megrant, Z. Chen, A. Dunsworth, B. Chiaro, R. Barends, B. Campbell, Yu Chen, I.-C. Hoi, E. Jeffrey, J. Kelly, J. Y. Mutus, P. J. J. O'Malley, C. Neill, P. Roushan, D. Sank, A. Vainsencher, J. Wenner, T. C. White, A. N. Cleland, and John M. Martinis. Characterization and reduction of microfabrication-induced decoherence in superconducting quantum circuits. *Appl. Phys. Lett.*, 105(6):062601, August 2014.

[176] A. Bruno, G. de Lange, S. Asaad, K. L. van der Enden, N. K. Langford, and L. DiCarlo. Reducing intrinsic loss in superconducting resonators by surface treatment and deep etching of silicon substrates. *Appl. Phys. Lett.*, 106(18):182601, May 2015.

[177] J. J. Pla, A. Bienfait, G. Pica, J. Mansir, F. A. Mohiyaddin, A. Morello, T. Schenkel, B. W. Lovett, J. J. L. Morton, and P. Bertet. Strain-induced nuclear quadrupole splittings in silicon devices. *arxiv*, 2017.

[178] E. N. Kaufmann and R. J. Vianden. The electric field gradient in noncubic metals. *Rev. Mod. Phys.*, 51(1):161, 1979.

[179] F. D. Feiock and W. R. Johnson. Atomic Susceptibilities and Shielding Factors. *Phys. Rev.*, 187(1):39, 1969.

[180] B. V. Van Zeghbroeck. *Principles of Semiconductor Devices and Heterojunctions*. Prentice Hall, Upper Saddle River, N.J.; London, 1 edition edition, December 2009.

[181] R. E. Hummel. *Electronic Properties of Materials*. Springer New York, New York, NY, 2011.

[182] B. Julsgaard and K. Mølmer. Reflectivity and transmissivity of a cavity coupled to two-level systems: Coherence properties and the influence of phase decay. *Phys. Rev. A*, 85:013844, 2012.

[183] F. Mentink-Vigier, A. Collauto, A. Feintuch, I. Kaminker, V. Tarle, and D. Goldfarb. Increasing sensitivity of pulse EPR experiments using echo train detection schemes. *J. Magn. Reson.*, 236:117–125, 2013.

[184] T. Gullion, D. B. Baker, and M. S. Conradi. New, compensated Carr-Purcell sequences. *J. Magn. Reson. (1969)*, 89(3):479–484, October 1990.

[185] C. Santori, P. Tamarat, P. Neumann, Jörg Wrachtrup, D. Fattal, R. G. Beausoleil, J. Rabeau, P. Olivero, A. D. Greentree, S. Prawer, and others. Coherent population trapping of single spins in diamond under optical excitation. *Phys. Rev. Lett.*, 97(24):247401, 2006.

[186] M. G. Shapiro, G. G. Westmeyer, P. A. Romero, J. O. Szablowski, B. Küster, A. Shah, C. R. Otey, R. Langer, F. H. Arnold, and A. Jasanoff. Directed evolution of a magnetic resonance imaging contrast agent for noninvasive imaging of dopamine. *Nat. Biotechnol.*, 28(3):264–270, 2010.

[187] T. Sleator, E. L. Hahn, C. Hilbert, and J. Clarke. Nuclear-spin noise. *Phys. Rev. Lett.*, 55(17):1742–1745, October 1985.

[188] E. M. Purcell. Spontaneous emission probabilities at radio frequencies. *Phys. Rev.*, 69:681, 1946.

[189] S. Haroche and D. Kleppner. Cavity Quantum Electrodynamics. *Physics Today*, 42(1):24, 1989.

[190] M. O. Scully and M. Suhail Zubairy. *Quantum Optics*. Cambridge University Press, 1997.

[191] D. Kleppner. Inhibited Spontaneous Emission. *Phys. Rev. Lett.*, 47(4):233–236, July 1981.

[192] I. V. Hertel and C.-P. Schulz. *Atoms, Molecules and Optical Physics 2: Molecules and Photons - Spectroscopy and Collisions*. Springer, October 2014.

[193] K. H. Drexhage. Influence of a dielectric interface on fluorescence decay time. *J. Lumin.*, 1:693–701, January 1970.

[194] G. Gabrielse and H. Dehmelt. Observation of inhibited spontaneous emission. *Phys. Rev. Lett.*, 55(1):67–70, July 1985.

[195] R. G. Hulet, E. S. Hilfer, and D. Kleppner. Inhibited Spontaneous Emission by a Rydberg Atom. *Phys. Rev. Lett.*, 55(20):2137–2140, 1985.

[196] W. Jhe, A. Anderson, E. A. Hinds, D. Meschede, L. Moi, and S. Haroche. Suppression of spontaneous decay at optical frequencies: Test of vacuum-field anisotropy in confined space. *Phys. Rev. Lett.*, 58(7):666–669, February 1987.

[197] D. J. Heinzen, J. J. Childs, J. E. Thomas, and M. S. Feld. Enhanced and inhibited visible spontaneous emission by atoms in a confocal resonator. *Phys. Rev. Lett.*, 58(13):1320–1323, March 1987.

[198] F. De Martini, G. Innocenti, G. R. Jacobovitz, and P. Mataloni. Anomalous Spontaneous Emission Time in a Microscopic Optical Cavity. *Phys. Rev. Lett.*, 59(26):2955–2958, December 1987.

[199] E. Yablonovitch. Inhibited Spontaneous Emission in Solid-State Physics and Electronics. *Phys. Rev. Lett.*, 58(20):2059–2062, May 1987.

[200] Y. Yamamoto, S. Machida, Y. Horikoshi, K. Igeta, and G. Bjork. Enhanced and inhibited spontaneous emission of free excitons in GaAs quantum wells in a microcavity. *Opt. Commun.*, 80:337 – 342, 1991.

[201] B. Gayral, J.-M. Gérard, B. Sermage, A. Lemaître, and C. Dupuis. Time-resolved probing of the Purcell effect for InAs quantum boxes in GaAs microdisks. *Appl. Phys. Lett.*, 78(19):2828–2830, May 2001.

[202] D. Englund, D. Fattal, E. Waks, G. Solomon, B. Zhang, T. Nakaoka, Y. Arakawa, Y. Yamamoto, and J. Vučković. Controlling the Spontaneous Emission Rate of Single Quantum Dots in a Two-Dimensional Photonic Crystal. *Phys. Rev. Lett.*, 95(1):013904, July 2005.

[203] J. Riedrich-Möller, L. Kipfstuhl, C. Hepp, E. Neu, C. Pauly, F. Mücklich, A. Baur, M. Wandt, S. Wolff, M. Fischer, S. Gsell, M. Schreck, and C. Becher. One- and two-dimensional photonic crystal microcavities in single crystal diamond. *Nat. Nanotechnol.*, 7(1):69–74, jan 2012.

[204] S. Schietinger, M. Barth, T. Aichele, and O. Benson. Plasmon-Enhanced Single Photon Emission from a Nanoassembled Metal-Diamond Hybrid Structure at Room Temperature. *Nano Letters*, 9(4):1694–1698, April 2009.

[205] R. C. Bialczak, M. Ansmann, M. Hofheinz, M. Lenander, E. Lucero, M. Neeley, A. D. O'Connell, D. Sank, H. Wang, M. Weides, J. Wenner, T. Yamamoto, A. N. Cleland, and J. M. Martinis. Fast Tunable Coupler for Superconducting Qubits. *Phys. Rev. Lett.*, 106(6), February 2011.

[206] J. Kerckhoff, R. W. Andrews, H. S. Ku, W. F. Kindel, K. Cicak, R. W. Simmonds, and K. W. Lehnert. Tunable Coupling to a Mechanical Oscillator Circuit Using a Coherent Feedback Network. *Phys. Rev. X*, 3:021013, 2013.

[207] N. Bloembergen. On the interaction of nuclear spins in a crystalline lattice. *Physica*, 15(3):386–426, May 1949.

[208] A. Abragam and M. Goldman. Principles of dynamic nuclear polarisation. *Rep. Prog. Phys.*, 41(3):395, 1978.

[209] T. R. Carver and C. P. Slichter. Polarization of Nuclear Spins in Metals. *Phys. Rev.*, 92(1):212–213, October 1953.

[210] D. Stoler. Equivalence Classes of Minimum Uncertainty Packets. *Phys. Rev. D*, 1(12):3217–3219, June 1970.

[211] H. P. Yuen. Two-photon coherent states of the radiation field. *Phys. Rev. A*, 13(6):2226–2243, June 1976.

[212] T. Eberle, S. Steinlechner, J. Bauchrowitz, V. Händchen, H. Vahlbruch, M. Mehmet, H. Müller-Ebhardt, and R. Schnabel. Quantum Enhancement of the Zero-Area Sagnac Interferometer Topology for Gravitational Wave Detection. *Phys. Rev. Lett.*, 104(25):251102, June 2010.

[213] The LIGO Scientific Collaboration. A gravitational wave observatory operating beyond the quantum shot-noise limit. *Nat. Phys.*, 7(12):962–965, December 2011.

[214] E. S. Polzik, J. Carri, and H. J. Kimble. Spectroscopy with squeezed light. *Phys. Rev. Lett.*, 68(20):3020–3023, May 1992.

[215] M. A. Taylor, J. Janousek, V. Daria, J. Knittel, B. Hage, H. A. Bachor, and W. P. Bowen. Biological measurement beyond the quantum limit. *Nat. Photonicsics*, 7(3):229–233, February 2013.

[216] F. Mallet, M. A. Castellanos-Beltran, H. S. Ku, S. Glancy, E. Knill, K. D. Irwin, G. C. Hilton, L. R. Vale, and K. W. Lehnert. Quantum State Tomography of an Itinerant Squeezed Microwave Field. *Phys. Rev. Lett.*, 106(22):220502, June 2011.

[217] K. W. Murch, S. J. Weber, K. M. Beck, E. Ginossar, and I. Siddiqi. Reduction of the radiative decay of atomic coherence in squeezed vacuum. *Nature*, 499(7456):62–65, July 2013.

[218] D. F. Walls. Squeezed states of light. *Nature*, 306(5939):141–146, November 1983.

[219] N. Didier, A. Kamal, W. D. Oliver, A. Blais, and A. A. Clerk. Heisenberg-Limited Qubit Read-Out with Two-Mode Squeezed Light. *Phys. Rev. Lett.*, 115(9):093604, August 2015.

[220] N. Didier, J. Bourassa, and A. Blais. Fast Quantum Nondemolition Readout by Parametric Modulation of Longitudinal Qubit-Oscillator Interaction. *Phys. Rev. Lett.*, 115(20):203601, November 2015.

[221] C. W. Gardiner. Inhibition of Atomic Phase Decays by Squeezed Light: A Direct Effect of Squeezing. *Phys. Rev. Lett.*, 56(18):1917–1920, May 1986.

[222] T. Holstein and H. Primakoff. Field Dependence of the Intrinsic Domain Magnetization of a Ferromagnet. *Phys. Rev.*, 58:1098, 1940.

[223] Z. Kurucz, J. H. Wesenberg, and K. Mølmer. Spectroscopic properties of inhomogeneously broadened spin ensembles in a cavity. *Phys. Rev. A*, 83:053852, 2011.

[224] I. Diniz, S. Portolan, R. Ferreira, J. M. Gérard, P. Bertet, and A. Auffèves. Strongly coupling a cavity to inhomogeneous ensembles of emitters: Potential for long-lived solid-state quantum memories. *Phys. Rev. A*, 84:063810, 2011.

[225] J. Kerckhoff, K. Lalumière, B. J. Chapman, A. Blais, and W. Lehnert, K.˙On-Chip Superconducting Microwave Circulator from Synthetic Rotation. *Appl. Phys. Lett.*, 4(3):034002, September 2015.

[226] M. Sliwa, K. M. Hatridge, A. Narla, S. Shankar, L. Frunzio, J. Schoelkopf, R. and H. Devoret, M.˙ Reconfigurable Josephson Circulator/Directional Amplifier. *Phys. Rev. X*, 5(4):041020, November 2015.

[227] A. Facon, E.-K. Dietsche, D. Grosso, S. Haroche, J.-M. Raimond, M. Brune, and S. Gleyzes. A sensitive electrometer based on a Rydberg atom in a Schrödinger-cat state. *Nature*, 535(7611):262–265, July 2016.

[228] H. Strobel, W. Muessel, D. Linnemann, T. Zibold, D. B. Hume, L. Pezzè, A. Smerzi, and M. K. Oberthaler. Fisher information and entanglement of non-Gaussian spin states. *Science*, 345(6195):424–427, July 2014.

[229] V. Mourik, K. Zuo, S. M. Frolov, S. R. Plissard, E. P. a. M. Bakkers, and L. P. Kouwenhoven. Signatures of Majorana Fermions in Hybrid Superconductor-Semiconductor Nanowire Devices. *Science*, 336(6084):1003–1007, May 2012.

[230] M. R. Delbecq, V. Schmitt, F. D. Parmentier, N. Roch, J. J. Viennot, G. Fève, B. Huard, C. Mora, A. Cottet, and T. Kontos. Coupling a Quantum Dot, Fermionic Leads, and a Microwave Cavity on a Chip. *Phys. Rev. Lett.*, 107(25):256804, December 2011.

[231] Y.-Y. Liu, D. Petersson, K. J. Stehlik, M. Taylor, J. and R. Petta, J.˙ Photon Emission from a Cavity-Coupled Double Quantum Dot. *Phys. Rev. Lett.*, 113(3):036801, July 2014.

[232] G. Tosi, F. A. Mohiyaddin, H. Huebl, and A. Morello. Circuit-quantum electrodynamics with direct magnetic coupling to single-atom spin qubits in isotopically enriched 28Si. *AIP Advances*, 4(8):087122, August 2014.

[233] C. P. Poole. *Electron Spin Resonance: A Comprehensive Treatise on Experimental Techniques*. Courier Corporation, 1996.

[234] M. Mas-Torrent, N. Crivillers, C. Rovira, and J. Veciana. Attaching Persistent Organic Free Radicals to Surfaces: How and Why. *Chem. Rev.*, 112(4):2506–2527, April 2012.

[235] E. J. Hill and J. H. Burgess. Vapor deposition of thin films of DPPH and BDPA. *Thin Solid Films*, 11(1):99–103, July 1972.

[236] H. Bernien, B. Hensen, W. Pfaff, G. Koolstra, M. S. Blok, L. Robledo, T. H. Taminiau, M. Markham, D. J. Twitchen, and R. Hanson. Heralded entanglement between solid-state qubits separated by three metres. *Nature*, 497:86, 2013.

[237] J. J. Pla, K. Y. Tan, J. P. Dehollain, W. H. Lim, J. J. L. Morton, F. Zwanenburg, D. N. Jamieson, A. S. Dzurak, and A. Morello. High-fidelity readout and control of a nuclear spin qubit in silicon. *Nature*, 496:334–8, 2013.

[238] J. Koch, T. M. Yu, J. Gambetta, A. A. Houck, D. I. Schuster, J. Majer, A. Blais, M. H. Devoret, S. M. Girvin, and R. J. Schoelkopf. Charge-insensitive qubit design derived from the Cooper pair box. *Phys. Rev. A*, 76:042319, 2007.

[239] J. Gambetta, A. Blais, D. I. Schuster, A. Wallraff, L. Frunzio, J. Majer, M. H. Devoret, S. M. Girvin, and R. J. Schoelkopf. Qubit-photon interactions in a cavity: Measurement-induced dephasing and number splitting. *Phys. Rev. A*, 74(4):042318, 2006.

[240] A. Blais, J. Gambetta, A. Wallraff, D. I. Schuster, S. M. Girvin, M. H. Devoret, and R. J. Schoelkopf. Quantum-information processing with circuit quantum electrodynamics. *Phys. Rev. A*, 75(3):032329, March 2007.

[241] V. Schmitt, X. Zhou, K. Juliusson, B. Royer, A. Blais, P. Bertet, D. Vion, and D Esteve. Multiplexed readout of transmon qubits with Josephson bifurcation amplifiers. *Phys. Rev. A*, 90(6):062333, 2014.

[242] A. Wallraff, D. I. Schuster, A. Blais, L. Frunzio, J. Majer, M. H. Devoret, S. M. Girvin, and R. J. Schoelkopf. Approaching Unit Visibility for Control of a Superconducting Qubit with Dispersive Readout. *Phys. Rev. Lett.*, 95(6):060501, August 2005.

[243] M.D. Reed, L. DiCarlo, B. R. Johnson, L. Sun, D. I. Schuster, L. Frunzio, and R. J. Schoelkopf. High-fidelity readout in circuit quantum electrodynamics using the Jaynes-Cummings nonlinearity. *Phys. Rev. Lett.*, 105(17):173601, 2010.

[244] C. Rigetti, J. M. Gambetta, S. Poletto, B. L. T. Plourde, J. M. Chow, A. D. Córcoles, J. A. Smolin, S. T. Merkel, J. R. Rozen, G. A. Keefe, M. B. Rothwell, M. B. Ketchen, and M. Steffen. Superconducting qubit in a waveguide cavity with a coherence time approaching 0.1 ms. *Phys. Rev. B*, 86(10):100506, September 2012.

[245] D. M. Pozar. *Microwave engineering*. John Wiley & Sons, 2009.

[246] M. Boissonneault, J. M. Gambetta, and A. Blais. Dispersive regime of circuit QED: Photon-dependent qubit dephasing and relaxation rates. *Phys. Rev. A*, 79(1):013819, 2009.

université PARIS-SACLAY | ÉCOLE DOCTORALE Physique en Île-de-France (EDPIF)

Titre : Résonance magnétique avec des champs micro-ondes quantiques

Mots clés : spins, RPE, détection, sensibilité, effet Purcell, états comprimés

Résumé : Dans une expérience classique de résonance paramagnétique électronique (RPE), le couplage entre les spins et leur environnement électromagnétique est faible, limitant considérablement la sensibilité de la mesure. Grâce à l'utilisation combinée d'un amplificateur paramétrique Josephson et de micro-résonateurs supraconducteurs de hauts facteurs de qualité refroidis à quelques millikelvins, ce travail rapporte la conception et la mise en œuvre d'un spectromètre RPE dont la sensibilité de détection est limitée par les fluctuations quantiques du champ électromagnétique au lieu d'un bruit d'origine thermique ou technique. Des mesures de RPE pulsée sur un ensemble de donneurs Bismuth dans le silicium permettent de démontrer une sensibilité de 1700 spins détectés par écho de Hahn avec un signal-sur-bruit unitaire. La sensibilité est encore améliorée en générant un état de vide comprimé dans le guide d'onde de détection, ce qui réduit les fluctuations quantiques au-delà de la limite quantique. Le petit volume de mode du résonateur supraconducteur accroit également le couplage spin-résonateur jusqu'au point où les fluctuations quantiques ont un effet dramatique sur la dynamique des spins. En effet, l'émission spontanée de photons dans le résonateur micro-onde est considérablement renforcée par l'effet Purcell, ce qui en fait le mécanisme de relaxation de spin dominant. Le taux de relaxation est augmenté de trois ordres de grandeur lorsque les spins sont accordés à résonance, démontrant que la relaxation de spin peut-être contrôlée sur demande. Nos résultats fournissent une méthode nouvelle et universelle pour initialiser des systèmes de spin dans leur état fondamental, avec des applications en résonance magnétique et en information quantique.

Title : Magnetic resonance with quantum microwaves

Keywords : spins, ESR, detection, sensitivity, Purcell effect, squeezed-states

Abstract : In usual electron-spin resonance (ESR) experiments, the coupling between spins and their electromagnetic environment is quite weak, severely limiting the sensitivity of the measurements. Using a Josephson parametric microwave amplifier combined with high-quality factor superconducting micro-resonators cooled at millikelvin temperatures, this work reports the design and implementation of an ESR setup where the detection sensitivity is limited by quantum fluctuations of the electromagnetic field instead of thermal or technical noise. Pulsed ESR measurements on an ensemble of Bismuth donors in Silicon spins demonstrate a sensitivity of 1700 spins within a single Hahn echo with unit signal-to-noise (SNR) ratio. The sensitivity of the setup is improved one step further by generating squeezed vacuum in the detection waveguide, reducing the amount of noise beyond the quantum limit. The small mode volume superconducting microwave ESR resonator also enhances the spin-resonator coupling up to the point where quantum fluctuations have a dramatic effect on the spin dynamics. As a consequence, the spin spontaneous emission of microwave photons in the resonator is dramatically enhanced by the Purcell effect, making it the dominant spin relaxation mechanism. The relaxation rate is increased by three orders of magnitude when the spins are tuned to resonance, showing that spin relaxation can be engineered and controlled on-demand. Our results provide a novel and general way to initialize spin systems into their ground state, with applications in magnetic resonance and quantum information processing.

Université Paris-Saclay
Espace Technologique / Immeuble Discovery
Route de l'Orme aux Merisiers RD 128 / 91190 Saint-Aubin, France